Multimode vibronic dynamics of photo-ionized molecules and clusters

A Thesis submitted for the degree of
Doctor of Philosophy

by
Rudraditya Sarkar

School of Chemistry
University of Hyderabad
Hyderabad 500046
India

February 2017

Dedicated to my beloved GRAND MA,
family and friends...

"The true laboratory is the mind, where behind illusions we uncover the laws of truth."

Jagadish Chandra Bose.

Statement

I hereby declare that the matter embodied in this thesis is the result of investigations carried out by me in the School of Chemistry, University of Hyderabad, Hyderabad, under the supervision of Prof. Susanta Mahapatra.

In keeping with the general practice of reporting scientific observations, due acknowledgement has been made whenever the work described is based on the findings of other investigators.

Rudraditya Sarkar

February 2017
Hyderabad-500046

CERTIFICATE

This is to certify that the thesis entitled **"Multimode vibronic dynamics of photo-ionized molecules and clusters"** submitted by **Rudraditya Sarkar** bearing registration number **11CHPH07** in partial fulfilment of the requirements for award of Doctor of Philosophy in the School of Chemistry is a bonafide work carried out by him under my supervision and guidance.

The thesis is free from plagiarism and has not been submitted previously in part or in full to this or any other University or Institution for award of any degree or diploma.

Further, the student has the following publications before submission of the thesis for adjudication and has produced evidence for the same in the form of acceptance letter or the reprint in the relevant area of his research:

1. **Rudraditya Sarkar**, S. Rajagopala Reddy, S. Mahapatra and Horst. Köppel., Chem. Phys. **482**, 39, 2017. **(Chapter 3)**.

2. **Rudraditya Sarkar** and S. Mahapatra., Molecular Physics. **113**, 3073, 2015. **(Chapter 4 and Chapter 5)**.

3. **Rudraditya Sarkar** and S. Mahapatra., J. Phys. Chem. A. **120**, 3504, 2016. **(Chapter 4 and Chapter 5)**.

4. **Rudraditya Sarkar**., J. Phys. Conference series. **759**, 012058, 2016. **(Chapter 4)**.

and
has made presentations in the following conferences:

1. Oral Presentation at XXVII IUPAP Conference on Computational Physics, December 2-5 2015, IIT Guwahati, India. (International).

2. Frontiers in Electronic Structure Theory symposium, May 26-28, 2015 at Goa, India. (National).

3. Current Trends in Theoretical Chemistry symposium, September 26-28, 2013 at Bhabha Atomic Research Centre, Mumbai, India. (National).

Further, the student has passed the following courses towards fulfilment of coursework requirement for Ph.D.

Course Code	Name	Credits	Pass/Fail
1. CY-801	Research Proposal	3	Pass
2. CY-802	Chemistry Pedagogy	3	Pass
3. CY-806	Instrumental Methods B	3	Pass
4. CY-822	Symmetry and Spectroscopy	3	Pass

February 2017
Hyderabad-500046

Prof. Susanta Mahapatra
Supervisor

Prof. M. Durga Prasad
Dean of School

Acknowledgements

Some have the pleasure of seeing distinguished men in their lifetime, some have the privilege of meeting them, but I had the honor to undertake a memorable journey alongside them. I certainly am lucky to have chance of learning "Vibronic Dynamics" from one of the leading scientists in India, Professor Susanta Mahapatra. He kept on trying to teach me. Unfortunately without much success... In all my years immersed in different healing modalities, Prof. Mahapatra's relaxed approach is the deepest way of transforming darkest core issues into pure light bliss. As a navigator and explorer of transparent authenticity, he holds such a sacred space for vulnerable insights and self-revelations nourishing a sense of trust and goodness for those blessed to cross his path. I thank him for accepting me in his group. A hearty "thank you" and profound gratitude to Professor M. Durga Prasad and Professor T. P. Radhakrishnan for availability and assistance on many aspects of this arduous pursuit. I offer my enduring gratitude and deep regards to Professor Horst Köppel, Professor Samar Kumar Das and Dr. Surojit Dhara for giving me the opportunity for scientific discussion and study with them. I find myself relishing few serendipitous moments to have been under the tutelage of some outstanding scientists, spatially, Prof. L. S. Cederbaum, Prof. W. Domcke, Prof. N. Sathyamurthy, Prof. K. D. Sen, Prof. A. Samanta, Prof. D. B. Ramachary and Dr. D. Barik along the way. I cannot let this opportunity pass without expressing my gratitude to my favorite teachers, PranabDa, SwapanDa, ManasDa, AlokeDa, NasrinDi, BijoyDa, PraneshDa, GouravDa, SusantaDa, MatinDa, BulaDi, Shakti Sir, Onkar Sir, Megnath Sir, Sibnath Sir, Mujibar Sir, Ekram Sir, Gope Sir, Arun Sir, Bhakat Sir, Tapan Kar Sir, Tapan Dutta Sir, Praduth Sir, Kishore Sir, Surjyo Sir, Sibprasanna Sir and my dearest colleague and teacher Rajagopala (Sr.) who for the last few years has aided me in every possible way, whatever, whenever, and wherever it was needed. It has been a great pleasure and exciting experience to study at School of Chemistry, HCU. My sincere thanks to the former and present Deans and all the faculty members for their assistance during my Ph.D. time. I also thank all the non-teaching staff of the School of Chemistry for their assistance on various occasions. I want to use this opportunity to express my regards to Mr. Durgesh Singh and Mr. Macha V. Rao for their help and accompany in various fields of academic and non-academic perspective.

I thank Mrs. Gitashree Mahapatra (madam), Anusha and Anish for providing me a homely atmosphere in several occasions. I do not want to forget the memorable time spent with little Papai (Anish) as a hero and Pedda anna as a villian in various occasions. I cannot let this opportunity pass without expressing a special thanks to a special person of my life, Miss Sreetama Pal for her continuous support and motivation throughout this journey. Conveying special thanks to AchintyaDa (Baba), SudipDa (Jethu), SamiranDa

(BaruDa), KhairulDa, ManasDa (Gope), SabyaDa, BapiDa, ArunDa, Ranjan, Tatha, Tanmoy, Soumen, Pintu, Atanu for providing me the encourgement to pass the darkest phase of my life. A hearty "thank you" and profound gratitude to SamiranDa for providing me the energy to come back from the worst situation of my life. Thanks to PuspitaDi (JagannathDa) for a sisterly relation in Hyderabad and provide me, my favourite foods, whenever I needed.

The success of any project depends largely on the encouragement and guidelines from many individuals. This section attempts to capture a mere snapshot of my thoughts and experiences over the last five years in black and white. To start with, I express sincere appreciation to my former colleagues Siva anna, Tanmoy da (Sr.), Susanta Ghanta, Pedda anna (Rajgopal Sr.), Chinna anna (Rajgopal Jr.), Tanmoy da (Jr.) and Napanna (Nagaprasad) for their help both in professional and personal perpective. Special thanks to Chinna anna and Napaanna for their keen interest and many fruitful discussions throughout this training period. The process of working with Arun, Daradi, Divya, Sammer, Sibu, Avinash, Ligesh, Samragni and Pavel always feels organic and exciting. Thanks to Sugata, Krishna, Arpita, Arun, Jayakrushna, Karunamoy Da, Hamid, Debojyoti, Samragni and Shruti and also from MDP sir's Lab Shridhar, Dinesh, SarithaDi, LalithaDi and Prachi for offering a unique progressive atmosphere in the lab. Thanks for tolerating me over these years. Special thanks to SubrataDa for making life much more painful than it could be (Jokes apart). Thanks for your sharings and encouragement when it seemed too difficult to be completed. Constant encouragement and company from all of my friends specially Tanmoy Da (Jr.), RajaDa, NayanDa, Sugata, Suman (Layd), Navendu, Suman (Dana), Olivia, Soutrick, Sharmistha, Debobrata, Indrani, Riju, Anku, Moinak, Sanchayita, Arup, Diksha, Sandip, Ranjan (Mojo), Tathagata (Tatha), Tanmoy (Police) Arka (Gani), Soumen (Mouno), Atanu (room mate), Pintu (Sar), Biplov, Abhijeet (Santu), Malay and Atreyee (Nutu), Rimi, Appa ensured that there was always scope for subtle humor and entertainment so as to prevent the work from becoming monotonous and tiring and made it more enjoyable than one could ever expected. I really appreciate their loving support, tireless encouragement, and unfailing optimism. Thanks to all the personnel of HCU who supported me in the mechanics of producing this thesis. Also, I am grateful to numerous local and global "peers" who have contributed towards shaping this thesis.Thanks to TulikaDi, TanmoyDa (Ghanada), ShanghamitraDi, SumanDa, SantanuDa, ArpitaDi, DinuDa, RisiDa, ParomitaDi, MaityDa, AnupDa, PatiDa, NayanDa, RajaDa, SatyaDa, ShaliniDi, Mana, Pradeep, Raju, Koushik, Kallol, Subho, Olivia, Tanmoy (SKD), Arindom, Nilanjan, MehebubDa, Sabari, Mou, Shipra, Sameeta, Pritam, Suchana, Anupam, Soutrick, Alim, Navendu, Sudipta, Sneha, Apurbo, Saddam, Tasnim, Shubham, Suman, Tausif, Jaga, Sritam, Anwesha, Arijit, Bappa, Arnab, Soumen, Joy, Bhakti, Dipta, Ayan, Deepan, Parichita, Suranjan, Dayeta, Parijat, Saheli, Azahar, Mohonbagani (Saurav), Sayantan, Debottam, Khali (Ankit), Rajib, Ujjal, Atindra, Barun for offering a unique positive atmosphere and keeping the vital balance between the academic and social spheres. Apart from my bengali friends, I want to convey my regards and thanks to KishoreAnna, ChanduAnna, Ashok, Vkrant,

Sunil, GuptaAnna, HariAnna, DurgaAnna, SanatanDa, Ranjendra, Rangu, Krishna (SKD), ShekarBhaiya, Sudhir, TirupatiAnna, Raju, Abhishek Mahapatra, VigiBhaiya, DurgaAnna, SashiAnna, Zunaith, Showkat, Swati, Shruti, Kesab, BrijeshBhaiya, Jagjeet, Ankit, Ramkrishna, RameshBhaiya, GaneshBhaiya, Mahendar, Irfan, Satish for offering me homely atmosphere in School of Chemistry. Thanks for tolerating me over these years. Thanks to my cricket team (CHEM-MATH) members, NayanDa (C), Sugata, Dana, Sandeep, Sudipta, Suman, Souvik, Arup, Shakti Bhel, Showkat, Tausif, Mir, Debobrata (C), Moinak, Soutrick (C), Arnab, Avratanu, Kalyan, Jayakrushna, Debojyoti, Debottam, Mohonbagani, Khali, Krishnendu to support the team and giving us memorable journey throughout my Ph.D life. I do not want to forget to convey my regards and thanks to the team members of LYAD (football), REACTION-DYNAMICS (CCL) and School of Chemistry cricket team (School Cup) for number of memorable events.

Partial financial support from the Council of Scientific and Industrial Research (UGC-CSIR), government of India, is gratefully acknowledged. Thanks to School of Chemistry, HCU and Centre for Modelling Simulation and Design (CMSD), HCU for computer recourses. Thanks to the research grant (Grant No.SB/S1/PC-052/2013) from the Department of Science and Technology, New Delhi, India, of Professor Susanta Mahapatra for giving permission to work as a research assitant during Sep 05, 2016 - Feb 28, 2017. Thanks to Indra Krishna Naik and D. V. Sai for giving me opportunity to do work with them.

Finally, I return to my spiritual mainstay, the most basic source of life energy,my family. The very word evokes a myriad of feelings, responses, feel-good emotions, warmth, safety, welcome, love, reward and indulgence. First of all, I am indebted to my didimoni for her unconditional love, encouragement and care. Special and profound thanks to my elder brother Kanchan (Paltu) and my brother come friend Appa, who have been instrumental in the successful completion of this project through offering altruistic and steadfast support over the years. I convey special acknowledgement to Chhotomama and Mamima for taking my responsibility at home to allow me the freedom to pursue my career. I express my appreciation to my parents whose dedication, love and persistent confidence in me, has taken the load off my shoulder. I owe them for unselfishly letting their intelligence, passions, and ambitions collide with mine. Thanks Dada for always being there, for cheering me up and standing by me through the good times and bad. Certainly I am missing the epitome of elegance and hawkish, the strongest persons I have ever known, my dadu, Late Taraknath Bandopadhyay and my boroma, Late Manturani Sarkar.

-Rudraditya Sarkar

Glossary

ADT	adiabatic to diabatic transformation
BO	Born-Oppenheimer
CIs	conical intersections
CASSCF	complete active space self consistent field
CCSD	coupled cluster singles and doubles
cc-pVTZ	correlation-consistent polarized Valence Triple-ζ
DOF	degrees of freedom
DVR	discrete variable representation
EOM-CCSD	equation of motion-coupled cluster singles and doubles
FC	Franck-Condon Principle
FWHM	full width at the half maximum
HO	Harmonic oscillator
HOMO	highest occupied molecular orbital
IREP	irreducible representation
JT	Jahn-Teller
LIF	laser-induced fluorescence
LVC	linear vibronic coupling
MCTDH	multi-configuration time-dependent Hartree
MO	molecular orbital
MP2	Møller-Plesset perturbation theory
MRCI	multi-reference configuration interaction
OVGF	outer valence Greens function
PE	photo-electron
PESs	potential energy surfaces
PJT	pseudo-Jahn-Teller
QVC	quadratic vibronic coupling
REMPI	resonance-enhanced multiphoton ionization
RT	Renner-Teller
SPFs	single particle functions
TOF	time-of-flight
VC	Vibronic Coupling
VIEs	vertical ionization energies
VEEs	vertical excitation energies
WP	wave packet
ZEKE	zero electron kinetic energy

Contents

1 Introduction

Theoretical study of interactions between electronic and nuclear degrees of freedom and their impact on chemical dynamics constitutes the main theme of this thesis. It is well established that the so-called adiabatic approximation [1] breaks down to deal with nuclear dynamics of polyatomic molecular systems. While this approximation worked qualitatively well in the development of the theoretical research in chemical dynamics in initial years, the modern experiments witnessed its shortcomings to a large extent. The validity of the approximation relied on the energy gap between electronic states. This is usually larger than the relevant vibrational quanta of a molecule. Now, if two electronic states approach energetically very close to each other, this approximation remains no longer valid. The interaction of two or more electronic states through nuclear motion is termed as Vibronic coupling (VC) [2–5] in the text. The VC in polyatomic molecules is an ubiquitous phenomenon because of the availability of more nuclear degrees of freedom which goes beyond the well-known non-crossing rule [6,7]. Such coupling introduced conical intersections (CIs) of electronic potential energy surfaces (PESs) and allows the nuclei to move concurrently on more than one electronic state. The crossing of electronic PESs was historically invented in early 1930s [8–10] and an intense research in this field was started nearly two decades later of this invention. Further monumental growth on this subject [11–17] predicted a variety of physical phenomena related to the PES crossings and CIs. The latter play crucial role in various photophysical and photochemical transitions and known as photochemical funnels in the literature [18, 19]. Jahn-Teller (JT) active systems represent a well-known subclass of conically intersecting PESs, where the symmetry-enforced electronic degeneracy is lifted upon distortion along suitable symmetry reducing nuclear (vibrational) motion [10, 12, 16]. Another subclass of VC, which deals with the interaction between the components of two different degenerate electronic states or one component of split-degenerate electronic state and a non-degenerate electronic state is referred as pseudo-Jahn-Teller (PJT) interaction in the literature [15, 20–23]. While the dominating coupling goes first-order in nuclear displacement coordinates in the above case, another type of intersections of glancing type, which goes second-order or higher-order in nuclear displacement coordinates is known as Renner-Teller interactions occurs in linear systems with an axial component of electronic angular momentum [8, 9, 24].

1.1 Vibronic coupling

The occurrence of CIs of electronic states can have dramatic effects on the nuclear dynamics of polyatomic molecules. The electronic spectra become broad and with a

huge increase of vibronic line density. The adiabatic PESs have "cusp" like behavior near the vicinity of the CIs and the adiabatic electronic wavefunction diverges at CIs. A (quasi)-diabatic approach to transform the singular kinetic coupling of the adiabatic representation [15, 16, 25, 26] to smooth potential coupling is exercised to deal with this situation [27–29]. The existence of CIs in multimode system replace the avoided crossing encountered in a single mode vibronic coupling problem [7, 30]. Let us take a simple example of a model two-states vibronic coupling problem of two nondegenerate electronic states $|1\rangle$ and $|2\rangle$ of different symmetry to elucidate the above mentioned point. The total molecular Hamiltonian of the above model system can be expresed in the following form:

$$\mathcal{H} = \mathcal{T}_N \mathbf{1} + \begin{pmatrix} \mathcal{V}_{11} & \mathcal{V}_{12} \\ \mathcal{V}_{21} & \mathcal{V}_{22} \end{pmatrix}. \tag{1.1}$$

Here, $\mathcal{T}_N$ and $\mathcal{V}_i$ (i = 11, 12, 22) are the nuclear kinetic energy operator and the potential energy matrix elements within a diabatic two electronic states representation, respectively. **1** denotes the 2×2 unit matrix. The adiabatic PESs of the Hamitonian 1.1 can be written as,

$$\mathcal{V}_{\pm} = \frac{\mathcal{V}_{11} + \mathcal{V}_{22}}{2} \pm \left[\left(\frac{\mathcal{V}_{11} - \mathcal{V}_{22}}{2} \right)^2 + \mathcal{V}_{12}^2 \right]^{\frac{1}{2}} \tag{1.2}$$

If only one coupling vibrational mode is considered, then the adiabatic surfaces ($\mathcal{V}_{\pm}$) exhibit an avoided crossing-type of behavior. The totally symmetric modes present in a polyatomic system and do not mix the electronic states however only modulate the energy gap $\mathcal{V}_{11}$-$\mathcal{V}_{22}$. The totally symmetric vibrational mode transforms the avoided crossing of the single-coupling-mode problem to CIs through the modulation (tuning) of energy gap between the electronic states. This shows the importance of the combined influence of coupling and tuning vibrational modes on the electronic states. The resulting combined effect of coupling and tuning vibrational modes was initially proposed to explain the characteristic features of photoelectron spectra of C_4H_4 [4] and HCN [31]. Qualitatively, the strength of nonadiabatic interaction increases with the inclusion of more vibrational modes in the vibronic coupling, which can be traced by observing rapidly growing density of vibronic energy levels.

It is observed that even the contribution from individual tuning mode has a minor influence on the vibronic coupling problem, the combined effect of several tuning modes may be strong enough to introduce the nonadiabaticity into the dynamics of a molecule. For example, C-H stretching mode ν_1 has been found to nearly decouple from the coupling torsional vibration ν_4 in the vibronic structure of $C_4H_4^+$ [4]. It is found that the indirect tuning effect of ν_1, which is mediated by C-C stretching motion ν_2, has the profound impact on the total nonadiabaticity prevailed in the second vibronic band of $C_4H_4^+$ (cf. Figure 2 of Ref. [4]). It is suggested that great care is necessary to choose the effective vibrational mode(s) to deal with vibronic coupling problem. Another interesting fact encountered in Ref. [32, 33] is that the nonadiabatic effects can be very

strong even though a large energy separation exists between electronic states within the FC zone. The energy separation between the ground electronic state ($\widetilde{X}$) and second excited state ($\widetilde{B}$) of $CH_2F_2^+$ ∼2.00 eV at the FC zone [32]. It is found that these two states are coupled through H-C anti-symmetring stretching (ν_6) and H-C-H in-plane anti-symmetric bending (ν_7) vibrational motions. The impact of nonadiabatic effect of the ν_7 vibrational mode on the $\widetilde{X}$ state of $CH_2F_2^+$ is depicted in Figure 2b in Ref. [33]. Thus it can be concluded that the vibronic structure of well-separated electronic states can also be perturbed by nonadiabatic coupling effects.

Until now, characteristic features of the totally symmetric vibrational mode(s) on the nonadiabatic effects in the electronic states have been discussed. The effect of coupling vibrational mode(s) on the electronic states will be discussed here. The elaborated form of Eq. 1.2 in terms of vertical excitation energy (E_i, where i=1,2), second-order intrastate coupling (γ^i, where i=1,2), first-order interstate coupling (λ), ground state frequency (ω) of the coupling mode and normal coordinate (Q) along that mode is as follows:

$$V_{\pm}(Q) = \frac{1}{2}\omega Q^2 + \frac{1}{2}(\gamma^2+\gamma^1)Q^2 + \frac{1}{2}(E_1+E_2) \pm \sqrt{\left\{(E_1-E_2)+\frac{1}{2}(\gamma^2-\gamma^1)Q^2\right\}^2 + 4\lambda^2Q^2}. \quad (1.3)$$

A characteristic feature of new minima is observed in lower adiabatic surface $V_-(Q)$, whereas the upper surface becomes steeper. The symmetry of the nuclear geometry at the new minima is lower than the symmetry of equilibrium geometry of the reference state, this phenomenon is known as "the breaking of molecular symmetry". It is known that the symmetry breaking is simply a consequence of repulsion of the diabatic surfaces via the vibronic coupling [15, 34, 35]. The value of dimensionless normal coordinate at the minimum of the lower adiabatic PES is represented by following equation (excluding the γ^i):

$$Q\left(\omega - \frac{\lambda^2}{\sqrt{\left(\frac{E_2-E_1}{2}\right)^2+\lambda^2Q^2}}\right) = 0. \quad (1.4)$$

In this equation, $\Delta=\frac{E_2-E_1}{2}$ and $x=\frac{\lambda^2}{\omega_k\Delta}$ and x is a dimensionless quantity. The three roots of Eq. 1.4 have the following forms:

$$Q = 0; \quad Q = \pm\frac{\lambda}{\omega_k}\sqrt{1-\frac{1}{x^2}}. \quad (1.5)$$

If the value of $x < 1$, then the second and third roots of Eq. 1.5 become imaginary. So the validity of second and third roots remain only when $x \geq 1$ and when $x < 1$ first root $Q = 0$ is valid. As a result, two equivalent minima form at $Q \neq 0$ in the lower adiabatic

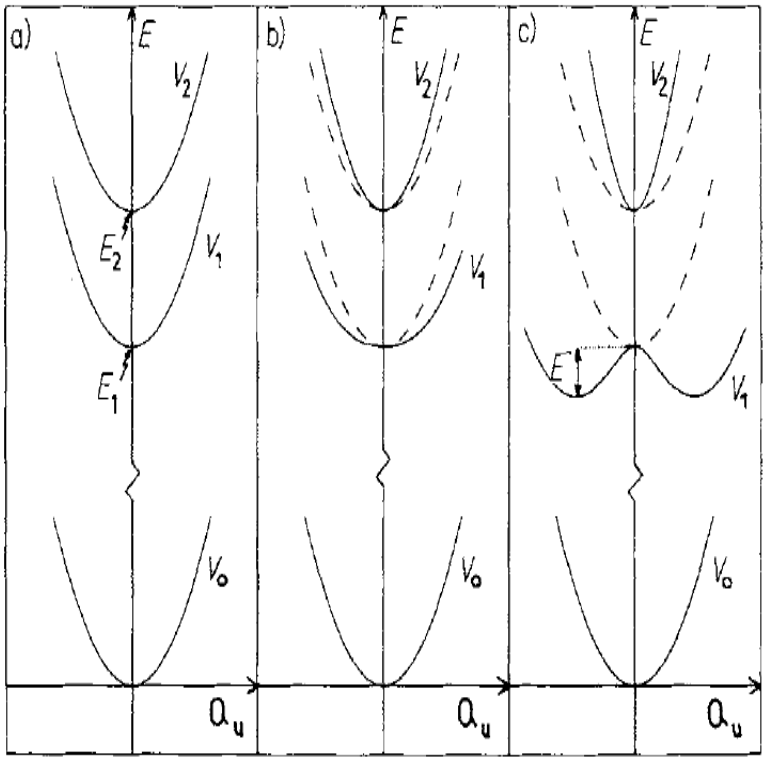

Figure 1.1: Diabatic (dashed lines) and adiabatic (full lines) torsional potential curves for the two lowest cationic states of ethylene [34] are shown here. Here, V_1 and V_2 corresponds to V_- and V_+ according to Eq. 1.3. In each case the potential curve V_0 represent the neutral ground (reference) state of ethylene, assuming the same frequency ω_o for all the states. E_1 and E_2 are the vertical ionization potentials. Vibronic coupling is shown only for the ionic states: a) a case of zero coupling, λ=O, b) the limit of weak vibronic coupling, $x < 1$ and c) a case of strong vibronic coupling, $x > 1$. E is the stabilization energy in case of strong vibronic coupling problem, depicted in panel c. The figure is reproduced from Ref. [34].

PES when $x > 1$ and the previous minimum at $Q = 0$ is converted to local maximum. The stabilization energy due to this symmetry breaking phenomenon is $E_s = \Delta(\frac{(1-x)^2}{2x})$. No symmetry breaking occur for $x < 1$ and molecule does not get any stabilization due to this phenomenon. Only just above the threshold value of $x = 1$, the stabilization energy quadratically increases with x, whereas at the larger value of x, a linear dependence is observed. The pictorial representation of the above discussion is presented in Fig. 1.1.

After inclusion of M number of coupling vibrational modes in Eq. 1.4, the generalized formula of x becomes:

$$x = \sum_{k=1}^{M} x_k. \tag{1.6}$$

Where, x_k is the dimensionless x parameter for k^{th} coupling mode and $x_k = \frac{\lambda_k^2}{\omega_k \Delta}$. It is seen from Eq. 1.6 that due to multi-mode effect x is generated from the contribution (x_k) of each coupling vibrational mode. In this way symmetry breaking phenomenon of a molecule becomes cumulative effect of all coupling vibrational modes. So in order to give an explanation of Eq. 1.6, one can say that if a single coupling vibrational mode fails to introduce a minimum at $V_-(Q)$ at $Q \neq 0$, then due to the multi-mode effect of the other coupling vibrational modes, there is a possibility to form a minimum in the Q sub-space under the condition of $x \geq 1$. The symmetry breaking by a single coupling mode is a well-known phenomenon and it is discussed several times in the literatures [15, 36–43]. It is found that symmetry breaking occurs at the lower adiabatic coupled $\widetilde{A}$-$\widetilde{B}$ surfaces of $CH_2F_2^+$ due to the cumulative effect of F-C antisymmetric stretching (ν_8) and H-C-H out-of-plane symmetric bending (ν_9) vibrational motions [35].

1.2 The Jahn-Teller effect

In contrast to the discussion above, yet another type of CIs is formed in JT active system. This is symmetry enforced in a non-linear system, the electronic degeneracy is lifted upon distortion along a JT active vibrational mode. The lifting of degeneracy causes symmetry breaking of molecular system, which develops a reduced symmetry equilibrium minimum [44–46]. It is established that non-totally symmetric vibrational modes lift the degeneracy of degenerate electronic states and the JT effect corresponds to vibronic coupling between these split components of the degenerate electronic states [2,7,12,47–49]. The two-fold degeneracy (E) of a molecule with three (six) fold symmetry is lifted by degenerate mode of e symmetry. This is known as $E \otimes e$ JT effect [12, 15, 16, 50–52]. Likewise, the two fold degeneracy of molecules possessing two or four fold axis of symmetry, belonging to, C_4, C_{4v}, C_{4h}, D_4, D_{2d}, D_{4h}, S_4, and D_{4d} symmetry point groups, the vibrational modes of b symmetry lifts the degeneracy and is known as $E \otimes \beta$ JT effect [12, 15, 16, 47, 53–59].

Let us consider the Hamiltonian of Eq. (1.1). The inclusion of one totally symmetric vibrational mode along with the coupling mode in the Hamiltonian of Eq. (1.1), makes it a two-states-two-mode problem. Then the eigen value form of Eq. (1.2) becomes more

complicated and it has the following form in linear coupling scheme:

$$V_{\pm}(Q_g, Q_u) = \frac{1}{2}\omega_g {Q_g}^2 + \frac{1}{2}\omega_u {Q_u}^2 + \frac{1}{2}(E_1 + E_2) + \frac{1}{2}\kappa^1 Q_g + \frac{1}{2}\kappa^2 Q_g \pm \sqrt{\{(E_2 - E_1) + (\kappa^2 - \kappa^1)Q_g\}^2 + 4\lambda^2 {Q_u}^2}. \quad (1.7)$$

Here, g stands for totally symmetric representation and u stands for non-totally symmetric representation. κ is the first-order intra-state coupling parameter for totally symmetric mode and other parameters are already described in Section 1.1. Now, we consider a special case of a doubly degenerate electronic state with $E_1 = E_2 = E$, $\kappa^2 = -\kappa^1 = \lambda$, $Q_g^2 + Q_u^2 = Q^2$ and $\omega_g = \omega_u = \omega$ that correspond to the $E \otimes e$-JT case. With these Eq. (1.7) modifies to

$$V_{\pm}(Q) = \frac{1}{2}\omega Q^2 + E \pm \lambda Q. \quad (1.8)$$

Where Q is the dimensionless normal coordinate of one component of the degenerate vibrational mode. This creates a "Mexican Hat" type PESs in E⊗e Jahn-Teller problem. In this case curve crossing occurs at the symmetric configuration of the nuclei between the two components of the degenerate electronic states and at this configuration the potential gradient with respect to some JT-active vibrational coordinate is nonzero. This gives rise to linear JT coupling and degeneracy of the electronic state lifts upon the distortion along that vibrational coordinate. Two symmetric energetic minima form along the JT-active vibrational coordinate and the molecule stabilizes due to first-order or linear JT effect. The presence of second-order or higher order JT couplings makes the situation more complicated by hindering the molecule to pseudorotate around the potential energy moat. As a result of this, the existence of one local minimum and one local maximum is observed instead of two symmetric minima in PES and PES becomes "tricon" in two dimensional subspace. A beautiful pictorial description of the above discussion is available in the Fig. 1 of Ref. [60] and here it is reproduced in Fig. 1.1. The details of the figure is described in the figure caption. The pictorial description of a general CI found in a photochemical reaction and JT CI is reproduced from Ref. [61] and presented in Fig. 1.2. It is not always necessary to cross PES to observe the JT activity. Accidental mixing of electronic states through vibronic coupling is named as pseudo-Jahn-Teller (PJT) effect. As its name implies, it is closely related to Jahn-Teller effect and there is no necessity of curve crossing or electronic degeneracy to observe the PJT effect in the molecule. The only requirement is the energetic proximity between electronic states.

Another important aspect of JT effect, static and dynamic JT effect, is discussed in this paragraph. A strong JT coupling which distorts the molecule permanently to the lower symmerty point group is called static JT effect. In this case potential well of the distorted molecule becomes very deep and vibronic energy levels are mainly localized in that potential well. That is why, it is suitable to construct Hamiltonian at the point

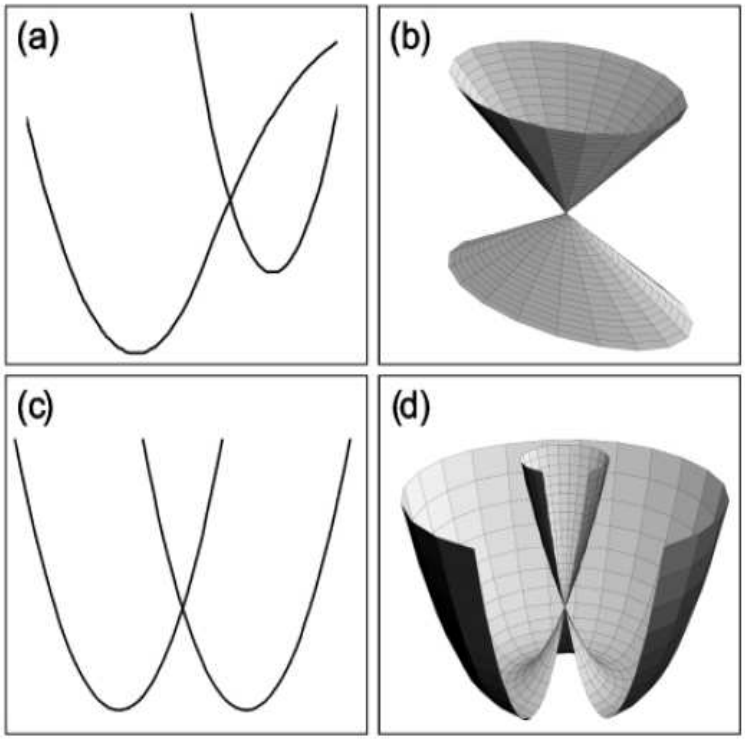

Figure 1.2: Examples of conical intersections. (a) A cut through a molecule's PES illustrating a conical intersection of two electronic surfaces, such as that found along the reaction path in many organic photochemical reactions. (b) An expanded view in three dimensions of the CI illustrated in (a). (c) A cut through a PES with a JahnTeller CI. (d) The three-dimensional form of the PES for a JahnTeller CI. The figure is reproduced from the Ref. [61].

group of distorted molecule for the analysis of the vibronic energy levels of this type of JT activity. On the other hand, in case of dynamic JT effect, the JT coupling is moderate and an equilibrium exists between the higher symmetric and the lower symmetric molecular structure. Thus, the Hamiltonian at the higher symmetric point group of molecule is often used to analyse the dynamic JT effect.

1.3 Connection with experiment

Photoelectron (PE) spectroscopy measurement is one of the direct tool to probe the core as well as the valence electronic structure of molecules [62, 63]. The Koopmans' theorem [64] is validated by this experiment. Helium (He) discharge lamp is applied to ionize the molecule and then kinetic energy distribution of the photoelectrons yields the spectrum. This procedure qualitatively provides the adiabatic ionization energy of molecules. The conventional PE spectroscopy cannot achieve a resolution more than 800 cm^{-1} [65]. Consequently, the vibronic energy levels appear as a broad structure

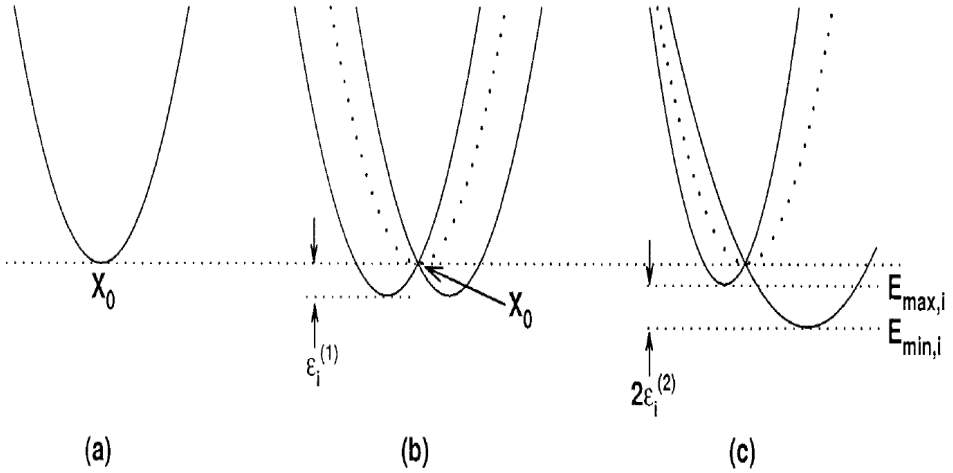

Figure 1.3: Slices through the JT PES. Curves (a), (b), and (c) are slices through the surface that correspond to (i) zero JT coupling, (ii) nonzero linear JT coupling and (iii) nonzero linear and nonzero quadratic JT coupling, respectively. In curves (b) and (c), the dotted lines correspond to the average potential, which is a harmonic curve. The figure is reproduced from the Ref. [60].

in this measurement. Recent technique of Zero Kinetic Energy pulsed-field-ionization-energy (PFI-ZEKE) spectroscopy, developed by Müller-Dethlefs, Schlag, and coworkers [66–70], provides the PE spectrum with a resolution of $\sim$1 cm^{-1} or less. The main difference between the conventional PE spectroscopy and the ZEKE spectroscopy lies in the basic principles of the respective techniques. In case of conventional PE spectroscopy molecules are used to stay at ambient temperature in their ground state. Then molecules are excited by a single photon, which removes one electron from the occupied (valence) molecular orbital (MO) and the excess energy of the photon is carried away by the ejected electron as its kinetic energy. The PE spectrum is defined as the intensity of the ejected electron as a function of its kinetic energy. The gas-phase PE spectra are usually measured at ambient or elevated temperatures, vibrational congestion causes additional overlap between the ionization bands. Thus, it is very difficult to get exact adiabatic ionization energy of a molecule by conventional PE spectroscopy. To overcome the drawbacks of conventional PE spectroscopy, Müller-Dethlefs and coworkers [66–70] developed the PFI-ZEKE experiments, where molecules are excited to their first excited state by a photon and then a second photon is used to ionize the molecule. A supersonic jet expansion is applied to keep the molecule vibrationally cold (all ν_i=0). So in ZEKE spectroscopy excitation starts from a vibrationless ground state of the molecule with first photon and then second photon with exactly enough energy is applied to ionize the molecule to a given vibrational level of the ion. In that way, care is taken to produce the ejected electrons with zero kinetic energy. A outline of the ZEKE experiment is given below, where we have taken the example of MCH_3 radical cation as discussed in Ref. [65] to make the discussion lucid. The pictorial comparison between the conventional PE spectroscopy and ZEKE spectroscopy is shown in Fig. 1.4. The ZEKE spectroscopy

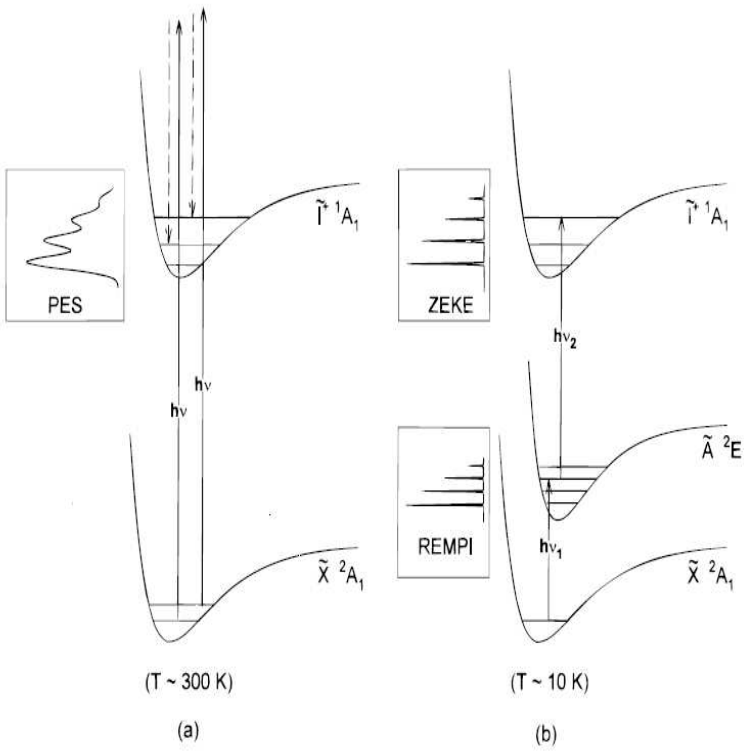

Figure 1.4: Qualitative depiction of the difference between (a) conventional photoelectron spectroscopy and (b) ZEKE spectroscopy. In PE spectroscopy, the relatively low resolution is caused by a combination of several factors: the ground-state molecule is usually at ambient temperature, the incident radiation is not monochromatic, and the high-energy kinetic electrons (the dashed arrows) formed upon ionization are kinetic-energy analyzed to produce the spectrum. In ZEKE spectroscopy, the groundstate molecule is cooled to its vibrationless level and the ionizing radiation $h\nu_2$ is nearly monochromatic. Because only "zero kinetic energy" electrons are detected, the result is much narrower spectral bands. The figure also shows the principal behind REMPI spectroscopy, in which $h\nu_2$ is kept sufficiently high in energy to ionize the excited state, while $h\nu_1$ is scanned, producing a REMPI spectrum of the excited state of the neutral radical. The figure is reproduced from Ref. [65].

of the MCH_3 radicals relies on the excitation (by $h\nu_1$) of the radicals from the ground electronic state ($\widetilde{X}^2A_1$) to its well-defined first excited state, $\widetilde{A}^2E$, from which they are ionized by a second photon. Because the radicals are cooled by supersonic expansion, nearly all of them exist in the vibrationless (all ν_i=0) level of the $\widetilde{X}^2A_1$ ground state; hence, only the ν=0 level is drawn for it in Figure 1.4b. Excitation of the radicals will occur when the first photon ($h\nu_1$), is in resonance with a transition from the vibrationless level of the ground state to a vibronic level of the excited state. The second photon ($h\nu_2$), plays the role of the photon used in a normal PE spectroscopy experiment, with

the difference being that the ionization is occurring from a resonant excited state of the radical rather than from the ground state. For the radicals discussed here, both the $\widetilde{A}^2E \leftarrow \widetilde{X}^2A_1$ and the $\widetilde{I}^{+1}A_1 \leftarrow \widetilde{A}^2E$ transitions are electric-dipole allowed. The exciting frequency $h\nu_1$ is fixed to be in resonance with one of the levels of the excited-state of neutral molecule. The ionizing frequency $h\nu_2$ is then varied. If the second photon has exactly enough energy to ionize the molecule to a given vibrational level of the ionic state, but no more, then an ion and an electron with zero kinetic energy will be created. Following ionization, any electrons with nonzero kinetic energy drift away from the ionization volume. The ZEKE electrons have no kinetic energy and remain in the ionization region. Several microseconds after the ionization, a small negative potential is applied to force the ZEKE electrons through the time-of-flight (TOF) tube, providing the signal of the ZEKE experiment. Thus, the ZEKE spectrum records the production of zero-kinetic energy electrons as a function of $h\nu_2$, and the spectrum generally consists of very sharp peaks that correspond to specific vibrational or even rotational levels of the ion. This description of ZEKE spectroscopy is somewhat simplified, but will suffice for our purposes here.

The present thesis deals with the vibronic dynamics of different cationic and neutral molecules in their ground as well as excited electronic states. The theoretical results are compared to the related available experimental data to validate the developed models. It is well known that in PE spectroscopy, electron(s) is removed from the occupied molecular orbital(s) (MOs) and produces a different system with different number of number of electrons than the parent molecule. We assumed that reference state of the neutral molecule has the simple harmonic type of potential and we treated ionization as a perturbation. The electronic potential of the target molecules (ions) is expanded in a Taylor series. Removal of an electron from the highest occupied molecular orbital (HOMO), HOMO-1, HOMO-2 ... produces the ground state, first excited state, second excited state ..., respectively, of the target molecules (ions). Ionization from the optimized geometry of the reference state produces the vertical ionization energy (VIE), which is then compared with the experimental findings. The one dimensional potential energy surfaces (1-D PESs) are calculated by distorting reference state along each normal mode and performing single point (SP) energy calculations. All the representative molecules (anions) in this thesis are nonlinear and polyatomic and hence, coupling between the electronic states and vibrational modes (vibronic coupling) is ubiquitous. We constructed diabatic molecular Hamiltonian of the representative molecules (ions) to deal with the vibronic coupling in those molecules (ions). The adiabatic potential energies evaluated by different ab initio quantum chemistry methods are equated with the diabatic to adiabatic transformation in our model Hamiltonian to get the vibronic coupling parameters. The dynamics of the representative molecules (ions) are studied by both time-independent and time-dependent quantum mechanical methods. The complex experimental PE spectra of different molecules (ions) are systematically examined through various reduced dimensional calculations. The multi-states-multi-modes diabatic Hamiltonian is split into two-states-two (multi)-modes Hamiltonian to find out

role of a particular or a set of vibrational mode(s) in the dynamics of different electronic states . This exercise helped us to find out the role of individual or collective vibrational motions in the complex structure of PE spectrum. The block-improved relaxation calculations [72, 73] as implemented in MCTDH programing module [71]. Thus the different vibrational levels of ZEKE spectrum are assigned by our theoretical calculations. In this thesis, we have studied the conventional as well as the ZEKE spectrum of CH_2F_2 (CD_2F_2), CH_3F and $H_2B_7^-$ ($D_2B_7^-$). Among these molecules (ions), CH_3F belongs to C_{3v} point group symmetry at its reference neutral geometry. It possesses electronic degeneracy in its cationic ground states and is a $E \otimes e$ JT system. Both CH_2F_2 and $H_2B_7^-$ belong to equilibrium C_{2v} point group symmetry in their respective electronic ground state. We examined the vibronic interactions of four electronic states of $CH_2F_2^+$ and five electronic states of H_2B_7.

1.4 Content of the thesis

A detailed theoretical framework of the present work is outlined in Chapter 2. The fundamental concept of adiabatic and diabatic electronic basis is illustrated. A general form of diabatic electronic Hamiltonian is presented that can be constructed with tha aid of symmetry selection rules. An extended symmetry selection rule is exercised to construct a higher-order JT Hamiltonian in three-fold symmetry point group. The strategy to estimate the parameters of the electronic Hamiltonian is described in each chapter. Technical details of the first principles quantum dynamics calculations are also discussed. Calculation of vibronic spectrum by both time-independent and time-dependent methods is discussed at length.

In Chapter 3, the Jahn-Teller effect in the degenerate $\widetilde{X}^2$E electronic ground state of CH_3F^+ is discussed in conjunction with the observed high level ZEKE spectrum. The electronic potential energy surfaces and the coupling surfaces are calculated employing state-of-the-art ab initio quantum chemistry methods. The vibronic Hamiltonian is constructed with the aid of multimode vibronic coupling theory and symmetry selection rules. It is systematically extended to higher order in the Taylor series expansion and the parameters are carefully estimated in the present study. First principles quantum dynamics study is carried out to calculate the vibronic eigenvalue spectrum of this degenerate electronic state of CH_3F^+. The vibronic energy levels are assigned and compared with the experimental PFI-ZEKE spectrum and one photon ZEKE spectra of CH_3F^+ and also with the earlier theoretical results reported in the literature.

The vibronic coupling in the energetically lowest first four electronic states of $CH_2F_2^+$ and $CD_2F_2^+$ are discussed in Chapter 4. A model 4×4 Hamiltonian is constructed in a diabatic electronic representation employing normal coordinates of vibrational modes and standard vibronic coupling theory. Extensive ab initio quantum chemistry calculations are carried out to determine the parameters of the Hamiltonian and energetic ordering

of the electronic states. The topographical features of the latter are examined at length and several conical intersections are established. The effect and consequence of the inter-state coupling between the two energetically close-lying excited electronic states, $\widetilde{A}^2B_2$ and $\widetilde{B}^2A_1$, of $CH_2F_2^+$ is discussed in detail. The result shows that the symmetry breaking and stabilization of lower $\widetilde{A}$-$\widetilde{B}$ coupled adiabatic surface is not possible through single mode interaction rather it is possible via cumulative interaction of both coupling modes.

The vibronic structural envelope and nonradiative decay dynamics of energetically low-lying electronic states of $CH_2F_2^+$ and its isotopomer ($CD_2F_2^+$) are presented and discussed in Chapter 5. A comparison of the results obtained from the nuclear dynamics on the electronic states of these isotopomers are also discussed in this chapter. The results are compared with both broad band as well as high resolution experimental spectroscopy data available in the literature. The progression of vibrational modes in the spectra is identified, assigned and discussed in relation to the assignments available in the literature. Both time-independent and time-dependent quantum mechanical methods are used to carry out nuclear dynamics calculations.

The vibronic structure of the partially hydrogenated boron cluster, H_2B_7 is discussed in Chapter 6. Detailed electronic structures of the first five electronic states of H_2B_7 are discussed in this chapter. The topography of the 1-D potential energy surfaces along the totally symmetric vibrational modes in relation with several static points on these surfaces are discussed. Primarily, the effect of $\widetilde{X}$-$\widetilde{A}$, $\widetilde{X}$-$\widetilde{B}$ and $\widetilde{A}$-$\widetilde{B}$ interstate coupling is discussed through $\widetilde{X}$-$\widetilde{A}$-$\widetilde{B}$ coupled states dynamics on H_2B_7 and the obtained theoretical results are compared with the available experimental findings. Latter, on the basis of some speculations, $\widetilde{C}$ and $\widetilde{D}$ electronic states are included in the dynamics and a improved set of theoretical data is obtained. The calculated theoretical findings are good in acorrd with the available ZEKE spectrum study on this system.

An overall conclusion and future direction of this Ph. D work is made on Chapter 7.

References

[1] M. Born and R. Oppenheimer, Ann. Phys. (Paris) 84, 457(1927): M. Born and K. Huang, Dynamical Theory of Crystal Lattices (Clarendon, Oxford; 1954).

[2] H. Köppel, L. S. Cederbaum, and W. Domcke, J. Chem. Phys. **77**, 2014 (1982).

[3] J. von Neumann and E. P. Wigner, Physik. Z. **30**, 467 (1929).

[4] G. Herzberg and H. C. Longuet-Higgins, Discuss. Faraday. Soc. **35**, 77 (1963).

[5] S. Mahapatra, Acc. Chem. Res. **42**, 1004 (2009).

[6] G.Herzberg, Electronic Spectra and Electronic s.tructure of Polyatomic Molecules (Van Nostrand, Princeton, 1967).

[7] W. Domcke, H. Köppel, and L. S. Cederbaum, Mol. Phys. **43**, 851 (1981).

[8] E. Renner, Z. Phys. **92**, 172 (1934).

[9] E. Teller, J. Phys. Chem. **41**, 109 (1937).

[10] H. Jahn and E. Teller, Proc. Roy. Soc. London, Ser. A. **161**, 220 (1937).

[11] M. D. Sturge, Solid State Phys. **20**, 91 (1967).

[12] R. Englman, The Jahn-Teller Effect in Molecules and Crystals. (Wiley, New York, 1972).

[13] T. Carrington, Discuss. Faraday. Soc. **53**, 27 (1972).

[14] C. A. Mead and D. G. Truhlar, J. Chem. Phys. **70**, 2284 (1979).

[15] H. Köppel, W. Domcke and L. S. Cederbaum, Adv. Chem. Phys. **57**, 59 (1984).

[16] I. B. Bersuker, The Jahn-Teller Effect and Vibronic Interactions in Modern Chemistry (Plenum Press, New York, 1984); G. Fischer, Vibronic Coupling (Academic Press, New York, 1984); I. B. Bersuker and V. Z. Polinger, Vibronic Interations in Molecules and Crystals (Springer-Verlag, Berlin, 1989).

[17] W. Domcke and G. Stock, Adv. Chem. Phys. **100**, 1 (1997).

[18] F. Bernardi, M. Olivucci abd M. Robb, Isr. J. Chem. **33**, 265 (1993); Chem. Soc. Rev. **25**, 321 (1996).

[19] H. Köppel and W. Domcke, in: Encyclopedia of Computational Chemistry, P. v. R. Schleyer, Ed., (Wiley, New York), 1998).

[20] H. Köppel, L. S. Cederbaum and W. Domcke, J. Chem. Phys. **89**, 2023 (1988).

[21] M. Döscher and H. Köppel, Chem. Phys. **225**, 93 (1997).

[22] S. Mahapatra, L. S. Cederbaum and H. Köppel, J. Chem. Phys. **111**, 10452 (1999).

[23] S. Mahapatra, G. A. Worth, H. -D. Meyer, L. S. Cederbaum and H. Köppel, J. Phys. Chem. A. **105**, 5567 (2001).

[24] Ch. Jungen and A. Merer, J. Mol. Phys. **40**, 1 (1980).

[25] M. Born and R. Oppenheimer, Ann. Phys. **84**, 457 (1927).

[26] C. J. Ballhausen and A. E. Hansen, Ann. Rev. Phys. Chem. **23**, 15 (1972).

[27] W. Lichten, Phys. Rev. **131**, 229 (1963).; F. T. Smith, Phys. Rev. **179**, 111 (1969).

[28] M. Bear, Chem. Phys. Lett. **35**, 112 (1975).; Chem. Phys. **15**, 49 (1976).

[29] C. A. Mead and D. G. Truhlar, J. Chem. Phys. **77**, 6090 (1982).

[30] L. S. Cederbaum, W. Domcke, H. Köppel and W. v. Niessen, Chem. Phys. **26**, 169 (1977).

[31] H. Köppel, W. Domcke, L. S. Cederbaum and W. v. Niessen, Chem. Phys. **37**, 303 (1979).

[32] R. Sarkar and S. Mahapatra, Mol. Phys. **113**, 3073 (2015).

[33] R. Sarkar and S. Mahapatra, J. Phys. Chem. A. **120**, 3504 (2016).

[34] H. Köppel, L. S. Cederbaum, W. Domcke and S. S. Shaik, Angew. Chem. Int. Ed. Engl. **22**, 210 (1983).

[35] R. Sarkar, J. Phys:Conference Series. **759**, 012058 (2016).

[36] R. L. Fulton and M. Gouterman, J. Chem. Phys. **35**, 1059 (1961).

[37] R. L. Fulton and M. Gouterman, J. Chem. Phys. **41**, 2280 (1964).

[38] M. Gouterman, J. Chem. Phys. **42**, 351 (1965).

[39] R. Lefebvre and M. Garcia Sucre, Int. J. Quant. Chem. **1S**, 339 (1967).

[40] M. Garcia Sucre, F. Gény and R. Lefebvre, J. Chem. Phys. **49**, 458 (1968).

[41] R. L. Fulton, J. Chem. Phys. **56**, 1210 (1972).

[42] J. Brickmann, Mol. Phys. **35**, 155 (1978).

[43] S. B. Piepho, E. R. Krausz and P. N. Schatz, J. Amer. Chem. Soc. **100**, 2996 (1978).

[44] *The Jahn-Teller Effect:Fundamentals and Implications for Physics and Chemistry* edited by H. Köppel, D. R. Yarkony and H. Barentzen, Springer series in Chemical Physics 97 (2009).

[45] M. C. M. O'Brien and C. C. Chancey, Am. J. Phys. **61**, 688 (1993).

[46] H. Jhan and E. Teller, Phys. Rev. **49**, 874 (1936).

[47] M. D. Sturge, Solid State Phys. **20**, 91 (1967).

[48] J. C. Tully and R. K. Preston, J. Chem. Phys. **55**, 562 (1971).

[49] W. H. Miller and T. F. George, J. Chem. Phys. **56**, 5637 (1972).

[50] I.B. Bersuker and V.Z. Polinger, Vibronic Interactions in Molecules and Crystals. (Springer-Verlag, Berlin, 1989).

[51] I.B. Bersuker, The JahnTeller Effect. (Cambridge University Press 2006).

[52] H. Köppel, L. S. Cederbaum and S. Mahapatra, Theory of the JahnTeller Effect. in: M. Quack, F. Merkt (Eds.), Handbook of High-Resolution Spectroscopy, Wiley, New York (2011) .

[53] M. S. Child, Mol. Phys. **37**, 601 (1960).

[54] C. J. Ballhausen, Theor. Chim. Acta. **3**, 368 (1965).

[55] B. M. Hoffmann and M. A. Ratner, Mol. Phys. **35**, 901 (1978).

[56] S. Muramatsu and N. Sakamoto, J. Phys. Soc. Japan, **44**, 1640 (1978).

[57] I. B. Bersuker, Chem. Rev. **101**, 1067 (2001) and the references therein.

[58] S. Mahapatra, L. S. Cederbaum and H. Köppel, J. Chem. Phys. **111**, 10452 (1999).

[59] S. Mahapatra, G. A. Worth, H. -D. Meyer, L. S. Cederbaum, and H. Köppel, J. Phys. Chem. A. **105**, 5567 (2001).

[60] T. A. Barckholtz and T. A. Miller, J. Phys. Chem. A. **103**, 2321 (1999).

[61] B. E. Applegate, T. A. Barckholtz and T. A. Miller, Chem. Soc. Rev. **32**, 38 (2003).

[62] K. Siegbahn, ESCA Applied to Free Molecules; North-Holland: Amsterdam, 1969.

[63] D. W. Turner, Molecular Photoelectron Spectroscopy; Wiley: London, 1970.

[64] T. Koopmans, Physica. **1**, 104 (1933).

[65] T. A. Barckholtz, D. E. Powers, T. A. Miller and B. E. Bursten, J. Am. Chem. Soc. **121**, 2576 (1999).

[66] K. Müller-Dethlefs and E. W. Schlag, Annu. ReV. Phys. Chem. **42**, 109 (1991).

[67] K. Müller-Dethlefs, J. Electron Spectrosc. Relat. Phenom. **75**, 35 (1995).

[68] K. Müller-Dethlefs and E. W. Schlag, Angew. Chem., Int. Ed. Engl. **37**, 1346 (1998).

[69] P. B. Armentrout and T. Baer, J. Phys. Chem. **100**, 12866 (1996).

[70] A. Held and E. W. Schlag, Acc. Chem. Res. **31**, 467 (1998).

[71] G. A. Worth, M. H. Beck, A. Jäckle, and H.-D. Meyer, The mctdh package, version 8.4; University of Heidelberg: Heidelberg, Geramny, 2007 (see: http://mctdh.uni-hd.de).

[72] Q. Meng and H. -D. Meyer, J. Chem. Phys. **139**, 164709 (2013).

[73] D. Peláez, K. Sadri, K and H. -D. Meyer, Spectrochim. Acta, Part A.**119**, 42 (2014).

2 Theoretical methodology

2.1 Adiabatic electronic representation and breakdown of Born-Oppenheimer approximation

The molecular Hamiltonian in a time-independent Schrödinger representation can be expressed as

$$\mathcal{H}(q,Q)\Psi(q,Q) = \mathcal{E}\Psi(q,Q), \tag{2.1}$$

where the Hamiltonian ($\mathcal{H}$) and the wavefunction (Ψ) are the simultaneous function of electronic coordinate (q) and nuclear coordinate (Q). The energy of the molecular system ($\mathcal{E}$) can be obtained by solving the above eigenvalue equation. The $\mathcal{H}$ consists of kinetic and potential energy terms corresponding to the electrons and nuclei, is given by

$$\mathcal{H}(q,Q) = \mathcal{T}_e(q) + \mathcal{T}_N(Q) + \mathcal{U}(q,Q) \tag{2.2}$$

$\mathcal{T}_e$ and $\mathcal{T}_N$ are electronic and nuclear kinetic energy terms, respectively. $\mathcal{U}(q,Q)$ is the total potential energy of the molecule, which includes the electron-electron repulsion ($\mathcal{U}_{ee}(q)$), electron-nuclear attraction ($\mathcal{U}_{Ne}(q,Q)$) and nuclear-nuclear repulsion ($\mathcal{U}_{NN}(Q)$). Spin-orbit coupling, which is the function of electronic coordinates is excluded from the total potential energy of the molecule [1]

The nonseparability of $\mathcal{U}(q,Q)$ in terms of electronic and nuclear motions makes the solution of Eq. 2.2 cumbersome. The nonseparability of electronic and nuclear motions can be approximated by considering the fact that nuclei are much heavier than electrons. Hence, electrons move much faster than nuclei, classically, the change of nuclear configuration is negligible during a complete cycle of electronic motion. Thus $\mathcal{T}_N$ can be set as zero by considering the nuclei as fixed. This approximation is know as Born-Oppenheimer (BO) approximation in quantum chemistry. This is also called clamped nuclei approximation [1, 2] because at a particular electronic configuration, the nuclear configuartion is approximated as fixed. So Born-Oppenheimer adiabatic electronic states are obtained by setting $\mathcal{T}_N = 0$ and solving the fixed-nuclei electronic Schrödinger equation

$$\mathcal{H}_e(q,Q)\psi_n(q;Q) = (\mathcal{T}_e(q) + \mathcal{U}(q;Q))\psi_n(q;Q) = \mathcal{V}_n(q;Q)\psi_n(q;Q) \tag{2.3}$$

Where, $\psi_n(q;Q)$ is the BO adiabatic electronic wavefunctions and $\mathcal{V}_n(q;Q)$ is the adiabatic potential energies, respectively. These quantities depend parametrically on set

of nuclear coordinates Q. The quantity $\mathcal{V}_n(q;Q)$ converts to potential energy surfaces (PESs) by solving the above electronic Schrödinger Eq. 2.3 at different configuration of nuclei (Q). Now, the total molecular wavefunction $\psi_n(q;Q)$ can be expanded as a product of nuclear wavefunction ($\chi_n(Q)$) and parametrically depended electronic wavefunction ($\psi_n(q;Q)$) as follows:

$$\Psi_i(q,Q) = \sum_n \psi_n(q;Q)\chi_{ni}(Q). \tag{2.4}$$

Insertion of Eq. 2.3 and Eq. 2.4 into TISE of Eq. (2.1) provides the following coupled differential equations of nuclear wavefunction $\chi_n(Q)$

$$\left[\mathcal{T}_N(Q) + \mathcal{V}_n(q;Q) - \mathcal{E}\right]\chi_n(Q) = \sum_m \Lambda_{nm}(Q)\chi_m(Q) \tag{2.5}$$

where

$$\sum_m \Lambda_{nm}(Q) = -\int dq\psi_n^*(q;Q)\left[\mathcal{T}_N(Q), \psi_m(q;Q)\right] \tag{2.6}$$

Where Λ_{nm} defines the coupling between two electronic states n and m through the nuclear kinetic energy operator. This is known as nonadiabatic coupling in quantum chemistry. The quantity $\Lambda_{nm}(Q)$ can be expressed in terms of first-order and second-order derivative coupling as follows [2, 3]

$$\Lambda_{nm}(Q) = -\sum_i \frac{\hbar^2}{M_i} A_{nm}^{(i)}(Q)\frac{\partial}{\partial Q_i} - \sum_i \frac{\hbar^2}{2M_i} B_{nm}^{(i)}(Q), \tag{2.7}$$

where M_i are nuclear masses and

$$A_{nm}^{(i)}(Q) = \langle\psi_n(q;Q)|\nabla_i|\psi_m(q;Q)\rangle, \tag{2.8}$$

and

$$B_{nm}^{(i)}(Q) = \langle\psi_n(q;Q)|\nabla_i^2, |\psi_m(q;Q)\rangle \tag{2.9}$$

represents the derivative coupling vector and scalar coupling, respectively. It can be seen from Eqs. 2.8 and 2.9 that the elements of nonadiabatic matrix Λ_{nm} are the derivative of electronic wavefunctions with respect to the nuclear coordinates and nuclear kinetic energy operator is non-diagonal, whereas potential energy operator is diagonal, in adiabatic electronic representation. The off-diagonal element Λ_{nm} defines the coupling between electronic states through nuclear kinetic energy operator. If we set $\Lambda_{nm} = 0$, then one can arrive at the well-known BO or adiabatic approximation. In this situation nuclear movement is confined in one (uncoupled PES) PES only. Considering the nuclear movement, total molecular wavefunction and electonic Schrödinger equation can be now expressed as

$$\left[\mathcal{T}_N(Q) + \mathcal{V}_n(q;Q) - \mathcal{E}\right]\chi_n(Q) = 0$$

$$\Psi_i^{BO}(q,Q) = \sum_n \psi_n(q;Q)\chi_{ni}^{BO}(Q)$$

$$\left[\mathcal{T}_e(q) + \mathcal{U}(q,Q) - \mathcal{V}_n(q;Q)\right]\psi_n(q;Q) = 0 \tag{2.10}$$

This BO approximation holds for energetically widely separated PESs. The above situation can dramatically change when differenet PESs of molecule closely approach or intersect with each other. The off-diagonal elements of nonadiabatic coupling matrix Λ_{nm} become extremely large and the electronic states can strongly couple with each other. In this situation, the nuclear movement can not be confined on a single electronic state rather it gains the energy (through coupling) to move concurrently on the available relevent electronic states. In this situation, the classical approximation of large ratio of nuclear masses to electronic masses is overcome by the large derivative coupling A_{nm}. Thus BO approximation is no longer valid in this situation. Eq. 2.3 represents the electronic Schrödinger equation which can be rewritten as

$$\begin{aligned}\langle\psi_m(q;Q)|\mathcal{H}_e(q;Q)|\psi_n(q;Q)\rangle &= \langle\psi_m(q;Q)|\mathcal{V}_n(q;Q)|\psi_n(q;Q)\rangle \\ \langle\psi_m(q;Q)|\mathcal{H}_e(q;Q)|\psi_n(q;Q)\rangle &= \mathcal{V}_n(q;Q)\delta_{mn}\end{aligned}$$

After differentiation with respect to Q, the above equation transforms to

$$\mathcal{V}_n\langle\frac{\partial}{\partial Q}\psi_m|\psi_n\rangle + \langle\psi_m|\frac{\partial\mathcal{H}_e(q;Q)}{\partial Q}|\psi_n\rangle + \mathcal{V}_m\langle\psi_m|\frac{\partial}{\partial Q}\psi_n\rangle = 0 \tag{2.11}$$

$$\langle\psi_m|\frac{\partial}{\partial Q}|\psi_n\rangle = \frac{1}{(\mathcal{V}_n - \mathcal{V}_m)}\langle\psi_m|\frac{\partial\mathcal{H}_e(q;Q)}{\partial Q}|\psi_n\rangle$$

Finally, using the above equation, $A_{nm}^{(i)}(Q)$ can be expressed as Hellmann-Feynman type of relation [2, 6, 7]

$$A_{nm}^{(i)}(Q) = \frac{\langle\psi_m(q;Q)|\nabla_i\mathcal{H}_e(q;Q)|\psi_n(q;Q)\rangle}{\mathcal{V}_n(Q) - \mathcal{V}_m(Q)}, \tag{2.12}$$

where $\mathcal{H}_e$ represents the electronic Hamiltonian for fixed nuclear configuration. The derivative coupling elements of Eq. (2.12) exhibit a singularity at near degeneracy or degeneracy of the two PESs, as at this situation $\mathcal{V}_n(Q) \sim \mathcal{V}_m(Q)$ or $\mathcal{V}_n(Q) = \mathcal{V}_m(Q)$. In principle this leads to discontinuity in both the electronic wavefunction and the derivative of energy. In these circumtances the adiabatic or BO representation is completely unsuitable for the computational study of the nuclear dynamics. Inelastic atom-atom collisions and ultrafast radiationless decay of excited electronic states are the typical examples associated with the violation of the BO approximation [7, 8]. To overcome the

problem of singular derivative couplings of the adiabatic representation, the basis functions are replaced with diabatic electronic basis which are smooth and slowly varying functions of nuclear coordinates [2, 9–15].

2.2 Diabatic electronic representation

In a diabatic electronic representation, the adiabatic electronic wavefunctions, $\psi(q;Q)$, are replaced by new electronic wavefunctions, $\phi(q;Q)$, which are slowly varying functions of the nuclear coordinates. The corresponding eigenstates of these new diabatic wavefunctions may cross at the avoided crossing of the adiabatic potential energy surfaces. In this representation, the nuclear kinetic energy operator becomes diagonal and the coupling between different electronic states is introduced by potential energy operator in off-diagonal positions of the molecular Hamiltonian. Diabatic basis functions are generally constructed by a suitable unitary transformation of the adiabatic basis as shown in Eq. 2.13.

$$\phi(q;Q) = \mathbf{S}(Q)\ \psi(q;Q), \tag{2.13}$$

where $\mathbf{S}(Q)$ is the transformation matrix which reads as

$$\mathbf{S}(Q) = \begin{pmatrix} \cos\theta(Q) & -\sin\theta(Q) \\ \sin\theta(Q) & \cos\theta(Q) \end{pmatrix} \tag{2.14}$$

The matrix $\mathbf{S}(Q)$ is called the adiabatic-to-diabatic transformation (ADT) matrix. $\theta(Q)$ represents the transformation angle. The necessary condition for such transformation is that the first-order derivative couplings of Eq. (2.8) should vanish in the new representation for all nuclear coordinates [16, 17] i.e.,

$$\int dq \psi_n^*(q;Q) \frac{\partial}{\partial Q_i} \psi_m(q;Q) = 0. \tag{2.15}$$

This condition leads to the following differential equations for the transformation matrix [16, 18, 19]

$$\frac{\partial \mathbf{S}}{\partial Q_i} + \mathbf{A^{(i)}}\mathbf{S} = 0, \tag{2.16}$$

where the elements of the first-order derivative coupling matrix $\mathbf{A^{(i)}}$ are given by Eq. (2.8). A unique solution of the above equation can be obtained only when starting from a finite subspace of electronic states [17]. Therefore, rigorous diabatic electronic states of polyatomic molecular systems do not exist [17]. The concept of diabatic electronic basis was introduced quite early in the literature in the context of describing the electron-nuclear coupling in atomic collision processes [9–12] as well as in molecular spectroscopy [13, 14]. However, construction of the latter for polyatomic molecular systems is tedious and difficult since it is a problem depending on multi-coordinates rather than a single nuclear coordinate. Therefore, various approximate mathematical schemes have been

proposed in the literature [12, 19–24] to accomplish this task.

2.2.1 The model diabatic Hamiltonian

Vibronic Hamiltonian

Quasi diabatic Hamiltonian method as proposed by Köppel, Domcke and Cederbaum [2] (KDC approach) is one such approximation. It is assumed in this approximation that ground state of the reference geometry is well separated from the final (excited/inonized) states and the molecular Hamiltonian is constructed in a diabatic electronic basis. The matrix elements of the model diabatic Hamiltonian are constructed by following the symmetry selection rules. The vibronic Hamiltonian of the final states is constructed in terms of the dimensionless normal coordinates of the reference (electronic ground state of the corresponding anion or neutral species) electronic state. The dimensionless normal coordinates are obtained by performing electronic structure calculations of the reference state, employing a suitable quantum chemistry software. The mass-weighted normal coordinates (q_i) obtained during the diagonalization of the force field are then converted into the dimensionless form by following the Eq. 2.17

$$Q_i = (\omega_i/\hbar)^{\frac{1}{2}} q_i, \tag{2.17}$$

where ω_i represents the harmonic frequency of the i^{th} vibrational mode. The normal displacement coordinates Q_i represents, the displacement from the equilibrium configuration of the reference state,i.e., $\mathbf{Q} = 0$. The vibronic Hamiltonian of different photoinduced molecular process is then given by [2]

$$\mathcal{H} = (\mathcal{T}_\mathcal{N} + \mathcal{V}_0)\mathbf{1}_n + \Delta\mathcal{H}. \tag{2.18}$$

The zeroth-order or unperturbed Hamiltonian of the reference state is represented by $(\mathcal{T}_\mathcal{N} + \mathcal{V}_0)$ in Eq. 2.18. The quantity $\mathbf{1}_n$ is a $(n \times n)$ (where n depends on the number of electronic states participating in the nuclear dynamics study) unit matrix. $\Delta\mathcal{H}$ in Eq. (2.18) describes the change in the electronic energy upon excitation/ionization and which is treated as perturabation. The nuclear kinetic energy and the potential energy at the reference state in dimensionless normal coordinate representation is given in the following equations,

$$\mathcal{T}_\mathcal{N} = -\frac{1}{2}\sum_i \omega_i \left[\frac{\partial^2}{\partial Q_i^2}\right], \tag{2.19}$$

and

$$\mathcal{V}_0 = \frac{1}{2}\sum_i \omega_i Q_i^2, \tag{2.20}$$

It is assumed that all vibrational motions in this reference state are harmonic. The diagonal elements of the electronic Hamiltonian, $\Delta\mathcal{H}$, represent the diabatic potential energy surfaces of the electronic states and the off-diagonal elements represent the coupling between different diabatic surfaces. Particularly, the non-adiabaticity in the molecules is

taken care by these off-diagonal elements. In this case, different electronic states are coupled through potential energy operator. The elements of the $\Delta\mathcal{H}$ matrix can be expanded in Taylor series in terms of normal displacement coordinates as [2]

$$W_{nn}(Q) = E_n + \Sigma_i \kappa_i^{(n)} Q_i + \Sigma_{ij} \gamma_{ij}^{(n)} Q_i Q_j + ... \tag{2.21}$$

and

$$W_{nn'}(Q) = W_{nn'}(0) + \Sigma_i \lambda_i^{(nn')} Q_i + ..., \tag{2.22}$$

respectively. The quantities, κ and γ, are termed as intra-state coupling parameters. λ is the inter-state coupling parameter. These set of coupling parameters are derived by using the following equations:

$$\kappa_i^{(n)} = (\partial W_{nn}/\partial Q_i)_0 \tag{2.23}$$

$$\lambda_i^{(nn')} = (\partial W_{nn'}/\partial Q_i)_0 \tag{2.24}$$

$$\gamma_{ij}^{(n)} = \frac{1}{2}[(\partial^2 W_{nn}/\partial Q_i Q_j)_0] \tag{2.25}$$

Here E_n denotes the vertical excitation/ionization energy of the n^{th} excited electronic state from the reference state.

Vibronic Jahn-Teller Hamiltonian

The conversion of the vibronic Hamiltonian to the Jahn-Teller Hamiltonian (special case of vibronic coupling) is already discussed in Chapter 1. So, instead of details of that conversion, the representation of the Jahn-Teller Hamiltonian in dimensionless normal coordinate is discussed here. The matrix elements of the perturbed Hamiltonian is expanded in a Taylor series to get the fully coupled diabatic potential matrix for general D_{3h} or C_{3v}, $E\otimes e$ system. Particularly, this $E\otimes e$ Hamiltonian can be applied to potential energy surfaces of the degenerate states with pronounced anharmonicity. In case of less anharmonic surfaces, one can use the reduced order expansion. Following the recipe given in Ref. [24], a Taylor expansion of the (E⊗e)-JT diabatic electronic Hamiltonian matrix up to fifth order is carried out. The general form of the Hamiltonian is same as Eq. 2.18.

$$\mathcal{H} = \mathcal{H}_0 \mathbf{1} + \mathbf{\Delta}\mathcal{H}, \tag{2.26}$$

with,

$$\mathcal{H}_0 = T_N + V_0.$$

A full description of all the terms of the above equations are already given in previous section.

$$T_N = -\frac{1}{2}\sum_{i\in e}\omega_i\left[\frac{\partial^2}{\partial Q_{ix}^2}+\frac{\partial^2}{\partial Q_{iy}^2}\right], \tag{2.27}$$

$$V_0 = \frac{1}{2}\sum_{i\in e}\omega_i(Q_{ix}^2+Q_{iy}^2). \tag{2.28}$$

Here, the two components of the degenerate vibrational mode (x,y) can be represented by Q_{ix} and Q_{iy}, respectively. The diabatic electronic Hamiltonian $\Delta\mathcal{H}$ can be written as

$$\Delta\mathcal{H} = \begin{pmatrix} \mathcal{W}_{++} & \mathcal{W}_{+-} \\ \mathcal{W}_{-+} & \mathcal{W}_{--} \end{pmatrix}. \tag{2.29}$$

Following Ref. [24], the elements of the electronic Hamiltonian matrix of Eq. 2.29 are expanded in a Taylor series as:

$$\begin{aligned}
\mathcal{W}_{\pm\pm} = E_E^0 &+ \frac{1}{2!}\sum_{i\in e}a_i^{(2)}(Q_{ix}^2+Q_{iy}^2) + \frac{1}{2!}\sum_{i\in e}\sum_{j\in e,i\neq j}a_{ij}(Q_{ix}Q_{jx}+Q_{iy}Q_{jy}) \\
&+ \frac{1}{3!}\sum_{i\in e}a_i^{(3)}(2Q_{ix}^3-6Q_{ix}Q_{iy}^2) + \frac{1}{4!}\sum_{i\in e}a_i^{(4)}(Q_{ix}^4+2Q_{ix}^2Q_{iy}^2+Q_{iy}^4) \\
&+ \frac{1}{5!}\sum_{i\in e}a_i^{(5)}(2Q_{ix}^5-4Q_{ix}^3Q_{iy}^2-6Q_{ix}Q_{iy}^4) \pm \sum_{i\in e}\lambda_i^{(1)}Q_{ix} \pm \frac{1}{2!}\sum_{i\in e}\lambda_i^{(2)}(Q_{ix}^2-Q_{iy}^2) \\
&\pm \frac{1}{2!}\sum_{i\in e}\sum_{j\in e,i\neq j}\lambda_{ij}(Q_{ix}Q_{jx}-Q_{iy}Q_{jy}) \pm \frac{1}{3!}\sum_{i\in e}\lambda_i^{(3)}(Q_{ix}^3+Q_{ix}Q_{iy}^2) \\
&\pm \frac{1}{4!}\sum_{i\in e}\lambda_i^{(4)}(Q_{ix}^4-6Q_{ix}^2Q_{iy}^2+Q_{iy}^4) \pm \frac{1}{4!}\sum_{i\in e}\lambda_i^{(4')}(Q_{ix}^4-Q_{iy}^4) \\
&\pm \frac{1}{5!}\sum_{i\in e}\lambda_i^{(5)}(Q_{ix}^5-10Q_{ix}^3Q_{iy}^2+5Q_{ix}Q_{iy}^4) \pm \frac{1}{5!}\sum_{i\in e}\lambda_i^{(5')}(Q_{ix}^5+2Q_{ix}^3Q_{iy}^2+Q_{ix}Q_{iy}^4),
\end{aligned} \tag{2.30}$$

$$\mathcal{W}_{+-} = \mathcal{W}^*_{-+} = \sum_{i\in e} \lambda_i^{(1)} Q_{iy} - \sum_{i\in e} \lambda_i^{(2)} Q_{ix}Q_{iy} - \sum_{i\in e}\sum_{j\in e, i\neq j} \lambda_{ij} Q_{ix}Q_{jy}$$
$$+\frac{1}{3!}\sum_{i\in e} \lambda_i^{(3)}(Q_{ix}^2 Q_{iy}+Q_{iy}^3)+\frac{1}{4!}\sum_{i\in e} \lambda_i^{(4)}(4Q_{ix}^3 Q_{iy}-4Q_{ix}Q_{iy}^3)+\frac{1}{4!}\sum_{i\in e} \lambda_i^{(4')}(-2Q_{ix}^3 Q_{iy}-2Q_{ix}Q_{iy}^3)$$
$$+\frac{1}{5!}\sum_{i\in e} \lambda_i^{(5)}(-5Q_{ix}^4 Q_{iy} + 10Q_{ix}^2 Q_{iy}^3 - Q_{iy}^5) + \frac{1}{5!}\sum_{i\in e} \lambda_i^{(5')}(Q_{ix}^4 Q_{iy} + 2Q_{ix}^2 Q_{iy}^3 + Q_{iy}^5). \tag{2.31}$$

The various parameters introduced in Eqs. 2.30 and 2.31, have the following meaning. The x and y components of the degenerate vibrational mode in the present nomenclature are denoted by Q_{ix} and Q_{iy}, respectively. The vertical ionization energy of the degenerate state is defined as E_E^0. The parameter $\lambda_i^{(n)}$ is the n^{th} order JT coupling parameter for the degenerate vibrational modes and λ_{ij} is the inter-mode JT coupling parameter. The quantities $a_i^{(n)}$ are the n^{th} -order intra-state coupling parameter for the degenerate modes, a_{ij} is the inter-mode intra-state coupling parameters for the degenerate modes.

2.2.2 Symmetry selection rule

Symmetry selection rules are then employed to determine the possible coupling between the states:

$$\Gamma_m \otimes \Gamma_{Q_i} \otimes \Gamma_n \supset \Gamma_A, \tag{2.32}$$

where Γ_m, Γ_n and Γ_{Q_i} denote the irreducible representations (IREPs) of the electronic states m, n and the i^{th} vibrational mode, respectively. Γ_A denotes the totally symmetric representation. From above description, it should be noted that the totally symmetric vibrational modes are always active within a given electronic state. A truncation of the Taylor series in Eqs. 2.21 2.22 at the first-order term leads to the linear vibronic coupling (LVC) model [2]. In case of quadratic vibronic coupling (QVC) model, Eq. 2.32 becomes,

$$\Gamma_m \otimes \Gamma_{Q_i} \otimes \Gamma_{Q_j} \otimes \Gamma_n \supset \Gamma_A, \tag{2.33}$$

where, Q_J represents the same or other vibrational mode.

Extended symmetry selection rules for JT Hamiltonian

It is well-known that the total Hamiltonian $\hat{\mathcal{H}}$ must be invariant under the symmetry operation $\hat{\mathcal{S}}$. The derivation of the nonvanishing terms in the Taylor expansion of the Hamiltonian are identified by this invariance condition. Here, we transform the real nuclear coordinates (x, y) of the degenerate mode and the degenerate electronic functions ($\langle\psi_x|$, $\langle\psi_y|$) to their complex representation by the unitary transformation $\mathcal{U}^\dagger$,

$$\sqrt{2}\,\mathcal{U}^\dagger \begin{pmatrix} x \\ y \end{pmatrix} = \begin{pmatrix} 1 & i \\ 1 & -i \end{pmatrix} \begin{pmatrix} x \\ y \end{pmatrix} = \begin{pmatrix} x+iy \\ x-iy \end{pmatrix} = \begin{pmatrix} Q_+ \\ Q_- \end{pmatrix} \tag{2.34}$$

and

$$\mathcal{U}^{\dagger}\begin{pmatrix} \langle\psi_x| \\ \langle\psi_y| \end{pmatrix} = \frac{1}{\sqrt{2}}\begin{pmatrix} \langle\psi_x| + i\langle\psi_y| \\ \langle\psi_x| - i\langle\psi_y| \end{pmatrix} = \begin{pmatrix} \langle\psi_+| \\ \langle\psi_-| \end{pmatrix} \tag{2.35}$$

The coordinates Q_+ and Q_- and the state functions $\langle\psi_+|$ and $\langle\psi_-|$ are eigenfunctions of the symmetry operator $\hat{C}_3$ with $e^{\pm\frac{2\pi i}{3}}$. Thus these complex coordinates rotate during this operation in the following way:

$$\hat{C}_3 Q_+ = e^{+\frac{2\pi i}{3}} Q_+ \qquad \hat{C}_3 Q_- = e^{-\frac{2\pi i}{3}} Q_- \tag{2.36}$$

$$\hat{C}_3\langle\psi_+| = e^{+\frac{2\pi i}{3}}\langle\psi_+| \qquad \hat{C}_3\langle\psi_-| = e^{-\frac{2\pi i}{3}}\langle\psi_-| \tag{2.37}$$

$$\hat{C}_3|\psi_+\rangle = e^{-\frac{2\pi i}{3}}|\psi_+\rangle \qquad \hat{C}_3|\psi_-\rangle = e^{+\frac{2\pi i}{3}}|\psi_-\rangle \tag{2.38}$$

The electronic Hamiltonian in $(|\psi_+\rangle, |\psi_-\rangle)$ can be written as,

$$\hat{\mathcal{H}_e} = \sum_{i,j} |\psi_+\rangle \mathcal{H}_{+-} \langle\psi_-| \tag{2.39}$$

where, $\mathcal{H}_{+-} = \langle\psi_+|\mathcal{H}_e|\psi_-|$ and it is expanded in Taylor series up to fifth-order in Q_+, Q_- coordinate space. The diagonal element of this $\mathcal{H}_{+-}$ matrix has the following form:

$$\mathcal{H}_{++} = \langle\psi_+|\mathcal{H}_e|\psi_+\rangle \tag{2.40}$$

$$\tag{2.41}$$

$$\mathcal{H}_{++} = \sum_{p+q=0}^{5} \frac{c_{p,q}^{(++)}}{(p+q)!} Q_+^p Q_-^q \tag{2.42}$$

Invariance condition under the symmetry operations has to be applied in each term in Eq. 2.42. Let us first apply $\hat{C}_3$ operation on each of the term of Eq. 2.42.

$$\hat{C}_3 \left(|\psi_+\rangle Q_+^p Q_-^q \langle\psi_+|\right) \tag{2.43}$$

Where, the constant term $\frac{c_{p,q}^{(++)}}{(p+q)!}$ is excluded from Eq. 2.43 as symmetry operation does not have any impact on this constant term. At the end of this operation, Eq. 2.43 transforms in the follwing form:

$$e^{(p-q)\frac{2\pi i}{3}} \left(|\psi_+\rangle Q_+^p Q_-^q \langle\psi_+|\right) \tag{2.44}$$

Table 2.1: Nonvanishing terms of the Hamiltonian matrix of Eq. 2.39.

Expansion order	Diagonal $\mathcal{H}_{++} = \mathcal{H}_{--}$	Off-diagonal $\mathcal{H}_{+-} = (\mathcal{H}_{-+})^*$
0	$Q_+^0\ Q_-^0$	-
1	-	$Q_+^0\ Q_-^1$
2	$Q_+^1\ Q_-^1$	$Q_+^2\ Q_-^0$
3	$Q_+^3\ Q_-^0$ and $Q_+^0\ Q_-^3$	$Q_+^1\ Q_-^2$
4	$Q_+^2\ Q_-^2$	$Q_+^0\ Q_-^4$ and $Q_+^3\ Q_-^1$
5	$Q_+^4\ Q_-^1$ and $Q_+^1\ Q_-^4$	$Q_+^2\ Q_-^3$ and $Q_+^5\ Q_-^0$

or,

$$\left(cos(p-q)\frac{2\pi}{3} + isin(p-q)\frac{2\pi}{3}\right)(|\psi_+\rangle Q_+^p Q_-^q \langle\psi_+|) \tag{2.45}$$

The invariance condition is fullfilled by Eq. 2.45, only when, the combined value of (p, q) follows the relation $|p-q| = 0, 3, 6...$, because only in this condition Eq. 2.45 becomes unity. The same procedure is followed to find out the other off-diagonal nonvanishing terms of Eq. 2.39. It is also verified that this invariance condition is followed at the other symmetry operations, $\hat{C}_2$, $\hat{\sigma_v}$ and $\hat{\sigma_h}$. To make the analysis more easier a tabulation of nonvanishing terms of Eq. 2.39 is given in Table 2.1. The matrix representation of Eq. 2.39 can be converted into the real representation by the back transformation.

2.3 Electronic structure calculations

The estimation of the Hamiltonian parameters of the vibronic Hamiltonian (cf. Eqs. 2.21, 2.22, 2.30 and 2.31) is a computationally demanding and time-consuming task. First, the equilibrium geometry and corresponding vibrational frequencies of the reference state of the system are obtained through electronic structure calculations by quantum chemistry method (such as, MP2, CCSD, CCSD(T) etc.). In the next step, single point energy calculations are carried out along normal displacement coordinates. These single point energy calculations are performed by using for example, OVGF (ROVGF), EOM-CCSD, MCSCF and MRCI quantum chemistry method. Depending upon the electronic configuration of the system (total number of electrons, closed or open shell configuration), the most appropriate quantum chemistry method is chosen for these single point calculations. The computed excitation energies are then fit to the adiabatic Hamiltonian to extract the parameters of the Hamiltonian introduced in Eqs. 2.21, 2.22, 2.30 and 2.31. A non-linear least square fittings method or Levenberg-Marquardt algorithm [38,39] is for the fit. The ab initio potential enegy surfaces (PESs) relative to the reference geometry at $\mathbf{Q} = 0$ [29,30], are calculated by adding the potential energy of the system at its reference geometry with the calculated excitation energy along each

vibrational mode. In this thesis, we have calculated ab inito excitation points for a large normal displacement coordinate, -5.0≤Q_i≤5.00, along each normal mode. Finally, the model Hamiltonian constructed is used in the subsequent dynamics calculations.

2.4 Vibronic eigenvalue spectrum

The excitation spectrum of a molecule within the Fermi's golden rule is given by

$$P(E) = \sum_v \left|\langle \Psi_v^f | \hat{T} | \Psi_0^i \rangle\right|^2 \delta(E - E_v^f + E_0^i), \tag{2.46}$$

where the quantity $\hat{T}$ represents the transition dipole operator that describes the interaction of the electron with the external radiation of energy E during the photoexcitation/ionization process. $|\Psi_0^i\rangle$ is the initial vibronic ground state or reference state with energy E_0^i. $|\Psi_v^f\rangle$ corresponds to the final vibronic state of the photoionized/excited molecule with energy E_v^f. The reference ground electronic state is approximated to be vibronically decoupled from the other states and can be written as simple product of the electronic Φ^0 and nuclear (χ_0^0) components:

$$|\Psi_0^i\rangle = |\Phi^0\rangle|\chi_0^0\rangle, \tag{2.47}$$

The final vibronic state $|\Psi_v^f\rangle$ in the coupled electronic manifold of n interacting states is expressed as

$$|\Psi_v^f\rangle = \sum_n |\Phi^n\rangle|\chi_v^n\rangle, \tag{2.48}$$

The superscripts refer to the ground and excited states. Using Eqs. (2.47-2.48), the excitation function Eq. (2.46) is rewritten as

$$P(E) = \sum_v \left|\sum_n \tau^n \langle \chi_v^n | \chi_0^0 \rangle\right|^2 \delta(E - E_v^f + E_0^i), \tag{2.49}$$

where

$$\tau^n = \langle \Phi^n | \hat{T} | \Phi^0 \rangle \tag{2.50}$$

represent the matrix elements of the transition dipole operator of the final electronic state n. In a diabatic basis, these elements depend very weakly on nuclear coordinates Q. Hence, in the study of photoinduced processes presented in this thesis, the transition dipole matrix elements are treated as constants within the Condon approximation [31].

2.4.1 Time-independent matrix diagonalization approach

The time-independent vibronic Schrödinger equation

$$\mathcal{H}|\Psi_n^f\rangle = E_n|\Psi_n^f\rangle, \tag{2.51}$$

is solved by expanding the vibronic eigenstates $\{|\Psi_n^f\rangle\}$ in the direct product harmonic oscillator basis of the electronic ground state [2]

$$|\Psi_n^f\rangle \;=\; \sum_{\{|K_i\rangle\}} a^n_{K_1,\ldots,K_l}|K_1\rangle|K_2\rangle...|K_l\rangle|\phi_n\rangle \tag{2.52}$$

Here K^{th} level of i^{th} vibrational mode is denoted by $|K_i\rangle$. $|\phi_m\rangle$ is the electronic wavefunction. For each vibrational mode, the oscillator basis is suitably truncated in the numerical calculations. In practice, the maximum level of excitation for each mode is estimated from the convergence behavior of the spectral envelope. The Hamiltonian matrix expressed in a direct product Harmonic oscillator basis is highly sparse and is tri-diagonalized by the Lanczos algorithm [32]. The diagonal elements of the resulting eigenvalue matrix give the position of the vibronic lines and the relative intensities are obtained from the squared first component of the Lanczos eigenvectors [2,15]. The stick vibronic lines obtained from the matrix diagonalization calculations are convoluted [2] with a Lorentzian line shape function of appropriate FWHM Γ to be on par with the the experimental resolution

$$L(E) \;=\; \frac{1}{\pi}\;\frac{\frac{\Gamma}{2}}{E^2+(\frac{\Gamma}{2})^2}. \tag{2.53}$$

2.4.2 Time-dependent wavepacket propagation approach

In a time-dependent approach the Fourier representation of the Dirac delta function is used in the Fermi's golden rule, $\delta(x) = \frac{1}{2\pi}\int_{-\infty}^{+\infty} e^{ixt/\hbar}$, including the delta function, the golden rule equation transforms Eq. (2.46) to the following useful form, readily utilized in a time-dependent picture

$$P(E) \approx 2Re\int_0^\infty e^{iEt/\hbar}\langle\Psi_i(0)|\tau^\dagger e^{-i\mathcal{H}t/\hbar}\tau|\Psi_i(0)\rangle dt, \tag{2.54}$$

$$\approx 2Re\int_0^\infty e^{iEt/\hbar}\; C_i(t)\; dt. \tag{2.55}$$

In the above Eq. 2.54, the elements of the transition dipole matrix $\tau^\dagger$ is given by, $\tau^f = \langle\phi^f|\hat{T}|\phi^i\rangle$. The quantity $C_f(t) = \langle\Psi_f(0)|\Psi_f(t)\rangle$, is the time autocorrelation function of the WP initially prepared on the f^{th} electronic state and, $\Psi_f(t) = e^{-i\mathcal{H}t/\hbar}\;\Psi_f(0)$.

The time autocorrelation function is calculated above damped with a suitable time-dependent function before Fourier transformation. The usual choice has been a function of type

$$f(t) \;=\; exp[-t/\tau_r] \;\;, \tag{2.56}$$

where τ_r represents the relaxation time. Multiplying $C(t)$ with $f(t)$ and then Fourier transforming it is equivalent to convoluting the spectrum with a Lorentzian line shape function (cf., Eq. (2.53)) of FWHM, $\Gamma = 1.31/\tau_r$.

2.4.3 Propagation of wave packet by MCTDH algorithm

The matrix diagonalization approach requires huge computational overheads and is impracticable with systems of growing size in terms of the electronic and nuclear degrees of freedom. Therefore, the matrix diagonalization approach fails for large molecules and with complex vibronic coupling mechanism. The WP propagation approach within the MCTDH scheme has emerged as an alternative and very promising tool to circumvent the computational cost in such situations [33–36]. This is a grid based method which utilizes DVR basis combined with fast Fourier transformation and powerful integration schemes. The efficient multiset ansatz of this scheme allows for an effective combination of vibrational degrees of freedom and thereby reduces the dimensionality problem. In this ansatz the wavefunction for a nonadiabatic system is expressed as [34–36]

$$\Psi(Q_1,...,Q_f,t) \;=\; \Psi(R_1,...,R_p,t) \tag{2.57}$$

$$\;=\; \sum_{\alpha=1}^{\sigma}\sum_{j_1=1}^{n_1^{(\alpha)}}...\sum_{j_p=1}^{n_p^{(\alpha)}} A^{(\alpha)}_{j_1,...,j_p}(t)\prod_{k=1}^{p}\varphi_{jk}^{(\alpha,k)}(R_k,t)|\alpha\rangle, \tag{2.58}$$

where, f and p represents the number of vibrational degrees of freedom and MCTDH particles, which are combined by the vibrational degrees of freedom. α is the electronic state index, $A^{(\alpha)}_{j_1,...,j_p}$ denote the MCTDH expansion coefficients and $\varphi_{jk}^{(\alpha,k)}$ are the n_k SPFs for each degree of freedom k associated with the electronic state α. In this scheme all multi-dimensional quantities are expressed in terms of one-dimensional ones employing the idea of mean-field or Hartree approach. This provides the efficiency of the method by keeping the size of the basis optimally small. Furthermore, multi-dimensional SPFs are designed by appropriately choosing the set of system coordinates so as to reduce the number of particles and hence the computational overheads. The operational principles, successes and shortcomings of these schemes are detailed in the literature [34–36]. The Heidelberg MCTDH package [33] is employed to propagate WPs in the numerical simulations for present molecules. The spectral intensity is finally calculated using Eq. (2.54) from the time-evolved WP.

Here we provide a brief overview on the memory requirements for the MCTDH method to understand the efficiency of time-dependent WP calculations. In general, the memory required by standard method is proportional to N^f, where N is the primitive basis functions/total number of grid points. In contrast, memory needed by the MCTDH method scales as

$$memory \sim fnN + n^f \tag{2.59}$$

where, n represent the SPFs. The memory requirements can however be reduced if SPFs are used that describe a set of degrees of freedom, termed as *multimode* SPFs. By combining few (d) degrees of freedom together to form a set of particles (p=f/d), the memory requirement changes to

$$memory \sim f\tilde{n}N^d + \tilde{n}^f \tag{2.60}$$

where $\tilde{n}$ is the number of multimode functions needed for the new particles. If only single-mode functions are used i.e. d=1, the memory requirement, Eq. (2.60), is dominated by n^f. By combining degrees of freedom together this number can be reduced, but at the expense of longer product grids required to describe the multimode SPFs.

References

[1] G. Fisher, *Vibronic coupling*, Academic press, London (1984).

[2] H. Köppel, W. Domcke and L. S. Cederbaum, Adv. Chem. Phys. **57**, 59 (1984).

[3] B. H. Lengsfield and D. R. Yarkony, Adv. Chem. Phys. **82**, 1 (1992).

[4] C. J. Ballhausen and A. E. Hansen, Ann. Rev. Phys. Chem. **23**, 15 (1972).

[5] M. Born and R. Oppenheimer, Ann. Phys. **84**, 457 (1927).

[6] H. Köppel, L.S. Cederbaum and S. Mahapatra, *Theory of the JahnTeller Effect*, in *Handbook of high-resolution spectroscopy*, John Wiley & Sons, (2011).

[7] S. Mahapatra, Acc. Chem. Res. **42**, 1004 (2009).

[8] M. Baer, *Beyond Born-Oppenheimer: electronic non-adiabatic coupling terms and conical intersections*, John Wiley and Sons, (2006).

[9] W. Lichten, Phys. Rev. **131**, 229 (1963).

[10] F. T. Smith, Phys. Rev. **179**, 111 (1969).

[11] T. F. O'Malley, Adv. At. Mol. Phys. **7**, 223 (1971).

[12] T. Pacher, L. S. Cederbaum and H. Köppel, Adv. Chem. Phys. **84**, 293 (1993).

[13] H. C. Longuet-Higgins, in Advances in Spectroscopy , H. W. Thompson (Ed.), Interscience, New York, 1961, Vol. II, p.420.

[14] H. C. Longuet-Higgins, Proc. Roy. Soc. London, Ser. A, 344, 147 (1975).

[15] H. Köppel and W. Domcke: in *Encyclopedia of computational chemistry* edited by P. v. R. Schleyer, Wiley,New York (1998), p 3166.

[16] M. Baer, Chem. Phys. Lett. **35**, 112 (1975).

[17] C. A. Mead, D. G. Truhlar, J. Chem. Phys. **77**, 6090 (1982).

[18] M. Baer, Chem. Phys. **15**, 49 (1976).

[19] V. Sidis, Adv. Chem. Phys. **82**, 73 (1992).

[20] A. Thiel and H. Köppel, J. Chem. Phys. **110**, 9371 (1999).

[21] R. K. Preston and J. C. Tully, J. Chem. Phys. **54**, 4297 (1971).

[22] G. Hirsch, P. J. Bruna, R. J. Buenker, and S. D. Peyerimhoff, Chem. Phys. **45**, 335 (1980).

[23] H. J. Werner and W. Meyer, J. Chem. Phys. **74**, 5802 (1981).

[24] H. Köppel, J. Gronki, and S. Mahapatra, J. Chem. Phys. **115**, 23771 (2001).

[25] A. Viel, W. Eisfeld, J. Chem. Phys. **120**, 4603 (2004).

[26] M. J. Frisch, *et al.* Gaussian 03, Revision B. 05, Gaussian, Inc., Pittsburgh PA, 2003.

[27] K. Levenberg, Q. Appl. Math. **2**, 164 (1944).

[28] D. W. Marquardt, SIAM J. Appl. Math. **11**, 431 (1963).

[29] L. S. Cederbaum and W. Domcke, Adv. Chem. Phys. **36**, 205 (1977).

[30] L. S. Cederbaum, J. Phys. B, **8**, 290 (1975).

[31] W. Domcke, H. Köppel and L. S. Cederbaum, Mol. Phys. **43**, 851 (1981).

[32] J. Cullum and R. Willoughby, *Lanczos algorithms for large symmetric eigenvalue problems*, Birkhäuser, Boston (1985), Vols. I and II.

[33] G. A. Worth, M. H. Beck, A. Jäckle, and H. -D. Meyer, *The MCTDH Package*, Version 8.2, (2000), University of Heidelberg, Heidelberg, Germany. H. -D. Meyer, Version 8.3 (2002), Version 8.4 (2007). See http://mctdh.uni-hd.de.

[34] H. -D. Meyer, U. Manthe and L. S. Cederbaum, Chem. Phys. Lett. **165**, 73 (1990).

[35] U. Manthe, H. -D. Meyer and L. S. Cederbaum, J. Chem. Phys. **97**, 3199 (1992).

[36] M. H. Beck, A. Jäckle, G. A. Worth and H. -D. Meyer, Phys. Rep. **324**, 1 (2000).

3 The Jahn-Teller effect in the $\widetilde{X}^2$E electronic ground state of CH_3F^+

3.1 Introduction

The electronic ground $\widetilde{X}^2$E state of the methyl fluoride radical cation (CH_3F^+) is orbitally degenerate at the equlibrium geometry of the neutral molecule (CH_3F) belongs to C_{3v} point group symmetry. This orbital degeneracy is lifted upon distortion along vibrational modes of e symmetry. This so-called (E⊗e)-Jahn-Teller (JT) effect [1] leads to a coupling of the electronic and nuclear motion. As a result, the adiabatic Born-Oppenheimer (BO) approximation remains no longer valid and nuclei move concurrently on the JT split component electronic states [2–6]. These component JT states remain degenerate at the C_{3v} symmetry configuration and form conical intersections (CIs) [7–9] in multi-dimensional nuclear coordinate space. As discussed in Chapter 1, the CIs of electronic surfaces are ubiquitous in polyatomic molecular systems [2–15] and have been proven to be the mechanistic pathway of triggering ultrafast molecular processes [5, 6, 16, 17]. The associated nonadiabatic effects yield broad and complex molecular electronic spectra, and an assignment of vibronic energy levels often becomes a cumbersome task. The theoretical study in this chapter is aimed to elucidate the nature of the energetically low-lying vibronic structures of the doubly degenerate $\widetilde{X}^2$E electronic state of CH_3F^+. The motivation behind this exercise stems from recent experimental studies [18,19] on this subject. In contrast to the other halogenated methane derivatives (*e.g.* Cl, Br and I), the spin-orbit (SO) coupling is very weak (discussed later in the text) as compared to the JT coupling in CH_3F^+. Therefore, the SO coupling is not considered in this study. The first excited $\widetilde{A}^2A_1$ electronic state of CH_3F^+ is energetically well separated (∼3.64 eV) from its electronic ground state at the vertical configuration. The pseudo-Jahn-Teller (PJT) coupling of the $\widetilde{X}$-$\widetilde{A}$ states was found to be quite weak and does not influence the vibronic progressions in the low-energy part of the $\widetilde{X}$ band [20, 21]. Therefore, $\widetilde{X}$-$\widetilde{A}$ PJT coupling is also not considered in this study.

In earlier works [20, 21], the vibronic structure of the $\widetilde{X}^2$E state of CH_3F^+ was calculated with the aid of ab initio complete active space self consistent field and multi-reference configuration interaction (CASSCF-MRCI) quantum chemistry and time- independent quantum dynamics methods. Linear plus quadratic (E⊗e)-JT couplings as

[0]The subject of this Chapter is published by: Rudraditya Sarkar, S. R. Resddy, S. Mahapatra and H. Köppel in Chem. Phys.**482**, 39 (2017).

well as PJT coupling between $\widetilde{X}^2E$ and $\widetilde{A}^2A_1$ electronic states of CH_3F^+ [20, 21], were considered to understand and interpret the experimental photoelectron (PE) spectrum of Karlsson et al. [22]. Recent high resolution experimental results of Grütter [18] and Mo et al. [19] differ from the experimental findings of Karlsson et al. [22], mainly in the low energy wing of the spectrum.

In the low-energy part of the spectrum, excitation of the vibrational mode ν_2 was not found in the experiment of Grütter [18] which is consistent with earlier experiments [22, 23]. The vibrational line at ∼1300 cm^{-1} was assigned to the fundamental of ν_5 and ν_3 by Karlsson et al. [22] and Locht et al. [23], respectively. The fundamental of ν_3 and first overtone of ν_6 was reported at ∼1293 cm^{-1} and 1267 cm^{-1}, respectively, by Grütter [18]. While the fundamental of ν_6 was not found in the experiment of Grütter [18], it is tentatively assigned at ∼650 cm^{-1} in that experiment. The same peak was reported at ∼690 cm^{-1} by both Karlsson et al. [22] and Locht et al. [23]. While the fundamental of ν_6 was not found in the experiment of Grütter [18], it is reported in the experiment of Mo et al. [19] in the 101092-101954 cm^{-1} energy range, at 565 cm^{-1} from the 0_0^0 peak. In the former experiment this region of the spectrum was attributed due to absorption of residual H_2O in the sample chamber and was designated as a ″dark″ region. The combined experimental and theoretical study of Mo et al. [19] established a tunneling splitting level at 56 cm^{-1} (not found in their experimental results) of the origin 0_0^0 line and was attributed due to higher pseudo-rotation barrier along the JT-active modes ν_5 and ν_6. However, no clear assignment of this level was available.

The mentioned discrepancies motivated us to undertake this study in order to understand the origin of the observed discrepancies. In the present study we carry out new quantum chemistry calculations and critically examine the coupling parameters of the theoretical model developed in Refs. [20, 21]. As compared to the latter studies, in the present work, we devised a higher order vibronic coupling model in terms of the dimensionless normal coordinates of the electronic ground state of neutral CH_3F. The model is based on a large number of potential energy data computed ab initio over an extended range of nuclear configurations. Both one and two dimensional fittings of ab initio points are carried out in order to obtain an improved description of the electronic Hamiltonian. Using this Hamiltonian, nuclear dynamics calculations are carried out by both time-independent and time-dependent quantum mechanical methods. The results of the nuclear dynamics are compared with the recent experimental high resolution pulsed-field-ionization zero-electron-kinetic energy (PFI-ZEKE) [18] and one photon ZEKE spectra [19] as well as available theoretical results.

3.2 Theoretical framework

3.2.1 The vibronic Hamiltonian

In order to treat the nuclear dynamics in the JT split $\widetilde{X}^2$E eletronic manifold of CH_3F^+, a vibronic Hamiltonian is constructed in a diabatic electronic basis using dimensionless normal displacement coordinates (NCs) of the electronic ground state of neutral CH_3F and symmetry selection rules. Following the recipe given in Ref. [24], a Taylor expansion of the (E⊗e)-JT diabatic electronic Hamiltonian matrix up to fifth order is carried out. The nine vibrational modes of CH_3F transform according to the following irreducible representations (IREPs) of the C_{3v} equilibrium symmetry point group

$$\Gamma = 3a_1 \oplus 3e. \tag{3.1}$$

The symmetric direct product of two degenerate (E) representations yields

$$[E \otimes E]^+ = a_1 \oplus e. \tag{3.2}$$

The IREPs of electronic states and vibrational modes are denoted by the upper and lower case letters, respectively. With the above description, the vibronic Hamiltonian of the $\widetilde{X}^2$E electronic manifold of CH_3F^+ can be symbolically represented as

$$\mathcal{H} = \mathcal{H}_0\mathbf{1} + \mathbf{\Delta}\mathcal{H}, \tag{3.3}$$

with,

$$\mathcal{H}_0 = T_N + V_0.$$

In the above, $\mathcal{H}_0$ is the unperturbed Hamiltonian of the electronic ground state of neutral CH_3F, taken as a reference and treated within the harmonic approximation in the relm of standard vibronic coupling theory [2]. The term $\Delta\mathcal{H}$ represents the change in electronic energy upon ionization and $\mathbf{1}$ represents a (2×2) unit matrix. With this definition, the Hamiltonian ($\mathcal{H}_0$) for the reference state is given by [2]

$$T_N = -\frac{1}{2}\sum_{i\in a_1}\omega_i\left(\frac{\partial^2}{\partial Q_i^2}\right) - \frac{1}{2}\sum_{i\in e}\omega_i\left[\frac{\partial^2}{\partial Q_{ix}^2} + \frac{\partial^2}{\partial Q_{iy}^2}\right], \tag{3.4}$$

$$V_0 = \frac{1}{2}\sum_{i\in a_1}\omega_i Q_i^2 + \frac{1}{2}\sum_{i\in e}\omega_i(Q_{ix}^2 + Q_{iy}^2). \tag{3.5}$$

The diabatic electronic Hamiltonian $\Delta\mathcal{H}$ can be written as

$$\Delta\mathcal{H} = \begin{pmatrix} \mathcal{W}_{++} & \mathcal{W}_{+-} \\ \mathcal{W}_{-+} & \mathcal{W}_{--} \end{pmatrix}. \tag{3.6}$$

Following Ref. [24], the elements of the electronic Hamiltonian matrix of Eq. 3.6 are expanded in a Taylor series as:

$$\begin{aligned}
\mathcal{W}_{\pm\pm} = E_E^0 &+ \sum_{i\in a_1}\kappa_i^{(1)}Q_i + \frac{1}{2!}\sum_{i\in a_1}\kappa_i^{(2)}Q_i^2 + \frac{1}{2!}\sum_{i\in a_1}\sum_{j\in a_1, i\neq j}\kappa_{ij}Q_iQ_j + \frac{1}{3!}\sum_{i\in a_1}\kappa_i^{(3)}Q_i^3 + \frac{1}{4!}\sum_{i\in a_1}\kappa_i^{(4)}Q_i^4 \\
&+ \frac{1}{2!}\sum_{i\in e}a_i^{(2)}(Q_{ix}^2+Q_{iy}^2) + \frac{1}{2!}\sum_{i\in e}\sum_{j\in e, i\neq j}a_{ij}(Q_{ix}Q_{jx}+Q_{iy}Q_{jy}) \\
&+ \frac{1}{3!}\sum_{i\in e}a_i^{(3)}(2Q_{ix}^3-6Q_{ix}Q_{iy}^2) + \frac{1}{4!}\sum_{i\in e}a_i^{(4)}(Q_{ix}^4+2Q_{ix}^2Q_{iy}^2+Q_{iy}^4) \\
&+ \frac{1}{5!}\sum_{i\in e}a_i^{(5)}(2Q_{ix}^5-4Q_{ix}^3Q_{iy}^2-6Q_{ix}Q_{iy}^4) \pm \sum_{i\in e}\lambda_i^{(1)}Q_{ix} \pm \frac{1}{2!}\sum_{i\in e}\lambda_i^{(2)}(Q_{ix}^2-Q_{iy}^2) \\
&\pm \frac{1}{2!}\sum_{i\in e}\sum_{j\in e, i\neq j}\lambda_{ij}(Q_{ix}Q_{jx}-Q_{iy}Q_{jy}) \pm \frac{1}{2!}\sum_{i\in a_1}\sum_{j\in e}b_{ij}Q_iQ_{jx} \\
&\pm \frac{1}{3!}\sum_{i\in e}\lambda_i^{(3)}(Q_{ix}^3+Q_{ix}Q_{iy}^2) \pm \frac{1}{4!}\sum_{i\in e}\lambda_i^{(4)}(Q_{ix}^4-6Q_{ix}^2Q_{iy}^2+Q_{iy}^4) \pm \frac{1}{4!}\sum_{i\in e}\lambda_i^{(4')}(Q_{ix}^4-Q_{iy}^4) \\
&\pm \frac{1}{5!}\sum_{i\in e}\lambda_i^{(5)}(Q_{ix}^5-10Q_{ix}^3Q_{iy}^2+5Q_{ix}Q_{iy}^4) \pm \frac{1}{5!}\sum_{i\in e}\lambda_i^{(5')}(Q_{ix}^5+2Q_{ix}^3Q_{iy}^2+Q_{ix}Q_{iy}^4), \quad (3.7)
\end{aligned}$$

$$\begin{aligned}
\mathcal{W}_{+-} = \mathcal{W}_{-+}^* &= \sum_{i\in e}\lambda_i^{(1)}Q_{iy} - \sum_{i\in e}\lambda_i^{(2)}Q_{ix}Q_{iy} - \sum_{i\in e}\sum_{j\in e, i\neq j}\lambda_{ij}Q_{ix}Q_{jy} + \frac{1}{2!}\sum_{i\in a_1}\sum_{j\in e}b_{ij}Q_iQ_{jy} \\
&+ \frac{1}{3!}\sum_{i\in e}\lambda_i^{(3)}(Q_{ix}^2Q_{iy}+Q_{iy}^3) + \frac{1}{4!}\sum_{i\in e}\lambda_i^{(4)}(4Q_{ix}^3Q_{iy}-4Q_{ix}Q_{iy}^3) + \frac{1}{4!}\sum_{i\in e}\lambda_i^{(4')}(-2Q_{ix}^3Q_{iy}-2Q_{ix}Q_{iy}^3) \\
&+ \frac{1}{5!}\sum_{i\in e}\lambda_i^{(5)}(-5Q_{ix}^4Q_{iy}+10Q_{ix}^2Q_{iy}^3-Q_{iy}^5) + \frac{1}{5!}\sum_{i\in e}\lambda_i^{(5')}(Q_{ix}^4Q_{iy}+2Q_{ix}^2Q_{iy}^3+Q_{iy}^5).
\end{aligned} \quad (3.8)$$

The various parameters introduced in Eqs. 3.7-3.8 have the following meaning. The x and y components of the degenerate vibrational mode in the present nomenclature are denoted by Q_{ix} and Q_{iy}, respectively. The vertical ionization energy of the $\widetilde{X}^2E$ state is defined as E_E^0, $\kappa_i^{(n)}$ is the n^{th} order intra-state coupling constant for the totally symmetric modes, κ_{ij} is the inter-mode intra-state coupling constant for the totally symmetric modes, $\lambda_i^{(n)}$ is the n^{th} order inter-state JT coupling parameter for the degenerate vibrational modes and λ_{ij} is the inter-mode inter-state JT coupling parameter. It is noted that there are two independent coupling terms in 4^{th} and 5^{th} order expansion with even similarly large coupling constants (see below). The quantities $a_i^{(n)}$ are the n^{th} -order intra-state coupling parameter for the degenerate modes, a_{ij} is the inter-mode intra-state coupling parameters for the degenerate modes and b_{ij} is the bilinear coupling parameter between totally symmetric and degenerate modes. The vibronic Hamiltonian

constructed above is utilized below to examine the static and dynamic aspects of the JT effects in the $\widetilde{X}^2$E state of CH_3F^+.

3.2.2 Nuclear dynamics

The vibronic energy level structure of the photoionization band of CH_3F^+ is calculated by a time-independent matrix diagonalization approach [2, 25]. The spectral intensity, $P(E)$, is calculated by Fermi's golden rule,

$$P(E) = \sum_n |<\Psi_n^f|\hat{T}|\Psi_0^i>|^2 \delta(E - E_n^f + E_0^i) \quad . \tag{3.9}$$

In the above equation, $|\Psi_0^i>$ and $|\Psi_n^f>$ represent the initial and final vibronic states with energies E_0^i and E_n^f, respectively. The operator $\hat{T}$ is the transition dipole operator, which describes the transition from the reference neutral state to the cationic state with the aid of external radiation of energy E. The ground state $|\Psi_0^i>$ (ground state of neutral CH_3F) is assumed to be vibronically decoupled from the excited electronic states and can be written as

$$|\Psi_0^i\rangle = |\Phi_0^i\rangle|\chi_0^i\rangle, \tag{3.10}$$

where $|\Phi_0^i\rangle$ and $|\chi_0^i\rangle$ represent the electronic and vibrational components of this state, respectively. This state is assumed to be harmonic and the vibrational component of the above wavefunction is expressed in terms of the eigenfunctions of the reference Hamiltonian, $T_N + V_0$ [(cf. Eqs. 3.4-3.5] . These are, in practice, taken as the direct product of one-dimensional harmonic oscillator wavefunctions along the coordinates of all relevant vibrational modes. The final vibronic state of the $\widetilde{X}^2$E electronic state of CH_3F^+ can be expressed as

$$|\Psi_n^f\rangle = |\Phi^{E_x}\rangle|\chi_n^{E_x}\rangle + |\Phi^{E_y}\rangle|\chi_n^{E_y}\rangle, \tag{3.11}$$

where the superscripts E_x and E_y represent the x/y components of the $\widetilde{X}^2E$ electronic state of CH_3F^+, respectively. With the above definitions the spectral intensity of Eq. 3.9 can be rewritten as

$$P(E) = \sum_n |\tau^{E_x}\langle\chi_n^{E_x}|\chi_0\rangle + \tau^{E_y}\langle\chi_n^{E_y}|\chi_0\rangle|^2 \delta(E - E_n^f + E_0^i), \tag{3.12}$$

where,

$$\tau^m = \langle\Phi^m|\hat{T}|\Phi^0\rangle, \qquad m = \ E_x, \ E_y \tag{3.13}$$

represents the transition dipole matrix elements. These are treated as constants (see Eqs. 3.12, 3.13) in accordance with the applicability of the Condon approximation in a diabatic electronic basis [2]. The time-independent Schrödinger equation of the vibronically coupled states is solved by representing the Hamiltonian (cf. Eqs. 3.4-3.8) in a direct product harmonic oscillator (HO) basis of the reference state. The final

vibronic states, $|\Psi_n^f\rangle$, can be expressed as

$$|\Psi_n^f\rangle = \sum_{|K_i\rangle,m} a^n_{k_i,\ldots,k_f,m}|K_i\rangle\ldots|K_f\rangle|\Phi_m\rangle. \tag{3.14}$$

In the above equation the K^{th} quantum of the i^{th} vibrational mode is denoted by $|K_i\rangle$ and $|\Phi_m\rangle$ denotes the m^{th} electronic state of the interacting electronic manifold of CH_3F^+ radical cation. For each vibrational mode, the oscillator basis is suitably truncated in the numerical calculations. In practice, the maximum level of excitation for each vibrational mode can be approximately estimated from its excitation strength, $(\frac{\kappa_i^2}{2\omega_i^2})$ and $(\frac{\lambda_i^2}{2\omega_i^2})$ for the symmetric and degenerate modes, respectively. The Hamiltonian matrix expressed in a direct product HO basis is highly sparse. We tri-diagonalize this sparse Hamiltonian matrix employing the Lanczos algorithm [26] prior to its diagonalization. The diagonal elements of the resulting eigenvalue matrix give the positions of the vibronic lines and the relative intensities are calculated from the squared first components of the Lanczos eigenvectors [27].

In a time-dependent picture, the spectral intensity described by Eq. 3.12 relates to the Fourier transform of the time autocorrelation function of the wave packet (WP) propagating on the final electronic state [28]

$$P(E) \sim \sum_{m=1}^{2} 2Re\int_0^\infty e^{iEt/\hbar}\langle\chi_0|\tau^{m\dagger}e^{-iHt/\hbar}\tau^m|\chi_0\rangle dt, \tag{3.15}$$

$$\approx \sum_{m=1}^{2} 2Re\int_0^\infty e^{iEt/\hbar}C^m(t)dt, \tag{3.16}$$

where, $C^m = \langle\Psi^m(0)|\Psi^m(t)\rangle$, represents the time autocorrelation function of the WP, initially prepared on the electronic state m. The time-dependent WP propagation is carried out employing the multi-configuration time dependent Hartree (MCTDH) approach. For the details of this approach the reader is referred to the comprehensive literature [29–31]. The Heidelberg MCTDH program modules are used for the numerical calculations [32].

3.2.3 Details of electronic structure calculations

The equilibrium geometry of the reference electronic ground state of CH_3F is calculated by the Møller-Plesset perturbation (MP2) theory employing the cc-pVTZ basis set of Dunning [33]. The GAUSSIAN-03 suite of programs [34] is used for this purpose. The optimized equilibrium structure of CH_3F belongs to the C_{3v} symmetry point group. The optimized equilibrium structural parameters are given in Table 3.1 along with recent literature data. The molecular orbital (MO) sequence of the optimized configuration of CH_3F is, $(1a_1)^2$ $(2a_1)^2$ $(3a_1)^2$ $(4a_1)^2$ $(1e)^2$ $(1e)^2$ $(5a_1)^2$ $(2e)^2$ $(2e)^2$. Ionization of an

electron from the highest occupied 2e molecular orbital of CH_3F leads to CH_3F^+ in its $\widetilde{X}^2$E electronic ground state.

The harmonic vibrational frequency, ω_i, of the vibrational mode i of the $\widetilde{X}^1A_1$ state of CH_3F is calculated by diagonalizing the kinematic and ab initio force constant matrix obtained at its equilibrium geometry. The harmonic frequencies and descriptions of all vibrational modes of CH_3F are listed in Table 3.2 along with the recent literature data. Mass weighted normal displacement coordinates ($\mathbf{Q}_i$, measured relative to the equilibrium reference configuration of neutral CH_3F at $\mathbf{Q=0}$) of the vibrational modes are calculated from the resulting eigenvector matrix and after multiplication with $\sqrt{\omega}_i$, these are transformed to their dimensionless form. The vertical ionization energy (VIE) of the $\widetilde{X}^2E$ state of CH_3F^+, calculated at the CASSCF-MRCI level of theory employing the cc-pVTZ basis set, is tabulated in Table 3.3 along with the literature data.

The energy of the $\widetilde{X}^2$E electronic state of the CH_3F^+ is calculated as a function the of displacement coordinates of the vibrational modes (vide supra) in the range -5.0$\leq\mathbf{Q}_i\leq$5.0. The calculations are carried out employing CAS(14,11)SCF-MRCI ab initio quantum chemistry method and the cc-pVTZ basis set. The calculated adiabatic electronic energies are fitted to the adiabatic form of the diabatic electronic Hamiltonian to obtain the parameters introduced in Eqs. 3.7-3.8. The CASSCF-MRCI calculations have been performed by using the MOLPRO suite of programs [37]. Adiabatic electronic energies are calculated along each vibrational modes and pairs of vibrational modes. All one-dimensional fits are carried out by a non-linear least squares method and the Levenberg-Marquardt algorithm [38, 39] as implemented in MATLAB [40] is used to perform two-dimensional fits. The coupling parameters of the Hamiltonian derived from these fits are given in Table 3.4. We note that the root mean square deviation calculated in all the fits is < 16 cm^{-1}.

The spin-orbit (SO) coupling constant of CH_3F^+ ($\widetilde{X^2}$E) at the reference C_{3v} configuration is also calculated employing the MOLPRO [37] suite of programs. The MRCI wavefunction along with the cc-pVTZ basis set is used in this calculation. The SO matrix elements are calculated using the Breit-Pauli operator. The SO coupling constant is assumed to be independent of the nuclear coordinates. The estimated SO coupling constant is $\sim$ 150 cm^{-1}, which is close to the value of $\sim$155 cm^{-1} reported by Mo et al. [19].

Table 3.1: Minimum energy configuration of CH_3F and CH_3F^+ in C_{3v} and C_s symmetry, respectively , calculated at MP2/cc-pVTZ level of theory. Bond lengths and bond angles are given in $\mathring{A}$ and degrees, respectively. The experimental data of Ref. [41] are also given in the table.

	CH_3F				CH_3F^+		
	This work	Ref. [41]	Ref. [19]	Ref. [20]	This work	Ref. [19]	Ref. [20]
Level	MP2/cc-pVTZ				MP2/cc-pVTZ		
R(C-F)	1.380	1.383	1.366	1.385	1.274	1.275	1.274
R(C-H_a)	1.087	1.087	1.086	1.087	1.170	1.167	1.172
R(C-H_c)	1.087	1.087	1.086	1.087	1.083	1.081	1.084
$\angle$ H_a-C-F	109.15	108.67	108.66	109.50	111.01	111.0	110.78
$\angle$ H_c-C-F	109.15	108.67	108.66	109.50	118.12	118.3	118.02
$\angle$ H_a-C-H_c	109.79	110.26	110.27		118.23		118.23

Table 3.2: Description of the normal vibrational modes of the electronic ground state of CH_3F. The harmonic frequencies and the normal coordinates are calculated at the MP2 level of theory employing both aVTZ-aVQZ and cc-pVTZ basis sets. The fundamental frequencies from Ref. [35] are also given in the table. Frequencies are given in eV (cm^{-1}).

Symmetry	Mode	Vibrational Frequency ω_i/eV (cm^{-1})			Predominant nature	Coordinate	
		This work/aVTZ-aVQZ	This work/cc-pVTZ	Ref. [35]			
(a_1)	ν_1	0.3824 (3084)	0.3827 (3087)	0.3630 (2928)	C-H stretch		Q_1
(a_1)	ν_2	0.1865 (1504)	0.1876 (1513)	0.1810 (1460)	CH_3 symmetric bending		Q_2
(a_1)	ν_3	0.1333 (1075)	0.1365 (1101)	0.1300 (1049)	C-F stretch		Q_3
(e)	ν_4	0.3952 (3188)	0.3950 (3186)	0.3730 (3008)	C-H stretch	Q_{4x}	Q_{4y}
(e)	ν_5	0.1893 (1527)	0.1890 (1524)	0.1820 (1468)	H-C-H asymmetric bending	Q_{5x}	Q_{5y}
(e)	ν_6	0.1502 (1211)	0.1510 (1218)	0.1460 (1178)	H-C-F asymmetric bending	Q_{6x}	Q_{6y}

Table 3.3: Vertical ionization energy [VIE (in eV)] of the electronic ground $\tilde{X}^2E$ state of CH_3F^+.

Method	VIE (eV)
MRCI/CAS(14,11)/cc-pVTZ	13.270
MR-AQCC/aug-cc-pVTZ(C,H), aug-cc-pVQZ(F) Ref. [20]	13.318
MP4/6-31G** Ref. [36]	13.283

3.3 Potential energy surfaces

The topography of the adiabatic potential energy surfaces (PESs) of the $\widetilde{X}^2E$ state of methyl fluoride radical cation is discussed in this section. The adiabatic potential energies of this state are plotted along the coordinates of the symmetric vibrational modes ν_1, ν_2 and ν_3 in panels a, b and c of Fig. 3.1, respectively. In this figure the asterisks represent the adiabatic electronic energies calculated ab initio by the CASSCF-MRCI method and the solid lines represent the corresponding potential energies obtained from the vibronic model. As stated above, it can be seen that the calculated ab initio points are well reproduced by the present theoretical model along ν_1, ν_2 and ν_3. We note that a fourth-order Taylor expansion of the Hamiltonian along the symmetric vibrational modes is adequate to represent the ab initio points extremely well. Among the three symmetric vibrational modes, the Condon activity of mode ν_3 is strongest and as a result the minimum of the $\widetilde{X}^2$E electronic state along this mode is shifted considerably away from the minimum of the neutral reference state occuring at **Q=0** [cf. Fig. 4.1(c)].

In contrast to the symmetric vibrational modes, the degenerate vibrational modes are JT active and lift the electronic degeneracy of the $\widetilde{X}^2$E state of CH_3F^+. The potential energy cuts along one of the components of the JT active degenerate vibrational modes are shown in panels a, b and c of Fig. 3.2. As in Fig. 3.1, the calculated ab initio CASSCF-MRCI energies and those obtained from the vibronic model are shown by asterisks and solid lines, respectively. It can be seen from Fig.3.2 that the calculated ab initio points are well reproduced by our constructed vibronic model. In this case fourth-order and fifth-order Taylor expansions are carried out along ν_4 and (ν_5, ν_6), respectively. It is clear from panels a, b and c of Fig. 3.2, that the extent of splitting of electronic degeneracy is smallest along ν_4 and largest along ν_5. Therefore, the overall JT activity is expected to be weakest and strongest along these modes in that order. As can be seen from Fig. 3.2, the JT-split lower adiabatic PES develops new minima at reduced-symmetry configurations. The effect of second-order and other higher-order JT couplings is predominant along ν_6 (cf. Table 3.4), whereas combined effect of first and second-order JT coupling appears to be even stronger along the vibrational mode ν_5 near the CIs.

Table 3.4: Parameters of the vibronic Hamiltonian of the $\widetilde{X}^2E$ electronic state of CH_3F^+ calculated by fitting CASSCF-MRCI energy data. All quantities are given in cm^{-1}. Parameters of the Refs. [20, 21] are given in parentheses.

$\kappa_1^{(1)}$= -1498.4 (-1439.1),	$\kappa_1^{(2)}$= -96.3 (-81.8),	$\kappa_1^{(3)}$= -8.5,	$\kappa_1^{(4)}$= 3.6,
$\kappa_2^{(1)}$= -231.5 (251.7),	$\kappa_2^{(2)}$= -715.4 (-258.7),	$\kappa_2^{(3)}$= 48.4,	$\kappa_2^{(4)}$= 47.6,
$\kappa_3^{(1)}$= -754.1 (-882.2),	$\kappa_3^{(2)}$= -479.1 (-195.9),	$\kappa_3^{(3)}$= 8.9,	$\kappa_3^{(4)}$= 5.6,
κ_{12}= 170.6 (-107.7),	κ_{13}= -193.6 (114.8),	κ_{23}= 214.6 (133.3),	$a_4^{(2)}$= -68.6 (-104.2),
$a_4^{(3)}$= -0.8,	$a_4^{(4)}$= -4.8,	$a_5^{(2)}$= -690.9 (-289.8),	$a_5^{(3)}$= -13.1,
$a_5^{(4)}$= 60.0,	$a_5^{(5)}$=25.5,	$a_6^{(2)}$= -620.3 (-89.8),	$a_6^{(3)}$= -6.4,
$a_6^{(4)}$= 40.3,	$a_6^{(5)}$= 13.2,	a_{45}= 35.6 (60.5),	a_{46}= 122.2 (-50.8),
a_{56}= -32.0 (14.8),	$\lambda_4^{(1)}$= 1182.4 (1231.9),	$\lambda_4^{(2)}$= -222.6 (-41.1),	$\lambda_4^{(3)}$= -413.0,
$\lambda_4^{(4)}$= 1.6,	$\lambda_4^{(4')}$= -344.4,	$\lambda_5^{(1)}$= 1703.4 (1816.0),	$\lambda_5^{(2)}$= 85.6 (107.2),
$\lambda_5^{(3)}$= 33.4,	$\lambda_5^{(4)}$=228.8,	$\lambda_5^{(4')}$= -169.0,	$\lambda_5^{(5)}$= 27.6,
$\lambda_5^{(5')}$= -37.1,	$\lambda_6^{(1)}$= 970.8 (959.2),	$\lambda_6^{(2)}$= -198.5 (-8.5),	$\lambda_6^{(3)}$= -32.3,
$\lambda_6^{(4)}$= -323.4,	$\lambda_6^{(4')}$= 344.0,	$\lambda_6^{(5)}$= 25.2,	$\lambda_6^{(5')}$= 64.8,
λ_{45}=-72.2 (40.5),	λ_{46}= 32.6 (-147.8),	λ_{56}= 293.4 (168.0),	b_{14}= -148.7 (224.1),
b_{15}= -10.8 (275.7),	b_{16}= 8.9 (92.3),	b_{24}= 73.5 (228.7),	b_{25}= 731.6 (1006.2),
b_{26}= -351.6 (38.7),	b_{34}= -100.5 (-352.6),	b_{35}= -554.6 (-646.0),	b_{36}= -193.7 (-251.0).

Some remarks on the potential energy curves presented in Figs. 3.1 and 3.2 are in order here. The model energy curves obtained by higher order polynomial fits are expected to diverge at longer displacements. The *ab initio* energies obtained within -5.0≤**Q**≤5.0 are well reproduced by the these curves and as can be seen from Figs. 3.1 and 3.2, the latter do not show any diverging behaviour for longer displacements for which *ab initio* points are not calculated. The potential energy curves are therefore not expected to contribute any artefacts well within the energy range of the present application. This

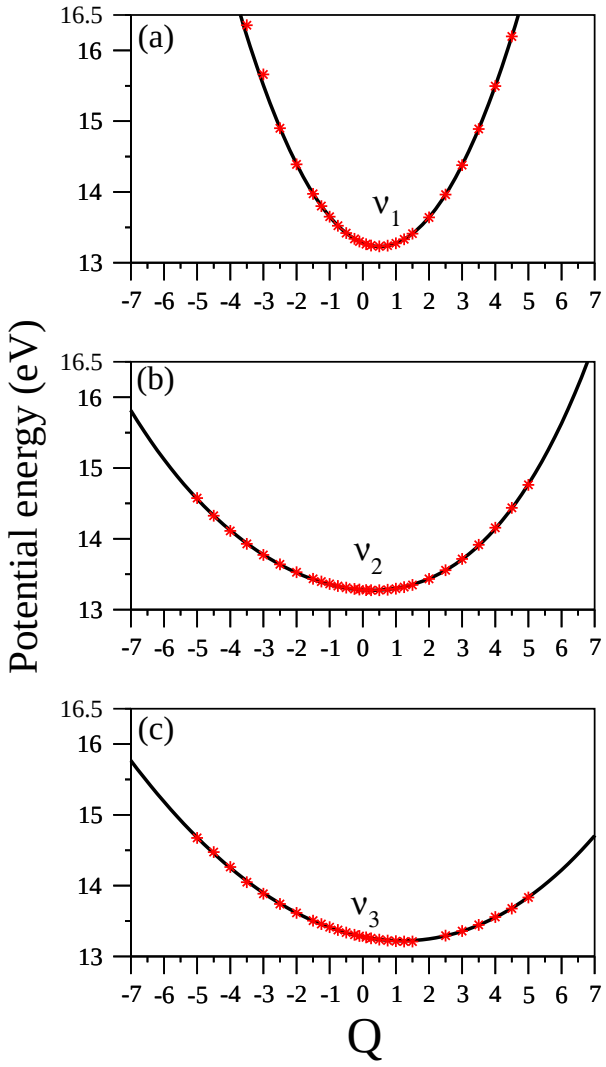

Figure 3.1: Adiabatic potential energy curves of the degenerate $\widetilde{X}^2E$ electronic state of CH_3F^+ along the dimensionless normal coordinates of totally symmetric: (a) ν_1, C-H stretching, (b) ν_2, CH_3 symmetric bending and (c) ν_3, C-F stretching vibrational modes. Potential energies obtained from the fourth-order Taylor expansion of the vibronic model and using the CASSCF-MRCI parameter values of Table 3.4 and calculated ab initio by the same method are shown by the lines and points in the diagram, respectively. Each curve in the figure represents one dimensional cut of the multidimensional potential energy hypersurface of the $\widetilde{X}^2E$ state of CH_3F^+.

statement is further confirmed by examining the snapshots of time evolved wave packets. The wave packet components do not reach beyond, $\mathbf{Q}=\pm 6.0$, during the entire duration of evolution.

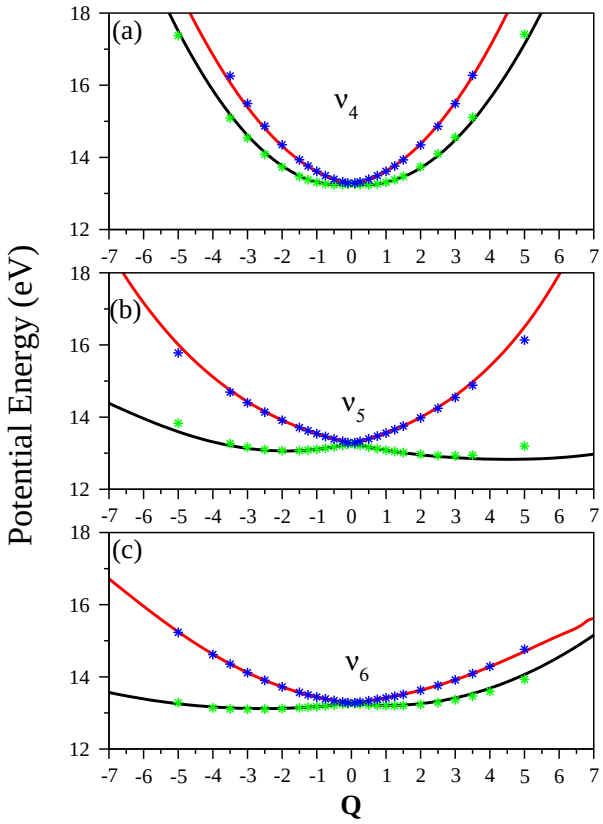

Figure 3.2: Adiabatic potential energy curves of the degenerate $\widetilde{X}^2E$ electronic state of CH_3F^+ along one component of the dimensionless normal coordinates of degenerate: (a) ν_4, C-H stretching, (b) ν_5, H-C-H asymmetric bending, (c) ν_6,H-C-F asymmetric bending vibrational modes. Potential energies obtained from the fourth-order and fifth-order Taylor expansion of the vibronic model along ν_4 and (ν_5, ν_6), respectively and using the CASSCF-MRCI parameter values of Table 3.4 and calculated ab initio by the same method are shown by the lines and points in the diagram, respectively. Each curve in the figure represents one dimensional cut of the multidimensional potential energy hypersurface of the $\widetilde{X}^2E$ state of CH_3F^+.

It is worthwhile now to examine the energies of various stationary points that appear on the JT-split electronic surfaces. Within a second-order vibronic coupling model the new energetic minima and saddle points on the lower adiabatic sheet occur at $(\frac{\lambda_i^{(1)}}{\omega_i+a_i^{(2)}-|\lambda_i^{(2)}|})$ and $(-\frac{\lambda_i^{(1)}}{\omega_i+a_i^{(2)}+|\lambda_i^{(2)}|})$, respectively, along the dimensionless normal coordinates of the JT active vibrational modes. The corresponding energies are given by [20]

$$V_-^{min} = E_E^0 - \frac{1}{2}\sum_{i\in a_1}\frac{\left(\kappa_i^{(1)}\right)^2}{(\omega_i+\kappa_i^{(2)})} - \frac{1}{2}\sum_{i\in e}\frac{(\lambda_i^{(1)})^2}{(\omega_i+a_i^{(2)}-|\lambda_i^{(2)}|)}, \tag{3.17}$$

$$V_{-}^{SP} = E_E^0 - \frac{1}{2}\sum_{i\in a_1}\frac{\left(\kappa_i^{(1)}\right)^2}{(\omega_i + \kappa_i^{(2)})} - \frac{1}{2}\sum_{i\in e}\frac{(\lambda_i^{(1)})^2}{(\omega_i + a_i^{(2)} + |\lambda_i^{(2)}|)} \tag{3.18}$$

The minimum of the seam of CIs occurs at an energy

$$V_{CI}^{min} = E_E^0 - \frac{1}{2}\sum_{i\in a_1}\frac{\left(\kappa_i^{(1)}\right)^2}{(\omega_i + \kappa_i^{(2)})}. \tag{3.19}$$

The JT stabilization energy is given by

$$E_{JT} = \frac{1}{2}\sum_{i\in e}\frac{(\lambda_i^{(1)})^2}{(\omega_i + a_i^{(2)} - |\lambda_i^{(2)}|)}. \tag{3.20}$$

The location of the distorted minima and saddle points along each vibrational mode and the JT-stabilization (E_{JT}) energies along each JT active mode are tabulated in Table 3.5. Using the parameters given in Table 3.4, the estimated values of the above energies are V_{-}^{min} = 12.75 eV, V_{-}^{SP} = 12.87 eV and V_{CI}^{min} = 13.16 eV. Total JT-stabilization energy is $\sim$ 0.42 eV. It is to be noted that the vibrational mode ν_5 contributes $\sim$ 58%, whereas ν_6 contributes $\sim$ 35% to this stabilization energy.

Unconstrained ab initio calculations were also carried out to estimate the energy of the minimum of the seam of CIs, minimum and saddle point on the lower adiabatic sheet of JT split PESs of CH_3F^+. The calculations are carried out by multi-configuration-self-consistent field method using the MOLPRO suite of programme [37]. The results are given in Table 3.6. In the latter V_{-}^{min} and V_{-}^{SP} are the energy of the minimum and saddle point on the JT split lower adiabatic sheet of the CH_3F^+ measured relative to the equilibrium minimum of the electronic ground PES of CH_3F. It can be seen that the ab initio results show good agreement with those calculated from the second-order vibronic model discussed above. The JT stabilization energy (E_{JT}) and the pseudo-rotation barrier height (ΔE_{JT}) are also well reproduced by the second-order model. The estimate of the latter quantities given in Ref. [19] is also included in the table.

The electronic degeneracy of the $\widetilde{X}^2$E state is split into two adiabatic surfaces of A$'$ and A$''$ symmetry at the distorted geometry (occuring at C_s configuration) from its C_{3v} equilibrium configuration. The spin-orbit coupling constant between the split A$'$ and A$''$ surfaces of CH_3F^+ at C_{3v} symmetry configuration is calculated. The magnitude of this constant is found to be $\sim$150 cm^{-1} ($\sim$0.019 eV). The interplay of JT and spin-orbit interactions in the $\widetilde{X}^2$E state of CH_3F^+ is shown in Fig. 3.3. The left and right column of Fig. 3.3 shows the adiabatic PESs plotted along the JT active vibrational modes without and with spin-orbit coupling, respectively. The inset of each panel shows the magnified view of the PESs in the neighborhood of C_{3v} equlibrium configuration. It can be seen from Fig. 3.3 that the spin-orbit coupling removes the electronic degeneracy at the equilibrium configuration. Owing to a very small value of the spin-orbit coupling

Table 3.5: Location of the minimum (C_s symmetry) and saddle point on the lower adiabatic sheet of the JT split $\widetilde{X}^2$E state of CH_3F^+. Contribution of individual JT-active mode to the stabilization energy is given in the table. The overall JT stabilization energy is given in the last row of the table. Calculations are carried out at the CASSCF-MRCI level of theory employing the cc-pVTZ basis set. Dimensionless normal displacement coordinates of neutral CH_3F (Q) are used to locate the stationary points.

Normal Mode	CASSCF-MRCI		
	Distorted minimum	Distorted saddle point	JT stabilization energy [eV (cm^{-1})]
Q_1	0.50	0.50	
Q_2	0.29	0.29	
Q_3	1.21	1.21	
Q_{4x}	0.41	-0.35	0.0300 (241.5)
Q_{5x}	2.28	-1.85	0.2406 (1940.8)
Q_{6x}	2.43	-1.22	0.1463 (1180.4)
Total JT stabilization energy			0.4169 (3362.52)

constant as compared to the JT coupling (given in Table 3.4), the former is expected to be of very minor importance in the coupled states nuclear dynamics. The spin-orbit coupling is therefore not included in the dynamics study below.

3.4 Vibronic structure of the $\widetilde{X}^2E$ state of CH_3F^+

The vibronic energy level spectrum of the $\widetilde{X}^2$E state of CH_3F^+ is calculated by solving the eigenvalue problem of the nuclear motion both by the time-independent and time-dependent quantum mechanical methods. In the former approach, the vibronic Hamiltonian constructed in section 3.2.2 is represented in a direct product harmonic oscillator basis of the reference state, using parameters of Table 3.4, and diagonalized. The harmonic oscillator basis functions along each vibrational mode (ν_i), the dimension of the corresponding secular matrix and number of Lanczos iterations used in the numerical calculations are given in Table 3.7 and Table 3.8, respectively. Numerical convergence of the energy eigenvalues is explicitly checked with respect to the parameters given in these tables. The wave packet calculations are done using the Heidelberg MCTDH program

Table 3.6: The energies of C_{3v} minimum of CH_3F electronic ground state, C_s minimum and saddle point on the JT-split lower adiabatic sheet of the CH_3F^+ PES and the minimum of the seam of CIs on the latter surface calculated ab initio at the MCSCF/cc-pVTZ level of theory are given in the table. The quantities of V_-^{min}, V_-^{SP}, E_{JT} and ΔE_{JT} calculated ab initio and second-order vibronic coupling model are also given along with the available literature data.

Species	Minimum electronic energy (Hartree) MCSCF/cc-pVTZ		Energy of stationary points (eV) ab initio calculation unconstrained	Second-order vibronic coupling model	Ref. [19]
CH_3F (min/C_{3v})	-139.24803	V_-^{min}	12.70	12.75	
CH_3F^+ (C_s/min/$^2A''$)	-138.78131	V_-^{SP}	12.86	12.87	
CH_3F^+ (C_s/SP/$^2A'$)	-138.77550	E_{JT}	0.42	0.42	0.52
CH_3F^+ (CIs)	-138.76584	ΔE_{JT}	0.16	0.12	0.16

Jahn-Teller stabilization energy E_{JT}= E(CIs)-E(C_s,$^2A''$) and pseudo-rotation barrier ΔE_{JT} = E(C_s,$^2A''$)-E(C_s,$^2A'$)

Table 3.7: Normal mode combinations, sizes of the primitive and single particle bases used in the MCTDH calculations for the $\tilde{X}^2$E electronic state of CH_3F^+ .

Normal modes	Primitive basis [a]	SPF basis [b]
ν_1	8	[4, 4]
ν_2	6	[3, 3]
ν_3	12	[6, 6]
ν_{4x}, ν_{4y}	6	[3, 3]
ν_{5x}, ν_{5y}	16	[8, 8]
ν_{6x}, ν_{6y}	10	[5, 5]

[a] The primitive basis is the number of Harmonic oscillator DVR functions for the relevant mode. The primitive basis for each particle is the product of the one-dimensional bases; the full primitive basis consists of a total of 5.31 $\times 10^8$ functions to get the vibronic structure of panels (a) and (b) of Figs. 3.4 and 3.10.
[b] The SPF basis is the number of single-particle functions used.

modules [32] and numerical details of these calculations are included in Table 3.7.

The resulting vibronic band structure of the $\widetilde{X}^2$E electronic state is shown in Fig. 3.4. Time-independent matrix diagonalization as well as time-dependent wave packet propagation results are shown in panels a and b, respectively. All calculations are carried

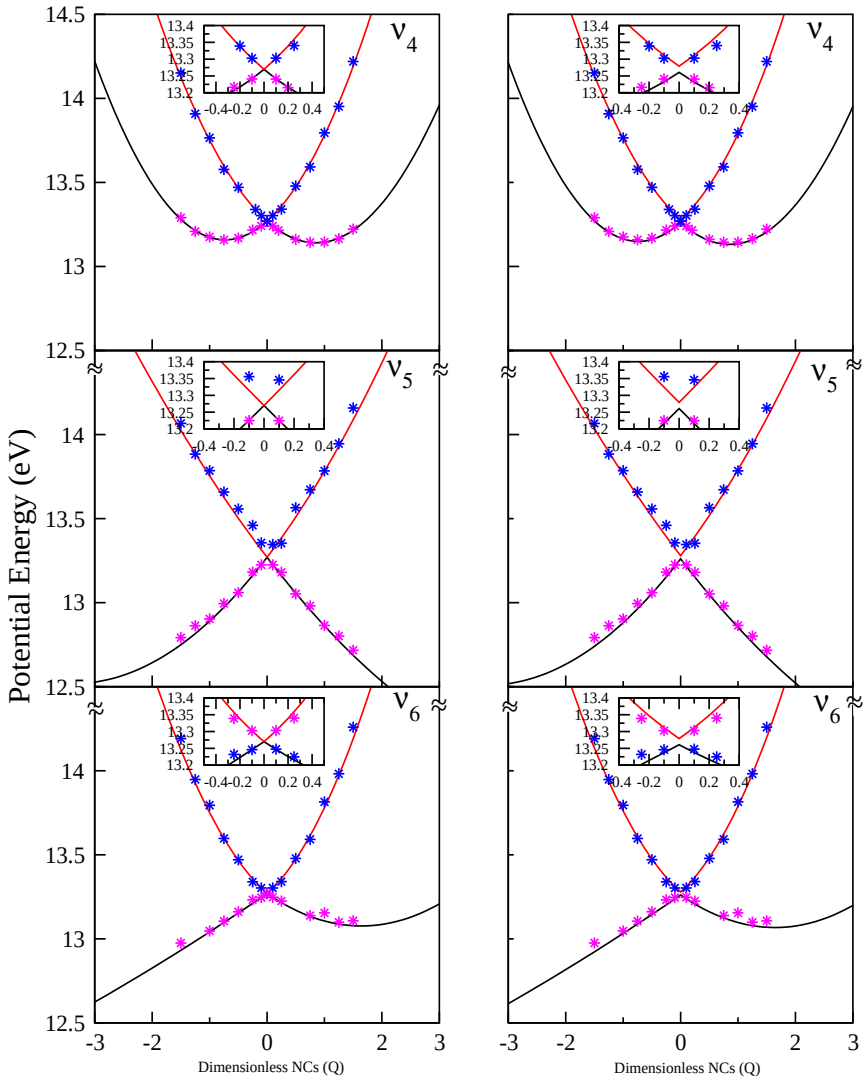

Figure 3.3: One dimensional cuts of the potential energy hypersurface of $\widetilde{X}^2$E state of CH_3F^+ plotted along the dimensionless normal coordinates of the degenerate vibrational modes. Potential energies obtained without and with spin-orbit coupling are plotted in the left and right columns of the diagram. It is to be noted that the spin-orbit coupling lifts the electronic degeneracy at the C_{3v} symmetry configuration at **Q=0**.

out with the second-order Hamiltonian parameters of Table 3.4. The stick spectrum of panel a is convoluted with a Lorentzian function of 20 meV FWHM to generate the corresponding spectral envelope. It can be seen from Fig. 3.4 that the matrix diagonalization result shown in panel a is in perfect accord with the corresponding wave packet propagation result shown in panel b. The overall band structure of the $\widetilde{X}^2$E state is shown in Fig. 3.4 in order to facilitate comparison with our earlier results [20,21] and also with the ones available in the literature [18,19,22,23]. In particular, the comparison

Table 3.8: Convergence behaviour of the vibronic levels of the $\tilde{X}^2E$ state of CH_3F^+. The convergence of energies (measured relative to the neutral reference state at zero) with respect to the number of Lanczos iterations as well as wave packet propagation time is given in the table. The assignment of the energies (cm^{-1}) are also given.

Assignment	Energy					
	Lanczos iterations			Block-improved-relaxation		
	Number of iterations			Propagation time		
	10000	13000	15000	450fs	500fs	550fs
ν_3	864.0346	864.0346	864.0346	864.6544	864.5655	866.5655
ν_5	948.7885	948.7885	948.7885	948.6762	948.6762	948.6762
ν_2	1133.2100	1133.2100	1133.2100	1133.5987	1133.5987	1133.5561
$2\nu_6$	1251.3174	1251.3174	1251.3174	1252.3588	1252.3587	1252.1167

with Ref. [21] (theory) and Ref. [22] (experiment) is favorable.

The low energy part (up to 3000 cm^{-1} above the band origin) of the vibronic stick spectrum is shown in Fig. 3.5(a) on an enlarged energy scale. We emphasize that this stick spectrum is calculated with the complete Hamiltonian and time-independent matrix diagonalization approach as discussed in section 3.2.1 and 3.2.2. In this figure the lower and upper abscissa represent the absolute and relative (to 0_0^0 line) energy scale, respectively. It can be seen from the figure that between 178-864 cm^{-1} of relative energy no lines are found. The results from the experiment of Grütter (Fig. 7.2 of Ref. [18]) are reproduced with slight smoothening of the rotational structure in Fig. 3.5(b). The available experimental recording of Mo et al. [19] in the energy range 0-1500 cm^{-1} is shown in panel c. In the work of Grütter [18], the region ∼200-800 cm^{-1} (in the relative energy scale) was obscured by photoionization transition of residual H_2O in the sample chamber. Mo et al. [19] found six sharp peaks corresponding to photoionization of residual H_2O in the energy range of ∼500-750 cm^{-1}. To the best of our belief, no vibronic levels of CH_3F^+ exists in this ″dark″ region.

Assignment of the low-energy vibronic levels is carried out in terms of the vibrational modes given in Table 3.2 and complemented by an analysis of the reduced density of the vibronic wavefunctions calculated by the block-improved-relaxation method [42, 43] as implemented in the MCTDH program modules [32]. The vibrational frequencies calculated at the C_{3v} symmetry configuration of CH_3F^+ are given Table 3.10 and compared with those of Ref. [19]. We also calculated the vibrational frequencies at the minimum of the JT split lower adiabatic sheet of the $\widetilde{X}^2$E electronic state of CH_3F^+. The calculated harmonic vibrational frequencies and the normal mode descriptions of the C_s minimum

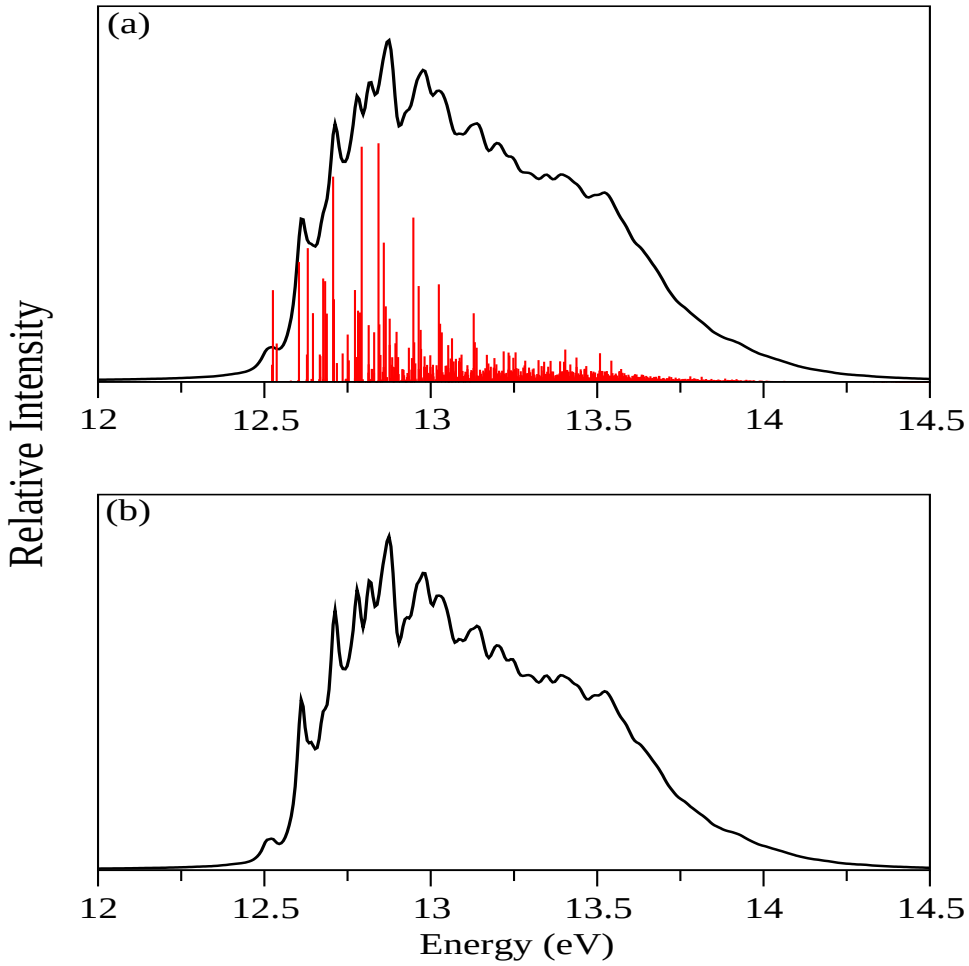

Figure 3.4: Vibronic structure of the $\widetilde{X}^2$E electronic state of CH_3F^+ calculated employing the second-order electronic Hamiltonian as discussed in section 3.2.1 and CASSCF-MRCI energy parameters of Table 3.4. Relative intensity in arbitary units is plotted as a function of the energy of the final state in eV. Time-independent matrix diagonalization results and time-dependent wave packet propagation are shown in panels a and b, respectively.

of CH_3F^+ are given in Table 3.11 and compared with those of Ref. [19]. We note that in the latter work vibronic lines are assigned in terms of these cationic normal modes. The lower energy part of the vibronic energy level spectrum of the $\widetilde{X}^2$E electronic state of CH_3F^+ is presented in Table 3.12. In the latter, in addition to the vibronic energy eigenvalues, their assignments arising from the present analysis are also given. Results from two recent experiments [18, 19] are included in the table along with the theoretical results obtained by Mo et al. [19]. The vibronic energies presented in Table 3.12 correspond to the whole range of the stick vibronic spectrum shown in Fig. 3.5a. We point out that the assignments of the vibronic energies were also confirmed through a series of reduced dimensional calculations. The energies given in Table 3.12 represent

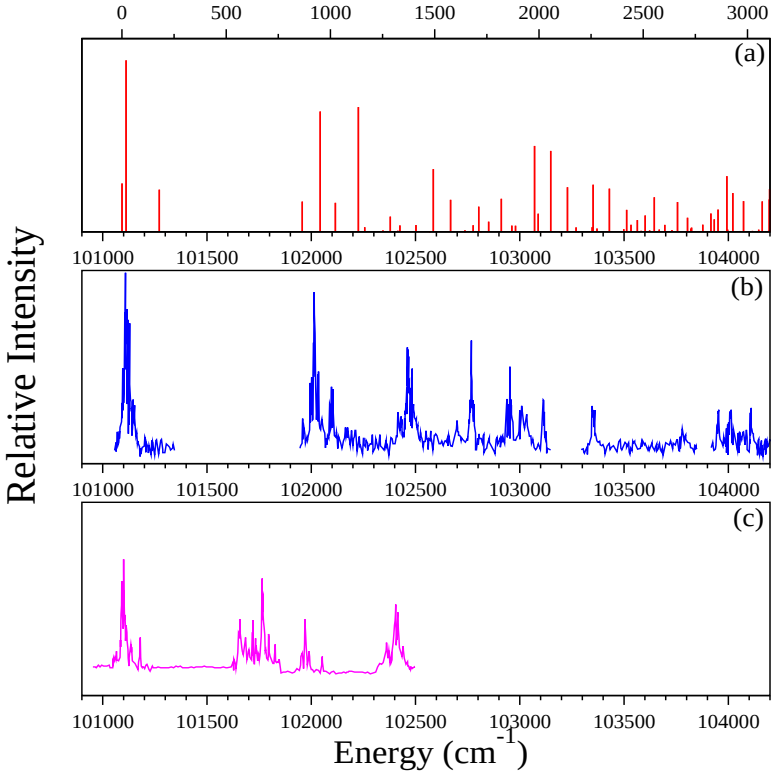

Figure 3.5: Vibronic energy levels and band structure of the $\widetilde{X}^2$E electronic manifold of CH_3F^+ in the energy range 0-3000 cm^{-1} relative to the band origin at zero. The absolute energy values are given in the abscissa. Theoretical results of panel a are obtained by employing the full Hamiltonian of section 3.2.1 and time-independent matrix diagonalization approach of section 3.2.2 with CASSCF-MRCI energy parameters of Table 3.4. In panel b the experimental recording of Grütter (cf. Fig. 7.2 of Ref. [18]) with some smoothening of rotational structure is reproduced with permission. In panel c the relevant part of the experimental recording of Mo *et al.* (reproduced from Ref. [19]) is shown. The origin line of the theoretical spectrum is placed at the adiabatic ionization position of 101092 cm^{-1} reported by the latter authors.

the location of the vibronic levels relative to the origin (0_0^0) peak (zero of energy) and the latter occurs at the adiabatic ionization energy of $\sim$ 101092 cm^{-1} as estimated in the experiment of Mo et al. [19].

A cursory look at the data given in Table 3.12 reveals that the vibrational modes ν_3 (C-F stretching), ν_5 (H-C-H bending) and ν_6 (C-F bending) are primarily involved in the spectral progression in the overall band structure of the $\widetilde{X}^2$E electronic manifold of CH_3F^+. This is consistent with earlier [12,20–22] and the most recent [18,19] studies on this system. However, the assignment of the spectral peaks seems ambiguous and effort is made in the following to arrive at a best possible assignment.

Table 3.9: Vibrational frequencies (in cm^{-1}) of CH_3F^+ calculated at the C_{3v} symmetry configuration.

Harmonic vibrational frequencies of CH_3F^+:					
$\omega_1^{'}$ = 3038,	$\omega_2^{'}$= 1099,	$\omega_3^{'}$= 827,	$\omega_4^{'}$= 3152,	$\omega_5^{'}$= 1195,	$\omega_6^{'}$= 866
Vibrational frequencies of CH_3F^+ tabulated in Ref. [19]:					
$\omega_1^{'}$ = 2755,	$\omega_2^{'}$= 1236,	$\omega_3^{'}$= 1021,	$\omega_4^{'}$= 2823,	$\omega_5^{'}$= 1196,	$\omega_6^{'}$= 999

Table 3.10: Vibrational frequencies (in cm^{-1}) of CH_3F^+ calculated at the C_{3v} symmetry configuration.

Harmonic vibrational frequencies of CH_3F^+:					
$\omega_1^{'}$ = 3038,	$\omega_2^{'}$= 1099,	$\omega_3^{'}$= 827,	$\omega_4^{'}$= 3152,	$\omega_5^{'}$= 1195,	$\omega_6^{'}$= 866
Vibrational frequencies of CH_3F^+ tabulated in Ref. [19]:					
$\omega_1^{'}$ = 2755,	$\omega_2^{'}$= 1236,	$\omega_3^{'}$= 1021,	$\omega_4^{'}$= 2823,	$\omega_5^{'}$= 1196,	$\omega_6^{'}$= 999

Table 3.11: Description of the normal vibrational modes of CH_3F^+ at the C_s minimum of the JT split lower adiabatic sheet of the $\widetilde{X}^2E$ electronic state. The frequencies (all given in cm^{-1}) are calculated at the MP2 and CCSD level of theory employing the cc-pVTZ basis set.

Mode symmetry	Frequency		Frequency	Description
	MP2	CCSD	Ref. [19]	
$\nu_1(a^{'})$	3257	3230	3286	C-H_a stretch
$\nu_2(a^{'})$	1509	1505	1507	C-H_b stretch
$\nu_3(a^{'})$	1383	1373	1340	F-C-H_a bend
$\nu_4(a^{'})$	2584	2562	2783	C-F stretch
$\nu_5(a^{'})$	1073	1080	1050	H_a-C-F bend
$\nu_6(a^{'})$	975	1017	905	H_a-C-H_b bending
$\nu_4(a^{''})$	2252	2178	2274	Anti-sym C-H_b stretch
$\nu_5(a^{''})$	1026	1037	1013	Anti-sym F-C-H_b bend
$\nu_6(a^{''})$	834	819	800	H-pivotal

The energy data presented in Table 3.12 reveals two levels, one at 19 cm^{-1} and another at 178 cm^{-1} above the origin 0_0^0 peak. These frequencies do not correspond to any of the normal vibrational modes of CH_3F^+. In order to understand their origin we carried out a set of two dimensional calculations (ν_6 with either ν_4 or ν_5) by altering the second-order JT coupling parameter that modulates the height of the pseudo-rotation barrier on the lower adiabatic sheet of the JT split $\widetilde{X}^2$E electronic state of CH_3F^+. It is found that the 0_0^0 line is split at moderate values of this parameter (as in the present case) for ν_6. At very low or large values of this parameter no splitting is observed. This is depicted in Fig. 3.6. It can be seen from panel a of this figure that the 0_0^0 line splits for $\lambda_6^{(2)}$= -198.5 cm^{-1} and a new line appears at ∼19 cm^{-1} for fixed $\lambda_4^{(2)}$=-222.6 cm^{-1}. For fixed $\lambda_5^{(2)}$=85.6 cm^{-1} a new line at ∼19 cm^{-1} is also found for $\lambda_6^{(2)}$= -198.5 cm^{-1} as shown in panel b. This indicates this low energy line primarily originates from the tunneling splitting of 0_0^0 line along ν_6. In order to confirm, the density plots of these levels are examined and shown in Fig. 3.7. While the probability density of the nuclear wavefunction of 19 cm^{-1} level is shown in panels a, b and c, the same for the 178 cm^{-1} level is shown in panel e, f anf g. It can be seen from these figures that the wavefunction exhibits a nodal pattern along both ν_6 and ν_5. Therefore, these levels are related to the tunnelling splitting of both ν_5 and ν_6. A reduced-dimensional calculation without ν_6 does not yield any lines at 19 and 178 cm^{-1}. This further confirms that ν_6 is the crucial vibrational mode behind the origin of these lines. We emphasize that except these two, there are no further lines found between 0-800 cm^{-1}. In an analogous manner the assignment of the fundamentals of the vibrational modes is carried out.

Table 3.12: Energetically low-lying vibronic energy levels (in cm^{-1}) of the JT split $\widetilde{X}^2$E electronic state of CH_3F^+. The vibronic energy levels caculated in this work are compared with the recent experimental and theoretical results available in the literature.

No.	This work		Grütter [18]			Mo et al. [19]			
	MRCI/cc-pVTZ								
	Neutral	Assign.	Energy	Prog.	Assign.	Energy	Prog.	Prog.	Assign.
	NCs						(Exp.)	(Theo.)	
1	0.0	0	101109.0 (2.0)	0.0	0-0	101092	0.0	0.0	0
2	19	0						56.4	0
3	178	0							
4						101657	565	562.2	$6''$
5	(666)	ν_6				101768	676	673.5	$6''+6'$
6	864	ν_3	101970.8 (5.0)	861.8	5_0^1	101954	862	850.9	$6'+6''$
7			101972.8 (5.0)	863.8	5_0^1				
8	949	ν_5	102053.0 (5.0)	944	5_0^1			931.3	$5''$
9	1023								
10	1133	ν_2							
11	1164								
12	1251	$2\nu_6$	(102376)	1267	6_0^2	102361	1269	1296.2	$(6'')^2$
13	1323		102402.3 (5.0)	1293.3	3_0^1	102405	1313	1336.5	3
14	1332							1392.2	3
15	1410							1393.0	$6''6'$
16								1461.7	$(6'')^3$
17								1503.4	2
18	1493	$\nu_3+\nu_6$	102628.4 (5.0)	1519.4	$5_0^1 6_0^1$	102629	1537	1526.3	$5''6''$
19	1575		102698.1 (5.0)	1589.1	$5_0^1 6_0^1$	102696	1604	1604.2	$5''6''$
20	1644							1606.8	$(6'')^2$
21	1684							1620.0	2
22	1710	$2\nu_3$							
23	1758		102878.5 (5.0)	1769.8	5_0^2	102873	1781	1776.0	$(6')^2$
24	1819	$2\nu_5$	102935.4 (5.0)	1826.4	5_0^2	102933	1841	1826.7	$5'5''$
25	1869	$3\nu_6$	(102969)	1860.0	6_0^3	102955	1863	1857.9	$5'6''$
26	1933		103035.2 (5.0)	1926.2	5_0^2	103034	1942	1942.5	$5''6'$
27			103035.2 (5.0)	1926.2	5_0^2				
28	2008								
29	2056	$\nu_2+\nu_5$				103140	2048		$3(6'+6'')$
30	2167	$\nu_5+2\nu_6$				103246	2154	2151.6	$4''$
31	2254	$2\nu_2$							
32	2337							2329.5	
33	2471	$\nu_3+\nu_5+\nu_6$							

– continued in next page

34	2508	$4\nu_6$	(103624)	2515	6_0^4				
35	2563	$2\nu_5+\nu_6$						2641.6	3^2
36	2586	$3\nu_3$							
37	2664	$2\nu_3+\nu_5$						2698.3	3^2
38	2752	$\nu_3+2\nu_5$	103860 (20)	2751	5_0^3	103845	2753		$35''6''$
39	2785	$\nu_3+2\nu_5$							
40	2814	$\nu_5+3\nu_6$	103910 (20)	2801	5_0^3	103897	2805		$35''6''$
41	2858	$3\nu_5$	103975 (20)	2866	5_0^3	103934	2842	2845.4	$4'$
42	2903		104010 (20)	2901	5_0^3	103998	2906	2877.0	$4'$
43	2991	ν_1				104090	2998		$3(6')^2$
44	3053	$2(\nu_3+\nu_6)$				104139	3047		$3(6')^2$
45	3077					104169	3077		$35'5''$
46	3140	ν_4				104233	3141		$35'6''$
47	3205	$3\nu_3+\nu_6$				104299	3207	3212.6	1
48	3251					104349	3257		$34''$
49	3315					104400	3308		$34''$
50	3353					104440	3348	3398.4	1
51	3442	$4\nu_3$				104533	3441		$3^2(5'+5'')$
52	3486	$3\nu_5+\nu_6$							
53	3556	$3\nu_3+\nu_5$				104649	3557		$4(6'+6'')$
54	3564								

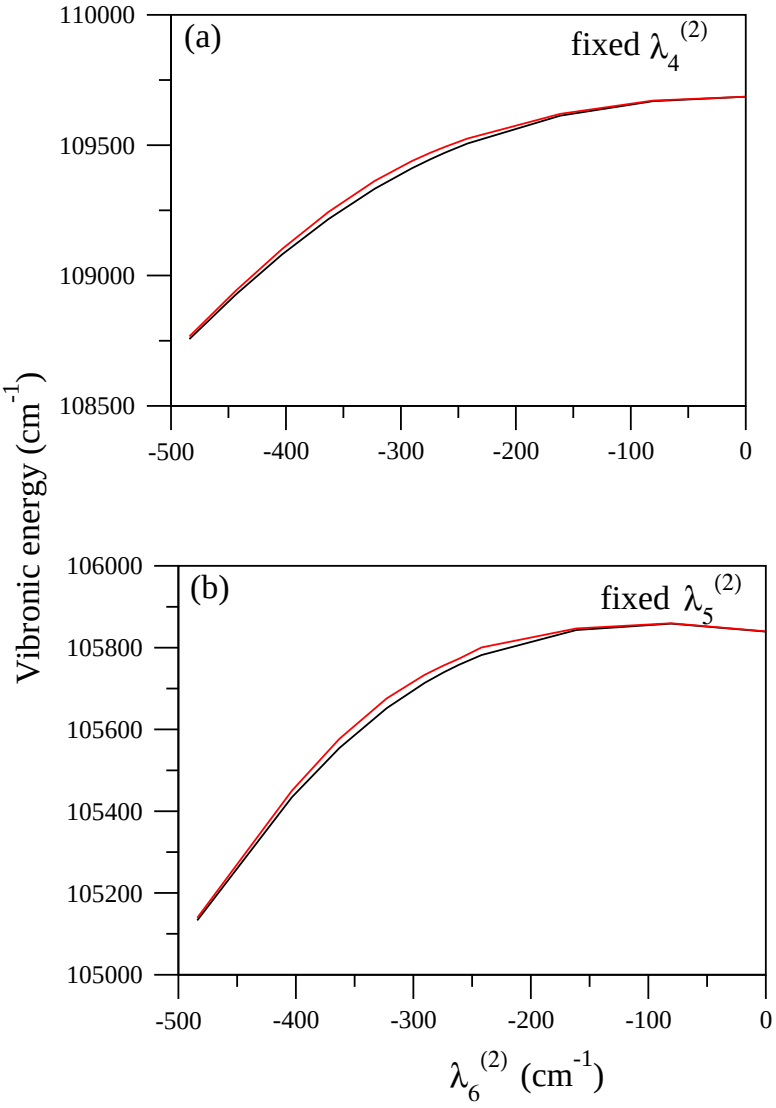

Figure 3.6: Energy of the origin 0_0^0 line as a function of the height of the pseudo-rotation barrier (quadratic JT parameter) for ν_6. The results obtained from two mode calculations (ν_4,ν_6) with $\lambda_4^{(2)}$ fixed and (ν_5,ν_6) with $\lambda_5^{(2)}$ fixed are shown in panel a and b, respectively.

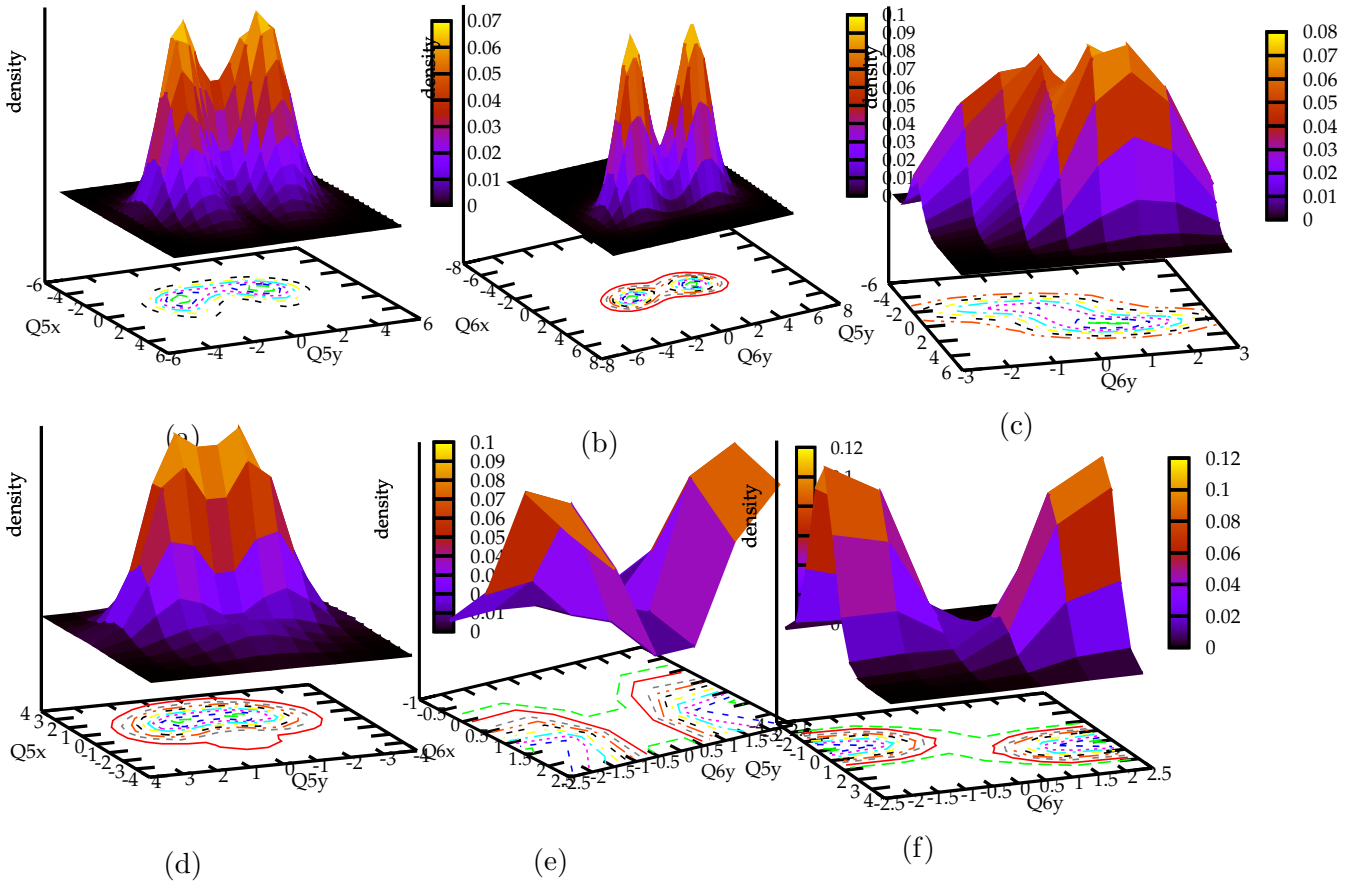

Figure 3.7: Reduced density plots of the vibronic wavefunctions of 19 cm^{-1} (panels a, b and c) and 178 cm^{-1} (panels d, e and f) levels. These are tunneling splitting levels (see text for details) formed by JT-active modes ν_5 and ν_6.

In the coupled states results presented in the above table, the JT spectrum due to the degenerate vibrational modes forms progressions around the lines of the symmetric modes. As a result numerous weak lines appear in the resulting spectrum. Some of the intense lines are therefore retained in the above table and are identified with the excitation of vibrational modes. Extensive reduced-dimensional calculations with different mode combinations are also carried out by the matrix diagonalization method as well as by block-improved-relaxation [42, 43], to identify and assign the fundamental of each mode given in Table 3.12. The convergence of these reduced dimensional calculations is explicitly checked. For illustration, the convergence behaviour of the first few vibronic level is given in Table 3.8 with corresponding assignments. In this table the results of matrix diagonalization with varying number of Lanczos iterations and block-improved-

relaxation calculations with different wave packet propagation times are given. The vibronic energies are measured relative to the energy of the neutral reference ground state at zero of energy. It can be seen from the table that the energies are converged with respect to both the parameters (typically within $\sim$1 cm^{-1}) as noted above.

The density plots of the vibronic wavefunction of the 864 cm^{-1} line are shown in the first row (panels a, b and c) of Fig. 3.8. It can be seen from this figure that the wavefunction has a node along the mode ν_3. Therefore, at 864 cm^{-1}, vibrational mode ν_3 is excited. Hence, this line is assigned to the fundamental of ν_3. In the same way, the density plots of 949 cm^{-1} and 1133 cm^{-1} lines, shown in second (panels d, e and f) and last row (panels g, h and i) of Fig. 3.8, are assigned to the fundamental of ν_5 and ν_2, respectively. Following the assignment of fundamentals, we have assigned also all other energy levels given in Table 3.12.

Among the symmetric vibrational modes the excitation strength of ν_3 is highest, whereas that of ν_1 is lowest. The energetic location of the fundamental of ν_1 remains almost unperturbed in the full dimensional calculations as compared to the reduced dimensional results. The vibronic line at $\sim$ 2991 cm^{-1} is assigned to the fundamental of this mode. As ν_3 is the strongest Condon active mode, many of its overtones appear in the spectrum. Lines at $\sim$ 1710, $\sim$2586 and $\sim$ 3442 cm^{-1} are assigned to the first, second and third overtones of this mode, respectively. For illustration, the density plots of the first overtone of ν_6, ν_3 and ν_5 occuring at 1251, 1710 and 1819 cm^{-1}, respectively, are shown in last row (panels j, k and l) of Fig. 3.8.

Further analysis of several possible reduced-dimensional as well as full mode results seem to confirm the location of the fundamental of JT active modes ν_5 at $\sim$ 949 cm^{-1}. This peak is observed at $\sim$ 944 cm^{-1} in the experiment of Grütter [18], whereas the same peak is not seen in the experiment of Mo et al. [19]. As stated earlier the fundamental of ν_6 did not show up in the experiment of Grütter [18]. This is proposed to appear at $\sim$650 cm^{-1} based on the finding of its overtone at $\sim$1267 cm^{-1} [18]. The fundamental of ν_6, on the other hand, was assigned in the "dark" region in the experiment of Mo et al. [19]. In our reduced-dimensional calculations, including ν_4 and ν_6, the fundamental of ν_6 is found at $\sim$666 cm^{-1}. This however disappears in the full mode calculations. A systematic analysis reveals that excitation of ν_6 fundamental is quenched by the combined effect of the ν_2, ν_3 and ν_5 vibrational modes. Analysis of the first overtone of ν_6 at 1251 cm^{-1} shows that the most probable position of the fundamental of ν_6 would be around 650 cm^{-1} above the 0_0^0 peak. The wave packet density plots of the $\sim$666 cm^{-1} line observed in the reduced-dimensional calculations are shown in Fig. 3.9 in the supplementary information. These plots confirm this line is due to the fundamental of ν_6. Peaks are found at $\sim$ 931 cm^{-1} and $\sim$ 673 cm^{-1}, respectively, in the theoretical calculations of Mo et al. [19] were assigned to the fundamental JT-active vibrational mode ν_5 and a combined peak corresponds to the components of ν_6, respectively. Excitation of several overtones of ν_5 and ν_6 and their combination levels reveals that the

JT activity of these modes is fairly strong. Like ν_1, the degenerate vibrational mode ν_4 does not have any significant contribution to the dynamics and its fundamental is found at $\sim$3140 cm^{-1}. The energy levels in the energy range 0-3500 cm^{-1} given in Table 3.12 compare well with the recent experimental results [18, 19].

It is clear from the above discussion that the symmetric mode ν_3 and the degenerate modes ν_5 and ν_6 mainly contribute to the vibronic structure of the JT split $\widetilde{X}^2$E electronic manifold of CH_3F^+. A similar conclusion can be derived from the earlier and latest experimental [18, 19, 22] and theoretical results [19–21]. However, the assignment of the observed peaks and their energetic locations differ from the results mentioned above. In our earlier study [20] two main spacings at $\sim$ 855 and $\sim$ 1218 cm^{-1} were observed and are attributed to the excitation of ν_3 and ν_6 ″together″ and to the fundamental of mode ν_5, respectively. In the present study, in particular, a substantial reduction of the frequency of the vibrational mode ν_5 is predicted. A larger value of the second-order intra-state coupling along both ν_5 and ν_6 is obtained in this work as compared to our earlier work [20] (cf. Table 3.4). The energy spacing of $\sim$ 1315 cm^{-1} was assigned to the fundamental of ν_5 in the experimental recording of Karlsson et al. [22]. Excitation of several overtones and combination peaks of this mode was also observed in the low-energy part of their measurements. This is in accord with the observed large JT splitting of the $\widetilde{X}^2$E electronic manifold along ν_5. These authors assigned the lines at $\sim$ 694 and $\sim$ 879 cm^{-1} to the fundamentals of mode ν_3 and ν_6, respectively. This is opposite to Table 3.12. The degenerate mode ν_6 was reported to be weakly excited. Locht et al. [23] proposed a different assignment of their experimental results. With the aid of ab initio calculations, these authors assigned the observed long $\sim$ 1290 cm^{-1} progression to the vibrational mode ν_3, and $\sim$ 970 cm^{-1} and $\sim$ 660 cm^{-1} progressions to the JT active vibrations ν_5 and ν_6, respectively. The latter agrees well with the assignments made in Table 3.12.

While the spectra calculated within a second-order coupling model and presented in Fig. 3.4 facilitated comparisons with the earlier results in the literature, it is felt by us that it would be worthwhile to look into the details of similar spectra that emerges from the complete Hamiltonian of Eqs. 3.7-3.8. Motivated by this suggestion we examined the spectra resulted from the complete Hamiltoninan and present them in Fig. 3.10, retaining the same format of Fig. 3.4. In Fig. 3.10a, the stick spectrum is convoluted with a Lorentzian function of 40 meV FWHM and in Fig. 3.10b, the time autocorrelation function is damped with an exponential function of τ_r= 33 fs. The essential differences between the spectra shown in Fig. 3.4 and Fig. 3.10 are the following.
i) In the higher-order coupling model the density of the vibronic lines increases as it allows more multimode interactions, which makes the spectral envelope much broader compared to the second-order model.
ii) The energetic location of a given vibronic line shifts to some other energy in the higher-order coupling model. For example, the fundamental of ν_5 occurs at 903 cm^{-1} in the second-order model, whereas, it appears at 949 cm^{-1} in the higher-order model.

Apart from the mentioned differences, the broad shape of the overall structural envelope remains identical in the two cases.

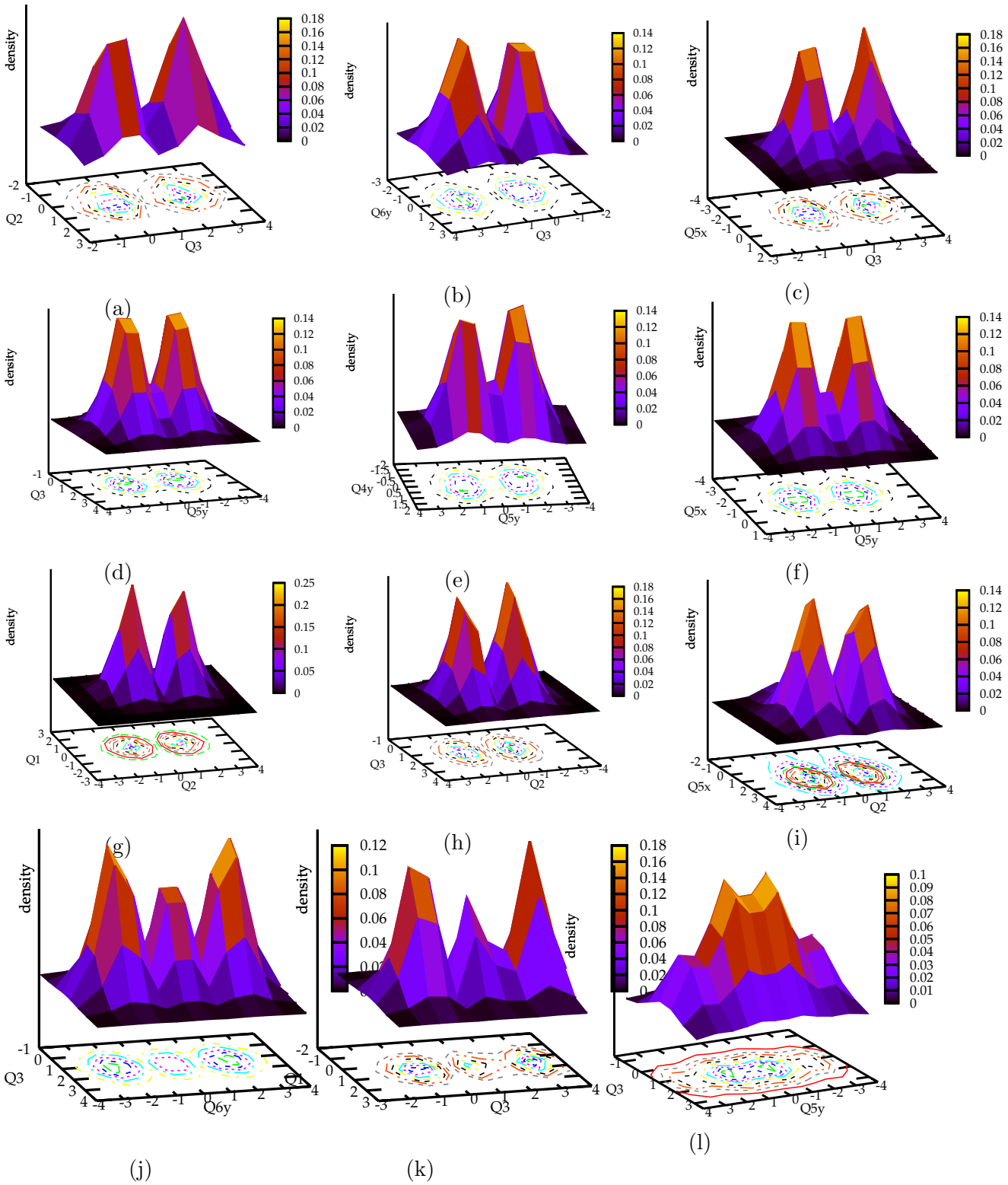

Figure 3.8: Reduced density plot of the vibronic wavefunction corresponding to the 864 cm^{-1} energy level is shown in first row of the figure. The density is plotted as a function of normal coordinates of two vibrational modes. The appearance of the nodal plane along ν_3 confirms the assignment of this line as the fundamental of this mode. Similarly the wavefunction density at 949 cm^{-1} and 1133 cm^{-1} energy levels are shown in second and third row of the figure. These energy lines are assigned to the fundamentals of ν_5 and ν_2 vibrational mode. First overtone of ν_6,ν_3 and ν_5 found at 1251, 1710 and 1819 cm^{-1}, respectively, are shown in last row, in panels j, k and l.

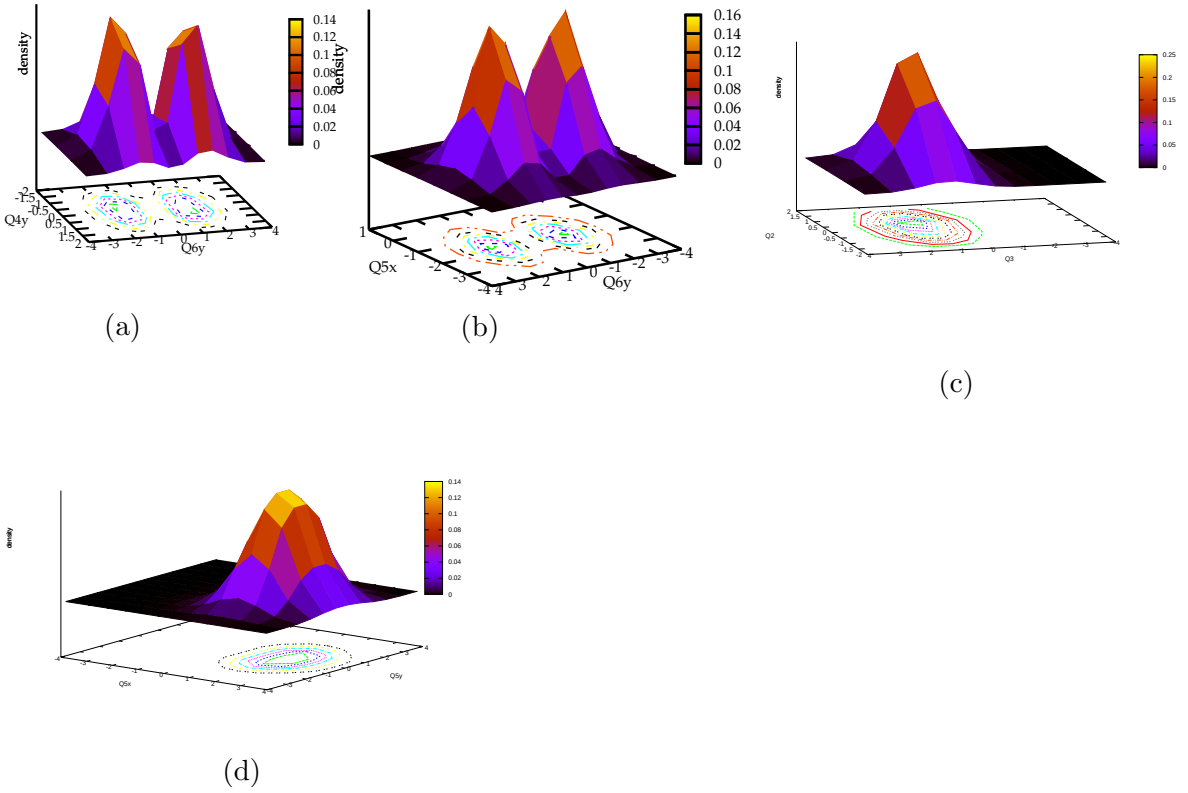

(a) (b) (c) (d)

Figure 3.9: Reduced density plot of the vibronic wavefunction corresponding to the 666 cm^{-1} energy level. The density is plotted as a function of normal coordinates of two vibrational modes. The appearance of the nodal plane along ν_6 confirms the assignment of this line as the fundamental of this mode.

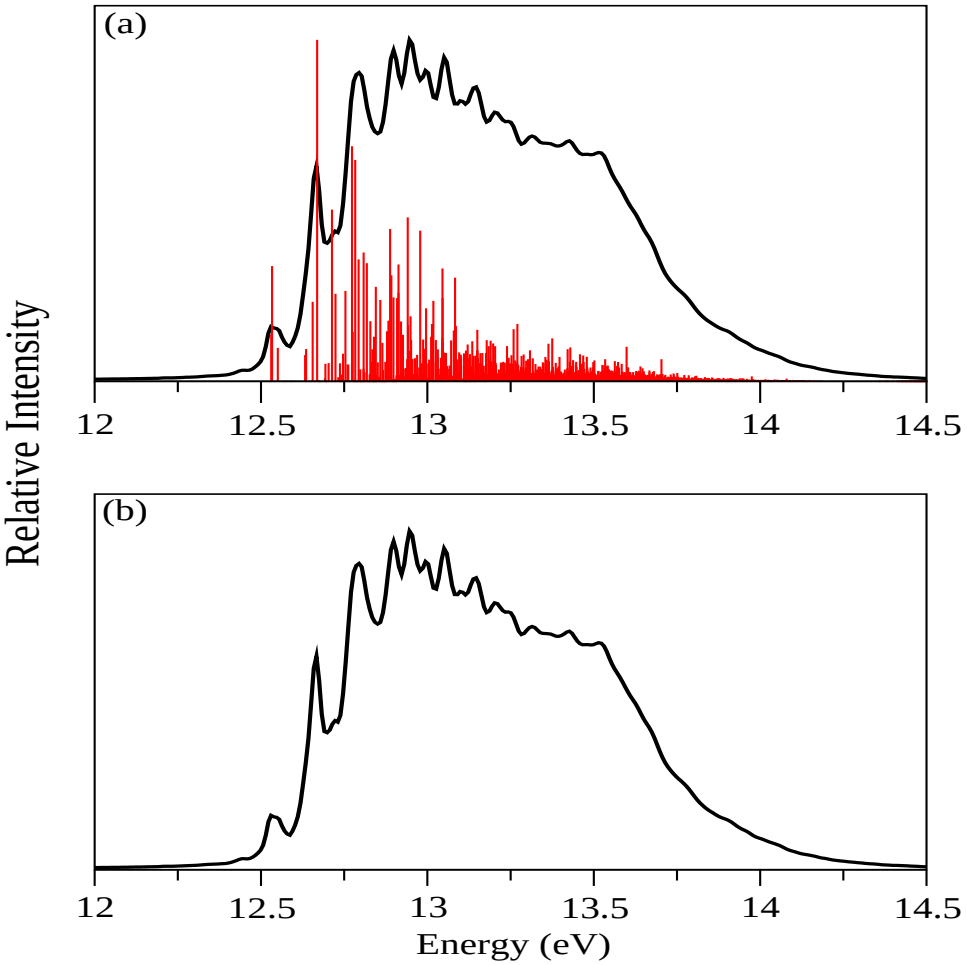

Figure 3.10: Same as in Fig. 3.4, calculated with the complete Hamiltonian of section 3.2.1

3.5 Summary

The theoretical study of the JT effect in the $\widetilde{X}^2$E ground electronic manifold of CH_3F^+ is carried outin this Chapter with a higher-order expansion of the E⊗e-JT Hamiltonian in terms of the normal coordinates of the electronic ground state of neutral CH_3F. We carried out a detailed analysis of the JT coupling effect in the vibronic dynamics of CH_3F^+ in the past. Revisiting these earlier studies is motivated by the recent experimental and theoretical developments on this subject. Conflicting assignments of vibronic energy level spacings around the origin peak of the $\widetilde{X}^2$E band in the earlier and latest experimental and theoretical results were addressed and discussed in this Chapter.

High-level quantum chemistry calculations of the electronic energy surfaces have been carried out and extended to larger normal mode displacements. An improved set of parameters of the vibronic Hamiltonaian was derived from the calculated electronic energies. The JT-stabilization energy is directly calculated ab initio by optimizing various stationary points on the JT-split lower adiabatic sheet of $\widetilde{X}^2$E electronic state of CH_3F^+. It is found that the results obtained from the present model are in well accord with the unconstrained ab initio data (cf. Table 3.6).

First principles nuclear quantum dynamics calculations were carried out by time-independent and time-dependent methods. The calculated vibronic energy levels closely correspond to the measured ones in the recent experiments which is another important result obtained in the present work. Assignment of vibronic levels are carried out by carefully examining their locations obtained in various reduced dimensional calculations as well as by an explicit analysis of the corresponding vibronic wavefunctions. Such extensive analyses seem to confirm the assignment of fundamentals, various overtones and combination levels.

A careful analysis reveals that the levels at 19 and 178 cm^{-1} are due to tunneling splitting of the 0_0^0 level due to vibrational modes ν_5 and ν_6. This ″two-mode″ tunneling splitting has rarely been discussed before in the literature and deserves further attention. The fundamental of the symmetric vibrational mode ν_3 is excited at ∼864 cm^{-1} and forms an extended progression in the spectrum. Similarly, the fundamental JT active degenerate vibrational mode ν_5 excited at ∼949 cm^{-1} forms an extended progression in the spectrum. However, this is in contrast to our earlier theoretical results, in which the fundamental of this mode was reported at 1218 cm^{-1}. While a line at ∼676 cm^{-1} is observed in the experiment of Mo et al. [19], this does not show up in the experiment of Grütter [18] and also in our full-mode calculation. The former authors assigned this line to the excitation of vibrational mode ν_6. We tentatively assigned the excitation of the fundamental of JT active vibrational mode ν_6 at 666 cm^{-1}, following the reduced-dimensional calculations. The excitation of the symmetric vibrational mode ν_2 is weak, but a combination peak of this mode with mode ν_5 is found at ∼2056 cm^{-1}. The excitation of the symmetric and the degenerate C-H stretching modes ν_1 and ν_4 is the

weakest. Overall, the approach adopted and results obtained in this work should prove useful to unravel complex Jahn-Teller dynamics also in other related molecular systems.

References

[1] H. A. Jahn and E. Teller, Proc. R. Soc. Lond. A. **161**, 220 (1937).

[2] H. Köppel, W. Domcke, L. S. Cederbaum, Adv. Chem. Phys. **57**, 59 (1984).

[3] I. B. Bersuker, Chem. Rev. **101**, 1067 (2001), and the references therein.

[4] T. A. Barckholtz, T. A. Miller, Int. Rev. Phys. Chem. **17**, 435 (1998).

[5] H. Köppel, L. S. Cederbaum, and S. Mahapatra, in *Handbook of High Resolution Spectroscopy,* edited by M. Quack and F. Merkt **Vol.3** (Wiley, Chichester, 2011) p. 1517-1550.

[6] I. B. Bersuker, *The Jahn-Teller Effect*, Cambridge University Press, Cambridge, England, 2006.

[7] G. Herzberg and H. C. Longuet-Higgins, Discuss. Faraday Soc. **35**, 77 (1963).

[8] D. R. Yarkony, Acc. Chem. Res. **31**, 511 (1998).

[9] S. Mahapatra, Acc. Chem. Res. **42**, 1004 (2009).

[10] W. Domcke, D. R. Yarkony and H. Köppel, *in Conical Intersections*, edited by W. Domcke, D. R. Yarkony and H. Köppel, Vol. 15, World Scientific, New Jersey (2004).

[11] W. Domcke, D. R. Yarkony and H. Köppel, *Conical Intersections: Theory, Computation and Experiment*, edited by W. Domcke, D. R. Yarkony and H. Köppel, Vol. 17, World Scientific Publishing Co. Pte. Ltd. Singapore (2011).

[12] D. W. Turner, C. Baker, A. D. Baker, C. R. Brundle, Molecular Photoelectron Spectroscopy, Wiley, New York, 1970.

[13] S. Stokes, A. B. F. Duncan, J. Am. Chem. Soc. **80**, 6177 (1958).

[14] J. W. Gauld, L. Radom, J. Phys. Chem. **98**, 777 (1994).

[15] C. L. Lugez, D. Forney, M. E. Jacox, K. K. Irikura, J. Chem. Phys. **106**, 489 (1997).

[16] M. Grütter, X. Qian, and F. Merkt, J. Chem. Phys. **137**, 084313 (2012).

[17] F. S. Ham, Phys. Rev. **138**, A1727 (1965).

[18] M. Grütter, Rotationally resolved spectroscopy of the Jahn-Teller effect in molecular cations. ETH (2011), Ph.D thesis ETH, http://dx.doi.org/10.3929/etha-a-006668589.

[19] S. Gao, Z. Dai, W. Sun, H. Li, J. Wang, and Y. Mo, J. Chem. Phys. **139**, 064302 (2013).

[20] S. Mahapatra, V. Vallet, C. Woywod, H. Köppel, and W. Domcke, Chem. Phys. **304**, 17 (2004).

[21] S. Mahapatra, V. Vallet, C. Woywod, H. Köppel, and W. Domcke, J. Chem. Phys. **123**, 231103 (2005).

[22] L. Karlsson, R. Jadrny, L. Mattsson, F. T. Chau, K. Siegbahn, Phys. Scripta. **16**, 225 (1977).

[23] R. Locht, B. Leyh, A. Hoxha, D. Dehareng, H. W. Jochims, H. Baumgärtel, Chem. Phys. **257**, 283 (2000).

[24] A. Viel, W. Eisfeld, J. Chem. Phys. **120**, 4603 (2004).

[25] W. Domcke, H. Köppel, and L. S. Cederbaum, Chem. Phys. Lett. **43**, 851 (1981).

[26] J. Cullum and R. Willoughby, *Lanczos Algorithms for Large Symmetric Eigenvalue Problems* (Birkhäuser, Boston, 1985), Vols. I and II.

[27] H. Köppel and W. Domcke, in *Encyclopedia of Computational Chemistry*, edited by P. V. R. Schleyer (Wiley, New York, 1998), p. 3166.

[28] L. S. Cederbaum, W. Domcke, H. Köppel, and W. von Niessen, Chem. Phys. **26**, 169 (1977).

[29] H.-D. Meyer, U. Manthe, L.S. Cederbaum, Chem. Phys. Lett. **165**, 73 (1990).

[30] U. Manthe, H.-D. Meyer, L.S. Cederbaum, J. Chem. Phys. **97**, 3199 (1992).

[31] M.H. Beck, A. Jäckle, G.A. Worth, H.-D. Meyer, Phys. Rep. **324**, 1 (2000).

[32] G. A. Worth, M. H. Beck, A. Jäckle, and H.-D. Meyer, The mctdh package, Version 8.4, (2007), University of Heidelberg, Heidelberg, Germany. See: http://mctdh.uni-hd.de.

[33] T. H. Dunning, Jr, J. Chem. Phys. **90**, 1007 (1989).

[34] M. J. Frisch, G. W. Trucks, H. B. Schlegel *et al.*, GAUSSIAN 03, Revision B. 05, Gaussian, Inc., Pittsburgh, PA, 2003.

[35] H. Kato, M. Hoshino, Y. Nagai, T. Tanaka, M. J. Brunger, O. Ingólfsson and H. Tanaka, J. Phys. B: At. Mol. Opt. Phys. **43**, 065205 (2010).

[36] B. Andes Hess. Jr., and R. Zahradnik, J. Am. Chem. Soc. **112**, 5731 (1990).

[37] H.-J. Werner, P. J. Knowles, G. Knizia, F. R. Manby, *et al.*, MOLPRO, version 2012.1, 2012.

[38] K. Levenberg, Q. Appl. Math. **2**, 164 (1944).

[39] D. W. Marquardt, SIAM J. Appl. Math. **11**, 431 (1963).

[40] MATLAB and Statistics Toolbox Release 2012b, The MathWorks, Inc., Natick, Massachusetts, United States.

[41] J. Demaison, J. Breidung, W. Thiel and D. Papousek, Structural Chemistry. **10**, 2 (1999).

[42] Q. Meng and H. -D. Meyer, J. Chem. Phys. **139**, 164709 (2013).

[43] D. Peláez, K. Sadri and H. -D. Meyer, Spectrochimica Acta Part A: Molecular and Biomolecular Spectroscopy. **119**, 42 (2014).

4 Electronic structure calculations of first four electronic states of $CH_2F_2^+$ and its deuterated isotopomer

4.1 Introduction

Difluoromethane (CH_2F_2) is one of the hydrofluorocarbon used in refrigerant industry. It has zero ozone depletion potential and is a weak green house gas [1]. The photophysics of CH_2F_2 received renewed attention of experimentalists [1–14] and theoreticians [15–17] over the past decades. Energetically low-lying electronic states of $CH_2F_2^+$ have been investigated by photoelectron spectroscopy using HeI [2,3,7,8] as well as X-ray [5, 6] radiation sources. Electron impact [4] and (e,2e) electron momentum spectroscopy [13,14] measurements were also carried out. Recently vibronically resolved pulsed-field-ionization zero-kinetic-energy (PFI-ZEKE) measurements were also carried out by Signorell and co-workers [1].

The observed photoelectron spectrum in the energy range ∼12.7-16.6 eV revealed two (three) bands. The first one contains resolved vibrational structure and the second one is mostly structureless and diffuse. The second one is actually a composite vibronic structure of three electronic states, which is discussed latter in the text with appropriate scientific justification. Theoretical studies with [17] and without [3, 15] configuration interactions revealed different energetic ordering of the first four electronic states of $CH_2F_2^+$. The Franck-Condon spectrum calculated in theoretical study revealed poor agreement with experiments [3,8]. The progression of vibrational modes in the electronic ground state of $CH_2F_2^+$ was not unambiguously resolved. Furthermore, theoretically calculated Franck-Condon spectrum extended beyond the experimentally measured one and so far no clear interpretation is available on this.

The resolved progression in the first band was found to have contribution from ν_1 (C-H stretching) and ν_3 (C-F stretching) [15] in addition to a major contribution from

[0]The subject of this Chapter is published by: Rudraditya Sarkar and S. Mahapatra in Molecular Physics **113**, 3073 (2015). and J. Phys. Chem. A. **120**, 3504 (2016)
There is also contribution from Rudraditya Sarkar by publishing a part of this work in J. Phys: Conference Series. **759**, 012058 (2016).

ν_2 (H-C-H bending) [3, 15]. The vibrational structure in the second band is assigned to the progression of ν_3 and ν_4 (F-C-F bending) [3] or ν_2 and ν_3 vibrational modes [10]. Analysis of the PFI-ZEKE spectrum of CH_2F_2 [1] confirms Takeshita's model [15] and reavels that the polyad structure arises from the vibrational progression of ν_2 and ν_3 vibrational modes.The latter modes are quasi-degenerate. An improved *ab initio* calculation with MP2/aug-cc-pVQZ level of theory was perfomed in Ref. [1] to derive harmonic vibrational wavenumbers and Franck-Condon factors in the context of photoionization of CH_2F_2, which was insufficient to describe the resolved vibronic PFI-ZEKE photoelectron spectrum. Latter fully coupled anharmonic calculations by the same authors [16] reveal breakdown of the Franck-Condon approximation and the importance of anharmonicity in the electronic states of $CH_2F_2^+$. In this paper [16], the authors could not establish the role of symmetric vibrational mode ν_1 in the vibronic structure, as proposed by Takeshita [15].

An interesting observation of disappearance of the vibrational structure of the ground state spectrum of $CH_2F_2^+$ upon isotopic deuterium substitution was made in the experimental recording of Brundle et al. [3]. To the best of our knowledge, the latter is the only experimental measurement of the photoionization spectrum of CD_2F_2. The loss of vibrational structure was postulated to be due to: 1) possible excitation of multiple vibrational modes and the existence of accidental degeneracies among them absent in the deuterated isotopomer and 2) the ease of predissociation in case of deuterated cation than the normal cation imposing a lifetime broadening of the spectrum [3]. It is also conjectured that vibrational modes of C-H character rather than C-F character predominantly contribute to the electronic ground state spectrum of $CH_2F_2^+$ [3]. The vibrational structure of the overlapping $\widetilde{A}$-$\widetilde{B}$-$\widetilde{C}$ band remains virtually unchanged upon deuteration, indicating the involvement of vibrational modes of C-F character rather than C-H character in these electronic states.

Apart from the studies noted above [15], a detailed theoretical study of the eletronic states of $CH_2F_2^+$ and nuclear dynamics on them is missing in the literature. Availability of numerous experimental results and existing ambiguity in their interpretation motivated us to undertake such an exercise. An extensive quantum chemistry calculations are carried out at three different levels of theory, outer-valance Green$'$s function (OVGF), equation-of-motion couple cluster singles and doubles (EOM-CCSD) and multi-reference configuration interaction (MRCI), to establish the electronic potential energy surfaces of the first four electronic states of $CH_2F_2^+$. The results of the electronic structure calculations of $CH_2F_2^+$ convinced us to apply preferably the best quantum chemistry method, MRCI, to study the electronic structure of $CD_2F_2^+$. So the different parameters of the electronic structure of $CD_2F_2^+$ correspond to MRCI calculations. It is found that strong nonadiabatic interactions [18, 19] among the electronic states lead to multiple conical intersections (CIs) both for $CH_2F_2^+$ and $CD_2F_2^+$. The energetic ordering of the electronic states is examined and discussed in relation to the results available in the literature. A four coupled states parameterized Hamiltonian is constructed in a diabatic electronic

basis for both $CH_2F_2^+$ and $CD_2F_2^+$. As the mass weighted normal coordinate representation is adapted in the construction of the Hamiltonian, the Hamiltonian parameters for the electronic states of $CH_2F_2^+$ and its isotopomer $CD_2F_2^+$ are different. As a result of this, the topography of the one dimensional potential energy surfaces are also different in these two system. The nuclear dynamics study on these potential energy surfaces are discussed in the next chapter.

4.2 Theoretical framework

4.2.1 Vibronic Hamiltonian

Energetically low-lying first four doublet electronic states of $CH_2F_2^+$ ($CD_2F_2^+$) are considered in this study. A vibronic Hamiltonian is constructed in a diabatic basis using dimensionless normal displacement coordinates of vibrational modes of neutral CH_2F_2 (CD_2F_2), which are considered as reference state, and symmetry selection rules in order to study nuclear dynamics on these electronic states. Nine vibrational modes of CH_2F_2 (CD_2F_2) transform according to the following irreducible representations (IREPs) of C_{2v} equilibrium symmetry point group

$$\Gamma = 4a_1 \oplus 2b_1 \oplus 2b_2 \oplus 1a_2. \tag{4.1}$$

Employing elementary symmetry selection rule and standard vibronic coupling theory, the Hamiltonian can be written in a diabatic electronic basis as [18]

$$\mathcal{H} = \mathcal{H}_0\mathbf{1} + \boldsymbol{\Delta}\mathcal{H}, \tag{4.2}$$

$$\mathcal{H}_0 = T_N + V_0. \tag{4.3}$$

In the above, $\mathcal{H}_0$ is the unperturbed Hamiltonian of the reference electronic ground state of CH_2F_2 (CD_2F_2) and $\Delta\mathcal{H}$ represents the change in electronic energy upon ionization. $\mathbf{1}$ represents a (4×4) unit matrix. In terms of the dimensionless normal displacement coordinates of the vibrational modes, the components of the reference Hamiltonian of Eq.4.3 within the harmonic approximation are given by

$$T_N = -\frac{1}{2}\sum_{i=1}^{9}\omega_i\left(\frac{\partial^2}{\partial Q_i^2}\right), \tag{4.4}$$

$$V_0 = \frac{1}{2}\sum_{i=1}^{9}\omega_i Q_i^2. \tag{4.5}$$

The ground and first three excited electronic states of $CH_2F_2^+$ ($CD_2F_2^+$) belong to the $\tilde{X}^2B_1$, $\tilde{A}^2B_2$, $\tilde{B}^2A_1$ and $\tilde{C}^2A_2$ symmetry species (see the discussion latter in the

text) of the C_{2v} symmetry point group. They result from ionization from the highest occupied molecular orbital (HOMO), HOMO-1, HOMO-2 and HOMO-3 of neutral CH_2F_2 (CD_2F_2). The quantity $\Delta\mathcal{H}$ in Eq.4.2 can be symbolically written as

$$\Delta\mathcal{H} = \begin{pmatrix} \mathcal{W}_{XX} & \mathcal{W}_{XA} & \mathcal{W}_{XB} & \mathcal{W}_{XC} \\ & \mathcal{W}_{AA} & \mathcal{W}_{AB} & \mathcal{W}_{AC} \\ h.c. & & \mathcal{W}_{BB} & \mathcal{W}_{BC} \\ & & & \mathcal{W}_{CC} \end{pmatrix}. \tag{4.6}$$

The elements of this electronic Hamiltonian matrix are expanded in a second-order Taylor series around the equilibrium geometry of the reference state ($\mathbf{Q}$=0) as

$$\mathcal{W}_{jj} = E_j^0 + \sum_{i\in a_1} \kappa_i^j Q_i + \frac{1}{2} \sum_{i\in a_1,a_2,b_1,b_2} \gamma_i^j Q_i^2, \tag{4.7}$$

and

$$\mathcal{W}_{jk} = \mathcal{W}_{kj}^* = \sum_i \lambda_i^{j-k} Q_i. \tag{4.8}$$

In the above, j and k, are the electronic state indices and i reprsents the vibrational modes. The vertical ionization energy of the j^{th} electronic state is defined as E_j^0, where, $j \in \widetilde{X}$, $\widetilde{A}$, $\widetilde{B}$ and $\widetilde{C}$, respectively. The quantity κ_i^j defines the linear intra-state coupling parameter and γ_i^j is the diagonal second-order coupling parameter of vibrational mode i in the j^{th} electronic state. The quantity, λ_i^{j-k} is linear inter-state coupling parameter between the states j and k, coupled through i^{th} vibrational mode. The vibronic Hamiltonian constructed above is utilized in the next chapter to study nuclear dynamics in the mentioned electronic states of $CH_2F_2^+$ ($CD_2F_2^+$).

4.2.2 Computational details of electronic structure calculations

The optimized equilibrium geometry of the electronic ground state of CH_2F_2 (CD_2F_2) (the reference state) is calculated by using second-order Møller-Plesset perturbation theory (MP2) as well as coupled-cluster singles and doubles (CCSD) method employing the correlation-consistent polarized valence triple zeta (cc-pVTZ) basis set of Dunning [20]. GAUSSIAN-09 [21] and MOLPRO [22] suite of programs are used for this purpose, respectively. Optimization of geometry of the electronic states of $CH_2F_2^+$ is carried out at the restricted Hartree-Fock and restricted CCSD (RHF-RCCSD) level of theory with cc-pVTZ and RHF-RMP2/cc-pVTZ level of theory using MOLPRO [22] suite of program. All electronic energy calculations are performed with multi-reference configuration interactions (MRCI), outer-valence Green′s function (OVGF) and equation-of-motion coupled cluster singles and doubles (EOM-CCSD) methods with cc-pVTZ basis set, using MOLPRO [22], GAUSSIAN-09 [21] and CFOUR [23] program modules, respectively, for $CH_2F_2^+$. Whereas, electronic energy calculations for $CD_2F_2^+$ are performed with MRCI

Table 4.1: Optimized geometry parameters of the equilibrium minimum of the electronic ground state of neutral CH_2F_2 (CD_2F_2).

State	parameters	Level of theory		Ref. [15]
		This Work MP2/cc-pVTZ	This work CCSD/cc-pVTZ	SCF Calculation
$^1A_1$	C-H(D) ($\AA$)	1.087 (1.087)	1.088 (1.088)	1.087
	C-F ($\AA$)	1.354 (1.354)	1.350 (1.350)	1.335
	∠H(D)-C-H(D) (deg.)	113.05 (113.05)	112.78 (112.78)	112.45
	∠H(D)-C-F (deg.)	108.75 (108.75)	108.85 (108.85)	
	∠F-C-F (deg.)	108.70 (108.70)	108.59 (108.59)	108.47

quantum chemistry method using the same basis set. The CASSCF-MRCI calculations are carried out with an (14,11) active space, which includes seven valence orbitals and four virtual orbitals with fourteen electrons for CH_2F_2 (CD_2F_2). The cationic states have open shell configuration and an (13,11) active space is used. We note that many test calculations are carried out with varying active spaces and the chosen ones yield the best results.

The optimized equilibrium structure of the CH_2F_2 (CD_2F_2) in the electronic ground state belongs to C_{2v} point group symmetry and leads to $^1A_1$ electronic term for this closed shell system. The equilibrium harmonic vibrational frequencies of the reference state, ω_i, are calculated by diagonalizing the kinematic and *ab initio* force constant matrix at the same level of theory. The eigenvectors of the force constant matrix yield the mass-weighted normal co-ordinates of the vibrational modes. The latter is transformed to the dimensionless form $\mathbf{Q}$ by multiplying with $\sqrt{\omega_i}$ (in a. u.) [24]. In an analogous way the geometry of $CH_2F_2^+$ in its first four electronic states are optimized. Since this radical cation has open shell configuration, RCCSD/cc-pVTZ level of theory is employed to obtain its optimized structure. The MOLPRO [22] suite of program is used for this purpose. All the optimized cationic structures belong to the C_{2v} symmetry point group.

4.3 Results and discussion

4.3.1 Electronic structure

The optimized equilibrium geometry parameters of the electronic ground state ($\tilde{X}^1A_1$) of CH_2F_2 (CD_2F_2) molecule are given in Table 4.1. The results are compared with the available literature data [15] for CH_2F_2. It can be seen from the table that the results obtained at two different theoretical levels are in good accord with each other and also with the literature data. The description of the normal vibrational modes of

the electronic ground state of CH_2F_2 along with their harmonic frequency (ω) is given in Table 4.2. The frequency values available in the literature are also included in the table for comparison. The same for the CD_2F_2 are given in Table 4.3. The optimized equlibrium structural parameters of the electronic ground states of CH_2F_2 and $CH_2F_2^+$ and electronic excited states of $CH_2F_2^+$ along with the available literature data are given in Table 4.4. Comparison of the data given in Table 4.4 reveals that although the equlibrium symmetry point group of $CH_2F_2^+$ in four electronic states is same as that of CH_2F_2 in its electronic ground state, ionization results an appreciable distortion of geometry in the cationic states. The largest distortion occurs in the $\tilde{X}^2B_1$ state, where all the equilibrium geometry parameters noticeably change. Among the cationic states the equlibrium C-H and C-F bond distances and H-C-H and H-C-F bond angles in the $\tilde{X}^2B_1$ state have the largest change, whereas F-C-F bond angle has largest change in the $\tilde{A}^2B_2$ state (cf. Table 4.4). In order to understand the mentioned geometry changes, four valence cannonical SCF molecular orbitals (MOs) of CH_2F_2 are shown in Fig. 4.1. Ionization from these MOs result $CH_2F_2^+$ in its $\widetilde{X}$, $\widetilde{A}$, $\widetilde{B}$ and $\widetilde{C}$ electronic states. It can be seen from the figure that the MO of b_1 symmetry is predominantly of C-H bonding type. Removal of electron from this MO results an elongation of the C-H bond. The Mulliken charge on H atom significantly increases (cf. Table 4.5) and it causes a large decrease of H-C-H bond angle (cf. Table 4.4). The MOs of b_2 and a_2 symmetry are fluorine lone pair MOs. Ionization from these MOs increase the Mulliken charge on F atom (cf. Table 4.5). As a result, the lone pair-lone pair repulsion decreases, causing a large reduction of the F-C-F angle and slight increase of C-F bond length (cf. Table 4.4). The C-H bonding character in the MO of a_1 symmetry reduced as compared to that in the MO of b_1 symmetry, due to an antibonding contribution of $2p_z$ orbital of fluorine atoms. As a result, ionization from this MO has relatively milder effect on the geometry parameters given in Table 4.4. The vertical ionization energies for CH_2F_2 (CD_2F_2) of each electronic states are also calculated and compared with the literature data in Table 4.6.

First four electronic states of $CH_2F_2^+$ have been identified in various theoretical works on this subject [2–9]. Following Koopmans' theorem, Brundle et al. [3] assigned these states to $^2B_2$, $^2A_1$, $^2B_1$, and $^2A_2$ with increasing energy. The configuration interaction (CI) calculations of Takeshita [15] on the other hand, yield a different energetic ordering of $^2B_2$, $^2B_1$, $^2A_1$ and $^2A_2$ electronic states. We have perfomed geometry optimization of CH_2F_2 and $CH_2F_2^+$ in their respective electronic ground state. The optimized closed shell structure of CH_2F_2 (CD_2F_2) gives rise to, ... $(3b_2)^2$ $(1a_2)^2$ $(4b_2)^2$ $(6a_1)^2$ $(2b_1)^2$ molecular orbital (MO) configuration. Therefore, removal of an electron from HOMO, HOMO-1, HOMO-2 and HOMO-3 would produce the cation in $\tilde{X}^2B_1$, $\tilde{A}^2A_1$, $\tilde{B}^2B_2$ and $\tilde{C}^2A_2$ electronic states, respectively. Considering Koopmans' theorem and electron correlation we have performed single point (SP) calculations of electronic energies of $CH_2F_2^+$ along the symmetric vibrational modes. Outer valence green function (OVGF) and multi-reference configuration interaction (MRCI) methods along with the cc-pVTZ basis set are used in these calculations. To illustrate, these energies are plotted along

the normal coordinate of vibrational mode ν_4 in Fig. 4.2.

Table 4.2: Symmetry, harmonic frequencies (in cm^{-1}) and description of nine vibrational modes of the electronic ground state of CH_2F_2.

Mode (Symmetry)	Frequency (ω) cm^{-1} (eV) MP2/cc-pVTZ	CCSD/cc-pVTZ	Ref. [15]	Ref. [1]	Description
ν_1 (a_1)	3119 (0.3867)	3100	3258	3125	H-C symmetric stretching
ν_2 (a_1)	1571 (0.1948)	1572	1659	1562	H-C-H symmetric bending (in plane)
ν_3 (a_1)	1146 (0.1421)	1166	1224	1132	F-C symmetric stretching
ν_4 (a_1)	538 (0.0667)	545	580	533	F-C-F symmetric bending
ν_5 (a_2)	1303 (0.1616)	1309		1293	H-C-H anti-symmetric bending (out of plane)
ν_6 (b_1)	3202 (0.3970)	3170		3212	H-C anti-symmetric stretching
ν_7 (b_1)	1211 (0.1502)	1215		1204	H-C-H anti-symmetric bending (in plane)
ν_8 (b_2)	1494 (0.1852)	1500		1476	F-C anti-symmetric stretching
ν_9 (b_2)	1140 (0.1414)	1166		1110	H-C-H symmetric bending (out of plane)

Table 4.3: Symmetry, harmonic frequency (in cm^{-1}) and description of nine vibrational modes of the electronic ground state of CD_2F_2.

Mode (Symmetry)	Frequency (ω) cm^{-1} (eV) MP2/cc-pVTZ	CCSD/cc-pVTZ	Description
ν_1 (a_1)	2261 (0.2804)	2248	D-C symmetric stretching
ν_2 (a_1)	1210 (0.1501)	1220	D-C-D symmetric bending (in plane)
ν_3 (a_1)	1060 (0.1314)	1066	F-C symmetric stretching
ν_4 (a_1)	531 (0.0658)	538	F-C-F symmetric bending
ν_5 (a_2)	938 (0.1163)	942	D-C-D anti-symmetric bending (out of plane)
ν_6 (b_1)	2390 (0.2964)	2366	D-C anti-symmetric stretching
ν_7 (b_1)	985 (0.1221)	989	D-C-D anti-symmetric bending (in plane)
ν_8 (b_2)	1213 (0.1504)	1236	F-C anti-symmetric stretching
ν_9 (b_2)	1036 (0.1285)	1044	D-C-D symmetric bending (out of plane)

Table 4.4: Optimized geometric parameters of the electronic ground states of CH_2F_2 and $CH_2F_2^+$ and three energetically lowest excited electronic states of $CH_2F_2^+$, calculated at RHF-RCCSD/cc-pVTZ level of theory. The results available literature are also given in the table. *Structural parameters correspond to this electronic state are calculated by RHF/cc-pVTZ level of theory.

State		C-H (Å)		C-F (Å)		∠H-C-H (deg.)		∠H-C-F (deg.)		∠F-C-F (deg.)	
This work	Ref. [15]	This work	Ref. [15]	This work	Ref. [15]	This work	Ref. [15]	This work	Ref. [15]	This work	Ref. [15]
$\tilde{X}^1A_1$	$^1A_1$	1.088	1.087	1.350	1.335	112.78	112.45	108.85		108.59	108.47
$\tilde{X}^2B_1$	$^2B_2$	1.172	1.185	1.265	1.246	83.04	77.66	113.05		116.95	117.00 [1]
$\tilde{A}^2B_2$	$^2B_1$	1.083	1.082	1.402	1.382	121.91	121.66	111.17		83.89	83.53
$\tilde{B}^2A_1$	$^2A_1$	1.115	1.119	1.361	1.335	126.48	128.50	103.29		118.62	118.95
$\tilde{C}^2A_2^*$	$^2A_2$	1.075	1.084	1.388	1.392	118.37	118.74	111.23		95.10	95.10

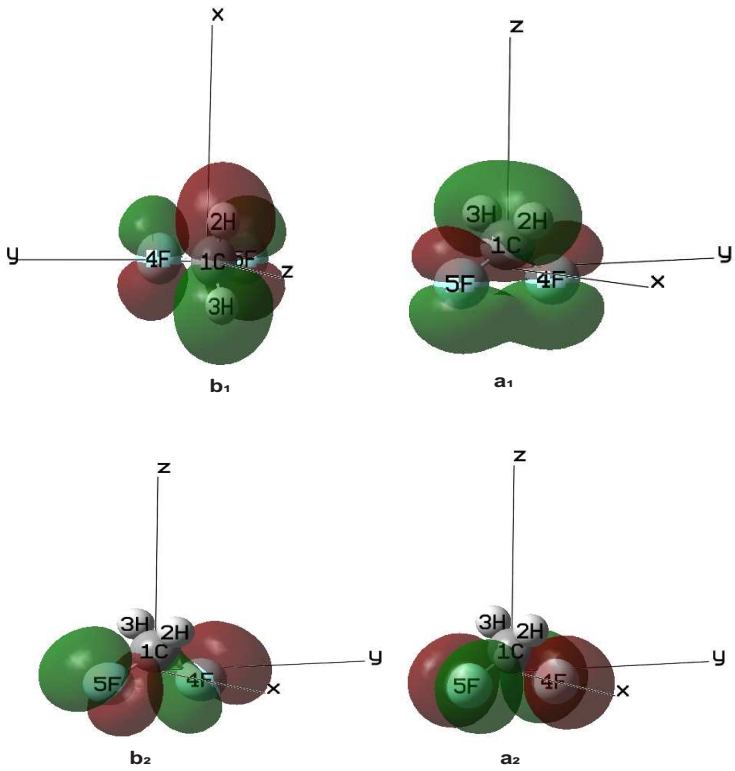

Figure 4.1: Cannonical SCF valence MOs of CH_2F_2.

In the latter, dotted lines represent Koopmans' energies and the full lines represent the energy including correlation corrections. It can be seen from Fig. 4.2 that the energies including correlation correction yield $\tilde{X}^2B_1$, $\tilde{A}^2B_2$, $\tilde{B}^2A_1$ and $\tilde{C}^2A_2$ as the energetic ordering of electronic states. It is seen that the $^2B_1$ and $^2B_2$ electronic states are interchanged in Ref. [15]. This swaping of states may have occured due to the choice of different principal plane (xz or yz) by different softwares. It should be mentioned that the present ordering of electronic states remain unchanged upto $\mathbf{Q} \leq 1.35$. Whereas, in the range of $\mathbf{Q} \sim 1.35$ to 1.69 two electronic states $\tilde{A}^2B_2$ and $\tilde{B}^2A_1$ become degen-

Table 4.5: Mulliken charge on the atoms in the $\tilde{X}^1A_1$ state of CH_2F_2 and $\tilde{X}^2B_1$, $\tilde{A}^2B_2$, $\tilde{B}^2A_1$ and $\tilde{C}^2A_2$ states of $CH_2F_2^+$

State	Mulliken charge on atoms		
	Carbon	Hydrogen	Fluorine
$\tilde{X}^1A_1$	0.4321	0.0452	-0.2613
$\tilde{X}^2B_1$	0.4524	0.2876	-0.0138
$\tilde{A}^2B_2$	0.3747	0.1994	0.1132
$\tilde{B}^2A_1$	0.4044	0.2268	0.0709
$\tilde{C}^2A_2$	0.3842	0.1782	0.1297

Table 4.6: Vertical Ionization energies (eV) of first four electronic states of $CH_2F_2^+$ and $CD_2F_2^+$.

	This work			Ref. [15]	
State	CAS(14,11)SCF MRCI/cc-pVTZ	OVGF cc-pVTZ	EOM-CCSD cc-pVTZ	State	SCF
$\tilde{X}^2B_1$	13.58	13.55	13.33	$^2B_2$	13.56
$\tilde{A}^2B_2$	15.34	15.29	14.99	$^2B_1$	15.15
$\tilde{B}^2A_1$	15.74	15.45	15.24	$^2A_1$	15.61
$\tilde{C}^2A_2$	16.02	16.03	15.69	$^2A_2$	16.34

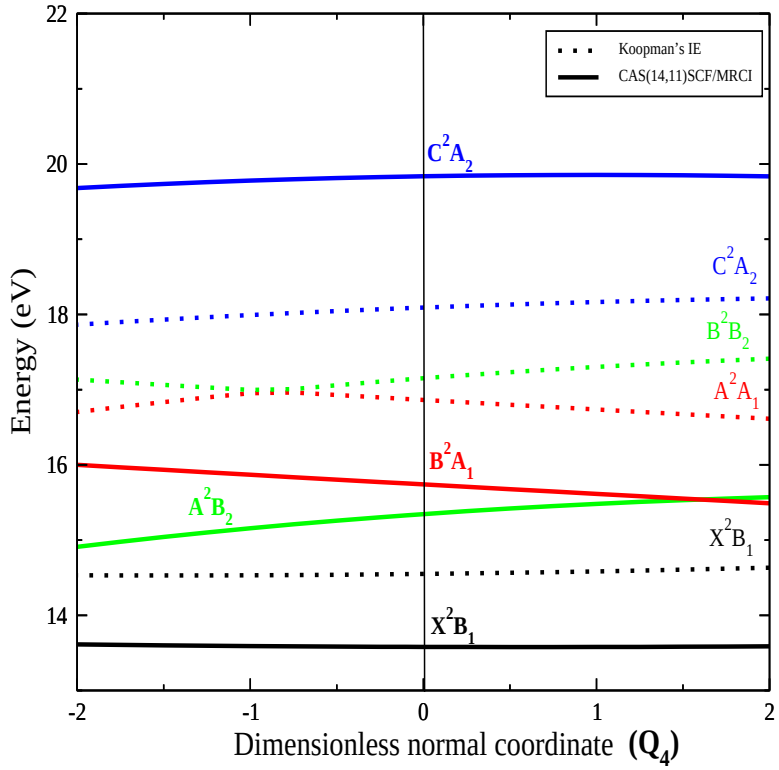

Figure 4.2: Energies of the first four electronic states of $CH_2F_2^+$ plotted along the symmetric vibrational mode ν_4. The Koopman′s and CAS(14,11)SCF-MRCI results are shown by the dotted and solid lines, respectively.

erate and thereafter these two electronic states interchange their position and follow the arrangement predicted by Koopmans' theorem. The CASPT2 and CASSCF results of Huang et al. [17] also yield the same energetic ordering as given by the present CASSCF-MRCI results.

4.3.2 Hamiltonian parameters for $CH_2F_2^+$

The Hamiltonian parameters introduced in Eqs. 4.7-4.8 are estimated by performing extensive ab initio calculations of electronic energies along the normal coordinates of the vibrational modes of the reference state. The calculations are performed with OVGF, CAS(14,11)SCF-MRCI and EOM-CCSD ab initio quantum chemistry methods employing the cc-pVTZ basis set. The calculated ab initio electronic energies are then fitted to the adiabatic form of the diabatic electronic Hamiltonian of Eq. 4.6 to estimate these parameters. The linear and quadratic intra-state coupling parameters of $\widetilde{X}^2B_1$, $\widetilde{A}^2B_2$, $\widetilde{B}^2A_1$ and $\widetilde{C}^2A_2$ electronic states of $CH_2F_2^+$ are given in Table 4.7. The linear inter-state coupling parameters are given in Table 4.8.

The coupling parameters of Table 4.7 reveal that the symmetric vibrational mode ν_2 is active in all four electronic states, whereas, ν_1 and ν_4 vibrational modes are active only in ($\widetilde{X}^2B_1$ and $\widetilde{B}^2A_1$) and ($\widetilde{A}^2B_2$ and $\widetilde{B}^2A_1$) electronic states, repectively, and ν_3 is active in the $\tilde{X}^2B_1$, $\tilde{A}^2B_2$ and $\tilde{C}^2A_2$ states. The strong inter-state coupling between $\widetilde{X}^2B_1$-$\widetilde{A}^2B_2$ states along ν_5 vibrational mode, $\widetilde{X}^2B_1$-$\widetilde{B}^2A_1$ states along ν_6 and ν_7 vibrational modes and $\widetilde{X}^2B_1$-$\widetilde{C}^2A_2$ states along ν_8 vibrational mode can be found from the data of Table 4.8. On the other hand, mild inter-state coupling between $\widetilde{A}^2B_2$, $\widetilde{B}^2A_1$ and $\widetilde{C}^2A_2$ states is found (cf. Table 4.8). The data in Table 4.7 reveal that the second-order intra-state coupling parameters of symmetric mode ν_2 and non-symmetric mode ν_8 is larger in the $\widetilde{X}^2B_1$ state compared to the other states. This would result into considerable reduction of frequency of these modes in the $\widetilde{X}^2B_1$ state of the cation as compared to that in the neutral reference state. Similarly, a reduction of frequency of mode ν_9 in the $\widetilde{A}^2B_2$ and $\widetilde{C}^2A_2$ states and symmetric mode ν_4 in the $\widetilde{A}^2B_2$ and $\widetilde{C}^2A_2$ states can be expected.

A regression method is employed to access the correlation between the Hamiltonian parameters derived from three sets of electronic energy data, given in Tables 4.7-4.8. Three sets of data are independent of each other and they are plotted in Fig. 4.3. It is found that three set of data are linearly correlated with each other in the scatter plots of Fig.4.3. The correlation coefficient (R) and F-statistics (F) are given in each panels of the figure. All the scatter plots and fittings are performed using the popular statistical software R [25]. It can be seen from Fig.4.3 that the three sets of data correlate among each other very well. Highest values of R (0.9919) and F (3461.2) (cf. panel b) indicates the best quality of correlation between MRCI and EOM-CCSD data or vice-versa. The latter sets of data are used to further investigate the topography of the electronic potential energy surfaces and nuclear dynamics.

4.3.3 Electronic structure and Hamiltonian parameters of $CD_2F_2^+$

The geometry of the equilibrium minimum of the reference electronic ground state of CD_2F_2 is calculated by the second-order Møller-Plesset perturbation (MP2) as well as coupled-cluster singles and doubles (CCSD) level of theory employing the cc-pVTZ basis set of Dunning [20]. The GAUSSIAN-09 suite of programs [21] is used for this purpose.

The optimized equilibrium structure of CD_2F_2 belongs to the C_{2v} symmetry point group. The molecular orbital (MO) configuration of the equilibrium minimum structure is, ... $(3b_2)^2$ $(1a_2)^2$ $(4b_2)^2$ $(6a_1)^2$ $(2b_1)^2$. The electronic states of $\widetilde{X}^2B_1$, $\widetilde{A}^2B_2$, $\widetilde{B}^2A_1$ and $\widetilde{C}^2A_2$ of the CD_2F_2 radical cation result from the ionization of an electron from its valence MO of appropriate symmetry. The energetic ordering of the $^2A_1$ and $^2B_2$ electronic states of $CH_2F_2^+$ is discussed in previous subsection. The harmonic vibrational frequency ω_i of the vibrational modes i of the $\tilde{X}^1A_1$ state of CD_2F_2 is calculated at its equilibrium geometry. The harmonic frequencies and description of the vibrational modes are given in Table 4.3. The vertical ionization energy (VIE) of the $\widetilde{X}$, $\widetilde{A}$, $\widetilde{B}$ and $\widetilde{C}$ states of $CD_2F_2^+$ ($CH_2F_2^+$), calculated at the CASSCF-MRCI level of theory employing the cc-pVTZ basis set, is given in Table 4.6. Understandably, the VIE values do not change upon isotopic substitution. The adiabatic energies of the above electronic states of $CD_2F_2^+$ are also calculated at the same level of theory in the range -5.0≤**Q**≤5.0, along all vibrational modes. The adiabatic electronic energies of $CH_2F_2^+$ and $CD_2F_2^+$ are different as mass-weighted normal coordinates are employed in this study.

The coupling parameters of the vibronic Hamiltonian (cf. Eqs. 4.7-4.8) are calculated by fitting the adiabatic form of its diabatic electronic part to the adiabatic electronic energies calculated ab initio. The linear and quadratic intra-state coupling parameters of $\widetilde{X}^2B_1$, $\widetilde{A}^2B_2$, $\widetilde{A}^2A_1$ and $\widetilde{C}^2A_2$ electronic states of $CD_2F_2^+$ are given in Table 4.9. The linear inter-state coupling parameters are given in Table 4.10. We note that all the coupling parameters are estimated by non-linear least squares fitting of adiabatic electronic energies. We reiterate that the electronic Hamiltonians (of $CH_2F_2^+$ and $CD_2F_2^+$) are different because of mass-weighting of the coordinates.

The excitation strength (defined as $\frac{\kappa_i^2}{2\omega_i^2}$ or $\frac{(\lambda_i^{j-k})^2}{2\omega_i^2}$) given in the parentheses in Table 4.9 reveals that the symmetric vibrational mode ν_2 is active in the $\widetilde{X}^2B_1$, $\widetilde{A}^2B_2$ and $\widetilde{C}^2A_2$ electronic states. The vibrational mode ν_4 is expected to be strongly excited in the $\widetilde{A}^2B_2$ and $\widetilde{B}^2A_1$ electronic states. A moderate activity of ν_3 is expected in all electronic states of $CD_2F_2^+$. The vibrational mode ν_1 has the lowest excitation strength in all four states of $CD_2F_2^+$. The data in Table 4.10 reveal a strong inter-state coupling between $\widetilde{X}^2B_1$-$\widetilde{A}^2B_2$ states through ν_5 (a_2 symmetry) vibrational mode and between $\widetilde{X}^2B_1$-$\widetilde{B}^2A_1$ states through ν_7 (b_1 symmetry) vibrational mode. Despite this, a milder inter-state coupling between the $\widetilde{X}^2B_1$-$\widetilde{B}^2A_1$states through ν_6 (b_1 symmetry) and between the $\widetilde{B}^2A_1$-$\widetilde{C}^2A_2$ states through ν_5 revealed by the data (cf. Table 4.10). An inspection of the data in Table 4.9 reveal that the second order intra-state coupling parameter of symmetric mode ν_2 and non-totally symmetric mode ν_7 is higher in the $\widetilde{X}^2B_1$ state than the other states. This would cause a drastic reduction of frequencies of these vibrational modes in the $\widetilde{X}^2B_1$ state. Similarly, a drastic reduction of frequencies of ν_8 vibrational mode in the $\widetilde{A}^2B_2$ and $\tilde{B}^2A_1$ state is expected. An analogous coupling scheme was found in case of $CH_2F_2^+$ as discussed previous subsection.

Table 4.7: Linear and second-order coupling parameters (eV) of the Hamiltonian of $CH_2F_2^+$ (cf. Eq. 4.7), calculated at three different levels of theory.

Mode	κ_i^j			γ_i^j		
	MRCI	OVGF	EOM-CCSD	MRCI	OVGF	EOM-CCSD
			$\tilde{X}^2B_1$			
ν_1	-0.3047	-0.3300	-0.2758	-0.0060	-0.0042	-0.0048
ν_2	-0.1733	-0.2295	-0.1775	-0.0650	-0.0777	-0.0719
ν_3	0.2109	0.2457	0.2158	-0.0199	-0.0149	-0.0183
ν_4	-0.0062	0.0025	-0.0053	0.0050	0.0063	0.0054
ν_5	-	-	-	-0.0352	-0.0575	-0.0525
ν_6	-	-	-	-0.0408	-0.0344	-0.0298
ν_7	-	-	-	-0.0494	-0.0507	-0.0535
ν_8	-	-	-	-0.0748	-0.0723	-0.0715
ν_9	-	-	-	-0.0184	-0.0118	-0.0182
			$\tilde{A}^2B_2$			
ν_1	0.0582	0.0559	0.0534	0.0061	0.0042	0.0044
ν_2	0.1614	0.1288	0.1336	0.0131	0.0002	-0.0002
ν_3	-0.2717	-0.2323	-0.2536	0.0070	0.0084	0.0068
ν_4	0.1635	0.1783	0.1817	-0.0263	-0.0222	-0.0252
ν_5	-	-	-	0.0254	0.0064	0.0061
ν_6	-	-	-	0.0049	0.0066	0.0065
ν_7	-	-	-	-0.0040	-0.0033	-0.0039
ν_8	-	-	-	-0.0467	0.0303	-0.0532
ν_9	-	-	-	-0.1005	-0.0734	-0.0953
			$\tilde{B}^2A_1$			
ν_1	-0.1078	-0.1267	-0.1031	-0.0105	-0.0126	-0.0168
ν_2	0.2303	0.1964	0.1973	0.0033	0.0024	-0.0180
ν_3	-0.0459	0.0130	-0.0183	-0.0236	-0.0205	-0.0402
ν_4	-0.1275	-0.1269	-0.1264	0.0014	0.0025	0.0033
ν_5	-	-	-	-0.0290	-0.0292	-0.0565
ν_6	-	-	-	0.0245	0.0215	0.0446
ν_7	-	-	-	0.0007	0.0032	0.0085
ν_8	-	-	-	-0.0068	-0.0759	0.0138
ν_9	-	-	-	0.0097	-0.0472	0.0009
			$\tilde{C}^2A_2$			
ν_1	0.0305	0.0358	0.0379	0.0043	0.0037	0.0038
ν_2	0.1312	0.0895	0.0971	0.0126	0.0011	0.0003
ν_3	-0.2718	-0.2339	-0.2503	0.0049	0.0059	0.0051
ν_4	0.0491	0.0659	0.0619	-0.0149	-0.0129	-0.0137
ν_5	-	-	-	0.0048	0.0048	0.0065
ν_6	-	-	-	0.0068	0.0053	0.0055
ν_7	-	-	-	-0.0035	-0.0013	-0.0022
ν_8	-	-	-	0.0136	0.0132	0.0181
ν_9	-	-	-	-0.0609	-0.0687	-0.0568

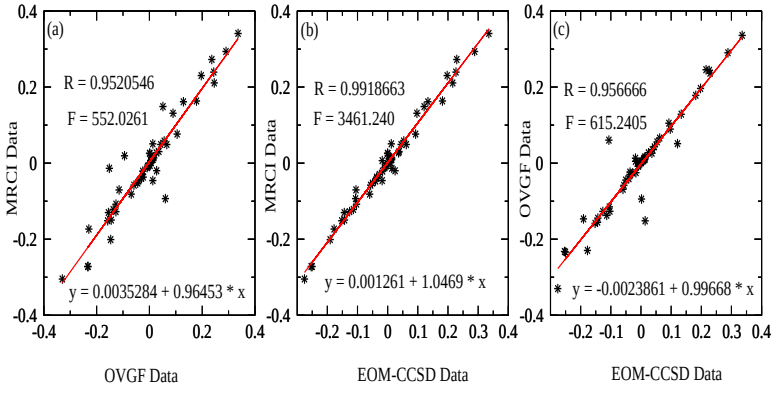

Figure 4.3: Least square fitting of all coupling parameters of $CH_2F_2^+$ derived from three different quantam mechanical methods by linear regression method.

Table 4.8: Linear inter-state coupling parameters (λ_i^{j-k}) of the Hamiltonian of $CH_2F_2^+$ (cf. Eq. 4.8). All parameters are given in eV unit.

Couple states	Mode	Curve fitting			Numerical		
		MRCI	OVGF	EOM-CCSD	MRCI	OVGF	EOM-CCSD
$\tilde{X}\tilde{A}$	ν_5	0.2394	0.2439	0.2265	0.2740	0.2401	0.2133
$\tilde{X}\tilde{B}$	ν_6	0.2726	0.2365	0.2292	0.2594	0.2323	0.2220
	ν_7	0.2936	0.2902	0.2884	0.2792	0.2887	0.2752
$\tilde{X}\tilde{C}$	ν_8	0.3410	0.3359	0.3355	0.5873	0.3370	0.3178
	ν_9						
$\tilde{A}\tilde{B}$	ν_8	0.0983		0.0990	0.0781		0.0974
	ν_9	0.1487	0.0513	0.1210	0.1505	0.0482	0.1148
$\tilde{A}\tilde{C}$	ν_6						
	ν_7		0.0273	0.0247		0.0280	0.0285
$\tilde{B}\tilde{C}$	ν_5	0.0765	0.1051	0.0926	0.1063	0.1019	0.0882

4.4 Adiabatic potential energy surfaces

One dimensional cuts of the adiabatic potential energy surfaces (PESs) of the $\widetilde{X}^2B_1$, $\widetilde{A}^2B_2$, $\widetilde{B}^2A_1$ and $\widetilde{C}^2A_2$ electronic states of difluoromethane radical cation are plotted along normal displacement coordinate of symmetric vibrational modes (ν_1-ν_4) in Figs. 4.4-4.5. In these figures points represent the calculated ab initio electronic energies by the CASSCF-MRCI (Fig. 4.4) and EOM-CCSD (Fig. 4.5) methods. The superimposed solid lines represent the potential energies obtained from the vibronic model using the respective parameters of Table 4.7. It can be seen from the figures that the calculated ab initio points are well reproduced by the constructed vibronic model. Among the four symmetric vibrational modes, the Condon activity of mode ν_3 is stronger in the $\widetilde{X}^2B_1$ and $\widetilde{C}^2A_2$ electronic states. On the other hand, the Condon activity of symmetric mode ν_4 and ν_2 is stronger in the $\widetilde{A}^2B_2$ and $\widetilde{B}^2A_1$ electronic states, respectively. Strong Condon activity of a vibrational mode results into a larger shift of the equilibrium minimum of the given electronic state along its coordinate relative to the reference equilibrium minimum at $\mathbf{Q}=\mathbf{0}$.

Numerous crossings of electronic states can be seen from Figs. 4.4-4.5. These crossings acquire the topography of conical intersections (CIs) in multi-dimensions. Energetic minimum of the seam of various CIs and equilibrium minimum of electronic states are estimated within a linear coupling model using the parameters of Table 4.7 and given in Table 4.11. In the latter, the diagonal and off-diagonal entries represent the equilibrium minimum of a state and the minimum of the seam of CIs, respectively. Energetic location

Table 4.9: Linear and second-order coupling parameters (in eV) of the Hamiltonian (cf. Eq. 4.7) of $CD_2F_2^+$, estimated from the calculated ab initio adiabatic electronic energies.

Mode	κ_i^j $(\frac{\kappa_i^2}{2\omega_i^2})$	γ_i^j	κ_i^j $(\frac{\kappa_i^2}{2\omega_i^2})$	γ_i^j
	$\widetilde{X}^2B_1$		$\widetilde{A}^2B_2$	
ν_1	-0.2773 (0.489)	-0.0099	0.0851 (0.046)	0.0084
ν_2	0.2677 (1.591)	-0.1017	-0.2678 (1.556)	0.0034
ν_3	0.0665 (0.128)	-0.0413	-0.1317 (0.502)	0.0081
ν_4	-0.0050 (0.003)	0.0092	0.1756 (3.560)	-0.0527
ν_5	-	-0.0724	-	0.0101
ν_6	-	-0.0580	-	0.0079
ν_7	-	-0.0962	-	-0.0121
ν_8	-	-0.0946	-	-0.1387
ν_9	-	-0.0444	-	-0.0260
	$\widetilde{B}^2A_1$		$\widetilde{C}^2A_2$	
ν_1	-0.0933 (0.055)	-0.0237	0.0571 (0.021)	0.0057
ν_2	-0.1670 (0.619)	-0.0185	-0.2430 (1.311)	-0.0011
ν_3	0.0630 (0.115)	-0.0358	-0.1551 (0.697)	0.0082
ν_4	-0.1341 (2.076)	0.0030	0.0539 (0.335)	-0.0293
ν_5	-	-0.0399	-	0.0099
ν_6	-	0.0415	-	0.0091
ν_7	-	-0.0050	-	-0.0100
ν_8	-	-0.1332	-	-0.0869
ν_9	-	-0.0228	-	-0.0399

of these stationary points on a state governs the mechanistic details of nuclear dynamics on it. It can be seen from the data given in Table 4.11 that $\widetilde{X}$-$\widetilde{A}$ CIs is quasi-degenerate with the minimum of the $\widetilde{A}$ state. Similar quasi-degeneracies can be seen between the minimum of $\widetilde{A}$-$\widetilde{B}$ and $\widetilde{B}$-$\widetilde{C}$ CIs with the minimum of $\widetilde{B}$ and $\widetilde{C}$ states, respectively. The $\widetilde{X}$-$\widetilde{B}$ and $\widetilde{X}$-$\widetilde{C}$ CIs occur ~ 0.62 eV and ~ 0.31 eV above the minimum of $\widetilde{B}$ and $\widetilde{C}$ states, respectively. These observations are also well supported by the EOM-CCSD data (cf. Table 4.11).

The adiabatic electronic energies of the $\widetilde{X}$, $\widetilde{A}$, $\widetilde{B}$ and $\widetilde{C}$ electronic states of $CD_2F_2^+$ radical cation calculated by the CASSCF-MRCI method are plotted as points along the dimensionless normal coordinates of the totally symmetric vibrational modes, ν_1-ν_4, in Fig. 4.6. A fit to these energies to the present vibronic model is also shown in Fig. 4.6 and indicated by the superimposed solid lines. It can be seen from each panel of the

Table 4.10: Same as in Table 4.9 for the linear inter-state coupling parameters (cf. Eq. 4.8). All parameters are given in eV unit.

Couple states j-k	Mode i	λ_i^{j-k} $(\frac{(\lambda_i^{j-k})^2}{2\omega_i^2})$
$\tilde{X}-\tilde{A}$	ν_5	0.2144 (1.700)
$\tilde{X}-\tilde{B}$	ν_6	0.2434 (0.337)
	ν_7	0.2463 (2.035)
$\tilde{X}-\tilde{C}$	ν_8	-
	ν_9	0.0530 (0.085)
$\tilde{A}-\tilde{B}$	ν_8	-
	ν_9	-
$\tilde{A}-\tilde{C}$	ν_6	0.0189 (0.002)
	ν_7	0.0191 (0.012)
$\tilde{B}-\tilde{C}$	ν_5	0.0824 (0.251)

Table 4.11: Estimated equilibrium minimum (diagonal entries) and minimum of the seam of various CIs (off-diagonal entries) of the electronic states of $CH_2F_2^+$. All quantities are given in eV.

	$\widetilde{X}^2B_1$	$\widetilde{A}^2B_2$	$\widetilde{B}^2A_1$	$\widetilde{C}^2A_2$
CASSCF-MRCI/cc-pVTZ				
$\tilde{X}^2B_1$	13.23	14.81	16.08	16.01
$\tilde{A}^2B_2$	-	14.81	15.47	17.22
$\tilde{B}^2A_1$	-	-	15.46	15.72
$\tilde{C}^2A_2$	-	-	-	15.70
EOM-CCSD/cc-pVTZ				
$\tilde{X}^2B_1$	12.99	14.47	15.62	15.80
$\tilde{A}^2B_2$	-	14.47	15.05	16.99
$\tilde{B}^2A_1$	-	-	15.00	15.01
$\tilde{C}^2A_2$	-	-	-	15.41

figure that the calculated ab initio points correspond well to the analytic form of the vibronic model discussed in Section 3.2.1. The curves in Fig. 4.6 reveal that the electronic ground state of the cation is energetically well separated from its excited states at the Franck-Condon geometry. The larger displacement of the equilibrium minimum of a given state along a given mode relative to the reference minimum at $\mathbf{Q}$=0, is in

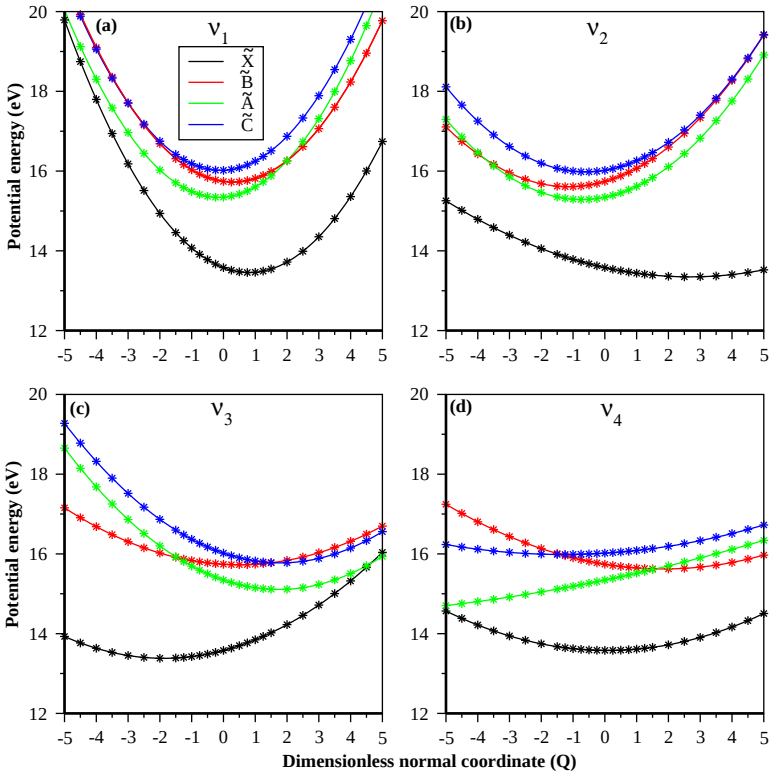

Figure 4.4: The adiabatic potential energy curves of the $\tilde{X}$, $\tilde{A}$, $\tilde{B}$ and $\tilde{C}$ electronic states of $CH_2F_2^+$ along the dimensionless normal coordinates of totally symmetric (a) ν_1, (b) ν_2, (c) ν_3 and (d) ν_4 vibrational modes. Each curve in the figure represents potential energy obtained from the present theoretical model. The ab initio potential energies with a harmonic contribution from the neutral ground electronic state are shown by the points on the diagram. The latter are calculated by the CASSCF-MRCI method employing cc-pVTZ basis set.

accord with its large excitation strength (Condon-activity) discussed above. It can be seen from Fig. 4.6 that the $\widetilde{B}$ state undergoes crossing with both $\widetilde{A}$ and $\widetilde{C}$ states. These curve crossings transform to conical intersections (CIs) in multi-dimensions. Energy of the minimum of various CIs and the equilibrium minimum of a state estimated from the present theoretical model are given in Table 4.12. In the latter, the entries in the diagonal and off-diagonal position represent the equilibrium minimum of a state and the minimum of the seam of CIs, respectively. It can be seen from the data given in Table 4.12 that the minimum of $\widetilde{A}$-$\widetilde{B}$ CIs is quasi-degenerate with the minimum of the $\widetilde{B}$ state. Similar quasi-degeneracies also exist between the minimum of the seam of $\widetilde{B}$-$\widetilde{C}$ CIs with the minimum of the $\widetilde{C}$ state. We note that the above stationary points are calculated with the full second-order vibronic coupling model [26]. In that article [26] these points were calculated within a linear coupling model. The stationary points obtained for $CH_2F_2^+$ with a second-order model are given in the parentheses of the Table 4.12 for comparison. We reiterate that mass scaling of the coordinates leads to different

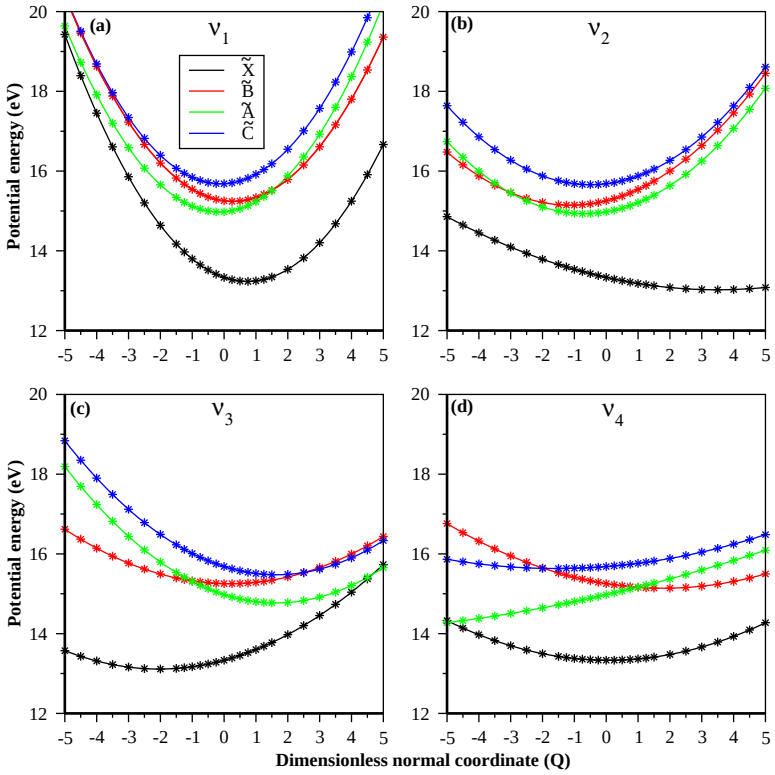

Figure 4.5: Same as Fig. 4.4. The adiabatic electronic energies are calculated by the EOM-CCSD method employing cc-pVTZ basis set.

Table 4.12: Estimated equilibrium minimum (diagonal entries) and minimum of the seam of various CIs (off-diagonal entries) of the electronic states of $CD_2F_2^+$. The same values for $CH_2F_2^+$ are given in the parentheses. All quantities are given in eV.

	Energy			
	$\tilde{X}^2B_1$	$\tilde{A}^2B_2$	$\tilde{B}^2A_1$	$\tilde{C}^2A_2$
$\tilde{X}^2B_1$	12.673 (13.160)	14.511 (14.705)	16.724 (16.266)	16.122 (16.191)
$\tilde{A}^2B_2$	-	13.855 (14.695)	15.479 (15.470)	16.381 (19.341)
$\tilde{B}^2A_1$	-	-	15.466 (15.462)	15.736 (15.725)
$\tilde{C}^2A_2$	-	-	-	15.690 (15.703)

parameters of the electronic Hamiltonian, which gives rise to different equilibrium and seam minima of $CH_2F_2^+$ and $CD_2F_2^+$.

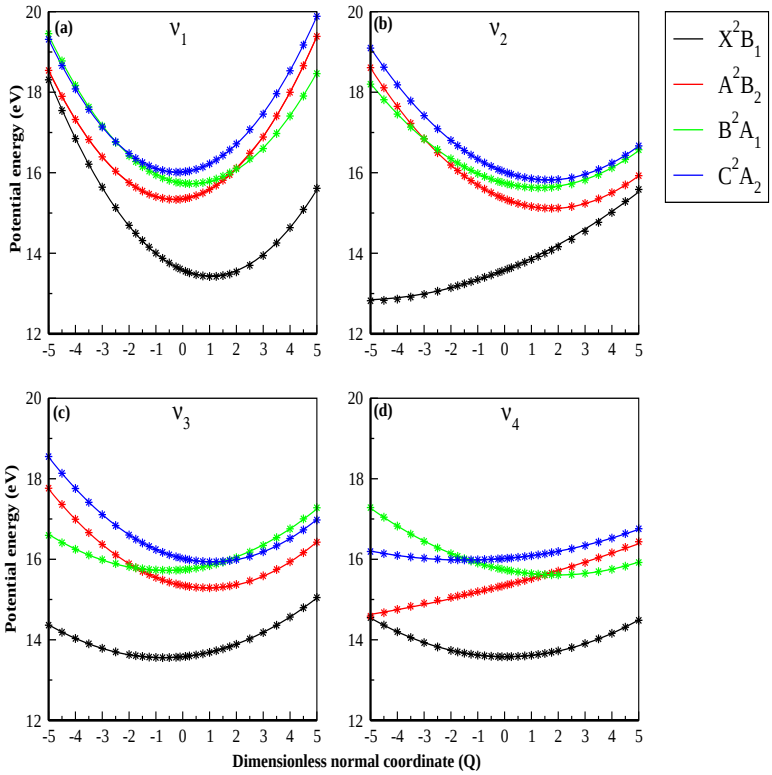

Figure 4.6: The adiabatic potential energy curves of the $\tilde{X}$, $\tilde{A}$, $\tilde{B}$ and $\tilde{C}$ electronic states of $CD_2F_2^+$ along dimensionless normal coordinates of totally symmetric (a) ν_1 (D-C symmetric stretching), (b)ν_2 (D-C-D symmetric in-plane bending), (c) ν_3 (F-C symmetric stretching) and (d) ν_4 (F-C-F symmetric bending) vibrational modes. The ab initio potential energies calculated by the CASSCF-MRCI method and fit to these energies to the present vibronic model are shown by the points and solid lines, respectively.

4.5 Non-adiabatic effects in the $\widetilde{A}^2\mathbf{B}_2$ and $\widetilde{B}^2\mathbf{A}_1$ states of $\mathbf{CH_2F_2^+}$

The first ($\widetilde{A}^2B_2$) and second ($\widetilde{B}^2A_1$) excited states of difluoromethane radical cation originate from removal of one electron from the ground state occupied b_2 and a_1 molecular orbitals (MOs), respectively, of neutral difluoromethane belonging to C_{2v} equilibrium symmetry. The selection of these two states are made because of their energetic proximity. As we are dealing with two electronic states of $CH_2F_2^+$, the constructed model diabatic vibronic Hamiltonian is represented by a $2\otimes2$ matrix,

$$\mathcal{H} = \begin{pmatrix} \mathcal{H}_{11} & \mathcal{H}_{12} \\ \mathcal{H}_{21} & \mathcal{H}_{22} \end{pmatrix}. \tag{4.9}$$

Where the diagonal matrix element (H_{11}/H_{22}) represents the diabatic electronic energy of the cationic electronic states and the off-diagonal element (H_{12}/H_{21}) represents the coupling between them. All the elements (H_{ij}) of this matrix are function of the dimensionless normal coordinate (NC) of the vibrational modes of neutral reference. The dimensionless NCs are represented here, as Q_g and Q_u, for totally symmetric vibrational modes and coupling vibrational modes, respectively. The nine vibrational modes of CH_2F_2 transform according to the following IREPs of C_{2v} symmetry point group

$$\Gamma = 4a_1 + 1a_2 + 2b_1 + 2b_2. \tag{4.10}$$

Elementary symmetry selection rule is presented in Eq. 4.11, allows coupling of $\widetilde{A}$ and $\widetilde{B}$ states (in first order) through the vibrational modes of b_2 symmetry

$$B_2 \otimes b_2 \otimes A_1 \supset A_1. \tag{4.11}$$

Where the symmetry of electronic states and vibrational modes are denoted by the upper and lower case letters, respectively. The matrix elements of the vibronic Hamiltonian (Eq. 4.9) are expanded in a Taylor series as

$$H_{ii} = \sum_{k\in a_1} \frac{1}{2}\omega_k Q_g^{k^2} + \sum_{k\in b_2} \frac{1}{2}\omega_k Q_u^{k^2} + E_i + \sum_{k\in a_1} \kappa_k^i Q_g^k + \sum_{k\in a_1} \frac{1}{2}\gamma_k^i Q_g^{k^2} + \sum_{k\in b_1,b_2,a_2} \frac{1}{2}\gamma_k^i Q_u^{k^2} \tag{4.12}$$

$$H_{ij} = \sum_{k\in b_2} \lambda_k^{i-j} Q_u^k. \tag{4.13}$$

The first two terms in Eq. 4.12 describe the harmonic potential energy surface of neutral molecule in its electronic ground state and corresponding ω_k values are the harmonic frequencies of the vibrational modes. The term E_i represents the vertical ionization energies of the $\widetilde{A}$ and $\widetilde{B}$ electronic states. The term κ_k corresponds to the linear intra-state coupling parameter of the totally symmetric (a_1) vibrational modes, whereas the term γ_k represents the quadratic intra-state coupling parameters for all vibrational modes. The off-diagonal coupling term, λ_k^{i-j} corresponds to the linear inter-state coupling parameter between $\widetilde{A}$ and $\widetilde{B}$ through coupling vibrational modes.

The adiabatic potential energy along a coupling vibrational mode is given by

$$V_{1,2}(Q_u^k) = \frac{1}{2}\omega_k Q_u^{k^2} + \frac{1}{2}(\gamma_k^2 + \gamma_k^1)Q_u^{k^2} + \frac{1}{2}(E_1 + E_2) \mp \sqrt{\left\{(E_1 - E_2) + \frac{1}{2}(\gamma_k^2 - \gamma_k^1)\right\}^+ 4\lambda^2 Q_u^{k^2}} \tag{4.14}$$

A characteristic feature of new minima is observed in lower adiabatic surface $V_1(Q_u^k)$, whereas the upper surface becomes steeper. The symmetry of the nuclear geometry at the new minima is lower than the symmetry of equilibrium geometry of the reference state, this phenomenon is known as ″the breaking of molecular symmetry″. It is known that the symmetry breaking is simply a consequence of repulsion of the diabatic surfaces via the vibronic coupling [18]. The value of dimensionless normal coordinate at the minimum of the lower adiabatic PES is represented by following equation (excluding the γ_k^i):

$$Q_u^k\left(\omega_k - \frac{\lambda^2}{\sqrt{\left(\frac{E_2-E_1}{2}\right)^2 + \lambda^2 {Q_u^k}^2}}\right) = 0. \tag{4.15}$$

In this equation, $\Delta=\frac{E_2-E_1}{2}$ and $x=\frac{\lambda^2}{\omega_k\Delta}$ and x is a dimensionless quantity. The three roots of Eq. 4.15 have the following forms:

$$Q_u^k = 0; \quad Q_u^k = \pm\frac{\lambda}{\omega_k}\sqrt{1-\frac{1}{x^2}}. \tag{4.16}$$

If the value of $x < 1$, then the second and third roots of Eq. 4.16 become imaginary. So the validity of second and third roots remain only when $x \geq 1$ and when $x < 1$ first root $Q_u^k = 0$ is valid. As a result, two equivalent minima form at $Q_u^k \neq 0$ in the lower adiabatic PES when $x > 1$ and the previous minimum at $Q_u^k = 0$ is converted as local maximum. The stabilization energy due to this symmetry breaking phenomenon is $E_s = \Delta(\frac{(1-x)^2}{2x})$. No symmetry breaking occur for $x < 1$ and molecule does not get any stabilization due to this phenomenon. Only just above the threshold value of $x = 1$, the stabilization energy quadratically increases with x, whereas at the larger value of x, a linear dependency is observed.

After inclusion of M number of coupling vibrational modes in Eq. 4.15, the generalized formula of x becomes:

$$x = \sum_{k=1}^{M} x_k. \tag{4.17}$$

Where, x_k is the dimensionless x parameter for k^{th} coupling mode and $x_k = \frac{\lambda_k^2}{\omega_k\Delta}$. It is seen from Eq. 4.17 that due to multi-mode effect x is generated from the contribution (x_k) of each coupling vibrational mode. In this way symmetry breaking phenomenon of a molecule becomes cumulative effect of all coupling vibrational modes. So in order to give an explanation of Eq. 4.17, one can say that if a single coupling vibrational mode fails to introduce a minimum at $V_1(Q_u^k)$ at $Q_u^k \neq 0$, then due to the multi-mode effect of the other coupling vibrational modes, there will be a possibility to form a minimum in the Q_u^k sub-space under the condition of $x \geq 1$.

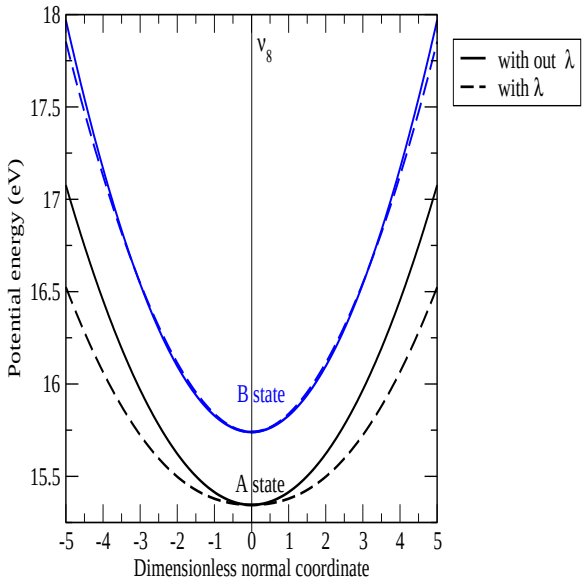

Figure 4.7: The effect of inter-state coupling between the $\widetilde{A}^2B_2$ and $\widetilde{B}^2A_1$ electronic states of $CH_2F_2^+$ through ν_8 vibrational mode is shown here. The solid (black and blue) lines represent the 1-D PESs in absence of inter-state coupling and the dashed (black and blue) lines represent the 1-D PESs in presence of inter-state coupling between these two states.

In the previous sections, we established a diabatic vibronic coupling model for the first four electronic states of $CH_2F_2^+$ by performing extensive electronic structure calculations. Here, we consider the first ($\widetilde{A}^2B_2$) and second ($\widetilde{B}^2A_1$) excited electronic states of $CH_2F_2^+$ because of their energetic proximity ($\sim$0.40 eV). It is found that the vibronic structures of three excited states, $\widetilde{A}^2B_2$, $\widetilde{B}^2A_1$ and $\widetilde{C}^2A_2$ of $CH_2F_2^+$ are highly overlapping and they form the second photoelectron band of CH_2F_2 [18, 26, 27]. These three states are coupled through multiple conical intersections (CIs) and are well separated from the ground electronic states ($\widetilde{X}^2B_1$) of $CH_2F_2^+$ [26].

The two vibrational modes of b_2 symmetry are represented as ν_8 and ν_9 vibrational modes.The vibrational frequencies, first-order (κ) and second-order (γ) intra-state coupling parameters of totally-symmetric modes (represented as ν_1,ν_2, ν_3 and ν_4) and the γ value of ν_8 and ν_9 vibrational modes are given in Tables 4.13 and 4.7. The vertical ionization energies of the considered states and the inter-state coupling (λ) of ν_8 and ν_9 vibrational modes are listed in Tables 4.6 and 4.8. The effect of inter-state coupling through these vibrational modes ν_8 and ν_9 are presented in Figs. 4.7 and 4.8, respectively.

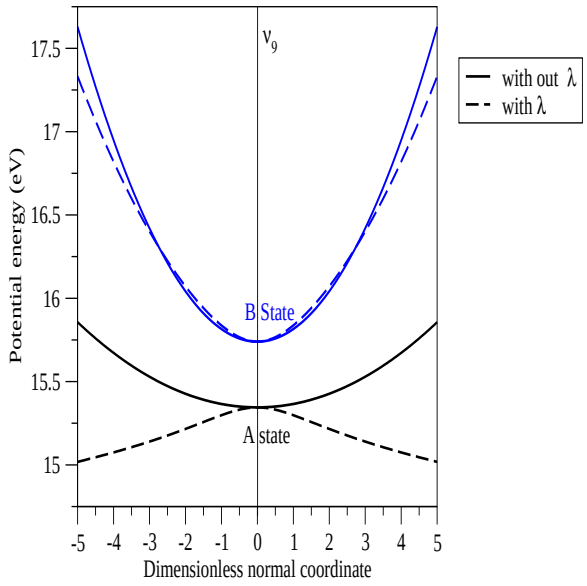

Figure 4.8: The effect of inter-state coupling between the $\widetilde{A}^2B_2$ and $\widetilde{B}^2A_1$ electronic states of $CH_2F_2^+$ through ν_9 vibrational mode is shown here. The solid (black and blue) lines represent the 1-D PESs in absence of inter-state coupling and the dashed (black and blue) lines represent the 1-D PESs in presence of inter-state coupling between these two states.

Table 4.13: The vertical ionization energies of the $\widetilde{A}^2B_2$ and $\widetilde{B}^2A_1$ electronic states of $CH_2F_2^+$ and the inter-state coupling parameters between these two states are reproduced here. The dimensionless x_k parameters and excitation strength are tabulated in last two columns in the table, respectively.

Electronic state	Vertical ionization energy (eV)	Vibrational mode	Inter-state coupling parameter (λ (eV))	Dimensionless x_k parameter	Excitation strength
$\widetilde{A}^2B_2$	15.34	ν_8	0.0983	0.2609	0.14
$\widetilde{B}^2A_1$	15.74	ν_9	0.1487	0.7810	0.55

The individual dimensionless x_k parameter values for the coupling modes ν_8 and ν_9 are calculated by using the parameters from Tables 4.1 and 4.13 and those values are given in Table 4.13. It is clear from this table that both the values are lower than the threshold value of x_k =1. Thus both these coupling vibrational modes unable to create double minima at the lower adiabatic surface $[V_1(Q_u^k)]$ due to their individual effect on the coupled-surfaces. The individual vibronic coupling effect of these two coupling vibrational modes is reflected in the curvature of two PESs (cf. Figs. 4.7 and 4.8): one

without considering the inter-state vibronic coupling (λ) and another with the inclusion of λ. The upper coupled-surface V_2, is steeper near the minimum at Q_u^k =0 than the upper uncoupled-surface, whereas the lower coupled-surface V_1 is relatively flat compared to the lower uncoupled-surface. This scenario is depicted in both Figs. 4.7 and 4.8, for the individual effect of ν_8 and ν_9 coupling vibrational modes, respectively. In these figures dashed lines reprsent the coupled-surfaces and the solid line represent the uncoupled surfaces. So it is established that the symmetry breaking and the formation of double minima at the coupled lower adiabatic surface is not possible due to the two-states-single-mode interaction. We mentioned in the above that the lowering of symmetry of the coupled lower surface also occurs due to the cumulative interaction of all participating coupling vibrational (here, ν_8 and ν_9) modes. The cumulative dimesionless x parameter value ($\sim$1.042) of these two coupling vibrational modes is just above the threshold value of x =1, which suggests a lowering of symmetry of the lower coupled surface due to the simultaneous distortion along two coupling vibrational modes. As a result of this two-states-multi-modes interaction, the lower coupled surface gets stabilization in (Q_u^8, Q_u^9) sub-space and the upper coupled surface becomes steeper.

4.6 Summary and conclusions

A theoretical account of vibronic coupling among energetically lowest four electronic states ($\widetilde{X}^2B_1$, $\widetilde{A}^2B_2$, $\widetilde{B}^2A_1$, $\widetilde{C}^2A_2$) of $CH_2F_2^+$ ($CD_2F_2^+$) is presented in this chapter. The study is motivated by numerous experimental spectroscopy data available on this system. A model Hamiltonian of the four coupled electronic states is developed in a diabatic representation in terms of normal coordinates of vibrational modes using standard vibronic coupling theory. The parameters of the Hamiltonian are determined by performing extensive calculations of adiabatic electronic energies using various state-of-the-art quantum chemistry methods. Among different sets, the parameter set derived from the CASSCF-MRCI electronic energies is found to yield best results. The calculated electronic energies including configuration interactions also confirmed the energetic ordering of electronic states. Detailed topographical analysis of four adiabatic electronic states of $CH_2F_2^+$ ($CD_2F_2^+$) is carried out and multiple conical intersections among them is established. It is found that the coupling among $\widetilde{A}$-$\widetilde{B}$-$\widetilde{C}$ electronic states is quite strong and the minimum of the seam of intersections quasi-degenerate to the equilibrium minimum of the higher electronic state in a pair.

A theoretical account of vibronic coupling between the two closely lying excited states ($\widetilde{A}^2B_2$ and $\widetilde{B}^2A_1$) of $CH_2F_2^+$ is also presented here . A model 2$\otimes$2 vibronic Hamiltonian is constructed for the purpose. The effect of coupling vibrational modes (ν_8 and ν_9) on the coupled $\widetilde{A}^2B_2$- $\widetilde{B}^2A_1$ surface is studied here by constructing the two-states-single-mode as well as two-states-multi-modes model Hamiltonian. The result shows that the symmetry breaking and stabilization of lower coupled adiabatic surface is not possible through single mode interaction rather it is possible via cummulative interaction of both coupling modes. The presence of moderate inter-state coupling and the quasi-degeneracy

between the $\widetilde{A}-\widetilde{B}$ CIs with the minimum of $\widetilde{B}$ state facilitates the internal conversion between these two states.

References

[1] P. W. Forysinski, P. Zielke, D. Luckhaus, and R. Signorell, Phys. Chem. Chem. Phys. **12**, 3121 (2010).

[2] B. P. Pullen, T. A. Carlson, W. E. Moddeman, G. K. Schweitzer, W. E. Bull and F. A. Grimm, J. Chem. Phys. **53**, 768 (1970).

[3] C. R. Brundle, M. B. Robin and H. Basch, J. Chem. Phys. **53**, 2196 (1970).

[4] W.R. Harshbarger, M.B. Robin and E.N. Lassettre, J. Electron Spectrosc. Relat. Phenom. **1**, 319 (1972).

[5] M.S. Banna, B.E. Mills, D.W. Davis and D.A. Shirley, J. Chem. Phys. **61**, 4780 (1974).

[6] M.S. Banna and D.A. Shirley, Chem. Phys. Lett. **33**, 441 (1975).

[7] G. Bieri,L. Åsbrink and W. Von Niessen, J. Electron Spectrosc. Relat. Phenom. **23**, 281 (1981).

[8] T. Pradeep, D. A. Shirley, J. Electron Spectrosc. Relat. Phenom. **66**, 125 (1993).

[9] G.L. Su et al., J. Chem. Phys. **122**, 054301 (2005).

[10] A. W. Potts, H. J. Lempka, D. G. Streets and W. C. Price, Philos. Trans. R. Soc. London, Ser. A. **268**, 59 (1970).

[11] D. P. Seccombe, R. P. Tuckett and B. O. Fisher, J. Chem. Phys. **114**, 4074 (2001).

[12] D. P. Seccombe, R. Y. L. Chim, R. P. Tuckett, H. W. Jochims and H. Baumgärtel, J. Chem. Phys. **114**, 4058 (2001).

[13] G.L. Su, C.G. Ning, S.F. Zhang, X.G. Ren, H. Zhou, B. Li, F. Huang, G.Q. Li, J.K. Deng, Y. Wang, Chem. Phys. Lett. **390**, 162 (2004).

[14] G.L. Su et al., J. Chem. Phys. **122**, 054301 (2005).

[15] K. Takeshita, Chem. Phys. Lett. **165**, 232 (1990).

[16] D. Luckhaus, P. W. Forysinski, P. Zielke and R. Signorell, Mol. Phys. **108**, 2325 (2010).

[17] H. -W. Xi and M. -B. Huang, Chem. Phys. Lett. **430**, 227 (2006).

[18] H. Köppel, W. Domcke, and L. S. Cederbaum, Multimode Molecular Dynamics Beyond the Born-Oppenheimer Approximation, in Advances in Chemical Physics, Volume 57 (2007) (eds I. Prigogine and S. A. Rice), John Wiley & Sons, Inc. Hoboken, NJ, USA. doi: 10.1002/9780470142813.ch2.

[19] L. S. Cederbaum, W. Domcke, H. Köppel, and W. von Niessen, Chem. Phys. **26**, 169 (1977).

[20] T. H. Dunning Jr., J. Chem. Phys. **90**, 1007 (1989).

[21] Gaussian 09, Revision B.01, M. J. Frisch, G. W. Trucks, H. B. Schlegel, G. E. Scuseria, M. A. Robb, J. R. Cheeseman, G. Scalmani, V. Barone, B. Mennucci, G. A. Petersson, H. Nakatsuji, M. Caricato, X. Li, H. P. Hratchian, A. F. Izmaylov, J. Bloino, G. Zheng, J. L. Sonnenberg, M. Hada, M. Ehara, K. Toyota, R. Fukuda, J. Hasegawa, M. Ishida, T. Nakajima, Y. Honda, O. Kitao, H. Nakai, T. Vreven, J. A. Montgomery, Jr., J. E. Peralta, F. Ogliaro, M. Bearpark, J. J. Heyd, E. Brothers, K. N. Kudin, V. N. Staroverov, T. Keith, R. Kobayashi, J. Normand, K. Raghavachari, A. Rendell, J. C. Burant, S. S. Iyengar, J. Tomasi, M. Cossi, N. Rega, J. M. Millam, M. Klene, J. E. Knox, J. B. Cross, V. Bakken, C. Adamo, J. Jaramillo, R. Gomperts, R. E. Stratmann, O. Yazyev, A. J. Austin, R. Cammi, C. Pomelli, J. W. Ochterski, R. L. Martin, K. Morokuma, V. G. Zakrzewski, G. A. Voth, P. Salvador, J. J. Dannenberg, S. Dapprich, A. D. Daniels, O. Farkas, J. B. Foresman, J. V. Ortiz, J. Cioslowski, and D. J. Fox, Gaussian, Inc. Wallingford CT, 2010.

[22] H.-J. Werner, P. J. Knowles, G. Knizia, F. R. Manby, et al., MOLPRO. version 2012.1, 2012.

[23] CFOUR, a quantum chemical program package written by J.F. Stanton, J. Gauss, M.E. Harding, P.G. Szalay with contributions from A.A. Auer, R.J. Bartlett, U. Benedikt, C. Berger, D.E. Bernholdt, Y.J. Bomble, L. Cheng, O. Christiansen, M. Heckert, O. Heun, C. Huber, T.-C. Jagau, D. Jonsson, J. Juslius, K. Klein, W.J. Lauderdale, D.A. Matthews, T. Metzroth, L.A. Mck, D.P. O'Neill, D.R. Price, E. Prochnow, C. Puzzarini, K. Ruud, F. Schiffmann, W. Schwalbach, C. Simmons, S. Stopkowicz, A. Tajti, J. Vzquez, F. Wang, J.D. Watts and the integral packages MOLECULE (J. Almlf and P.R. Taylor), PROPS (P.R. Taylor), ABACUS (T. Helgaker, H.J. Aa. Jensen, P. Jrgensen, and J. Olsen), and ECP routines by A. V. Mitin and C. van Wllen.
M.E. Harding, T. Metzroth, J. Gauss, and A.A. Auer, J. Chem. Theor. Comp. **4**, 64 (2008).

[24] E. B. Wilson Jr., J. C. Decius, and P. C. Cross, Molecular vibrations (McGraw-Hill, New York, 1995).

[25] R Core Team (2013). R: A language and environment for statistical computing. R Foundation for Statistical Computing, Vienna, Austria. ISBN 3-900051-07-0, URL http://www.R-project.org/.

[26] R. Sarkar and S. Mahapatra. Molecular Physics. **113**, 3073 (2015).

[27] R. Sarkar and S. Mahapatra. J. Phys. Chem. A. **120**, 3504 (2016).

5 Vibronic dynamics on the electronic states of $CH_2F_2^+$ and its deuterated isotopomer

5.1 Introduction

The photophysics of difluoromethane radical cation ($CH_2F_2^+$) and its deuterated isotopomer ($CD_2F_2^+$) has received renewed attention of experimentalists over the past decades. Broad band vibronic structures of the electronic ground and excited states of these radical cations were measured in several photoelectron spectroscopy experiments by using He I and X-ray radiation sources [1–7]. More recently, pulsed-field-ionization zero-electron-kinetic-energy (PFI-ZEKE) photoelectron spectroscopy measurements were carried out by Forysinki et al. [8], which unveiled the resolved vibronic fine structure of the electronic ground state of the $CH_2F_2^+$ radical cation.

The experimental He I photoelectron spectrum recorded by Pradeep et al. [5] revealed four bands in the ∼12.5-17.0 eV energy range. The results show partially resolved vibronic structure of the electronic ground ($\widetilde{X}$) state and highly overlapping band stuctures of the next three excited ($\widetilde{A}$, $\widetilde{B}$ and $\widetilde{C}$) electronic states. Theoretical studies with and without configuration interactions were carried out [1,9,10]. The results revealed different energetic ordering of the electronic states of $CH_2F_2^+$. Progression of C-H stretching (ν_1), H-C-H bending (ν_2) and C-F stretching (ν_3) vibrations in the $\widetilde{X}$-band was identified in the theoretical study of Takeshita [9] and these findings were in good agreement with the He I experiments [1–3]. Analysis of the PFI-ZEKE spectrum [8] of the $\widetilde{X}$ state revealed polyad structures, formed by ν_2 and ν_3 vibrational modes and the assignments correspond fairly well to Takeshita's [9] theoretical results. Harmonic Franck-Condon calculations at the MP2/aug-cc-pVQZ level of theory revealed poor agreement with the PFI-ZEKE results [8]. In a later study, the importance of anharmonicity and the breakdown of Franck-Condon approximation in interpreting the PFI-ZEKE results was examined by Luckhaus et al. [10].

Brundle et al. [1] and Potts et al. [3] found that the progression in the $\widetilde{X}$ band is formed by ν_3 vibrational mode only. Whereas Pullen et al. [2] found the same due to the

[0]The subject of this Chapter is published by: Rudraditya Sarkar and S. Mahapatra in Molecular Physics **113**, 3073 (2015). and J. Phys. Chem. A. **120**, 3504 (2016).

progression of H-C-H twisting (ν_5), H-C-H rocking (ν_7), F-C-F antisymmetric stretching (ν_8) and ν_2 vibrational modes. In a later study, Pradeep et al. [5] identified the progression of ν_2, ν_3 and the first overtone of ν_4 vibrational modes. This observation is in partial contradiction with the prediction of Takeshita [9], who found the progression of ν_1 instead of ν_4 vibrational mode. Analysis of the PFI-ZEKE spectrum revealed in addition to the excitation of symmetric ν_2 and ν_3 vibrational modes in the polyad structure, the excitation of non-totally symmetric vibrational modes as well. In case of other photoionization bands, Brundle et al. [1] observed progression of ν_3 and ν_4 vibrational modes in the $\widetilde{C}$ band. Potts et al. [3] found progression of ν_2 and ν_4 vibrational modes, repectively, in the $\widetilde{B}$ and $\widetilde{C}$ bands. Pradeep et al. [5] found both these vibrational modes contribute to the $\widetilde{B}$ and $\widetilde{C}$ bands and ν_2 and ν_3 modes form progression in the $\widetilde{A}$ band of $CH_2F_2^+$.

An interesting observation of disappearance of the vibrational structure of the ground state spectrum of $CH_2F_2^+$ upon isotopic deuterium substitution was made in the experimental recording of Brundle et al. [1]. To the best of our knowledge, the latter is the only experimental measurement of the photoionization spectrum of CD_2F_2. The loss of vibrational structure was postulated to be due to: 1) possible excitation of multiple vibrational modes and the existence of accidental degeneracies among them absent in the deuterated isotopomer and 2) the ease of predissociation in case of deuterated cation than the normal cation imposing a lifetime broadening of the spectrum [1]. It is also conjectured that vibrational modes of C-H character rather than C-F character predominantly contribute to the electronic ground state spectrum of $CH_2F_2^+$ [1]. The vibrational structure of the overlapping $\widetilde{A}$-$\widetilde{B}$-$\widetilde{C}$ band remains virtually unchanged upon deuteration, indicating the involvement of vibrational modes of C-F character rather than C-H character in these electronic states.

In Cahpter 4 and Ref. [11], we established a diabatic vibronic coupling [12–22] model for the $\widetilde{X}$-$\widetilde{A}$-$\widetilde{B}$-$\widetilde{C}$ electronic states of $CH_2F_2^+$ by performing extensive ab initio quantum chemistry, complete active space self consistent field multi-reference configuration interaction (CASSCF-MRCI) calculations. In addition to a detailed topographical analysis of the electronic states, various crossings among the potential energy surfaces are discussed in the Chapter 4. In this Chapter, we set out to study the vibronic structure of the electronic ground state of $CH_2F_2^+$ at finer resolution, assign the calculated vibronic levels and compare the results with the PFI-ZEKE experiment and other theoretical and experimental results available in the literature [1–3, 5, 8–10]. The vibronic band structures of the $CD_2F_2^+$ are also calculated, assigned and a comparative account with that of $CH_2F_2^+$ is presented.

5.2 Nuclear dynamics

The vibronic energy level spectrum of $CH_2F_2^+$ and its deuterated analogue is calculated by a time-independent matrix diagonalization approach [16] using Fermi's golden rule equation for the spectral intensity

$$P(E) = \sum_n |<\Psi_n^f|\hat{T}|\Psi_0^i>|^2 \delta(E - E_n^f + E_0^i), \tag{5.1}$$

where, $P(E)$ represents spectral intensity. $|\Psi_0^i>$ and $|\Psi_n^f>$ are the initial and final vibronic states with energy E_0^i and E_n^f, respectively. The operator $\hat{T}$ is the transition dipole operator. The reference electronic ground state $|\Psi_0^i>$ [ground state of neutral CH_2F_2 (CD_2F_2)] is assumed to be vibronically decoupled from the excited electronic states and is given by

$$|\Psi_0^i\rangle = |\Phi_0^i\rangle|\chi_0^i\rangle, \tag{5.2}$$

where $|\Phi_0^i\rangle$ and $|\chi_0^i\rangle$ represent the electronic and vibrational components of this state, respectively. This state is assumed to be harmonic and the vibrational component of the above wavefunction is expressed in terms of the eigenfunctions of reference harmonic Hamiltonian, $T_N + V_0$ (cf. Section 4.2.1 in the Chapter 4). In the normal coordinate representation of vibrational modes, the vibrational wavefunction is a direct product of one-dimensional oscillator functions along each mode. The final vibronic state of $CH_2F_2^+$ ($CD_2F_2^+$) can be expressed as

$$|\Psi_n\rangle = |\Phi^m\rangle|\chi_n^m\rangle, \tag{5.3}$$

where the superscript m represents the $\tilde{X}^2B_1$, $\tilde{A}^2B_2$, $\tilde{B}^2A_1$, $\tilde{C}^2A_2$ electronic states of $CH_2F_2^+$ ($CD_2F_2^+$), respectively. With the above definitions, the spectral intensity of Eq. 5.1 can be re-written as

$$P(E) = \sum_n |\tau^m \langle\chi_n^m|\chi_0\rangle|^2 \delta(E - E_n^f + E_0^i), \tag{5.4}$$

where,

$$\tau^m = \langle\Phi^m|\hat{T}|\Phi^0\rangle, \tag{5.5}$$

represents the transition dipole matrix elements. These are treated as constant assuming the general applicability of Condon approximation in a diabatic electronic basis [18].

The time-independent Schrödinger equation of the vibronically coupled states is solved by representing the Hamiltonian (cf. Section 4.2.1 in the Chapter 4) in the direct product harmonic oscillator (HO) basis of the reference state. The final vibronic states, $|\Psi_n^f\rangle$, can be expressed as

$$|\Psi_n^f\rangle = \sum_{|K_i\rangle,m} a^n_{k_i,\ldots,k_f,m}|K_i\rangle\ldots|K_f\rangle|\Phi_m\rangle. \tag{5.6}$$

In the above equation, the K^{th} quantum of the i^{th} vibrational mode is denoted by $|K_i\rangle$ and $|\Phi_m\rangle$ denotes the m^{th} electronic state of the interacting electronic manifold of $CH_2F_2^+$ ($CD_2F_2^+$) radical cation. The size of the oscillator basis is chosen based on the numerical convergence of the vibronic eigenvalue spectrum. The Hamiltonian matrix expressed in a direct product HO basis is highly sparse, it is tri-diagonalized using Lanczos algorithm [23,24] prior to diagonalization. The energetic location of the vibronic levels is given by the resulting diagonal eigenvalue matrix and the relative intensities are calculated from the squared first component of the Lanczos eigenvectors [25].

In a time-dependent picture, the spectral intensity is calculated by Fourier transforming the time autocorrelation function of the wavepacket (WP) propagating on the final electronic state [15]

$$P(E) \approx \sum_{m=1}^{2} 2Re \int_0^\infty e^{iEt/\hbar} \langle \chi_0 | \tau^\dagger e^{-iHT/\hbar} \tau | \chi_0 \rangle dt, \tag{5.7}$$

$$\approx \sum_{m=1}^{2} 2Re \int_0^\infty e^{iEt/\hbar} C^m(t) dt, \tag{5.8}$$

where, $C^m = \langle \Psi(0) | \Psi(t) \rangle$, represents the time autocorrelation function of the WP, initially prepared on the electronic state m. The time-dependent WP propagation is carried out within the multi-configuration time dependent Hartree (MCTDH) approach developed by Meyer et al. [26–29].

5.3 Results and discussions

5.3.1 Vibronic band structure of coupled $\widetilde{X}$-$\widetilde{A}$-$\widetilde{B}$-$\widetilde{C}$ states of $CH_2F_2^+$

The broad band vibronic structure of the $\widetilde{X}$-$\widetilde{A}$-$\widetilde{B}$-$\widetilde{C}$ coupled electronic states of $CH_2F_2^+$ is calculated and compared with the experimental photoionization spectroscopy results of Ref. [5]. The vibronic Hamiltonian constructed in section 4.2.1, the parameters of Tables 4.7 and 4.8 and a WP propagation method within the MCTDH framework [29] are used in the calculation. Full dimensional calculations are carried out including all nine vibrational modes, employing the Heidelberg MCTDH program modules [29]. An initial WP pertinent to the vibronic ground state of CH_2F_2 is vertically promoted to the ionic state and then propagated upto 200 fs in the coupled manifold of $\widetilde{X}$-$\widetilde{A}$-$\widetilde{B}$-$\widetilde{C}$ electronic states. Four separate calculations are carried out by initially promoting the WP to each of the four electronic states of the radical cation. During propagation, the autocorrelation function of the WP is recorded in time. The numerical details of the mode combination, sizes of the primitive and single particle bases used in the WP propagations are given in Table 5.1.

Table 5.1: Normal mode combinations, sizes of the primitive and single particle bases used in the MCTDH calculations for the coupled $\tilde{X} - \tilde{A} - \tilde{B} - \tilde{C}$ electronic states of $CH_2F_2^+$.

Normal modes	Primitive basis	SPF basis $[\tilde{X}, \tilde{A}, \tilde{B}, \tilde{C}]$
(ν_5, ν_8, ν_2)	(8, 20, 20)	[3, 3, 5, 6]
(ν_4, ν_1, ν_3)	(20, 8, 20)	[6, 3, 5, 6]
(ν_6, ν_7, ν_9)	(8, 10, 8)	[3, 3, 4, 5]

The composite vibronic band structure is generated by combining the autocorrelation functions obtained from four calculations (vide supra) with equal weightage, damping with an exponential function, $e^{\frac{-t}{\tau_r}}$ (with τ_r=66 fs) and Fourier transforming to the energy domain. The exponential damping in the time domain corresponds to a convolution of the energy spectrum with a Lorentzian line-shape function of 20 meV FWHM. The calculated band structure of the $\widetilde{X}$-$\widetilde{A}$-$\widetilde{B}$-$\widetilde{C}$ electronic states of $CH_2F_2^+$ is plotted in Fig. 5.1 along with the experimental results reproduced from Ref. [5], in panel a. The theoretical results in panel b and c are obtained by using CASSCF-MRCI and EOM-CCSD parameter sets of Table 4.7, respectively. In Fig. 5.1 relative intensity (in arbitrary units) is plotted as a function of energy of the final vibronic levels. A constant energy shift of ∼0.93 eV is applied along the abscissa in order to account for the zero-point energy and to reproduce the experimental adiabatic ionization position at ∼12.73 eV. The latter corresponds well with our theoretically calculated value of ∼12.80 eV by the RHF-RCCSD method and cc-pVTZ basis set. It can be seen from Fig. 5.1 that the theoretical results are in good accord with the experimental ones. Although the parameter sets derived from CASSCF-MRCI and EOM-CCSD energy data exhibit good correlation, the former parameter set better reproduces (cf. intensity pattern in panel a and b in Fig. 5.1) the experimental results. The disagreement of the experimental and theoretical results of panels a and c is reduced when the VIE values calculated by the CASSCF-MRCI method are used along with the EOM-CCSD coupling parameter set to calculate the spectrum. The results of such calculations are shown in panel d of Fig. 5.1. It is therefore clear that the CASSCF-MRCI method produces better VIEs than the EOM-CCSD method for CH_2F_2.

In Fig. 5.1 the first band corresponds mainly to the vibronic structure of the $\widetilde{X}$ state and the second overlapping band structure is formed by strongly coupled $\widetilde{A}$-$\widetilde{B}$-$\widetilde{C}$ states of $CH_2F_2^+$. As stated in chapter 4 that minimum of various CIs is quasi-degenerate to the equilibrium minimum of states in this coupled electronic manifold. As a result, fast nonradiative relaxation of the WP through CIs causes the observed huge broadening of the second band. The energetic separation of the minimum of the $\widetilde{X}$ state and its intersection minimum with the other state is large. As a result the nonadiabatic coupling effect on this state is very weak. The center-of-gravity of both the bands in Fig. 5.1 shifts considerably away from the respective origin line supporting large distortion of cationic geometry with respect to the neutral as discussed in chapter 4. While the broad band

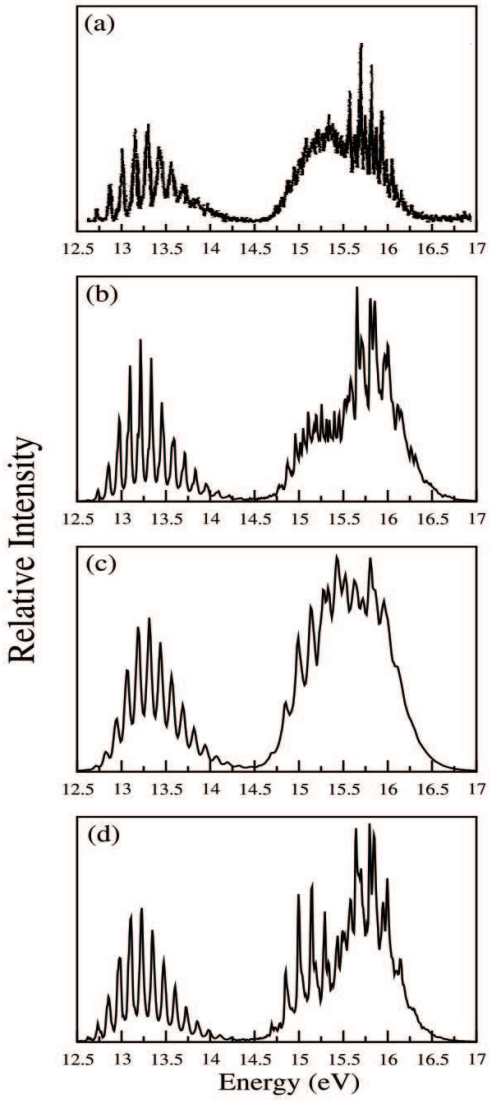

Figure 5.1: Composite vibronic band structure of the coupled $\tilde{X}$-$\tilde{A}$-$\tilde{B}$-$\tilde{C}$ electronic states of $CH_2F_2^+$. The band structures calculated using the CASSCF-MRCI and EOM-CCSD set of parameters of Tables 4.7-4.8 are shown in panel b and c, respectively. The experimental result reproduced from Ref. [5] is shown in panel a. Intensity in arbitary units is plotted along the energy of the cationic vibronic states. Band structure of panel d is calculated by using VIEs from CASSCF-MRCI method and coupling parameters from EOM-CCSD method. The zero of the energy scale corresponds to the energy of the equilibrium minimum of the electronic ground state of neutral CH_2F_2.

vibronic structure is presented in Fig. 5.1 in order to validate the present theoretical model, a detailed assignment of the spectrum and comparison with resolved PFI-ZEKE spectrum is presented in next section.

5.3.2 Vibronic energy level structure of the electronic ground state of $CH_2F_2^+$ and impact of nonadiabatic coupling

In order to understand the details of the progression of vibrational modes in the vibronic spectrum of the electronic ground $\widetilde{X}^2B_1$ state of $CH_2F_2^+$ and the effect of nonadiabatic coupling, we systematically carried out several reduced dimensional calculations. We performed an extensive reduced dimensional calculations to observe the effect of symmetric (ν_1, ν_2, ν_3 and ν_4) modes and coupling (ν_5, ν_6, ν_7, ν_8 and ν_9) modes on the first vibronic band of $CH_2F_2^+$. The partial spectra obtained with totally symmetric modes and totally symmetric modes plus one coupling mode are shown in Fig.5.2(a)-(f), the contributing coupling mode are mentioned in right corner of the each panel. The effect of only coupling modes and the complete spectra of the ground $\tilde{X}^2B_1$ electronic state of $CH_2F_2^+$ are shown in Fig.5.2(g)-(h), respectively. While the spectrum in panel a calculated with $\widetilde{X}$ state alone, the spectrum in other panels are calculated by including its coupling with the $\widetilde{A}$, $\widetilde{B}$ and $\widetilde{C}$ states. The calculations are carried out by the matrix diagonalization approach as discussed in Section 5.2 . The numerical details of the calculations are given in Table 5.2. The symmetric mode spectrum shown in panel a reveals dominant excitation of vibrational modes ν_2 and ν_4. Excitation of ν_3 and its combination peaks with ν_2 and ν_4 are also found from the spectrum. The excitation of vibrational mode ν_1 is extremely weak. The intensity of the origin 0_0^0 peak is extremely weak in accord with the large geometry change of the cation in the $\widetilde{X}$ state relative to the reference geometry of the neutral as found in Ref. [11]. The effect of coupling modes ν_5, ν_6 and ν_9 is extremely weak on the symmetric mode spectrum of panel a (cf. panels b, c and f in Fig. 5.2). On the other hand, the coupling modes ν_7 and ν_8 have considerable impact on the symmetric mode spectrum shown in panels d and e, respectively. As can be seen from the latter that the vibrational mode ν_8 has stronger effect than ν_7. The fundamental of ν_8 and its overtones participate in the spectral progression. The vibrational mode ν_7 is relatively weakly excited.

The vibronic spectrum of the $\widetilde{X}^2B_1$ state of $CH_2F_2^+$ calculated using full Hamiltonian (given in the section 4.2 in Chapter 4) and the CASSCF-MRCI parameter set given in Tables 4.7 and 4.8 is shown in Fig. 5.3. In the latter, the experimental result of Pradeep et al. [5] is shown in panel a. The theoretical results obtained by the WP propagation method in the MCTDH framework [29] and the matrix diagonalization method are shown in panels b and c, respectively. It can be seen from Fig. 5.3 that the results obtained by two different theoretical methods are consistent with each other and are in excellent accord with the broad band envelope obtained in the experiment. The numerical details of the matrix diagonalization and WP propagation calculations are given in Tables 5.2 and 5.3, respectively. The time autocorrelation function calculated

Table 5.2: Number of harmonic oscillator (HO) basis functions for vibrational mode, the dimension of the secular matrix and the number of Lanczos iterations used to calculate the converged theoretical stick spectrum shown in various figures.

Modes (HO basis functions)	Dimension of the matrix	Lanczos iterations	Figure(s)
ν_1, ν_2, ν_3, ν_4 (20, 20, 20, 20)	160000	3000	Figs. 5.2 (a)
ν_1, ν_2, ν_3, ν_4, ν_5 (20, 20, 20, 20, 16)	2560000	6000	Figs. 5.2 (b)
ν_1, ν_2, ν_3, ν_4, ν_6 (20, 20, 20, 20, 18)	2880000	6000	Fig.5.2 (c)
ν_1, ν_2, ν_3, ν_4, ν_7 (20, 20, 20, 20, 18)	2880000	6000	Figs. 5.2 (d)
ν_1, ν_2, ν_3, ν_4, ν_8 (20, 20, 20, 20, 20)	3200000	8000	Figs. 5.2 (e)
ν_1, ν_2, ν_3, ν_4, ν_9 (20, 20, 20, 20, 10)	1600000	4000	Figs. 5.2 (f)
ν_5, ν_6, ν_7, ν_8, ν_9 (15, 15, 20, 20, 10)	900000	3000	Fig. 5.2 (g)
ν_1, ν_2, ν_3, ν_4 (10, 20, 15, 20)	60000	3000	Figs. 5.5 (a)
ν_1, ν_2, ν_3, ν_4, ν_7 (10, 20, 15, 20, 20)	1200000	5000	Fig. 5.5 (b)
ν_1, ν_2, ν_3, ν_4, ν_5, ν_6, ν_7, ν_8, ν_9 (2, 12, 12, 12, 2, 4, 8, 10, 8)	17694720	11000	Figs. 5.3 (c)
ν_1, ν_2, ν_3, ν_4, ν_5, ν_6, ν_7, ν_8, ν_9 (6, 10, 10, 10, 10, 4, 6, 4, 4)	23040000	12000	Fig. 5.6(c)

Table 5.3: Normal mode combinations, sizes of the primitive and single particle bases used in the MCTDH calculations for the coupled $\widetilde{X} - \widetilde{A} - \widetilde{B} - \widetilde{C}$ electronic states of $CH_2F_2^+/CD_2F_2^+$.

Normal modes	Primitive basis	SPF basis $[\tilde{X}, \tilde{A}, \tilde{B}, \tilde{C}]$
Figs. 5.3(b)		
(ν_5, ν_8, ν_2)	(8, 20, 20)	[6, 6, 10, 12]
(ν_4, ν_1, ν_3)	(20, 8, 20)	[12, 6, 16, 20]
(ν_6, ν_7, ν_9)	(8, 10, 8)	[12, 12, 20, 24]
Fig. 5.6(b)		
(ν_5, ν_8, ν_1)	(20, 10, 10)	[6, 10, 6, 10]
(ν_4, ν_2, ν_3)	(24, 20, 20)	[10, 10, 8, 10]
(ν_6, ν_7, ν_9)	(14, 24, 10)	[6, 6, 7, 8]

during the WP propagation is damped with an exponential function [$e^{(-t/\tau_r)}$, with τ_r = 33 fs] to generate the spectral envelope shown in panel b. The envelope in panel c is generated by convoluting the stick line spectrum of panel c with a Lorenzian function of ∼40 meV full width at the half maximum (FWHM). To facilitate the comparison with experiment, the origin 0_0^0 peak of the spectrum is placed at the adiabatic ionization energy of ∼102636 cm^{-1} (12.725 eV) estimated in the experiment of Forysinski et al. [8]. The low-energy part of the stick line spectrum of 5.3c is given in Table 5.4 and compared with the results available in the literature.

A careful analysis of the data presented in Table 5.4 reveal the following. The vibrational modes ν_2 (H-C-H symmetric bending), ν_3 (F-C symmetric stretching), ν_4 (F-C-F symmetric bending), ν_7 (H-C antisymmetric stretching) and ν_8 (F-C antisymmetric stretching) mainly form the progression in the $\widetilde{X}^2B_1$ band. Weak excitation of ν_1 (H-C symmetric stretching) vibrational mode is also found from the data. The weak line at

$\sim$345 cm^{-1} arises from the fundamental of ν_8. The fundamental of ν_4 appears at $\sim$572 cm^{-1} and it forms an extended progression in the spectrum. Several overtones and combination peaks of ν_4 are found. The line at $\sim$1005 cm^{-1} is assigned to the fundamental of ν_7. The line found at $\sim$1054 cm^{-1} in the experiment of Pradeep et al. [5] was assigned to the first overtone of ν_4. The latter is found at $\sim$1144 cm^{-1} in our result. The fundamental of ν_2 is found at $\sim$1243 cm^{-1}. Brundle el al. [1] assigned the vibrational structure of the $\widetilde{X}^2B_1$ band to the progression of ν_2 vibrational mode only. Potts et al. [3] also arrived at a similar conclusion as Brundle et al. [1]. The fundamental of ν_5 (H-C-H antisymmetric bending) vibrational mode is also found at $\sim$1224 cm^{-1}. The fundamental of ν_3 is found at $\sim$918 cm^{-1} with a very weak intensity. Weak excitation of the fundamental of ν_1 is found at $\sim$3036 cm^{-1}. The spectral assignment discussed above is confirmed by performing block-improved relaxation calculations [31, 32] both in reduced dimensions and exploring full-dimensions. The probability density of the vibronic wavefunctions obtained in these calculations is carefully examined in relation to the assignments discussed above. The reduced density plots of some of the vibronic wavefunctions along some selected coordinate spaces are given in Fig. 5.4. The calculations are carried out with the Heidelberg MCTDH suite of programs [29]. The numerical details of the calculations are same as those of calculation of full-mode coupled state spectrum (cf. Fig. 5.3) given in Table 5.2.

The density plot of 345 cm^{-1} vibronic wavefunction shown in Fig. 5.4a reveals one node along the coordinate of mode ν_8, which indicates that the vibrational mode ν_8 is excited in this particular vibronic energy level. This level is therefore assigned to the fundamental of ν_8. Likewise, the density plots of 572 cm^{-1}, 918 cm^{-1}, 1005 cm^{-1}, 1224 cm^{-1} and 1243 cm^{-1} vibronic wavefunctions shown in panels b, c, d, e and f of Fig. 5.4 reveal that these levels are due to the fundamental of modes ν_4, ν_3, ν_7, ν_5 and ν_2, respectively. The density plots of the first overtone of ν_8 and ν_4 appearing at 765 cm^{-1} and 1144 cm^{-1} are shown in panels g and h of Fig. 5.4, respectively. In Fig. 5.4i the density of the vibronic wavefunction of a combination peak of ν_3 and ν_4 is shown. The wavefunction in Fig. 5.4i reveals one quantum excitation along both these modes. In a similar way the assignments of remaining energy levels given in Table 5.4 are carried out. It is clear from the above discussion that the symmetric mode ν_2, ν_4 and the non-symmetric modes ν_5, ν_7 and ν_8 mainly contributes to the vibronic structure of the ground $\widetilde{X}^2B_1$ electronic state of $CH_2F_2^+$. A similar conclusion can be derived from the earlier experimental [1, 3, 5, 8] and theoretical results [9, 10]. However, the assignment of the observed peaks and their energetic locations differ in various results mentioned above.

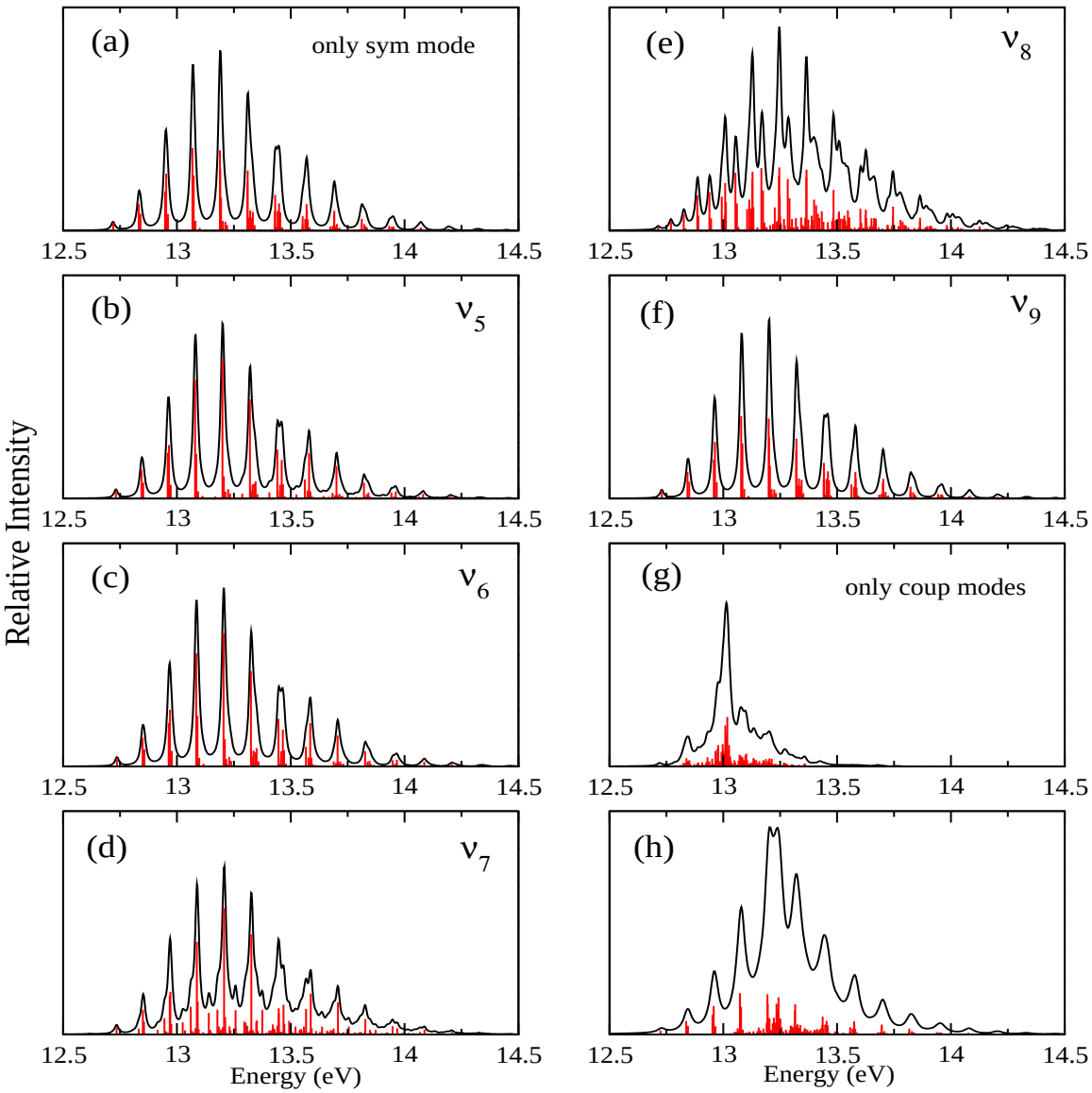

Figure 5.2: Vibrational energy level spectrum of the ground $\tilde{X}$ electronic state of $CH_2F_2^+$ computed with four totally symmetric vibrational modes (panel a) and four totally symmetric modes along with one coupling mode (panle b-f), using the Hamiltonian [Eq. (7) of Ref. [11]]. Panel g is computed with all coupling vibrational mode and panel h is the composite structure of all totally symmetric and all coupling modes. The theoretical stick spectrum in each case is convoluted with a Lorentzian function of 10 meV FWHM to calculate the spectral envelope (see the text for details).

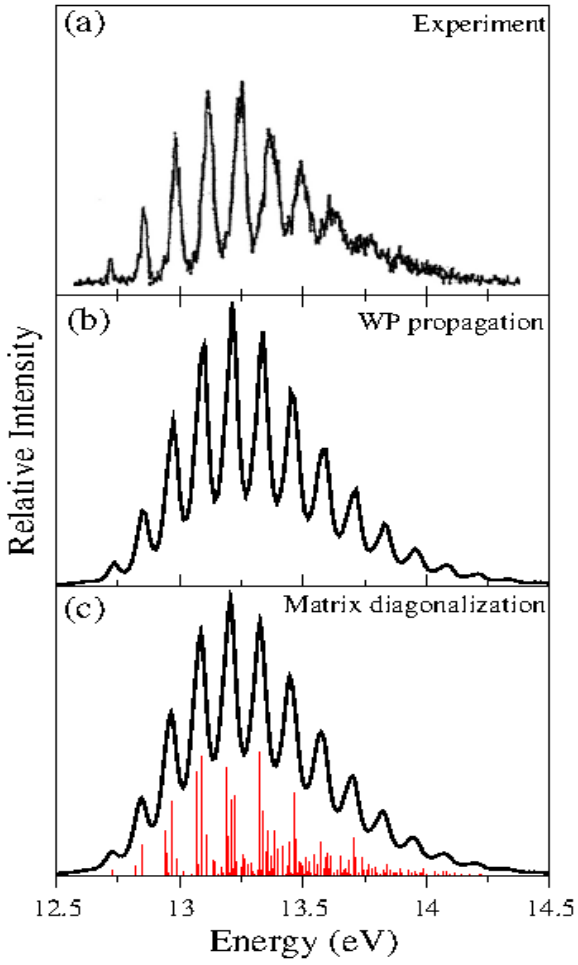

Figure 5.3: Vibronic structure of the electronic ground state ($\widetilde{X}^2B_1$) of $CH_2F_2^+$. The intensity (in arbitrary units) is plotted as a function of the energy (measured relative to electronic ground state of CH_2F_2) of the final vibronic states. The experimental result (reproduced from Ref. [5]) and the present theoretical results obtained by the WP propagation and matrix diagonalization methods are shown in panels a, b and c, respectively.

Table 5.4: Energetically low-lying vibronic energy levels (in cm^{-1}) of the $\widetilde{X}^2B_1$ electronic state of $CH_2F_2^+$. The vibronic energy levels caculated in this work (see text for details) are compared with the experimental and theoretical results available in the literature.

	This work		Experimental and theoretical Ref. [8,10]		
No.	Energy	Assignmnet	Energy Ref. [8]	Energy	Assignment Ref. [10]
1	0	0	0	0	0
2	345	ν_8			
3	572	ν_4		597	ν_4
4	765	$2\nu_8$			
5	918	ν_3			
6	1005	ν_7	969	959	ν_3;$2\nu_7$
7	1144	$2\nu_4$	1137	1131	$2\nu_7$; ν_3
8	1224	ν_5			
9	1243	ν_2	1246	1251	ν_2;$2\nu_2$
10	1336	$\nu_4+ 2\nu_8$			
11	1486	$\nu_3+\nu_4$			
12	1577	$\nu_4 + \nu_7$	1564	1559	$\nu_3 + \nu_4$;$\nu_4 + 2\nu_7$
13			1669		
14	1716	$3\nu_4$			
15	1748		1734	1732	$\nu_4 + 2\nu_7$;$\nu_3 + \nu_4$
16	1769	$\nu_7+2\nu_8$	1765		
17	1790	$\nu_4+\nu_5$			
18	1817	$\nu_2+\nu_4$	1817	1809	$\nu_3 + 2\nu_7$;$4\nu_7$;$2\nu_3 + \nu_7$
19	1880	$\nu_3+\nu_4+\nu_8$	1885		
20	1907	$2(\nu_4+\nu_8)$			
21	1966	$\nu_3+\nu_7$	1933	1936	$\nu_6 + \nu_7$;ν_1;$2\nu_5$
22	2016	$2\nu_7$			
23	2144	$2\nu_4+\nu_7$	2100	2078	$2\nu_3$;$2\nu_5$;$4\nu_7$
24	2229	$\nu_2+\nu_3$	2213	2213	$\nu_2 + \nu_3$;$\nu_2 + 2\nu_7$;$\nu_3 + 2\nu_7$
25			2257	2388	$\nu_2 + 2\nu_7$;$\nu_2 + \nu_3$;$2\nu_3$
26	2287	$4\nu_4$	2281	2494	$2\nu_2$;$3\nu_2$;$\nu_2 + 2\nu_7$
27	2390	$\nu_2+2\nu_4$	2400		
28	2448	$2\nu_5$			
29	2493	$2\nu_2$	2491		

In the latest high resolution PFI-ZEKE experiment of Forysinski et al. [8] the first polyad (near degeneracy levels) structure was observed in the range of 970-1250 cm^{-1}, which was predicted by Takeshita [9] in the energy range of 1300-1400 cm^{-1}. The same polyad structure is found in the energy range of 1000-1245 cm^{-1} in the present study. Inclusion of non-totally symmetric coupling vibrational modes provides improved results in the present case than Takeshita's model [9]. Weak excitation of ν_5 vibrational mode

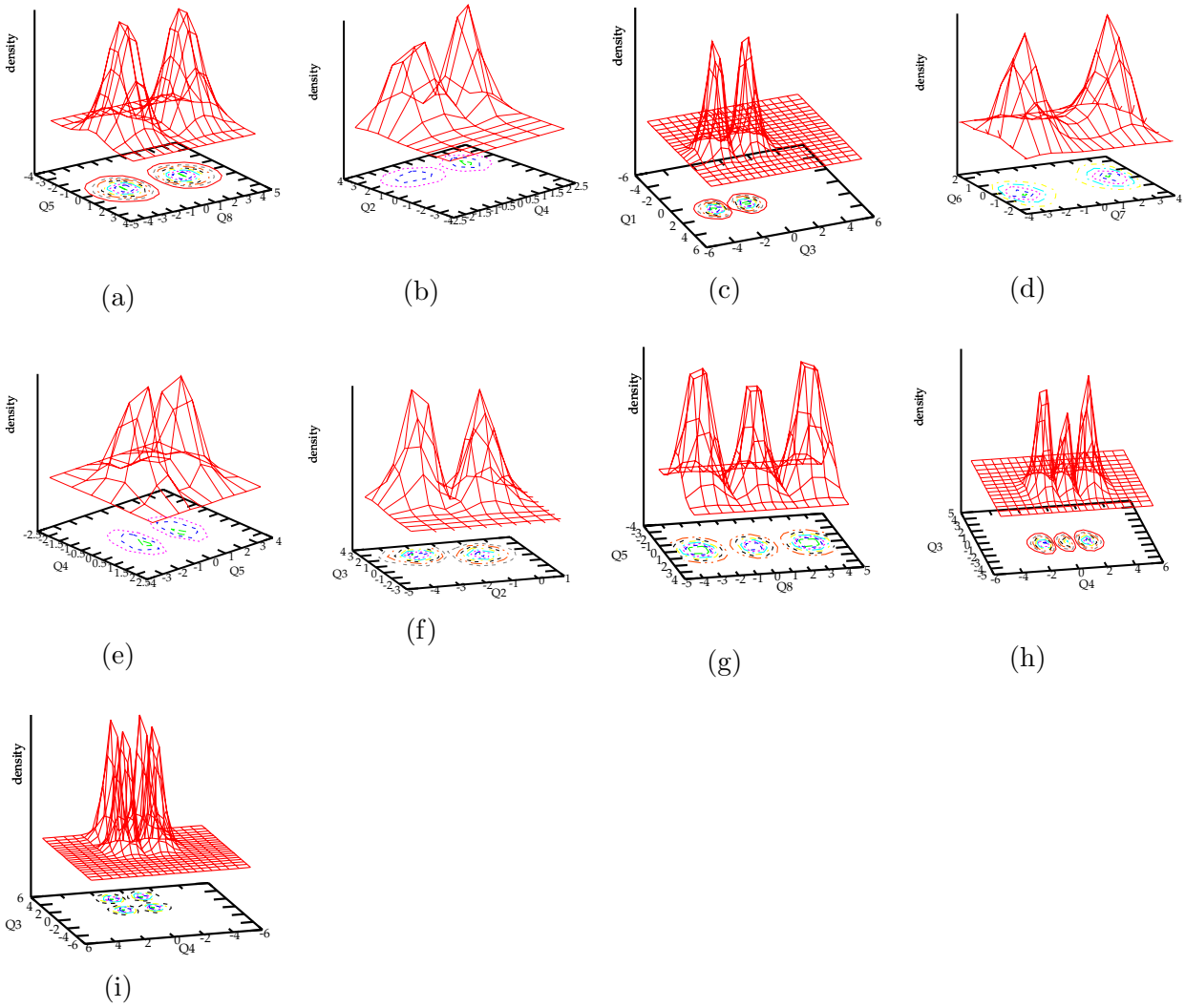

Figure 5.4: Assignment of fundamental of ν_8, ν_4, ν_3, ν_7, ν_5 and ν_2 vibrational modes, overtone of ν_8 and ν_4 vibrational mode and combination band of ν_3 and ν_4 are shown, following the reduced dimensional calculations as mentioned in section 5.3.2

is observed within the first polyad structure. The first peak of this polyad is observed at ∼969 cm^{-1} in the experiment of Forysinski et al. [8] and is found at ∼ 1005 cm^{-1} in the present theoretical results. This peak was assigned by Luckhaus et al. [10] to an excitation of ν_3 (49%) and $2\nu_7$ (32%) vibrational modes and we find it due to the fundamental of ν_7 vibrational mode (cf. Fig. 5.4d). Other two peaks of the first polyad are found at 1137 cm^{-1} and 1246 cm^{-1} in the experiment [8]. The same is found in the present study at ∼1144 cm^{-1} and ∼1243 cm^{-1} and are assigned to the first overtone of ν_4 (cf. Fig. 5.4h) and fundamental of ν_2 (cf. Fig. 5.4f) vibrational modes, respectively. Takeshita [9] assigned these peaks in the polyad as due to the excitation of ν_1, ν_2 and ν_3 vibrational modes. It is very unlikely that the mode ν_1 is excited near the onset of the spectrum due to its high frequency. Excitation of this mode was not observed in the

PFI-ZEKE experiment [8]. A second polyad with four intense peaks were recorded in the latter. We find these peaks in the energy range of ∼2144-2390 cm^{-1} and assigned them. The results are given in Table 5.4. To this end, we note that excitation of non-totally symmetric CF_2 anti-symmetric stretch, CH_2 rocking and CH_2 twist in the vibronic structure of the $\widetilde{X}^2B_1$ band was predicted by Pullen et al. [2]. This prediction is in excellent accord with our assignments discussed above.

5.3.3 Vibronic energy level structure of the electronic ground state of $CD_2F_2^+$ and impact of nonadiabatic coupling

At this point we discuss on the vibronic band structures of the $\widetilde{X}^2B_1$ state of $CD_2F_2^+$ and compare them with that of $CH_2F_2^+$. It can be seen from Tables 4.2 and 4.3 that the frequencies of all vibrational modes (except ν_4) are lowered upon deuteration. The quasi-degeneracy of (ν_3, ν_9) and (ν_2, ν_8) vibrational modes is also retained in the deuterated isotopomer. Lifting of this degeneracy as proposed to be one of the reasons behind the loss of vibronic structure of the $\widetilde{X}^2B_1$ state of $CD_2F_2^+$ [1] can not be validated. Furthermore, it is found above that vibrational modes related to both C-H and C-F motions makes important contribution to the vibronic dynamics of the electronic ground state of $CH_2F_2^+$. The latter findings are also supported by various experimental and theoretical findings in the literature [2, 5, 8, 10].

In order to understand the details of the vibronic structure of the $\widetilde{X}^2B_1$ state of $CD_2F_2^+$, we carried out the same systematic analysis as in case of $CH_2F_2^+$ discussed above. The uncoupled $\widetilde{X}^2B_1$ state spectrum calculated including the symmetric vibrational modes (ν_1-ν_4) only is shown in Fig. 5.5a. All three ν_2, ν_3 and ν_4 modes form progression in this spectrum. Only minor change in the spectrum occurs when the coupling vibrational modes ν_5, ν_6 and ν_9 are included in the calculations. However, a huge change of vibronic line structure occurs (shown in panel b in 5.5) when the coupling vibrational mode ν_7 (through $\widetilde{X}$-$\widetilde{B}$ coupling) is included. The latter mode strongly couples $\widetilde{X}$ and $\widetilde{B}$ states (cf. Table 4.10). The $\widetilde{X}^2B_1$ state spectrum of $CD_2F_2^+$ calculated with full coupled states Hamiltonian (Section 4.2.1 in Chapter 4) and the parameters of Tables 4.9 and 4.10 is shown in panels b and c of 5.6. The low-resolution experimental spectrum recorded by Brundle et al. [1] is reproduced in panel a. The theoretical results of panels b and c are obtained by WP propagation and matrix diagonalization methods, respectively. The time-autocorrelation function in the WP result is damped with an exponential function, $e^{(-t/\tau_r)}$, (with τ_r= 8 fs) before Fourier transformation to reproduce the experimental broadening. Likewise, the resolved stick spectrum of the time-independent result is convoluted with a Lorenzian function of 164 meV FWHM to reproduced the experimental broadening. It can be seen that overall shape of the broad band experimental spectrum is well reproduced by the present theoretical results. It is worth mentioning that the $\widetilde{X}$ state spectrum of $CD_2F_2^+$ (5.6) is much broader than that of $CH_2F_2^+$ (5.3). The frequency reduction (Table 4.3) and energetic proximity of the electronic states (Table 4.12) in the deuterated isotopomer increase the vibronic line

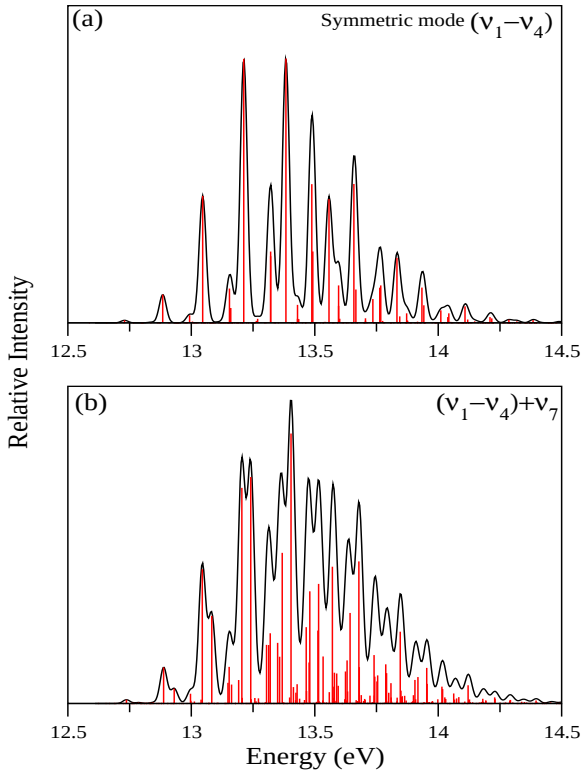

Figure 5.5: Same as in 5.2, for the $\widetilde{X}^2B_1$ state of $CD_2F_2^+$.

density in the $\widetilde{X}$ state spectrum of $CD_2F_2^+$ as compared to that of $CH_2F_2^+$. This causes relatively more broadening of the $CD_2F_2^+$ spectrum. Furthermore, the experimental [1] recording of the latter is old and poorly resolved. Resolved vibronic structure of time-dependent (with τ_r= 30 fs) and time-independent (with FWHM∼44 meV) calculations in the ground state of $CD_2F_2^+$ are shown in the inset of the respective panels of Fig. 5.6. The low-energy part of the theoretical stick spectrum of Fig. 5.6c is given in Table 5.5 along with the assignment of the levels. It is found that the vibrational modes ν_2, ν_3, ν_4, ν_5, ν_7 and ν_9 form progression in the spectrum. While the excitation of modes ν_3 and ν_7 is strong, the remaining modes are relatively weakly excited. Although the excitation strength (cf. Table 4.9) of the vibrational mode ν_2 is fairly large, its activity is quenched upon inclusion of the non-totally symmetric (particularly ν_7 and ν_9) modes in the coupled states dynamics. The weak excitation of ν_5 vibrational mode found in reduced dimensional calculation is also quenched in the full-mode calculations.

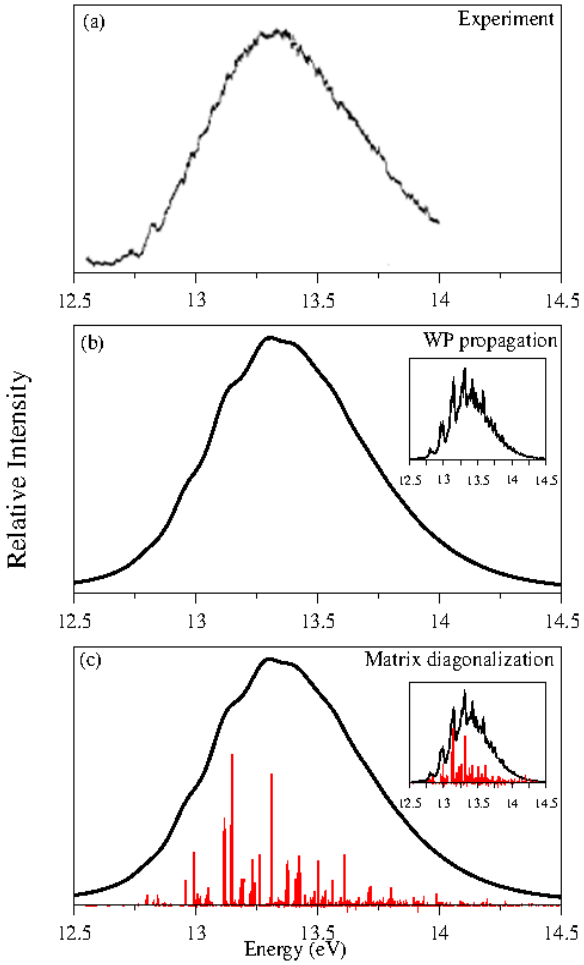

Figure 5.6: Vibronic structure of the electronic ground state ($\widetilde{X}^2B_1$) of $CD_2F_2^+$. The intensity (in arbitrary units) is plotted as a function of the energy (measured relative to electronic ground state of CD_2F_2) of the final vibronic states. The experimental result (reproduced from Ref. [1]) and the present theoretical results obtained by the WP propagation and matrix diagonalization methods are shown in panels a, b and c, respectively. The theoretical calculations are carried out with the full second-order Hamiltonian (cf. Section 4.2.1 in Chapter 4) and the coupling parameters given in Tables 4.9 and 4.10.

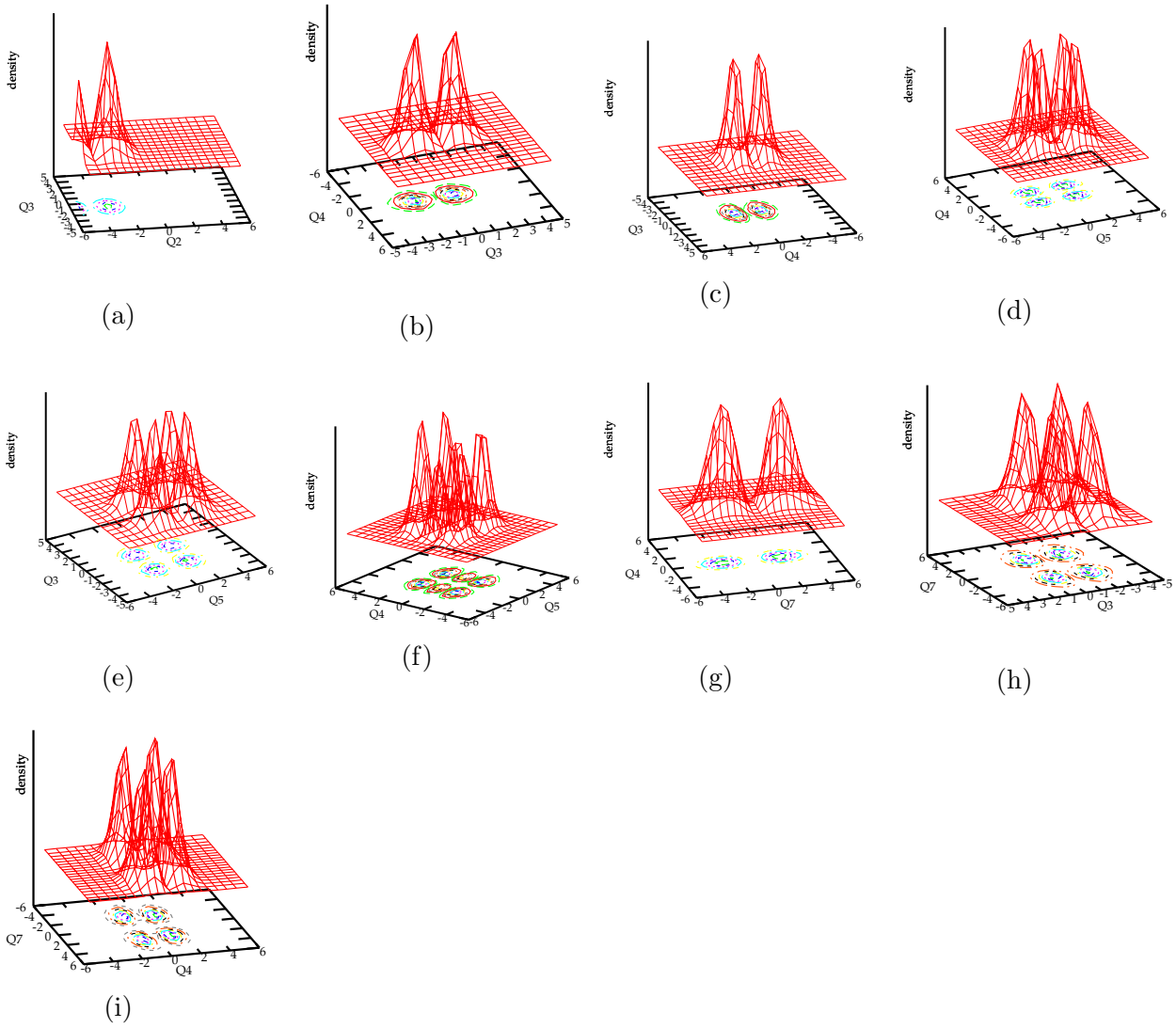

Figure 5.7: Assignments of fundamental of ν_2, ν_3, ν_4 and ν_7 vibrational modes and the various combination band between ν_3, ν_4, ν_5 and ν_7 vibrational modes of the ground state dynamics of $CD_2F_2^+$ are shown, following the reduced dimensional calculations as mentioned in the text.

Table 5.5: Same as in Table 5.4, for the $\widetilde{X}^2B_1$ electronic state of $CD_2F_2^+$.

No.	Vibronic energy level	Assignment
1	0.0	0
2	438	ν_7
3	565	ν_4
4	825	ν_9
5	877	ν_3
6	892	$2\nu_7$
7	1017	$\nu_4+\nu_7$
8	1044	$\nu_4+\nu_5$
9	1131	$2\nu_4$
10	1161	ν_2
11	1316	$\nu_3+\nu_5$
12	1325	$\nu_3+\nu_7$
13	1405	$\nu_4+\nu_9$
14	1442	$\nu_3+\nu_4$
15	1456	$\nu_4+2\nu_7$
16	1487	$\nu_4+2\nu_5$
17	1544	$2\nu_4+\nu_7$
18	1600	$2\nu_4+\nu_5$
19	1637	$2\nu_9$
20	1660	
21	1696	$3\nu_4$
22	1702	$\nu_3+\nu_9$
23	1727	$\nu_2+\nu_4$
24	1746	
25	1754	$2\nu_3$

Reduced density plots of some of the vibronic wavefunctions are shown in Fig. 5.7. The fundamentals of ν_2, ν_3 and ν_4 vibrational modes appearing at ∼1161, ∼877 and ∼565 cm^{-1} are shown in panels a, b and c, respectively. Fundamental of ν_5 mode appears at ∼467 cm^{-1} in the reduced dimensional calculations and it does not show up in the full-mode results given in Table 5.5. However, it can be seen from the data given in this table that several of its combination peaks appear in the spectrum. For example, the peaks appearing at ∼1044, ∼1316 and ∼1600 cm^{-1} can be assigned to $\nu_4+\nu_5$, $\nu_3+\nu_5$ and $2\nu_4+\nu_5$ in accordance with the nodal pattern of the vibronic wavefunctions shown in panels d,e and f of Fig. 5.7, respectively. The fundamental of ν_7 appears at ∼438 cm^{-1} and the density plot of its wavefunction is shown in Fig. 5.7g. Several overtones and combination peaks of this mode are also excited in the spectrum. For example, its one quantum combinations with one quantum of each ν_3 and ν_4 mode appear at ∼1325 and ∼1017 cm^{-1}, respectively. The reduced density plots of the wavefunction of the latter vibronic levels are shown in panels h and i of Fig. 5.7, respectively.

5.3.4 Compasion between the ground state vibronic dynamics of $CH_2F_2^+$ and $CD_2F_2^+$

We here, reiterate the essential differences between the vibronic dynamics of the electronic ground state of $CH_2F_2^+$ and $CD_2F_2^+$. It is seen that the frequency of vibrational modes decreases and their quasi-degeneracy remains upon deuteration. Because of this, density of vibronic levels in the $\widetilde{X}$ state spectrum of $CD_2F_2^+$ increases as compared to $CH_2F_2^+$. This causes a partial demolition of structures in the $\widetilde{X}$ band of $CD_2F_2^+$. Concerning the excitation of vibrational modes, both C-H/D and C-F type of vibrations form progression in the $\widetilde{X}$ band of both the isotopomers. The excitation of vibrational mode ν_3 is quenched in case of $CH_2F_2^+$. On the other hand, the activity of vibrational mode ν_2 is quenched in case of $CD_2F_2^+$ despite its large excitation strength. Such quenching arises due to multi-states and multi-modes vibronic coupling effect mainly caused by nontotally symmetric vibrational modes ν_7, ν_8 in case of $CH_2F_2^+$ and ν_7, ν_9 in case of $CD_2F_2^+$. Excitation of nontotally symmetric mode ν_7 and ν_8 is found in the $\widetilde{X}$ band of $CH_2F_2^+$, in good accrod with the prediction of Pullen et al. [2]. On the other hand, strong excitation of ν_7 and mild excitation of ν_9 vibrational modes is found in the $\widetilde{X}$ band of $CD_2F_2^+$. It therefore emerges from the above discussion that the vibronic dynamics of the electronic ground state of $CH_2F_2^+$ and $CD_2F_2^+$ is somewhat different. It would be worthwhile to record PFI-ZEKE spectrum of the $\widetilde{X}$ state of $CD_2F_2^+$ to validate the assignments made above.

5.3.5 Vibronic energy level structure and time-dependent dynamics of the excited electronic states of $CH_2F_2^+$ and $CD_2F_2^+$

In contrast to the ground state, the structure and the dynamics of excited states of both the isotopomers is strongly perturbed by the associated nonadiabatic coupling. As discussed in section 4.4 in Chapter 4, this is due to the energetic proximity of the minimum of the intersection seam to the equilibrium minimum of a given state. It can be seen from Table 4.12 that the minimum of the $\widetilde{X}$ state is energetically well separated from that of the $\widetilde{A}$, $\widetilde{B}$ and $\widetilde{C}$ states of $CH_2F_2^+$. The latter states are energetically close (occurs within an eV of energy). Therefore, despite a weak coupling between these states, they form highly overlapping band structures. A similar situation holds in case of $CD_2F_2^+$ except its $\widetilde{A}$ state is relatively more separated from its $\widetilde{B}$ and $\widetilde{C}$ states (cf. Table 4.12). The $\widetilde{X}$ state of both radical cations is relatively strongly coupled with their respective $\widetilde{A}$, $\widetilde{B}$ and $\widetilde{C}$ states (cf. Table 5.3 and 4.8). However, the minimum of the $\widetilde{X}$ state has large energy separation with the minimum of various intersection seams as can be seen from the data given in Table 4.12. Because of this the WP can hardly explore the vicinity of various intersection seams when the dynamics is started on the $\widetilde{X}$ state. This is also confirmed by examining the adiabatic electronic populations (not shown here). Most of the WP stays on the $\widetilde{X}$ state during entire course of evolution. Therefore, the $\widetilde{X}$ state dynamics is dominated by the totally symmetric vibrations, with mild excitation of non-totally symmetric modes.

The partial $\widetilde{A}$, $\widetilde{B}$ and $\widetilde{C}$ states spectrum obtained in the $\widetilde{X}$-$\widetilde{A}$-$\widetilde{B}$-$\widetilde{C}$ coupled states dynamics calculations is shown in Figs. 5.8 and 5.9 for $CH_2F_2^+$ and $CD_2F_2^+$, respectively. The partial spectra are plotted in different color mentioned in the caption. For completeness and to facilitate the latter discussion the partial spectrum of the $\widetilde{X}$ state is also included in each figure. It is clear from the spectra plotted in Figs. 5.8 and 5.9 that the vibronic structure of the $\widetilde{A}$, $\widetilde{B}$ and $\widetilde{C}$ states are highly overlapping. A careful examination reveals that the spectrum of the $\widetilde{B}$ state of $CH_2F_2^+$ is strongly perturbed by both $\widetilde{A}$ and $\widetilde{C}$ states, whereas the spectrum of $\widetilde{C}$ state of $CD_2F_2^+$ is mostly perturbed by its $\widetilde{B}$ state and relatively weakly by its $\widetilde{A}$ state. These observations are in accordance with the energetic proximity of the equilibrium minimum of a state with the minimum of its intersection seams with the other states. The associated relatively strong nonadiabatic interactions cause broadening of these spectra. The symmetric vibrational modes ν_2, ν_3 and ν_4 form progression in the $\widetilde{A}$, $\widetilde{B}$ and $\widetilde{C}$ electronic states of both the radical cations. The vibrational mode ν_4 is strongly excited in the $\widetilde{A}$ and $\widetilde{B}$ electronic states in contrast to the ground state. The mode ν_3 is also relatively strongly excited in the $\widetilde{A}$ and $\widetilde{C}$ states as compared to the ground state. Excitation of non-totally symmetric ν_8, ν_9 and ν_5 is found in the $\widetilde{B}$ state of $CH_2F_2^+$, whereas, ν_5, ν_6 and ν_7 contributes to the spectral progression in the $\widetilde{C}$ state of $CD_2F_2^+$.

The decay and growth of adiabatic electronic populations in the $\widetilde{X}$-$\widetilde{A}$-$\widetilde{B}$-$\widetilde{C}$ coupled states dynamics is shown in Figs. 5.10 and 5.11 for $CH_2F_2^+$ and $CD_2F_2^+$, respectively. In panels a, b and c of Fig. 5.10 the electron population dynamics of $CH_2F_2^+$ is shown when the WP is initially prepared on the $\widetilde{A}$, $\widetilde{B}$ and $\widetilde{C}$ diabatic state, respectively. Similar plots are presented for the population dynamics of $CD_2F_2^+$ in panels a, b and c of 5.11. Since, the initial excitation is to the diabatic state, the adiabatic population of the prepared state less than 1.0. It can be seen from panel a that the population flows mostly to the $\widetilde{X}$ state when the WP is initially on the $\widetilde{A}$ state, for both the radical cations. This is in accord with the data given in Tables 4.8 and 4.12 for $CH_2F_2^+$ and in Tables 4.10 and 4.12 of $CD_2F_2^+$. In the former case the minimum of the seam of $\widetilde{X}$-$\widetilde{A}$ conical intersections is quasi-degenerate to the $\widetilde{A}$ state equilibrium minimum, whereas, they are separated by $\sim$0.6 eV in the latter case. However, the coupling of these states through the ν_5 vibrational mode is much stronger in the latter case. It is suffice to say here that such interplay of the coupling strength and energy gap prevails, in general, in nonradiative electron population dynamics. The population flows mostly to the $\widetilde{A}$ state when the WP is initially prepared on the $\widetilde{B}$ state (panel b of Figs. 5.10 and 5.11). The minimum of $\widetilde{A}$-$\widetilde{B}$ intersection seam is quasidegenerate to the minimum of the $\widetilde{B}$ state of $CH_2F_2^+$ (cf. Table 4.12). In case of $CD_2F_2^+$ electron population flows to the $\widetilde{A}$ state via $\widetilde{C}$ state. The maximum population initially flows to the $\widetilde{B}$ state when dynamics is started on the $\widetilde{C}$ state (panel c of Fig. 5.10 and 5.11). At longer times both $\widetilde{A}$ and $\widetilde{B}$ state populations reach to the same limit in this case. It follows from the population dynamics that extremely fast decay of $\widetilde{A}$, $\widetilde{B}$ and $\widetilde{C}$ states of both $CH_2F_2^+$ and $CD_2F_2^+$ takes place and the WP explores multiple intersection seams. As a result the vibronic band structures of these states become broad and diffuse.

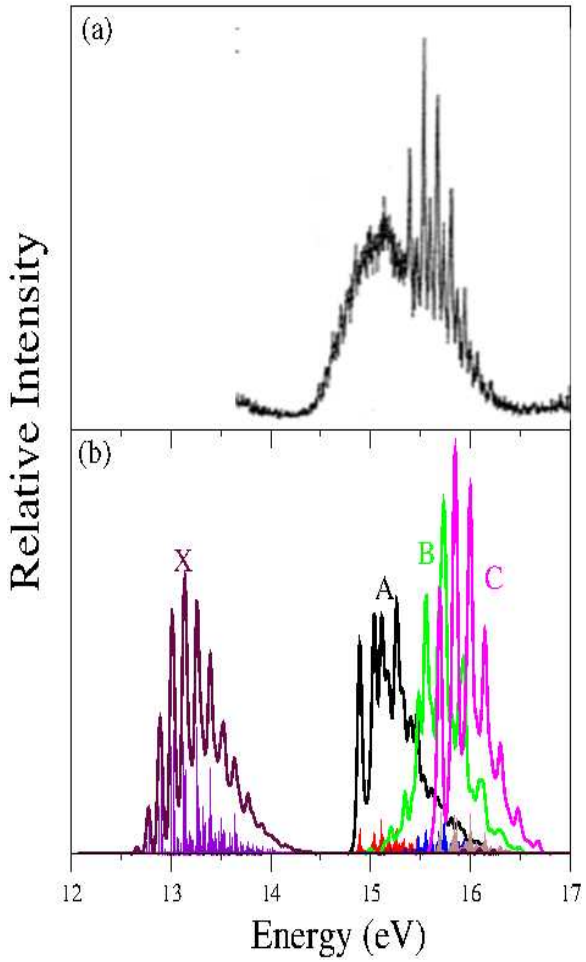

Figure 5.8: Vibronic structure of the coupled $\widetilde{A}$-$\widetilde{B}$-$\widetilde{C}$ states of $CH_2F_2^+$. The intensity (in arbitrary units) is plotted as a function of the energy (measured relative to electronic ground state of CH_2F_2) of the final vibronic states. The experimental result (reproduced from Ref. [5]) and the present theoretical results obtained by the matrix diagonalization methods are shown in panels a and b, respectively. The theoretical calculations are carried out with the full second-order Hamiltonian (cf. section 4.2.1 in the Cahpter 4) and the coupling parameters given in Tables 4.7 and 4.8. The partial spectrum of the $\widetilde{X}$ state is also presented in the figure.

5.4 Summary and outlook

Vibronic structure of energetically low-lying first four electronic states of $CH_2F_2^+$ and $CD_2F_2^+$ is theoretically studied in this article. Four states coupled diabatic Hamiltonian is constructed in the dimensionless normal coordinates of the electronic ground state of the neutral reference molecules and through extensive ab initio calculations of adiabatic electronic energies. The nuclear dynamics calculations are carried out quan-

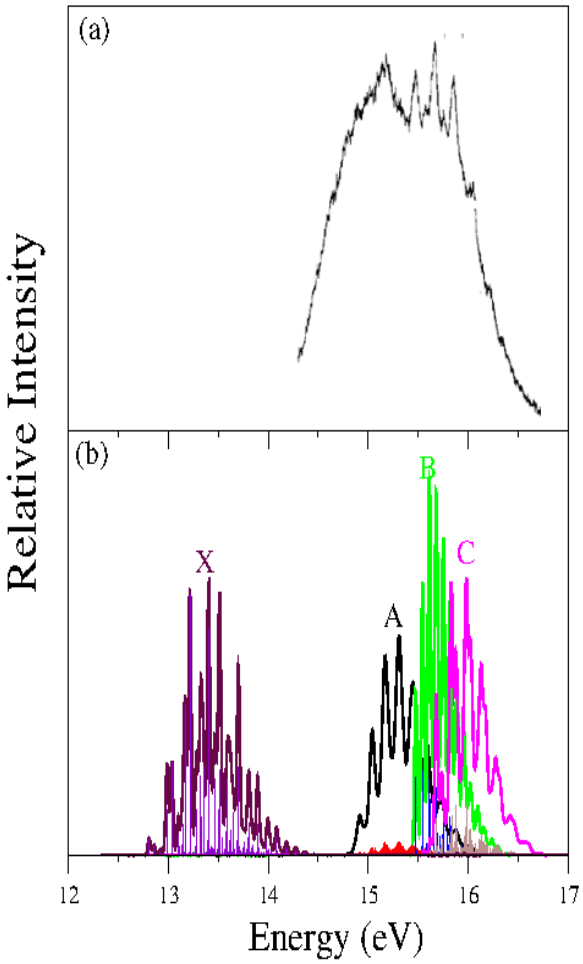

Figure 5.9: Same as in 5.8, for the $\widetilde{A}$-$\widetilde{B}$-$\widetilde{C}$ states of $CD_2F_2^+$. Experimental spectra in panel a is reproduced from Ref. [1]

tum mechanically both by time-independent and time-dependent methods. The vibronic energy level spectrum of the electronic ground state of both $CH_2F_2^+$ and $CD_2F_2^+$ is examined at length. The energy levels appeared in the low energy part are compared with the available experimental results. These energy levels are assigned and discussed in relation to the various assignments reported in the literature. The broad band photo-ionization spectrum of both the isotopomers compare well with the low-resolution experimental results. While high-resolution spectroscopy measurements (PFI-ZEKE) are carried out for $CH_2F_2^+$, the same is not available for $CD_2F_2^+$. Our analysis on the vibronic levels of the $\widetilde{X}$ state of $CH_2F_2^+$ shows a close resemblance with the PFI-ZEKE data. The progression on the $\widetilde{X}$ state spectrum of $CH_2F_2^+$ is mainly formed by the ν_2, ν_4, ν_7 and ν_8 vibrational modes. The excitation of the ν_3 vibrational mode is quenched by the ν_7 and ν_8 modes. The excitation of non-totally symmetric ν_7 and ν_8 vibrational modes is in good accord with the prediction of Pullen et al. [2]. In the $\widetilde{X}$ state of $CD_2F_2^+$, on the other hand, the vibrational modes ν_3, ν_4, ν_7 and ν_9 make most of the progression. The excitation

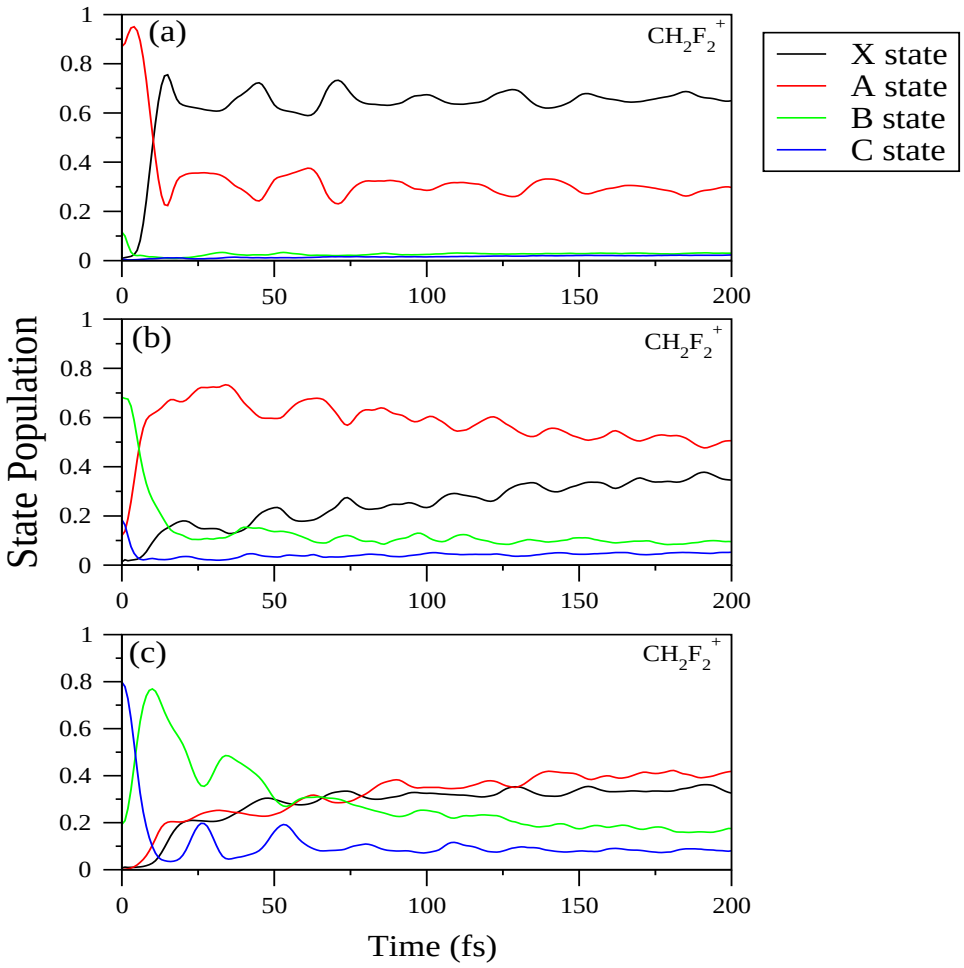

Figure 5.10: Adiabatic electronic population dynamics in the $\widetilde{X}-\widetilde{A}-\widetilde{B}-\widetilde{C}$ coupled-electronic states of $CH_2F_2^+$. The adiabatic population of different electronic states are shown by preparing the initial WP on the $\widetilde{A}$, $\widetilde{B}$ and $\widetilde{C}$ states, in panels a, b and c, respectively.

of the ν_2 vibrational mode is quenched by the non-totally symmetric vibrational modes in this case. Vibrations of both C-H/D and C-F characters participate in the spectral progression in the $\widetilde{X}$ state of both radical cations. Substantial reduction of vibrational frequencies (except ν_4) upon deuteration, increases the density of vibronic levels in the spectrum of $CD_2F_2^+$. This causes the spectral broadening in case of $CD_2F_2^+$. It would be worthwhile to carry out PFI-ZEKE measurements for the $\widetilde{X}$ state of $CD_2F_2^+$ in order to validate the proposed assignments of its vibronic levels.

In contrast to the dynamics of the $\widetilde{X}$ state, the nonadiabatic coupling has much stronger effect on the dynamics of the $\widetilde{A}$, $\widetilde{B}$ and $\widetilde{C}$ states of both $CH_2F_2^+$ and $CD_2F_2^+$. The WP explores multiple intersection seams and quickly relaxes when dynamics is started in any of the three states. Such a fast nonradiative decay of the excited states

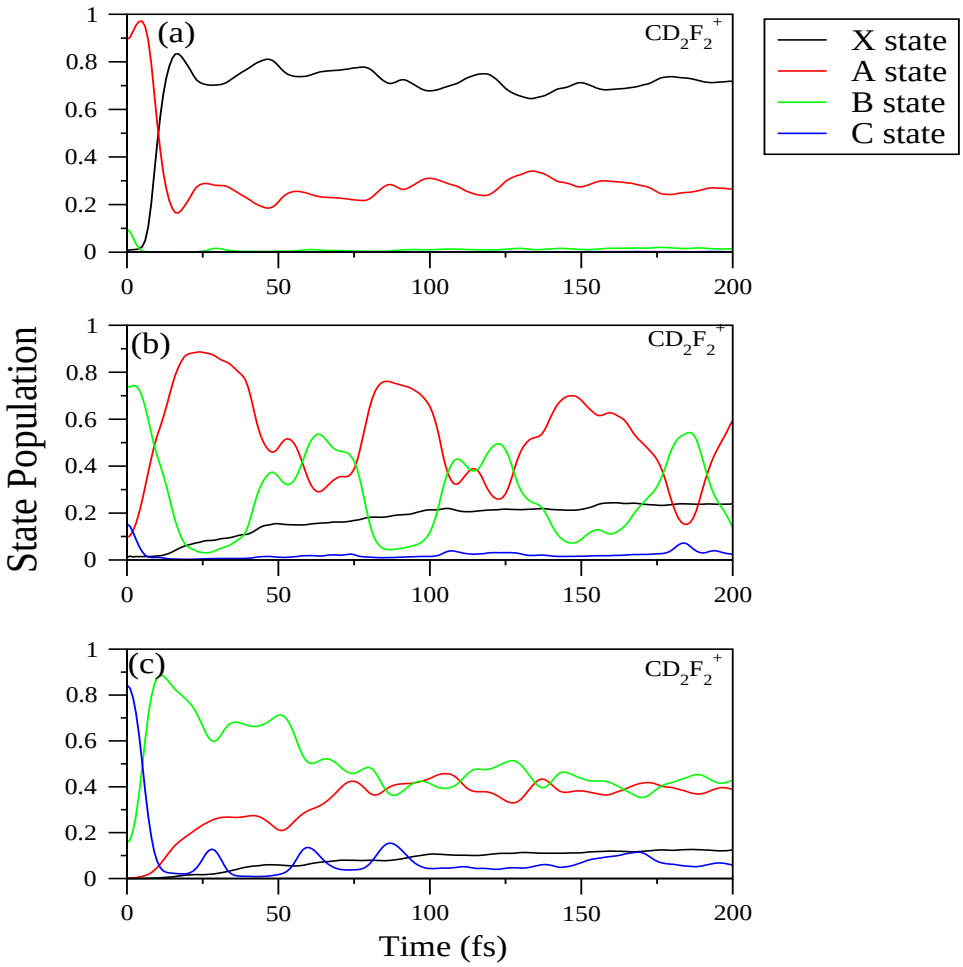

Figure 5.11: Same as in 5.10, in the $\widetilde{X}-\widetilde{A}-\widetilde{B}-\widetilde{C}$ coupled electronic states of $CD_2F_2^+$.

causes a huge broadening of their vibronic structure as observed in the experiments.

References

[1] C. R. Brundle, M. B. Robin and H. Basch, J. Chem. Phys. **53**, 2196 (1970).

[2] B. P. Pullen, T. A. Carlson, W. E. Moddeman, G. K. Schweitzer, W. E. Bull and F. A. Grimm, J. Chem. Phys. **53**, 768 (1970).

[3] A. W. Potts, H. J. Lempka, D. G. Streets and W. C. Price, Philos. Trans. R. Soc. London, Ser. A. **59**, 268 (1970).

[4] H. J. Lempka, D. G. Streets, A. W. Potts and W. C. Price, Phil. Trans. Roy. Soc. (London). **A268**, 59 (1970).

[5] T. Pradeep and D. A. Shirley, J. Electron Spectrosc. Relat. Phenom. **66**, 125-138 (1993).

[6] D. P. Seccombe, R. P. Tuckett and B. O. Fisher, J. Chem. Phys., **114**, 4074 (2001).

[7] A. Shastri, B. N. R. Sekhar, P. J. Singh and M. N. Deo, Spectrosc. Lett., **42**, 219 (2009).

[8] P. W. Forysinski, P. Zielke, D. Luckhaus, and R. Signorell, phys. chem. chem. phys., **12**, 3121-3130 (2010).

[9] K. Takeshita, Chem. Phys. Lett. **165**, 232 (1990).

[10] D. Luckhaus, P. W. Forysinski, P. Zielke, and R. Signorell, Molecular Physics, **108**, 2325-2333 (2010).

[11] R. Sarkar and S. Mahapatra, Mol. Phys. 2015, **113**, 3073.

[12] M. Born and R. Oppenheimer, Ann. Phys. 84, 457 (1927).

[13] M. Born and K. Huang, The Dynamical Theory of Crystal Lattices (Oxford University Press, Oxford, UK, 1954).

[14] R. Englman, The Jahn-Teller Effect (Wiley, New York, 1972).

[15] L. S. Cederbaum, W. Domcke, H. Köppel, and W. von Niessen, Chem. Phys. **26**, 169 (1977).

[16] L. S. Cederbaum, W. Domcke and H. Köppel, Chem. Phys. Lett. **33**, 319(1978).

[17] W. Domcke, H. Köppel and L. S. Cederbaum, Mol. Phys. **43**, 851 (1981).

[18] H. Köppel, W. Domcke, L. S. Cederbaum, Adv. Chem. Phys. **57**, 59 (1984).

[19] Conical Intersections: Electronic Structure, Dynamics and Spectroscopy, edited by Domcke. W.; Yarkony. D. R.; Köppel. H. (World Scientific, Singapore, 2004).

[20] S. Mahapatra. Int. Rev. Phys. Chem. **23**, 483 (2004).

[21] M. Baer. Beyond Born-Oppenheimer: Electronic Non-adiabatic Coupling Terms and Conical Intersections (*Wiley*. New York, 2006).

[22] S. Mahapatra. Acc. Chem. Res. **42**, 1004 (2009).

[23] C. Lanczos. J. Res. Nat. Bur. Stand. **45**, 255 (1950).

[24] J. Cullum and R. Willoughby, Lanczos Algorithms for Large Symmetric Eigenvalue Problems (Birkhäuser, Boston, 1985), Vols. I and II.

[25] W. Domcke and H. Köppel, Encyclopedia of Computational Chemistry, P. V. R. Schleyer, Ed.; Wiley: New York, 1998, P. 3166.

[26] H. -D. Meyer, U. Manthe, L. S. Cederbaum, Chem. Phys. Lett. **165**, 73 (1990).

[27] U. Manthe, H. -D. Meyer and L. S. Cederbaum, J. Chem. Phys. **97**, 3199 (1992).

[28] M. H. Beck, A. Jäckle, G. A. Worth and H. -D. Meyer, Phys. Rep. **324**, 1-105 (2000).

[29] G. A. Worth, M. H. Beck, A. Jäckle, and H.-D. Meyer, The mctdh package, Version 8.4, (2007), University of Heidelberg, Heidelberg, Geramny. See: http://mctdh.uni-hd.de.

[30] Gaussian 09, Revision B.01, M. J. Frisch, G. W. Trucks, H. B. Schlegel, G. E. Scuseria, M. A. Robb, J. R. Cheeseman, G. Scalmani, V. Barone, B. Mennucci, G. A. Petersson, H. Nakatsuji, M. Caricato, X. Li, H. P. Hratchian, A. F. Izmaylov, J. Bloino, G. Zheng, J. L. Sonnenberg, M. Hada, M. Ehara, K. Toyota, R. Fukuda, J. Hasegawa, M. Ishida, T. Nakajima, Y. Honda, O. Kitao, H. Nakai, T. Vreven, J. A. Montgomery, Jr., J. E. Peralta, F. Ogliaro, M. Bearpark, J. J. Heyd, E. Brothers, K. N. Kudin, V. N. Staroverov, T. Keith, R. Kobayashi, J. Normand, K. Raghavachari, A. Rendell, J. C. Burant, S. S. Iyengar, J. Tomasi, M. Cossi, N. Rega, J. M. Millam, M. Klene, J. E. Knox, J. B. Cross, V. Bakken, C. Adamo, J. Jaramillo, R. Gomperts, R. E. Stratmann, O. Yazyev, A. J. Austin, R. Cammi, C. Pomelli, J. W. Ochterski, R. L. Martin, K. Morokuma, V. G. Zakrzewski, G. A. Voth, P. Salvador, J. J. Dannenberg, S. Dapprich, A. D. Daniels, O. Farkas, J. B. Foresman, J. V. Ortiz, J. Cioslowski, and D. J. Fox, Gaussian, Inc. Wallingford CT, 2010.

[31] Q. Meng and H. -D. Meyer, J. Chem. Phys. **139**, 164709 (2013).

[32] D. Peláez, K. Sadri and H. -D. Meyer, Spectrochimica Acta Part A: Molecular and Biomolecular Spectroscopy. **119**, 42 (2014).

6 Photodetachment spectroscopy of Hydrogenated Boron Cluster anion $H_2B_7^-$

6.1 Introduction

Boron is electron deficient semi-metal type and is well-known in structural chemistry to form different types pure atomic boron clusters [1–18], as well as the cluster with heteroatoms, like hydrogen [19, 20] and gold [21]. The unusual three-centred two electron bonding property of boron makes *ab initio* quantum chemistry calculations more difficult to elucidate the structural properties of these clusters. In this context, pure-boron clusters have received much attention in theoretical research [1, 4, 22–31] over the past few decades. The major breakthrough in this regard is the joint experimental and theoretical findings of quasi-planar and planar structures of small boron clusters []. High level *ab initio* calculations in conjunction with the photoelectron spectroscopy mesurement emerged as a powerful tool to demostrate the complex structural properties of these atomic clusters. Chemical bonding analysis of these clusters revealed that σ and π aromaticity/anti-aromaticity [32] plays a pivotal role in their stability. Among the smaller boron clusters, B_7^- is the most interesting and complex cluster as it exists in three energetically close isomeric forms: i) doubly aromatic (σ and π aromatic) triplet C_{6v} quasi-planar wheel-type, ii) σ-aromatic and π-antiaromatic singlet C_{2v} quasi-planar form and iii) doubly antiaromatic C_{2v} planar from [33]. Among these isomers, isomer (i) possess global minimum structure of B_7^- due to the presence of double aromaticity, whereas, only the presence of σ-aromaticity in the isomer (ii) makes it less stable than isomer (i) and more stable than isomer (iii). An inversion of these stabilities are observed upon partial hydrogenation of these isomers [19]. The rearrangement of relative stability of B_7^- occurs upon addition of two hydrogen atoms due to the gain of σ-aromaticity and loss of antibonding character in σ-type of molecular orbitals (MOs) in the planar B_7^- cluster [isomer (iii)] [19]. Wheras, isomer (i) loses its double aromaticity upon hydrogenation. So in case of hydrogenated B_7^- cluster, $H_2B_7^-$, planar C_{2v} $^1A_1$ structure has the global minimum configuration. In addition to the interesting structural and bonding properties of $H_2B_7^-$, it plays an important role as a hydrogen-storage material [20]. First experimental characterization of this hydrogenated boron cluster was done by Wang and coworkers [20], through photoelectron spectroscopy. They found a ladderlike elongated structure with two terminal hydrogen atoms and chemical bonding analysis by them revealed π bonding pattern of this dihydride boron cluster similar to cojugated alkenes

and termed as polyboroene. Similar type of polyboroenes and their auroanalogues with conjugated π bonding form a new class of molecular wires [20]. The pictorial diagram of this hydrogenated boron cluster is depicted in panel a of Fig. 6.1. We follow the same ordering of atoms as indicated in Ref. [19].

The photodetachment spectra of hydorgenated B_7^- cluster recorded by Wang and coworker [20] reveals a much simpler structure than the very complex and congested band structure of pure B_7^- cluster recorded by the same group [8]. The reason behind the simpler band structure of $H_2B_7^-$ cluster is the absence of energetically close isomers in the vicinity of the global minimum structure. The photodetachment spectrum of anionic H_2B_7 was recorded at two different energy resolution using 193 nm and 266 nm laser sources. The spectra recorded at 266 nm reveals a well resolved vibronic structure of $\widetilde{X}$ state of neutral H_2B_7 and a band of much lower intensity corresponding to the $\widetilde{A}$ state of neutral H_2B_7. These bands are reproduced from Ref. [20] and shown in Fig. 6.7. In the 193 nm recording much broader envelopes of the $\widetilde{X}$ and $\widetilde{A}$ states were obtained. These band structures are also reproduced from Ref. [20] and shown in Fig. 6.7. In the 193 nm recording much higher intensity of the $\widetilde{A}$ band as compared to the 266 nm recording was obtained. This is because in this case the laser has sufficient energy to ionize electrons from HOMO-1 orbital of $H_2B_7^-$. The origin of the $\widetilde{X}$ band is identified with the theoretically calculated adiabatic and vertical detachment energies (ADE/VDE). It is noted that the photodetachment spectrum of $H_2B_7^-$ was measured in Ref. [20] by preparing $D_2B_7^-$ in the plasma reaction between the laser-vaporised boron and D_2 for better mass separation. Theoretical calculations for both $H_2B_7^-$ and $D_2B_7^-$ performed by the same group [20] indicates that, except the vibrational frequencies, the structures and electron binding energies of these isotopomers are same.

It is clear from the above disscussion that a large amount of structural data of boron clusters is available in the literature. At the same time, a detailed quantum dynamical study to elucidate the vibronic structure of the detachment spectrum is largely missing in the literatue. In the recent past we carried out detailed quantum dynamics studies of bare boron clusters upto B_7. It was found that in addition to the structural complexity, electronic nonadiabatic interactions play significant role on the vibronic structure of the detachment spectra [34, 35]. A careful look at the two spectra of $(D)H_2B_7^-$ (cf. panel A of Figure 1 and Figure S1 in Ref. [20]), indicate the change of band shape upon photodetachment of $(D)H_2B_7^-$ at two different laser sources, 266 nm and 193 nm. This is a clear indication of a significant role of nonadiabatic effect which is arised from the closely lying electronic states of $(D)H_2B_7$. On the other hand, the diffuse and broad second experimental band of $(D)H_2B_7^-$ (cf. Figure S1 in Ref. [20]) indicates that the broadness of the spectrum is not solely dependent on the contribution from the $\widetilde{A}$ state. We find that the $\widetilde{A}$ and $\widetilde{B}$ electronic states of $(D)H_2B_7^-$ are energetically very close (occurs vertically to within $\sim$0.1 eV). Therefore nonadiabatic interactions between these states would play crucial role in the detail structure of the detachment spectrum. Furthermore, $\widetilde{A}$ and $\widetilde{B}$ states of $(D)H_2B_7$ possess same spatial symmetry $^2A_1$. Thus in the

coupled $\widetilde{A}$-$\widetilde{B}$ state dynamics, the totally symmetric vibrational modes (a_1) would play a dual role of tunning and coupling mode, which is very rare in the literature. Because of same spatial symmetry of these states, they will also participate in the direct electronic coupling. The pure electronic coupling between the $\widetilde{A}$ and $\widetilde{B}$ states is calculated by applying the diabatization scheme and muticonfiguration quasi-degenerate perturbation theory (MCQDPT). In this way understanding of seemingly simple looking detachment spectrum of (D)$H_2B_7^-$ becomes quite a challenging task in theoretical study.

In the present chapter, we therefore set out to study the structure and dynamics of the first five electronic states of the neutral H_2B_7 cluster. Detailed *ab initio* electronic structure calculations are performed to establish a parametrized quasi-diabatic electronic Hamiltonian of these five states. Using this Hamiltonian quantum nuclear dynamics calculations are performed subsequently to understand the details of experimental detachment spectrum [20]. The theoretical results are examined in detail to assess the contribution of vibrational modes and electronic states in the spectrum and discussed at length in relation to the experimental findings.

6.2 Theoretical framework

6.2.1 The vibronic Hamiltonian

Enenergetically low-lying five electronic states of H_2B_7 are considered in this study. A model 5⊗5 vibronic Hamiltonian is constructed in a diabatic electronic basis using dimensionaless normal displacement coordinates of the vibrational modes of anionic H_2B_7. The equilibrium configuration of the ground state of $H_2B_7^-$ is treated as a reference in this study. The non-vanishing elements of the 5⊗5 matrix Hamiltonian is determined by the elementary symmetry selection of the vibronic coupling theory. The equilibrium ground state geometry of $H_2B_7^-$ belongs to C_{2v} symmetry point group and its twenty one vibrational modes belong to the follwing irreducible representations (IREPs):

$$\Gamma = 8a_1 \oplus 3b_1 \oplus 7b_2 \oplus 3a_2. \tag{6.1}$$

The non-vanishing terms in the matrix Hamiltonian is determined in the linear vibronic coupling (LVC) scheme by following the symmetry selection rule

$$\Gamma_i \otimes \Gamma_k \otimes \Gamma_j \supset \Gamma_{A1}, \tag{6.2}$$

where i, j represent the initial and final electronic states, respectively, and k represents the coupling vibrational mode ν_i. The non-vanishing quadratic terms are determined by the following symmetry selection rule:

$$\Gamma_i \otimes \Gamma_k \otimes \Gamma_{k'} \otimes \Gamma_j \supset \Gamma_{A1}, \tag{6.3}$$

where, k and $k^{'}$ represent the same or different vibrational modes. Employing above rules (cf. Eqs. 6.2-6.3) and standard vibronic coupling theory, vibronic Hamiltonian can be written in a diabatic electronic basis as [39]

$$\mathcal{H} = \mathcal{H}_0\mathbf{1} + \mathbf{\Delta}\mathcal{H}, \tag{6.4}$$

where, $\mathcal{H}_0$ is the unperturbed Hamiltonian of the reference electronic ground state of $H_2B_7^-$ and $\Delta\mathcal{H}$ represents the change in electronic energy upon electron detachment. **1** represents a (5 × 5) unit matrix. The unperturbed Hamiltonian of Eq. 6.4 consists of kinetic energy part, T_N, and potential energy part, V_0, of the reference state. The kinetic energy part can be written in dimensionless normal displacement coordinate representation as follows:

$$T_N = -\frac{1}{2}\sum_{i=1}^{21}\omega_i\left(\frac{\partial^2}{\partial Q_i^2}\right), \tag{6.5}$$

whereas, potential energy part in dimensionless normal displacement coordinate representation within the harmonic approximation can be written as:

$$V_0 = \frac{1}{2}\sum_{i=1}^{21}\omega_i Q_i^2. \tag{6.6}$$

The ground and first four excited electronic states of H_2B_7 belong to the $\widetilde{X}^2A_2$, $\widetilde{A}^2A_1$, $\widetilde{B}^2A_1$, $\tilde{C}^2B_2$ and $\tilde{D}^2B_1$ term of the C_{2v} symmetry point group. They result from electron detachment from the last five occupied molecular orbitals, ... b_1^2, b_2^2, a_1^2, a_1^2, a_2^2 of $H_2B_7^-$. The electronic Hamiltonian $\Delta\mathcal{H}$ can be represented as in Eq. 6.4,

$$\Delta\mathcal{H} = \begin{pmatrix} \mathcal{W}_{XX} & \mathcal{W}_{XA} & \mathcal{W}_{XB} & \mathcal{W}_{XC} & \mathcal{W}_{XD} \\ \mathcal{W}_{XA}^* & \mathcal{W}_{AA} & \mathcal{W}_{AB} & \mathcal{W}_{AC} & \mathcal{W}_{AD} \\ \mathcal{W}_{XB}^* & \mathcal{W}_{AB}^* & \mathcal{W}_{BB} & \mathcal{W}_{BC} & \mathcal{W}_{BD} \\ \mathcal{W}_{XC}^* & \mathcal{W}_{AC}^* & \mathcal{W}_{BC}^* & \mathcal{W}_{CC} & \mathcal{W}_{CD} \\ \mathcal{W}_{XD}^* & \mathcal{W}_{AD}^* & \mathcal{W}_{BD}^* & \mathcal{W}_{CD}^* & \mathcal{W}_{DD} \end{pmatrix}. \tag{6.7}$$

The elements of the electronic Hamiltonaian matrix of Eq. 6.7 are expanded in a second-order Taylor series around the reference equilibrium geometry of $Q = 0$, as follows:

$$\mathcal{W}_{jj} = E_j^0 + \sum_{i=a_1}\kappa_i^j Q_i + \frac{1}{2}\sum_{i=a_1,a_2,b_1,b_2}\gamma_i^j Q_i^2 \tag{6.8}$$

and,

$$\mathcal{W}_{jk} = \mathcal{W}^*_{kj} = \sum_i \lambda_i^{j-k} Q_i, \tag{6.9}$$

where, j and k, are the electronic state indices and i reprsents the coupling vibrational modes introduced in Eq. 6.2 (ν_1 to ν_{21}). Various Hamiltonian parameters introduced in Eqs. 6.8-6.9 have the following definitions. The vertical electron detachment energy of the $\widetilde{X}^2\mathrm{A}_2$, $\widetilde{A}^2\mathrm{A}_1$, $\widetilde{B}^2\mathrm{A}_1$, $\tilde{C}^2\mathrm{B}_2$ and $\tilde{D}^2\mathrm{B}_1$ states are defined by E_j^0, where, j= $\widetilde{X}$, $\widetilde{A}$, $\widetilde{B}$, $\widetilde{C}$ and $\widetilde{D}$ respecvtively. The quantity κ_i^j represents the linear intra-state coupling parameter and γ_i^j is the diagonal second-order intra-state coupling parameter of vibrational mode i in the j^{th} electronic state. The quantity, λ_i^{j-k} is linear inter-state coupling parameter between j^{th} and k^{th} state coupled through i^{th} vibrational mode. The vibronic Hamiltonian constructed above is utilized below to study vibronic dynamics on the mentioned electronic states of H_2B_7. It is noted that the $\widetilde{A}$ and $\widetilde{B}$ electronic states of H_2B_7 possess A_1 state symmetry. Following the electronic selection rule, it is found that both these states are also coupled via electronic correlation [54]. So in case of $\widetilde{A}$-$\widetilde{B}$ inter-state coupling, the Eq. 6.9 has the following form

$$\mathcal{W}_{jk} = \mathcal{W}^*_{kj} = R + \sum_i \lambda_i^{j-k} Q_i, \tag{6.10}$$

where, R is a constant at distorted geometries in $\widetilde{A}$-$\widetilde{B}$ coupled surface.

6.2.2 Nuclear dynamics

The vibronic energy level spectrum of H_2B_7 is calculated by a time-independent matrix diagonalization approach [40] using Fermi's golden rule equation for the spectral intensity

$$P(E) = \sum_n |<\Psi_n^f|\hat{T}|\Psi_0^i>|^2 \delta(E - E_n^f + E_0^i), \tag{6.11}$$

where, $P(E)$ represents spectral intensity. $|\Psi_0^i>$ and $\Psi_n^f>$ are the initial and final vibronic states with energy E_0^i and E_n^f, respectively. The operator $\hat{T}$ is the transition dipole operator. The reference electronic ground state $|\Psi_0^i>$ [ground state of anionic H_2B_7] is assumed to be vibronically decoupled from its excited electronic states and is given by

$$|\Psi_0^i\rangle = |\Phi_0^i\rangle|\chi_0^i\rangle, \tag{6.12}$$

where $|\Phi_0^i\rangle$ and $|\chi_0^i\rangle$ represent the electronic and vibrational components of this state, respectively. This state is assumed to be harmonic and the vibrational component of the above wavefunction is expressed in terms of the eigenfunctions of reference harmonic Hamiltonian, $T_N + V_0$ (cf. Eqs. 6.5-6.6). In the normal coordinate representation of vibrational modes, the vibrational wavefunction is a direct product of one-dimensional oscillator function along each mode. The final vibronic state of H_2B_7 can be expressed as

$$|\Psi_n\rangle = |\Phi^m\rangle|\chi_n^m\rangle, \tag{6.13}$$

where the superscript m represents the $\widetilde{X}^2\mathrm{A}_2$, $\widetilde{A}^2\mathrm{A}_1$, $\widetilde{B}^2\mathrm{A}_1$, $\widetilde{C}^2\mathrm{B}_2$, $\widetilde{D}^2\mathrm{B}_1$ electronic states of H_2B_7, respectively. With the above definitions the spectral intensity of Eq. 6.11 can be rewritten as

$$P(E) = \sum_n |\tau^m \langle \chi_n^m | \chi_0 \rangle|^2 \delta(E - E_n^f + E_0^i), \tag{6.14}$$

where,

$$\tau^m = \langle \Phi^m | \hat{T} | \Phi^0 \rangle, \tag{6.15}$$

represents the transition dipole matrix elements. These are treated as constant assuming the general applicability of Condon approximation in a diabatic electronic basis [39].

The time-independent Schrödinger equation of the vibronically coupled states is solved by representing the Hamiltonian (cf. Eq. 6.2) in the direct product harmonic oscillator (HO) basis of the reference state. The final vibronic states, $|\Psi_n^f\rangle$, can be expressed as

$$|\Psi_n^f\rangle = \sum_{|K_i\rangle, m} a^n_{k_i,\ldots,k_f,m} |K_i\rangle \ldots |K_f\rangle |\Phi_m\rangle. \tag{6.16}$$

In the above equation the K^{th} level of the i^{th} vibrational mode is denoted by $|K_i\rangle$ and $|\Phi_m\rangle$ denotes the m^{th} electronic state of the interacting electronic manifold of H_2B_7. The size of the oscillator basis is chosen based on the numerical convergence of the vibronic eigenvalue spectrum. The Hamiltonian matrix expressed in a direct product HO basis is highly sparse, it is tri-diagonalized using Lanczos algorithm [41, 42] prior to the diagonalization. The energetic location of the vibronic levels is given by the resulting diagonal eigenvalue matrix and the relative intensities are calculated from the squared first component of the Lanczos eigenvectors [43].

In a time-dependent picture, the spectral intensity is calculated by Fourier transforming the time autocorrelation function of the WP propagating on the final electronic state [44]

$$P(E) \approx \sum_{m=1}^{2} 2Re \int_0^\infty e^{iEt/\hbar} \langle \chi_0 | \tau^\dagger e^{-iHT/\hbar} \tau | \chi_0 \rangle dt, \tag{6.17}$$

$$\approx \sum_{m=1}^{2} 2Re \int_0^\infty e^{iEt/\hbar} C^m(t) dt, \tag{6.18}$$

where, $\mathrm{C}^m = \langle \Psi(0) | \Psi(t) \rangle$, represents the time autocorrelation function of the WP, initially prepared on the electronic state m. The time-dependent WP propagation is carried out within the multi-configuration time dependent Hartree (MCTDH) approach developed by Meyer and coworkers [45–48].

6.2.3 Computational details of electronic structure calculations

The optimized equilibrium geometry of the electronic ground state of $H_2B_7^-$ (the reference state) is calculated by using second-order Møller-Plesset perturbation theory (MP2) as well as coupled-cluster singles and doubles (CCSD) method employing the correlation-consistent polarized valence triple zeta (cc-pVTZ) basis set of Dunning [49]. GAUSSIAN-09 [50] and MOLPRO [51] suite of programs are used for this purpose, respectively. Rest of the single point electronic energy calculations are performed with multi-reference configuration interactions (MRCI) method with cc-pVTZ basis set, using MOLPRO [50] program modules. We performed CASSCF-MRCI vertical detachment energy (VDE) calculations at the energy minimized structure of $H_2B_7^-$ with (16,13), (16,12), (14,11), (12,12), (12,11) and (12,10) active spaces to find out the nearest VDE with the experiment [20]. Among these chosen active spaces, (14,11), (12,11) and (12,10) active spaces provide the same VDE of ∼3.27 eV, which is in good agreement with the experimental value [20]. We chose (12,10) active space among these three active spaces as it is computationally less expensive. The chosen active space includes six valence orbitals and four virtual orbitals with twelve electrons for $H_2B_7^-$. The neutral states have open shell configuration and a (11,10) active space is used to calculate the single point electronic energies at various distorted geometrices.

The optimized equilibrium structure of the $H_2B_7^-$ in the electronic ground state belongs to C_{2v} point symmetry group and leads to $^1A_1$ electronic term for this closed shell system. The equilibrium harmonic vibrational frequencies of the reference state, ω_i, are calculated by diagonalizing the kinematic and *ab initio* force constant matrix at the same level of theory. The eigenvectors of the force constant matrix yield the mass-weighted normal coordinates of the vibrational modes. The latter is transformed to the dimensionless form $\mathbf{Q}$ by multiplying with $\sqrt{\omega_i}$ (in a.u.) [52]. In an analogous way the geometry of neutral H_2B_7 in its ground electronic state is optimized. Since this neutral molecule has open shell configuration, UMP2/cc-pVTZ level of theory is employed to obtain its optimized structure. The optimized neutral ground state structure of H_2B_7 also belongs to the C_{2v} symmetry point group.

6.3 Results and discussion

6.3.1 Ground state electronic structure of anionic and neutral H_2B_7

The optimized structure of anionic H_2B_7 and the diagram of highest occupied molecular orbital (HOMO), HOMO-1, HOMO-2, HOMO-3, HOMO-4 are shown in panels a, b, c, d, e and f of Fig. 6.1, respectively. We followed the same numbering of atoms of the optimized structure as depicted in Fig. 2 of Ref. [19]. The results of the equilibrium geometry of $H_2B_7^-$, calculated by MP2 and CCSD levels of theory are compared in Table 6.1, along with the available literature data. The molecular orbital (MO) sequence of $H_2B_7^-$ is ... $(2b_2)^2$, $(3b_2)^2$, $(2b_1)^2$, $(9a_1)^2$, $(10a_1)^2$, $(1a_2)^2$. It can be seen from the MO

Table 6.1: Equilibrium configuration of $H_2B_7^-$ at its ground electronic state ($^1A_1$) in C_{2v} point group. Bond length and bond angle are indicated by R and $\angle$, respectively and their respective units are $\mathring{A}$ and degree. The numbering of atoms are followed from Ref. [19].

Parameter	This work		Ref. [19]		
	MP2/cc-pVTZ	CCSD/cc-pVTZ	B3LYP/6-311++G**	CASSCF(4,4)/6-311++G**	CCSD(T)/6-311++G**
R(B1-B2,3)	1.739	1.760	1.750	1.786	1.773
R(B1-B4,5)	1.606	1.602	1.595	1.597	1.618
R(B4,5-B6,7)	1.533	1.523	1.517	1.509	1.543
R(B2-B3)	1.611	1.603	1.597	1.615	1.620
R(B2-B6)	1.679	1.677	1.673	1.694	1.688
R(B6-H)	1.184	1.186	1.183	1.181	1.190
R(B4-B2)	1.679	1.684	1.676	1.691	1.707
$\angle B4-B6-H$	163.102	162.953	162.895	163.756	162.245

diagram of Fig. 6.1 that HOMO-1 (cf. panel c of Fig. 6.1) is the only delocalized σ-MO, produces σ-aromaticity in the $H_2B_7^-$. On the other hand, π-MOs of the $H_2B_7^-$ cluster give rise to π-antiaromaticity on the system. The frequency values of the vibrational modes (within harmonic approximation) at the MP2/cc-pVTZ and CCSD/cc-pVTZ level of theory, are given in Table 6.2. Available literature data are also included in the table. The latter results are in very good agreement with the present results. In an analogous way the geometry of neutral H_2B_7 in its ground electronic states is optimized. The optimized structure of H_2B_7 also belongs to C_{2v} symmetry point group. The optimized equlibrium structural parameters of the anionic and neutral ground state of H_2B_7 computed at (U)MP2/cc-pVTZ level of theory are given in Table 6.3 to make the comparison easier. After removal of one electron from HOMO, HOMO-1, HOMO-2, HOMO-3 and HOMO-4, produces $\widetilde{X}^2A_2$, $\widetilde{A}^2A_1$, $\widetilde{B}^2A_1$, $\widetilde{C}^2B_1$ and $\widetilde{D}^2B_2$ electronic states of H_2B_7. A careful look at the panel b of Fig. 6.1 indicates that the HOMO of $H_2B_7^-$ is a π-bonding type of MO and (B4, B6, B2) and (B5, B3, B7) atoms are involved to make this MO. Therfore, removal of one electron from this MO alters the geometry parameters compared to those of the anionic equilibrium structure. The overall bonding character of the ground state of the neutral H_2B_7 decreases compared to the anion as revealed by increase of bond lengths (cf. Table 6.3). The calculated VDEs of the above mentioned electronic states of H_2B_7 are given in Table 6.4 and compared with the reported literature data.

6.3.2 Hamiltonian parameters

All the Hamiltonian parameters defined in Eqs. 6.8-6.9 are derived by performing extensive *ab initio* calculations of electronic energies by taking $H_2B_7^-$ energy minmized ground state configuration [cf. Fig. 6.1(a)] as a reference. As mentioned earlier that the calculations are carried out by CASSCF-MRCI ab initio quantum chemistry methods employing the cc-pVTZ basis set. The calculated ab initio electronic energies are then fit to the adiabatic form of the diabatic electronic Hamiltonian of Eq. 6.7 to estimate these parameters. The linear and quadratic intra-state coupling parameters of totally symmetric (a_1) vibrational modes of $\widetilde{X}^2A_2$, $\widetilde{A}^2A_1$, $\widetilde{B}^2A_1$, $\widetilde{C}^2B_2$ and $\widetilde{D}^2B_1$ electronic states of H_2B_7 are given in Table 6.5. The quadratic intra-state coupling parameters of non-totally symmetric vibrational modes (a_2, b_1 and b_2) are given in Table 6.6. The

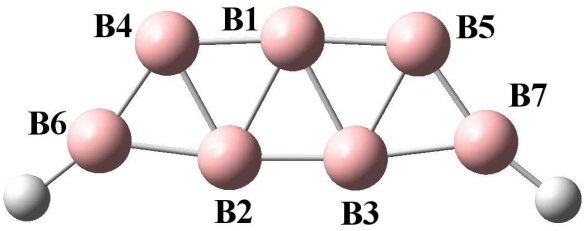

(a) C_{2v} ($^1A_1$)

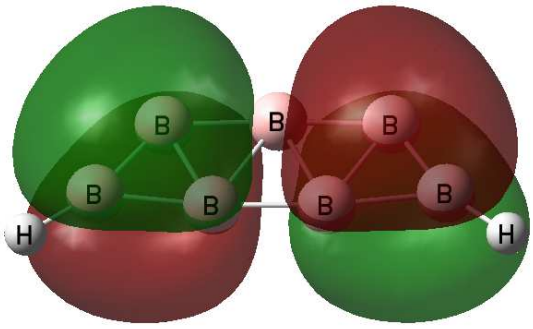

(b) HOMO ($1a_2$)

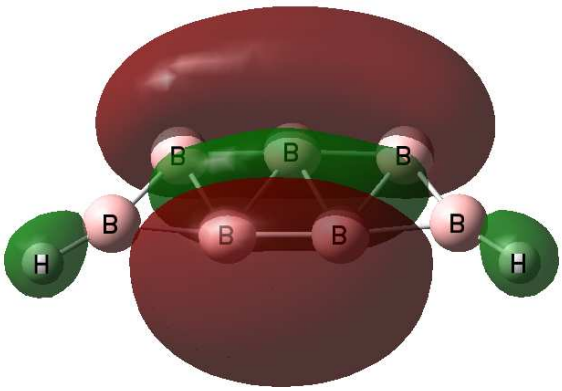

(c) HOMO-1 ($10a_1$)

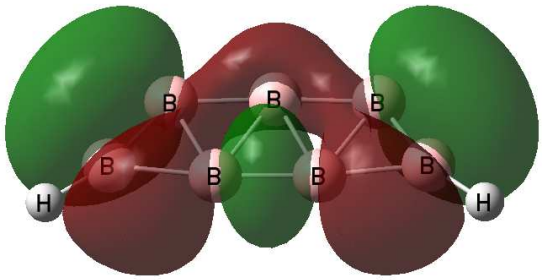

(d) HOMO-2 ($9a_1$)

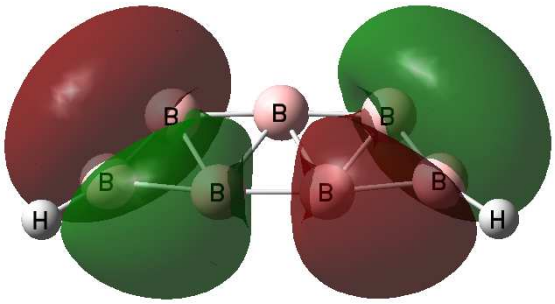

(e) HOMO-3 ($3b_2$)

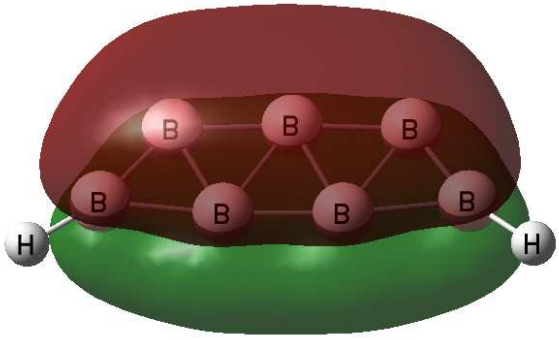

(f) HOMO-4 ($2b_1$)

Figure 6.1: Equilibrium geometry of the optimized electronic ground state of $H_2B_7^-$ is shown in panel a. The highest occupied molecular orbital (HOMO), HOMO-1, HOMO-2, HOMO-3 and HOMO-4 are shown in panels b, c, d, e and f, respectively.

linear inter-state coupling parameters are tabulated in Table 6.7. We note that the construction of several two-states model through the coupling vibrational modes are performed to evaluate the inter-state coupling parameters.

Table 6.2: Symmetry and harmonic frequencies (in cm^{-1}) of vibrational modes of the ground electronic state of $H_2B_7^-$.

Vibrational mode (symmetry)	This work MP2/cc-pVTZ cm^{-1} (eV)	This work CCSD/cc-pVTZ	Ref. [19] B3LYP/ 6-311++G**	Ref. [19] CASSCF(4,4) 6-311-G**
ν_1 (a_1)	2721 (0.3374)	2698	2686	2766
ν_2 (a_1)	1298 (0.1609)	1336	1312	2042
ν_3 (a_1)	1199 (0.1486)	1239	1210	932
ν_4 (a_1)	873 (0.1082)	867	858	794
ν_5 (a_1)	754 (0.0934)	769	754	726
ν_6 (a_1)	691 (0.0856)	696	683	642
ν_7 (a_1)	582 (0.0722)	584	566	567
ν_8 (a_1)	373 (0.0462)	386	381	398
ν_9 (a_2)	713 (0.0884)	731	731	809
ν_{10} (a_2)	456 (0.0566)	473	471	480
ν_{11} (a_2)	250 (0.0310)	248	258	174
ν_{12} (b_1)	707 (0.0876)	708	705	764
ν_{13} (b_1)	449 (0.0556)	464	469	485
ν_{14} (b_1)	161 (0.0199)	165	168	166
ν_{15} (b_2)	2718 (0.3370)	2694	2684	2762
ν_{16} (b_2)	1322 (0.1639)	1320	1314	1381
ν_{17} (b_2)	1123 (0.1393)	1140	1128	1362
ν_{18} (b_2)	903 (0.1120)	917	897	1151
ν_{19} (b_2)	779 (0.0965)	783	767	882
ν_{20} (b_2)	644 (0.0799)	650	641	809
ν_{21} (b_2)	531 (0.0659)	527	521	523

According to the symmetry selection rule of Eq. 6.2, only the totally symmteic modes are allowed for the intra-state vibronic coupling and the Huang-Rhys parameter, $\left(\frac{\kappa_i^2}{2\omega_i^2}\right)$ defines a measure of the strength of this coupling in first-order. The value of these parameters are given in the parentheses in the Table 6.5. The coupling parameters of Table 6.5 reveal that the symmetric vibrational mode ν_4 is active in all electronic states, excluding $\widetilde{A}^2A_1$ state. Whereas, ν_7 vibrational modes is active in $\widetilde{A}^2A_1$ and $\widetilde{B}^2A_1$ electronic states. The moderate to higher activity of ν_2 is found in $\widetilde{C}^2B_2$ and $\widetilde{X}^2A_2$ electronic states, respectively. The vibrational mode ν_8 is active in the $\widetilde{X}^2A_2$, $\widetilde{C}^2B_2$ and $\widetilde{D}^2B_1$ states. Although a moderate activity of ν_1 is found in all five electronic states, it is expected that this mode has less impact on the dynamics at the low-energy region due its higher frequency. The vibrational modes, ν_2, ν_7, ν_7, ν_4 and ν_4 possess the

Table 6.3: Equilibrium configuration of $H_2B_7^-$ and H_2B_7 at their electronic ground state ($^1A_1$ and $^2A_2$, respectively). They belong to the C_{2v} symmetry point group. Bond length and bond angle are indicated by R and $\angle$, respectively, and their respective units are $\mathring{A}$ and degree. The numbering of atoms is given in Fig. 6.1(a).

Parameter	This work	
	MP2/cc-pVTZ	UMP2/cc-pVTZ
R(B1-B2,3)	1.739	1.767
R(B1-B4,5)	1.606	1.590
R(B4,5-B6,7)	1.533	1.561
R(B2-B3)	1.611	1.710
R(B2-B6)	1.679	1.175
R(B6-H)	1.184	1.186
R(B4-B2)	1.679	1.729
$\angle B4-B6-H$	163.102	161.790

Table 6.4: Vertical electron detachment energies of first five electronic states of H_2B_7 evaluated by CAS(12,10)SCF/MRCI/cc-pVTZ level of theory. Units are given in eV.

State	This work	Ref. [20]	
	H_2B_7	Experiment	Theory
$\tilde{X}^2A_2$	3.27	3.49	3.47
$\tilde{A}^2A_1$	4.50		
$\tilde{B}^2A_1$	4.56		
$\tilde{C}^2B_2$	5.46		
$\tilde{D}^2B_1$	5.63		

highest activity in the $\widetilde{X}^2A_2$, $\widetilde{A}^2A_1$, $\widetilde{B}^2A_1$, $\widetilde{C}^2B_2$ and $\widetilde{D}^2B_1$ electronic states of H_2B_7, respectively. So, it can be concluded from this discussion that ν_2, ν_4, ν_7 nad ν_8 vibrational modes may have the major contribution in the dynamics of the H_2B_7 than the other totally symmetric vibrational modes.

The quadratic intra-state coupling parameters are related with the curvature of the PESs. Hence, the frequencies of the electronic states of H_2B_7 depend on these quadratic coupling paramters. The negative sign of the parameter indicates the frequency reduction and positive sign of the parameter indiactes an increase in frequency of a vibrational mode in a given electronic state. The quadratic intra-mode intra-state coupling parameters (γ_i^j) for five electronic states ae given in Table 6.5 and Table 6.6, respectively, for totally symmetric and non-totally symmetric vibrational modes. The data presented in Table 6.5 reveal an increase in frequency of toatlly symmetric vibrational modes in the vibronic dynamics of $\widetilde{X}^2A_2$, $\widetilde{B}^2A_1$ and $\widetilde{D}^2B_1$ (except ν_6) states and both an increase and

Table 6.5: Linear intra-state vibronic coupling parameters (κ_i^j) and quadratic intra-state vibronic coupling parameters (γ_i^j) of the totally symmetric vibrational modes (ν_1-ν_8) in $\tilde{X}^2A_2$, $\tilde{A}^2A_1$, $\tilde{B}^2A_1$, $\tilde{C}^2B_2$ and $\tilde{D}^2B_1$ electronic states of H_2B_7 derived at CAS(12,10)SCF/MRCI quantum mechanical methods with the cc-pVTZ basis set. All parameters are given in eV unit.

Mode	$\kappa_i^j \left(\frac{\left(\kappa_i^j\right)^2}{2\omega_i^2}\right)$	γ_i^j	$\kappa_i^j \left(\frac{\left(\kappa_i^j\right)^2}{2\omega_i^2}\right)$	γ_i^j
	$\tilde{X}^2A_2$		$\tilde{A}^2A_1$	
ν_1	0.1806 (0.143)	0.1320	0.1456 (0.093)	0.1241
ν_2	0.1836 (0.651)	0.0162	-0.0324 (0.020)	-0.0235
ν_3	-0.0350 (0.028)	0.0133	0.0101 (0.002)	-0.0123
ν_4	0.1036 (0.458)	0.0124	0.0014 (0.000)	-0.0138
ν_5	0.0228 (0.030)	0.0748	0.0063 (0.003)	-0.0197
ν_6	-0.0353 (0.085)	0.0097	-0.0125 (0.011)	-0.0557
ν_7	0.0192 (0.035)	0.0031	-0.0863 (0.714)	-0.0107
ν_8	-0.0250 (0.146)	0.0035	-0.0204 (0.097)	0.0036
	$\tilde{B}^2A_1$		$\tilde{C}^2B_2$	
ν_1	0.1902 (0.159)	0.0275	0.1924 (0.163)	0.0199
ν_2	0.0136 (0.004)	0.0505	0.1219 (0.287)	0.0056
ν_3	0.0501 (0.057)	0.0356	0.0237 (0.013)	-0.0049
ν_4	-0.0492 (0.103)	0.0246	-0.1088 (0.506)	0.0148
ν_5	0.0144 (0.012)	0.1025	0.0552 (0.175)	0.0212
ν_6	0.0131 (0.012)	0.1103	-0.0452 (0.139)	-0.0006
ν_7	-0.0482 (0.223)	0.0176	-0.0033 (0.001)	-0.0040
ν_8	-0.0054 (0.007)	0.0079	0.0329 (0.253)	0.0030
	$\tilde{D}^2B_1$			
ν_1	0.1662 (0.121)	0.0180		
ν_2	0.0414 (0.033)	0.0015		
ν_3	-0.0740 (0.124)	0.0005		
ν_4	0.1935 (1.599)	0.0167		
ν_5	0.0424 (0.103)	0.0699		
ν_6	-0.1197 (0.978)	-0.0040		
ν_7	-0.0155 (0.023)	0.0045		
ν_8	0.0261 (0.160)	0.0017		

Table 6.6: Quadratic intra-state vibronic coupling parameters (γ_i^j) along the coupling vibrational modes (ν_9-ν_{21}) in the $\tilde{X}^2A_2$, $\tilde{A}^2A_1$, $\tilde{B}^2A_1$, $\tilde{C}^2B_2$ and $\tilde{D}^2B_1$ electronic states of H_2B_7 derived at CAS(12,10)SCF/MRCI quantum mechanical methods with the cc-pVTZ basis set. All parameters are given in eV unit.

Vibrational modes	Electronic states				
(symmetry)	$\tilde{X}^2A_2$	$\tilde{A}^2A_1$	$\tilde{B}^2A_1$	$\tilde{C}^2B_2$	$\tilde{D}^2B_1$
ν_9 (a_2)	0.0735	0.0713	0.0980	0.0912	0.0898
ν_{10} (a_2)	-0.0090	-0.0075	0.0133	-0.0201	-0.0114
ν_{11} (a_2)	0.0147	0.0116	0.0079	0.0068	0.0104
ν_{12} (b_1)	0.0988	0.0958	0.1001	0.0985	0.0914
ν_{13} (b_1)	0.0034	-0.0113	0.0021	0.0032	0.0029
ν_{14} (b_1)	-0.0131	0.0125	0.0209	0.0174	-0.0096
ν_{15} (b_2)	0.1397	0.1384	0.1386	0.1405	0.1356
ν_{16} (b_2)	0.0124	-0.0093	-0.0015	0.0249	0.0124
ν_{17} (b_2)	-0.0065	-0.0014	-0.0076	-0.0035	0.0074
ν_{18} (b_2)	0.0102	-0.0325	-0.0168	0.0134	-0.0002
ν_{19} (b_2)	0.0379	0.0194	0.0230	0.0284	0.0336
ν_{20} (b_2)	0.0336	0.0044	0.0464	0.0406	0.0338
ν_{21} (b_2)	0.0141	0.0043	0.0125	0.0136	0.0149

decrease of these frequencies in the dynamics of $\widetilde{A}^2A_1$ and $\widetilde{C}^2B_2$ states. A similar analogy follows from the data given in Table 6.6, for the non-totally symmetric vibrational modes.

The linear inter-state coupling $\left(\lambda_i^{j-k}\right)$ between two different states via vibrational modes are governed by the symmetry selection rule presented in Eq. 6.2. The inter-state coupling values along with their symmetry and excitation strength $\left(\frac{\left(\lambda_i^{i-j}\right)^2}{2\omega_i^2}\right)$ are presented in Table 6.7. The data presented in Table 6.7 reveal a strong inter-state coupling between $\widetilde{X}^2A_2$-$\widetilde{A}^2A_1$ states through ν_{11} vibrational mode, whereas, $\widetilde{X}^2A_2$-$\widetilde{B}^2A_1$ states are moderately coupled via ν_{10} vibrational mode. A strong coupling between $\widetilde{A}^2A_1$-$\widetilde{B}^2A_1$ states is observed through symmetric vibrational modes ν_5, ν_6 and ν_8. The VDEs presented in Table 6.4 reveal that these states are energetically close. The coupling between the $\widetilde{A}^2A_1$ and $\widetilde{B}^2A_1$ states with the $\widetilde{C}^2B_2$ state via b_2 symmetric vibrational modes is also strong, while the same with the $\widetilde{D}^2B_1$ state via b_1 symmetric vibrational mode is weak. Although $\widetilde{C}^2B_2$ and $\widetilde{D}^2B_1$ states are energetically very close (cf. Table 6.4), the coupling between these two states are weakly coupled via ν_{10} vibrational mode. We note that inter-state coupling between the $\widetilde{X}^2A_2$-$\widetilde{A}^2A_1$, $\widetilde{X}^2A_2$-$\widetilde{B}^2A_1$ and $\widetilde{A}^2A_1$-$\widetilde{B}^2A_1$ coupled

states are discussed in detail below.

6.3.3 Adiabatic potential energy surfaces

One dimensional cuts of the adiabatic potential energy surfaces (PESs) of the $\widetilde{X}^2A_2$, $\widetilde{A}^2A_1$, $\widetilde{B}^2A_1$, $\widetilde{C}^2B_2$ and $\widetilde{D}^2B_1$ electronic states of H_2B_7 are plotted along normal displacement co-ordinate of symmetric vibrational modes (ν_1-ν_8) in Fig. 6.2. In this figure, points represent the calculated ab initio electronic energies by the CASSCF-MRCI method. The superimposed solid lines represent the potential energies obtain from the vibronic model using the respective parameters of Tables 6.4-6.5. It can be seen from the figure that the calculated ab initio points are well reproduced by the constructed vibronic model presented in section 6.2.1. The ab initio adiabatic energies of the above electronic states of H_2B_7 are calculated at the CASSCF-MRCI level of theory in the coordinate range -5.0≤Q≤5.0, along all vibrational mode. Among eight symmetric vibrational modes, the Condon activity of ν_2 and ν_4 are stronger in the $\widetilde{X}^2A_2$ electronic state and in $\widetilde{A}^2A_1$ electronic state, ν_7 vibrational mode has the strongest Condon activity. A mild Condon activity of ν_7, ν_1 and ν_4 vibrational modes is found in the $\widetilde{B}^2A_1$ state, while a stong Condon activity of ν_4 vibrational mode is found in both $\widetilde{C}^2B_2$ and $\widetilde{D}^2B_1$ electronic states. A comparable Condon activity of ν_6 with the ν_4 vibrational mode is also found in the $\widetilde{D}^2B_1$ electronic state. Analysis of the results of Table 6.5 indicates that the coupling strength ν_4 vibrational mode is moderate to high in all electronic states of H_2B_7, except in $\widetilde{A}^2A_1$ electronic state. The strong Condon activity of a vibrational mode results into a larger shift of the equilibrium minimum of the given electronic state along its co-ordinate relative to the reference equilibrium minimum at $\mathbf{Q}$=$\mathbf{0}$ and the direction of shift of the energy minima depends on the sign of the first-order intra-state coupling (κ_i), which defines the slope of the curve at Q=$\mathbf{0}$. For example, the shift of the energy minimum of the $\widetilde{X}^2A_2$ and $\widetilde{D}^2B_1$ electronic states occur in the negative direction from the reference equilibrium minimum at $\mathbf{Q}$=$\mathbf{0}$ along Q_4 dimensionless normal coordinate (cf. panel d in Fig. 6.2), whereas the same for $\widetilde{C}^2B_2$ occurs in the positive direction (cf. panel d in Fig. 6.2).

It is clear from Fig. 6.2 that the ground electronic state of H_2B_7 is well separated from the other electronic states at the Franck-Condon region, while beyond the Franck-Condon zone, at larger distance it bcomes energetically very close (sometimes crosses) with both $\widetilde{A}^2A_1$ and $\widetilde{B}^2A_1$ states. On the other hand, $\widetilde{A}^2A_1$ and $\widetilde{B}^2A_1$, $\widetilde{C}^2B_2$ and $\widetilde{D}^2B_1$ electronic states are vertically very close with each other (cf. Table 6.4) and the crossing of each pair of states are observed near the Franck-Condon region. These crossings acquire the topography of conical intersection (CI) in the multi-dimensions. Energetic minimum of the seam of various CIs and equilibrium minimum of electronic states are estimated within a quadratic vibronic coupling model using the parameters of Tables 6.4-6.5 and given in Table 6.8. In the latter, diagonal and off-diagonal entries represent the equilibrium minimum of a state and the minimum of the seam of CIs, respectively. We note that a constrained minimization by Lagrangian multiplier methods

Table 6.7: Linear interstate coupling parameters (λ_i^{j-k}) of the relevant electronic states of the H_2B_7 derived at at CAS(12,10)SCF/MRCI quantum mechanical methods with the cc-pVTZ basis set. All parameters are given in eV unit.

Coupled states	Vibrational mode (symmetry)	λ_i^{j-k}	$\frac{\left(\lambda_i^{j-k}\right)^2}{2\omega_i^2}$
$\tilde{X}\tilde{A}$	ν_9 (a_2)	0.0707	0.3198
	ν_{10} (a_2)	0.0571	0.5089
	ν_{11} (a_2)	0.0680	2.4058
$\tilde{X}\tilde{B}$	ν_{10} (a_2)	0.0906	1.2811
$\tilde{X}\tilde{C}$	ν_{12} (b_1)	0.1065	0.7390
	ν_{14} (b_1)	0.1637	33.8346
$\tilde{X}\tilde{D}$	ν_{20} (b_2)	0.0527	0.2175
$\tilde{A}\tilde{B}$	ν_1 (a_1)	0.0832	0.0304
	ν_2 (a_1)	0.1119	0.2418
	ν_3 (a_1)	0.0888	0.1785
	ν_4 (a_1)	0.0780	0.2598
	ν_5 (a_1)	0.1193	0.8157
	ν_6 (a_1)	0.1074	0.7870
	ν_7 (a_1)	0.0669	0.4290
	ν_8 (a_1)	0.0573	0.7690
$\tilde{A}\tilde{C}$	ν_{15} (b_2)	0.3780	0.6290
	ν_{16} (b_2)	0.3770	2.6454
	ν_{17} (b_2)	0.3307	2.8180
	ν_{18} (b_2)	0.3984	6.3266
	ν_{19} (b_2)	0.3872	8.0498
	ν_{20} (b_2)	0.3331	8.6901
	ν_{21} (b_2)	0.2131	5.2284
$\tilde{A}\tilde{D}$	ν_{13} (b_1)	0.3211	16.6763
$\tilde{B}\tilde{C}$	ν_{15} (b_2)	0.1711	0.1289
	ν_{16} (b_2)	0.2069	0.7968
	ν_{17} (b_2)	0.1588	0.6498
	ν_{18} (b_2)	0.2292	2.0939
	ν_{19} (b_2)	0.1857	1.8516
	ν_{21} (b_2)	0.0722	0.6002
$\tilde{C}\tilde{D}$	ν_{10} (a_2)	0.0420	0.2753

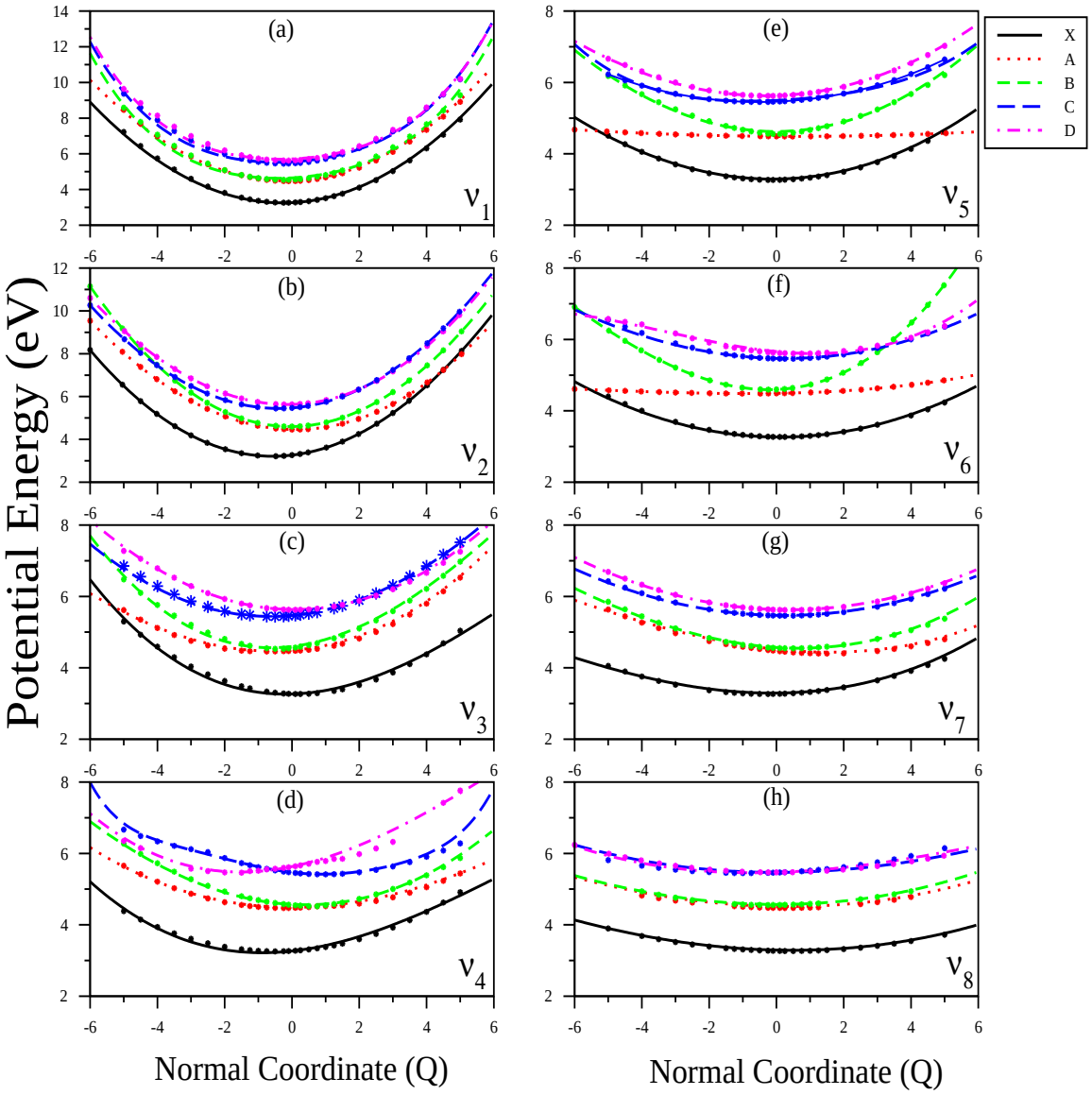

Figure 6.2: Adiabatic potential energy curves of the $\widetilde{X}^2A_2$, $\widetilde{A}^2A_1$, $\widetilde{B}^2A_1$, $\widetilde{C}^2B_2$ and $\widetilde{D}^2B_1$ electronic states of H_2B_7 along the dimensionless normal coordinates of totally symmetric vibrational modes. Potential energies obtained from the present vibronic model using the CASSCF-MRCI parameter values of Tables 6.4-6.5 and calculated ab initio points by the same method are shown by the solid lines and points in the diagram, respectively.

as implemented in Mathematica software [53] is used to derived the minimum energy and positions of the seams of CIs. Energetic location of these stationary points on a state governs the mechanistic details of nuclear dynamics on it. It can be seen from the stationary points given in Table 6.8 that $\widetilde{X}$-$\widetilde{A}$ CI (∼4.80 eV) is quite close to the minimum of the $\widetilde{A}$ (∼4.40 eV) state. A quasi-degeneracy can be seen between the

Table 6.8: Estimated equilibrium minimum (diagonal entries) and minimum of the seam of various CIs (off-diagonal entries) of the electronic states of H_2B_7 quadratic vibronic coupling model. All quantities are given in eV.

	$\widetilde{X}^2A_2$	$\widetilde{A}^2A_1$	$\widetilde{B}^2A_1$	$\widetilde{C}^2B_2$	$\widetilde{D}^2B_1$
$\tilde{X}^2A_2$	3.075	4.796	6.391	7.638	8.739
$\tilde{A}^2A_1$	-	4.405	4.482	5.932	6.038
$\tilde{B}^2A_1$	-	-	4.480	5.503	5.335
$\tilde{C}^2B_2$	-	-	-	5.277	5.412
$\tilde{D}^2B_1$	-	-	-	-	5.316

minimum of $\widetilde{A}$-$\widetilde{B}$ CI (∼4.48 eV) with the minimum of $\widetilde{B}$ (∼4.48 eV) state. The minimum of the $\widetilde{C}$-$\widetilde{D}$ CIs is ∼0.096 eV above the minimum of the and $\widetilde{D}$ state. On the other hand, a quasi-degeneracy exists between the $\widetilde{B}$-$\widetilde{D}$ CIs (∼5.33 eV) and the energy minimum of $\widetilde{D}$ (∼5.32 eV) state. From the data presented in Tables 6.4, 6.7 and 6.8, it is expected that there will be some impact of the $\widetilde{X}$-$\widetilde{A}$ and $\widetilde{X}$-$\widetilde{B}$ coupling on the nuclear dynamics of the $\widetilde{X}$ state, despite $\widetilde{X}$ is vertically >1.0 eV below compare to $\widetilde{A}$ and $\widetilde{B}$ states. The quasi-degeneracy between the $\widetilde{A}$-$\widetilde{B}$ CIs and energy minimum of $\widetilde{B}$ state and the near degenerate VDEs of $\widetilde{A}$ (∼4.50 eV) and $\widetilde{B}$ (∼4.56 eV) states would have strong coupling effects on the dynamics of both these states.

6.3.4 Vibronic dynamics on the coupled $\widetilde{X}$-$\widetilde{A}$-$\widetilde{B}$ states of H_2B_7 and the effect of nonadiabatic coupling

Effect of $\widetilde{X}$-$\widetilde{A}$ and $\widetilde{X}$-$\widetilde{B}$ inter-state coupling on the uncoupled $\widetilde{X}$ state dynamics

In order to understand the detailed vibronic dynamics on the $\widetilde{X}^2A_2$-$\widetilde{A}^2A_1$-$\widetilde{B}^2A_1$ coupled states of H_2B_7 and the effect of nonadiabatic coupling on the uncoupled states, we systematically carried out several reduced dimensional calculations. The two bands in the recorded detachment spectrum of (D)$H_2B_7^-$ [20] are assigned to $\widetilde{X}$ and $\widetilde{A}$ electronic states of H_2B_7 only. However, it will be seen below that the second band is a composite of $\widetilde{A}$ and $\widetilde{B}$ states and as discussed above the nonadiabatic effect is particularly strong between these states (cf. Table 6.7). The effect nonadiabatic interaction between the $\widetilde{X}$-$\widetilde{A}$ and $\widetilde{X}$-$\widetilde{B}$ electronic states on the uncoupled spectra of these states are shown in Fig. 6.3. The uncoupled spectra calculated with totally symmetric modes (ν_1-ν_8) is shown in panel a of Fig. 6.3, whereas parital $\widetilde{X}$-$\widetilde{A}$ coupled states spectra with totally symmetric modes plus one coupling mode ν_{10} and ν_{11} are shown in panels b and c, respectively, in the same figure. The partial $\widetilde{X}$-$\widetilde{B}$ coupled states spectra with totally symmetric modes plus coupling mode ν_{10} is shown in panel d of Fig. 6.3. The calculations are carried out by the matrix diagonalization approach as discussed in section 6.2.2. The numerical details of these calculation are given in Table 6.9. The symmetric mode

Table 6.9: Normal mode combinations, sizes of the primitive and single particle bases used in the MCTDH calculations for the coupled $\tilde{X} - \tilde{A} - \tilde{B}$ electronic states of H_2B_7 .

Normal modes	Primitive basis	SPF basis $[\tilde{X}, \tilde{A}, \tilde{B}, \tilde{C}]$
(ν_1, ν_2, ν_7, ν_8, ν_{11})	(12, 14, 12, 12, 16)	[8, 7, 7]
(ν_4, ν_{10})	(10, 10)	[6, 5, 5]
(ν_3, ν_5, ν_6, ν_9)	(6, 6, 8, 8)	[4, 4, 4]

spectrum shown in panel a reveals dominant excitation of vibrational modes ν_2 and ν_4. A moderate excitation of ν_8 and ν_6 vibrational modes is also found from the spectrum of panel a. Excitation of ν_3, ν_5 and ν_7 vibrational modes is weak in the ground state spectrum of H_2B_7. Despite, a moderate excitation strength (Huang-Rhys factor, cf. Table 6.5), excitation of ν_1 vibrational mode is not found in the low energy of part of the spectrum. The excitation of various totally symmetric modes is on par with the Huang-Rhys parameters presented in Table 6.5. Analysis of the uncoupled ground state spectrum of H_2B_7 (cf. panel a of Fig. 6.3) and block-improved relaxation calculations [36–38] reveal the location of the fundamental of ν_8, ν_7, ν_6, ν_4, ν_5, ν_3 and ν_2 at ∼386 cm^{-1}, ∼595 cm^{-1}, ∼728 cm^{-1}, ∼921 cm^{-1}, ∼1011 cm^{-1}, ∼1251 cm^{-1} and ∼1361 cm^{-1}, respectively, from the 0_0^0 line. The vibronic wavefunction density plots of these fundamental progressions are shown in panels a, b, c, e, f, h and k of Fig. 6.4. In these panels a nodal plane is observed along the respective normal coordinate, which indicates the fundamental of that particular mode. The excitation of first overtone of ν_8, ν_7 and ν_6 is obtained within ∼1500 cm^{-1} from the 0_0^0 line due to their low frequency values in the reference ground electronic state of $H_2B_7^-$. The relative intensity of the overtones of ν_8 and ν_6 vibrational modes is higher compared to ν_7. This is in good agreement with Huang-Rhys parameters presented in Table 6.5. The first overtone of ν_8 and ν_6 is found at ∼773 cm^{-1} and ∼1457 cm^{-1}, respectively. The wavefunction density plots othese overtones are shown in panel d and l of Fig. 6.4. Combination levels of ν_8 with ν_6 and ν_4 are also found from this spectrum at ∼1115 cm^{-1} and ∼1308 cm^{-1}. The corresponding wavefunction density plots are shown in panels g and i of Fig. 6.4. The combination peak of ν_6 and ν_7 is found at ∼1323 cm^{-1} (cf. panel j of Fig. 6.4). The fundamental of ν_1 is found at ∼3210 cm^{-1}.

The effect of $\widetilde{X}$-$\widetilde{A}$ and $\widetilde{X}$-$\widetilde{B}$ coupling via ν_{10} and ν_{11} modes of a_2 symmetry is shown in panels b, c and d in Fig. 6.3. The immediate effects of these couplings are reduction of peak intensities and the increase of number of stick lines, which makes the spectra of panels b, c and d more diffuse and broader than the spectrum of panel a (totally symmetric mode spectrum) in Fig. 6.3. This is the consequence of nonadiabatic coupling due to a_2 vibrational modes. As a result of this, the relative intensity of the totally symmetric vibrational modes decrease compared to the uncoupled spectra shown in panel a of Fig. 6.3. We note that realtive intensity of each panel has same initial and final value. The reduced dimensional results of Fig. 6.3b indicate fundamental progression of ν_{10} at ∼399

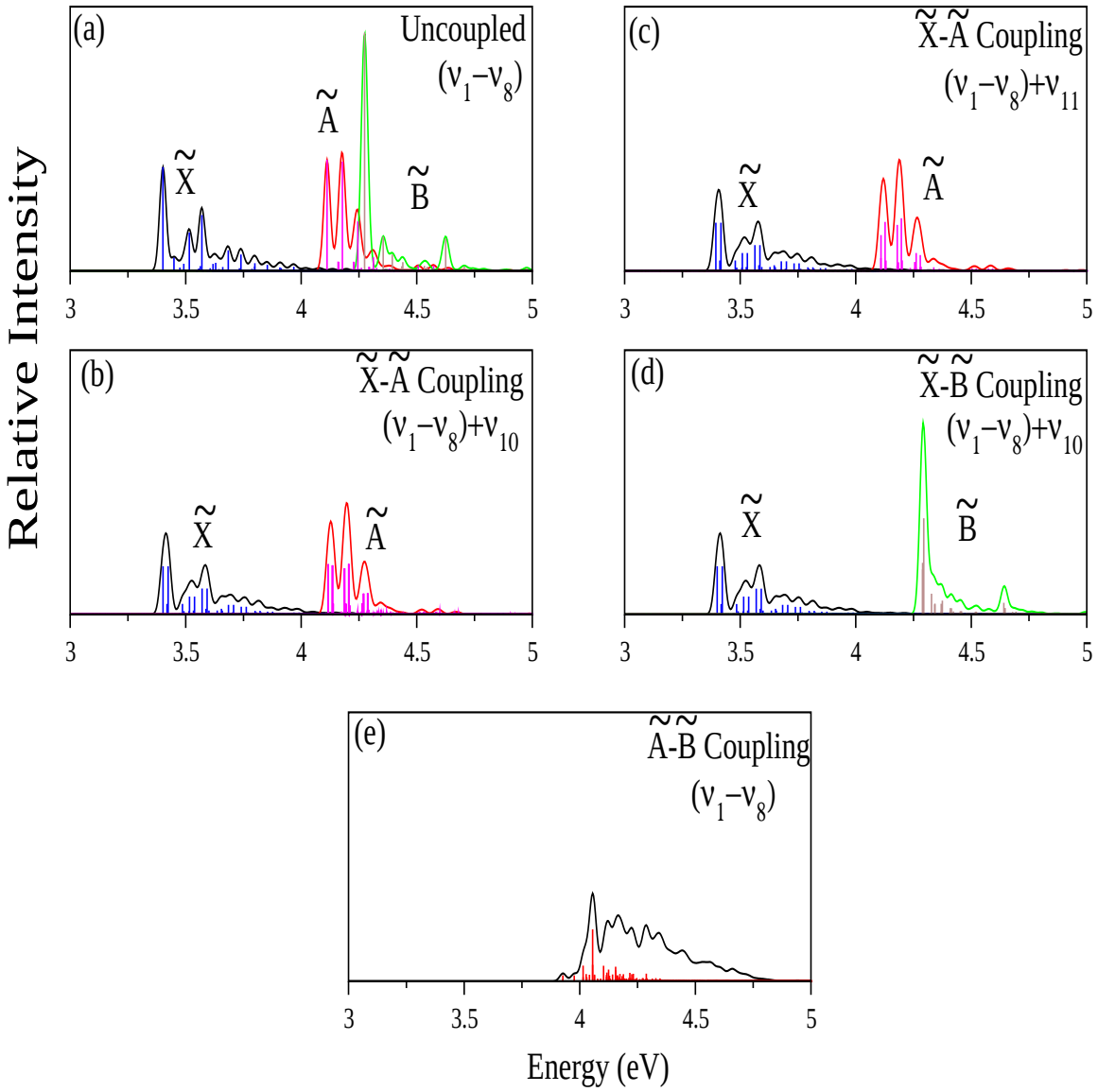

Figure 6.3: Vibrational energy level spectrum of the electronic ground $\widetilde{X}^2A_2$ state and excited $\widetilde{A}^2A_1$ and $\widetilde{B}^2A_1$ states of H_2B_7 calculated with eight totally symmetric vibrational modes (panel a) and eight totally symmetric modes along with one coupling mode, via $\widetilde{X}$-$\widetilde{A}$ in panels b, and c, and via $\widetilde{X}$-$\widetilde{B}$ coupling in panel d, respectively. The coupled $\widetilde{A}$-$\widetilde{B}$ states spectrum is shown in panel e. The theoretical stick spectrum in each case is convoluted with a Lorentzian function of 20 meV FWHM to calculate the spectral envelope (see the text for details). The intensity in arbitary units is plotted as a function of the energy of the vibronic levels of $\widetilde{X}^2A_2$ state. The zero of energy corresponds to the equilibrium minimum of the ground state of the neutral molecule.

cm^{-1} and it forms combination peaks with ν_4 and ν_2 at ∼1322 cm^{-1} and ∼1760 cm^{-1}, respectively. The wavefunction density plots of these vibronic energy levels are shown in panels a, b and c of Fig. 6.5. A quenching of the excitation of ν_8 vibrational mode is found here due to the inter-state ($\widetilde{X}$-$\widetilde{A}$) coupling via ν_{10} vibrational mode. Similarly, the reduced dimensional results of Fig. 6.3c indicates the excitation of ν_{11} fundamental at ∼282 cm^{-1} and its combination with ν_4 and ν_2 vibrational modes at ∼1205 cm^{-1} and ∼1643 cm^{-1}, respectively. One quantum excitation of both ν_6 and ν_{11} vibrational modes (a combination peak) is also observed at ∼1015 cm^{-1}. The wavefunction density plots of the excited levels of vibrational modes of ν_{11}, ν_6 and ν_2 are shown in panels d, e and f of Fig. 6.5, respectively. These reduced dimensional calculations indicate quenching of the excitation of ν_8 vibrational mode upon inclusion $\widetilde{X}$-$\widetilde{A}$ coupling. In case of $\widetilde{X}$-$\widetilde{B}$ coupled states only ν_{10} vibrational mode is active and the effect of $\widetilde{X}$-$\widetilde{B}$ coupling via this mode on both $\widetilde{X}$ and $\widetilde{B}$ states is shown in panel d of Fig. 6.3. The fundamentals of ν_{10}, ν_7, ν_4, ν_3 and ν_2 vibrational modes in spectrum Fig. 6.3d are found at ∼375 cm^{-1}, ∼595 cm^{-1}, ∼923 cm^{-1}, ∼1247 cm^{-1} and ∼1361 cm^{-1}, respectively. This vibrational mode (ν_{10}) forms combination peaks with ν_7, ν_4, ν_3 and ν_4 vibrational modes at ∼970 cm^{-1}, ∼1298 cm^{-1}, ∼1623 cm^{-1} and ∼1737 cm^{-1}. The wavefuntion density plots of the combination peaks of ν_{10} with the ν_7, ν_3 and ν_2 are shown in panels j, k and l of Fig. 6.5, respectively. In conclusion, one can say that the effect of totally symetric modes on the $\widetilde{X}$ state dynamics are reduced by the coupling vibrational modes. The coupling modes form combination peaks mainly with the ν_2 and ν_4 totally symmetric modes. In some cases, these coupling modes also form combination peaks with the ν_3, ν_6 and ν_7 totally symmetric modes. The activity of ν_8 vibrational mode is quenched by all coupling vibrational mode.

Effect of $\widetilde{X}$-$\widetilde{A}$, $\widetilde{X}$-$\widetilde{B}$ and $\widetilde{A}$-$\widetilde{B}$ inter-state coupling on the uncoupled $\widetilde{A}$ and $\widetilde{B}$ state dynamics

The uncoupled state spectra of $\widetilde{A}$ and $\widetilde{B}$ states of H_2B_7 shown in panel a of Fig. 6.3 reveal that the location of the fundamental of ν_8, ν_6, ν_7, ν_5, ν_4, ν_3, ν_2 and ν_1 at ∼387 cm^{-1}, ∼408 cm^{-1}, ∼537 cm^{-1}, ∼669 cm^{-1}, ∼815 cm^{-1}, ∼1148 cm^{-1}, ∼1199 cm^{-1} and ∼3183 cm^{-1}, respectively in the $\widetilde{A}$ state spectrum. The 0_0^0 line of the $\widetilde{A}$ state occurs at its adiabatic detachment position at ∼4.56 eV. Whereas, the fundamental of ν_8, ν_7, ν_4, ν_6, ν_5, ν_3, ν_2 and ν_1 appears at ∼403 cm^{-1}, ∼649 cm^{-1}, ∼967 cm^{-1}, ∼1044 cm^{-1}, ∼1091 cm^{-1}, ∼1334 cm^{-1}, ∼1487 cm^{-1} and ∼2830 cm^{-1}, respectively, in the $\widetilde{B}$ state spectrum. The assignment of these vibrational progressions are confirmed by block-improved releaxation calculations [36–38] of the vibronic wavefunctions. A dominant progression of ν_7 vibrational mode is observed in the both the states, which is in good agreement with the Huang-Rhys parameters given in Table 6.5. On the other hand, a moderate exciation of ν_8, ν_6 and ν_1 vibrational modes in $\widetilde{A}$ state and ν_4, ν_3 and ν_1 vibrational modes in $\widetilde{B}$ state is observed. The vibronic wavefunction density plots of the first overtone of ν_8 and ν_7, combination peaks between ν_7-ν_8, ν_6-ν_7 and ν_5-ν_8 and the fundamental of ν_2 are found in the uncoupled $\widetilde{A}$ state dynamics at ∼773 cm^{-1}, ∼1076 cm^{-1}, ∼924 cm^{-1}, ∼945 cm^{-1}, ∼1056 cm^{-1} and ∼1199 cm^{-1}, respectively, are shown in

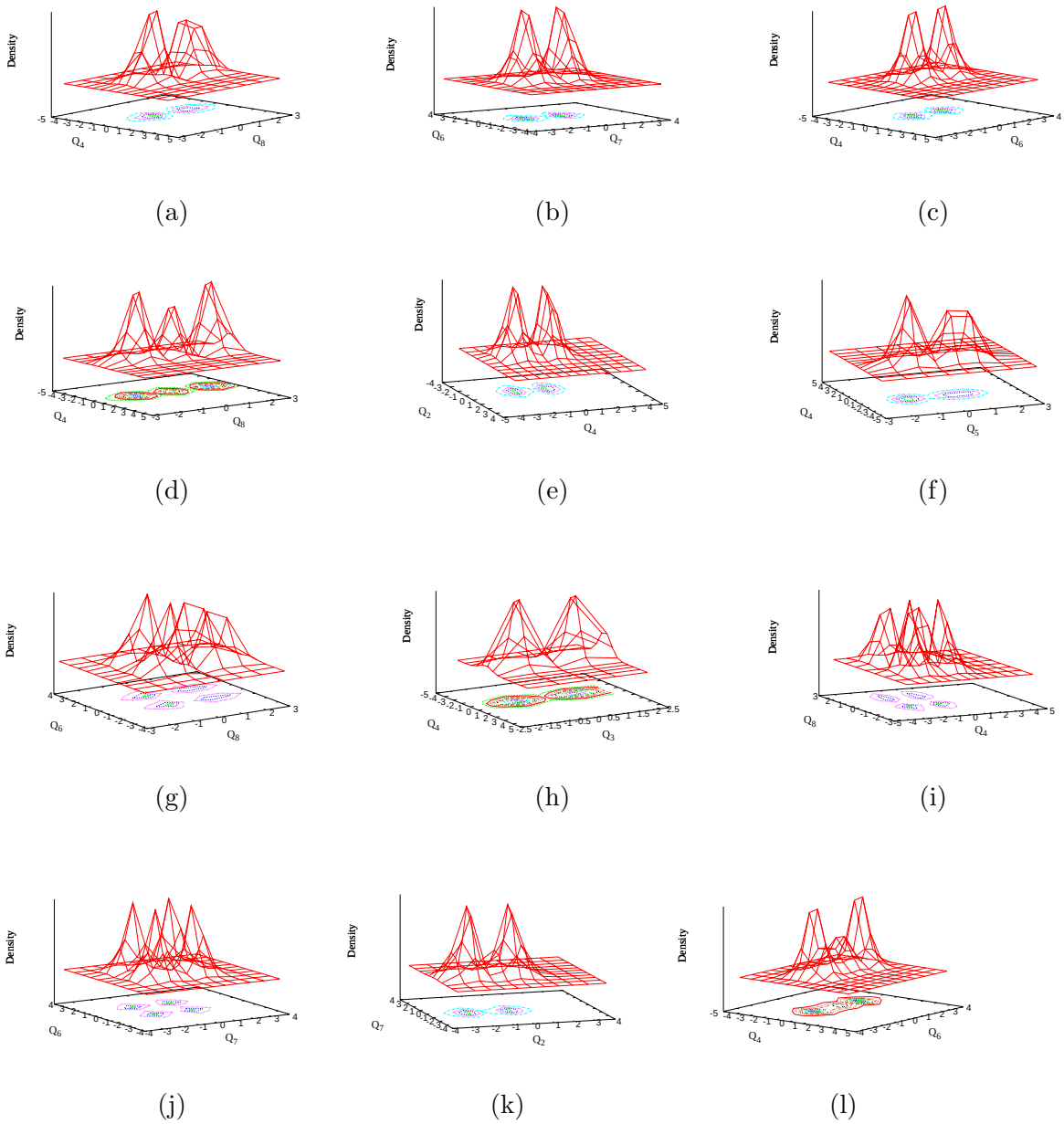

Figure 6.4: Assignments of fundamental of ν_8, ν_7, ν_6, ν_4, ν_5, ν_3 and ν_2 vibrational modes on the ground state dynamics of H_2B_7 are shown in panels a, b, c, e, f, h and k, respectively. First overtone of ν_8 and ν_6 vibrational modes and the combination band between ν_6-ν_8, ν_4-ν_8 and ν_6-ν_7 vibrational modes on the ground state dynamics of H_2B_7 are also shown in panels d, l, g, i and j, respectively, following the reduced dimensional calculations as mentioned in section 6.3.4.

panels a, e, b, c, d and f of Fig. 6.6. Similarly in the uncoupled $\widetilde{B}$ state dynamcs, the first overtone of ν_7 and ν_4, fundamental of ν_3 and combination peaks between ν_4-ν_7, ν_3-ν_7 and ν_3-ν_4 are found at ∼1299 cm^{-1}, ∼1934 cm^{-1}, ∼1334 cm^{-1}, ∼1616 cm^{-1}, ∼1984 cm^{-1} and ∼2301 cm^{-1}, respectively. The wavefunction desity plots of these vibrational progressions are shown in panels g, j, h, i, k and l, respectively, in Fig. 6.6.

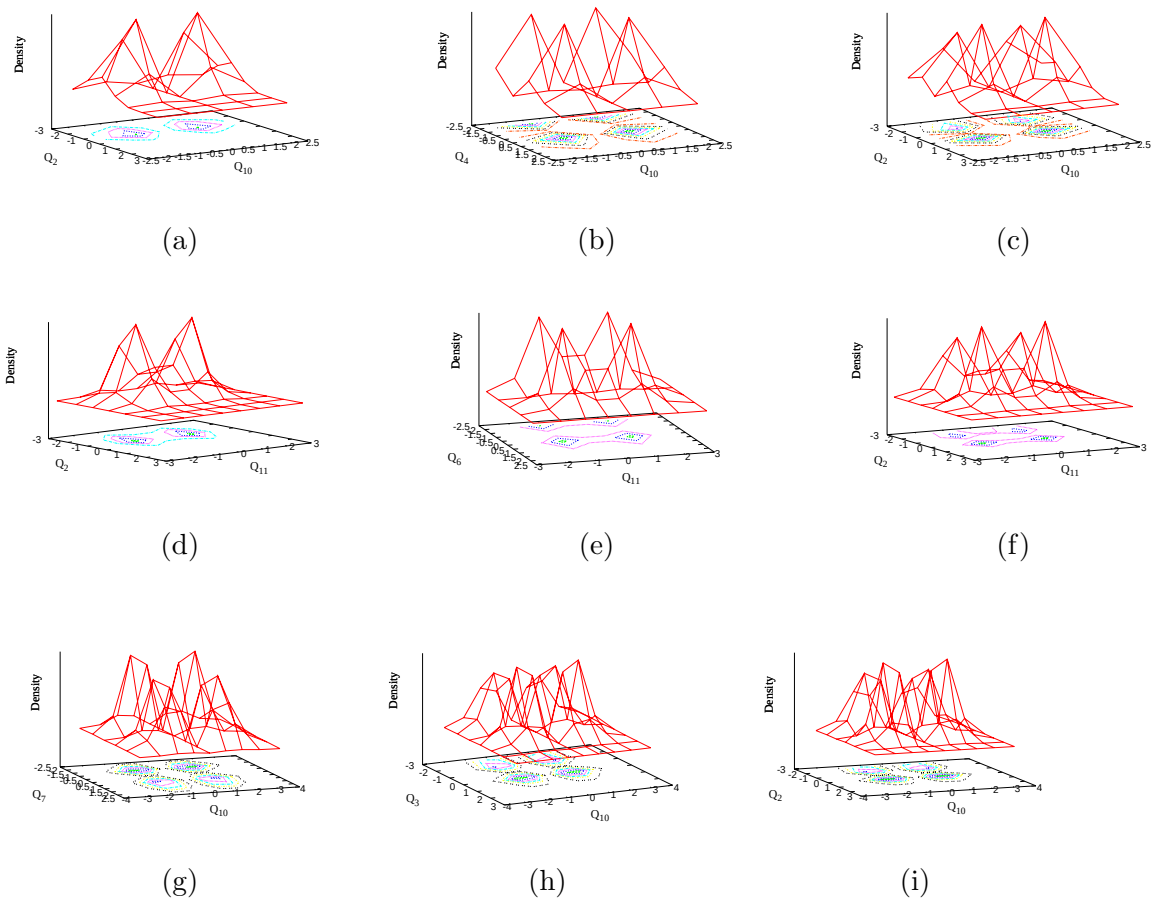

Figure 6.5: Assignments of fundamental of ν_{10} and its combination peaks with ν_4 and ν_2 vibrational modes on the $\widetilde{X}$ state dynamics coupled with $\widetilde{A}$ state (through ν_{10} vibrational mode) are shown in panels a, b and c, respectively. Similarly the assignment of the fundamental of ν_{11} and its combination peaks with ν_6 and ν_2 vibrational modes on the $\widetilde{X}$ state dynamics coupled with $\widetilde{A}$ state (through ν_{11} vibrational mode) are shown in panels d, e and f, respectively. The combination peaks between ν_{10} and ν_7, ν_3 and ν_2 on the $\widetilde{X}$ state dynamics coupled with $\widetilde{B}$ state (through ν_{10} vibrational mode) are shown in panels j, k and l, respectively.

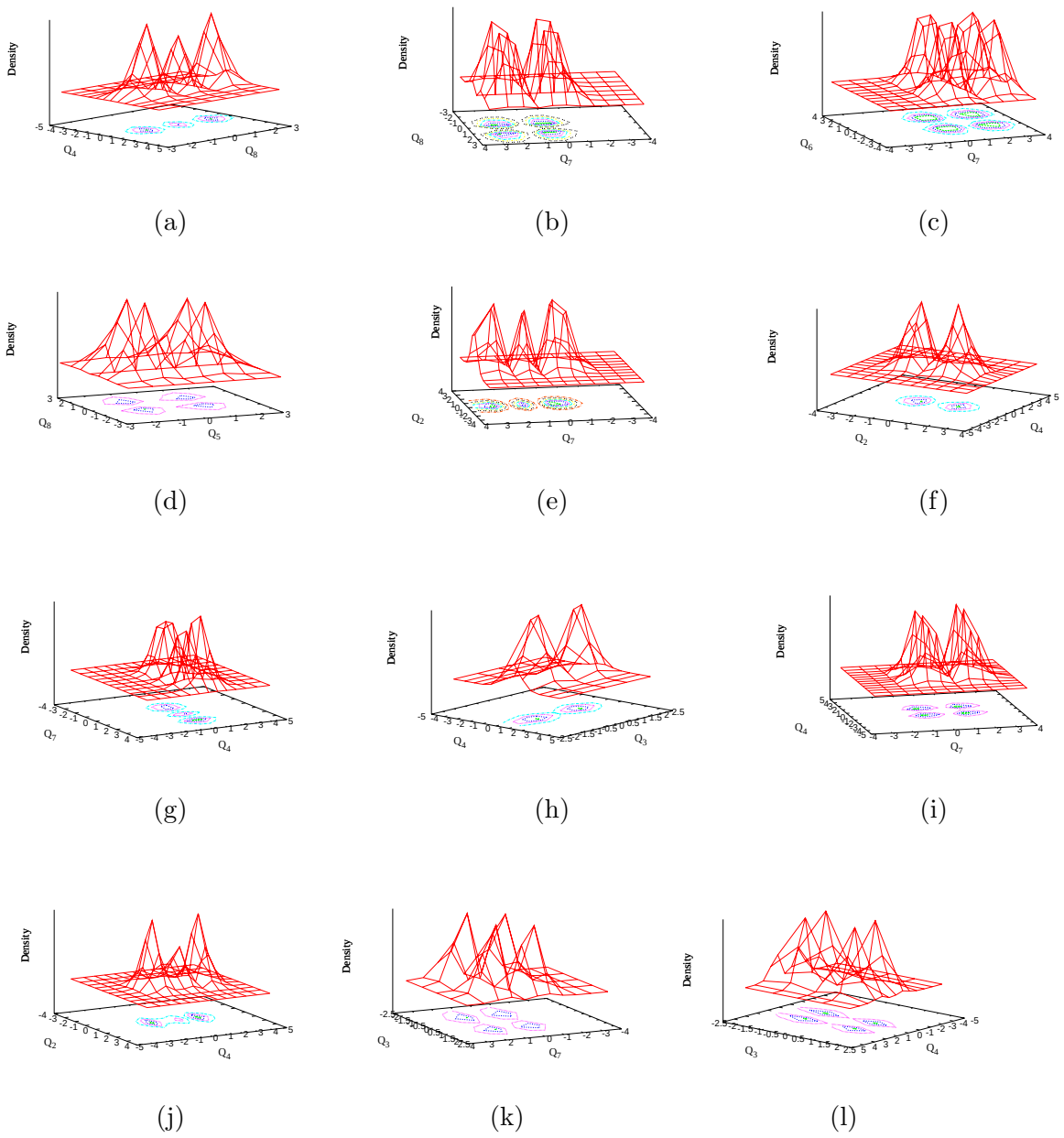

Figure 6.6: Assignments of first overtone of ν_8 and ν_7, combnation peaks between ν_7-ν_8, ν_6-ν_7 and ν_5-ν_8 and fundamental of ν_2 vibrational modes on the uncoupled $\widetilde{A}$ dynamics of H_2B_7 are shown in panels a, e, b, c, d and f respectively. Assignments of first overtone of ν_7 and ν_4, fundamental of ν_3 and combnation peaks between ν_4-ν_7, ν_3-ν_7 and ν_3-ν_4 vibrational modes on the uncoupled $\widetilde{B}$ dynamics of H_2B_7 are shown in panels g, j, h, i, k and l respectively.

The effect of $\widetilde{X}$-$\widetilde{A}$ interstate coupling through ν_{10} and ν_{11} vibrational modes on the $\widetilde{A}$ state dynamics is shown in panels b and c of Fig. 6.3. The consequences of this interstate coupling on the spectra is already discussed in the previous section. Now, we only focus on the results of these calculations. The fundamental excitation of the participated coupling vibrational modes, ν_{10} and ν_{11}, are found at ∼399 cm^{-1} and ∼282 cm^{-1} in panels b and c of Fig. 6.3. The relative intensities of the ν_5, ν_4 and ν_2 mode is decreased, whereas the excitation of the ν_8 and ν_6 vibrational modes are quenched due to the interstate coupling between $\widetilde{X}$ and $\widetilde{A}$ electronic states via ν_{10} vibrational mode. On the other hand, a noticeable excitation of ν_7 and ν_3 vibrational modes is observed and these modes form combination peaks with the coupling ν_{10} vibrational mode in the $\widetilde{X}$-$\widetilde{A}$ coupled state dynamics. Similar analysis with ν_{11} vibrational mode shows a quenching of the excitation of ν_8 vibrational mode and combination peaks of ν_{11} vibrational mode with the other totally symmetric modes. Previously it is noticed that the excitation of ν_8 vibrational mode is quenched in both $\widetilde{X}$ and $\widetilde{A}$ state in the coupled states results. In case of $\widetilde{X}$-$\widetilde{B}$ coupled states dynamics via ν_{10} vibrational mode, a noticeable excitation of ν_8 vibrational mode is observed in the $\widetilde{B}$ state. The other totally symmetric vibrational modes are also active in the $\widetilde{B}$ state in the $\widetilde{X}$-$\widetilde{B}$ coupled states dynamics. Both the $\widetilde{A}$ and $\widetilde{B}$ states possess same spatial symmtery $^2A_1$. As a result of this a pure electronic coupling between these two states exists, which is very rare in the literature. We calculated this electronic coupling by using multiconfiguration quasidegenerate perterbation theory (MCQDPT) with cc-pVTZ basis set. Gamess programing package [55] is used for this purpose. The value of this electronic coupling is ∼67 cm^{-1} (0.0084 eV). As both states has the same spacial symmetry, totally symmetric vibrational modes (ν_1-ν_8) take part in the interstate coupling. The fundamental progression of the ν_8, ν_7, ν_4, ν_3, and ν_2 are found at ∼396 cm^{-1}, ∼706 cm^{-1}, ∼856 cm^{-1}, ∼1211 cm^{-1} and ∼1276 cm^{-1} in the $\widetilde{A}$-$\widetilde{B}$ coupled state dynamics. The fundamentals of the ν_5 and ν_6 vibrational modes are found with very less intensity, which is in accordance with their intrastate excitation strength (cf. Table 6.5), whereas due to their higher interstate coupling activity (cf. Table 6.7), a frequency shift of the other vibrational modes is observed compared to the uncoupled spectrum. Several combination peaks correspond simultaneous excitations of ν_7-ν_8, ν_4-ν_8, ν_4-ν_7, ν_3-ν_8, ν_3-ν_2, ν_3-ν_7, ν_2-ν_7, ν_3-ν_4, ν_2-ν_4 and ν_2-ν_3 are found at ∼1103 cm^{-1}, ∼1250 cm^{-1}, ∼1561 cm^{-1}, ∼1606 cm^{-1}, ∼1670 cm^{-1}, ∼1916 cm^{-1}, ∼1982 cm^{-1}, ∼2069 cm^{-1}, ∼2129 cm^{-1} and ∼2481 cm^{-1}.

Overall $\widetilde{X}$-$\widetilde{A}$-$\widetilde{B}$ coupled states spectra

The vibronic spectrum of the $\widetilde{X}^2A_2$-$\widetilde{A}^2A_1$-$\widetilde{B}^2A_1$ coupled states of H_2B_7 is calculated using three-states Hamiltonian (given in the section 6.2.1) with relevant vibrational modes (ν_1-ν_{11}) and the CASSCF-MRCI parameter set given in Tables 6.5,6.6 and 6.7 is shown in Fig. 6.7. In the latter, the experimental result of Wang and coworkers [20] is shown in panel a. Both the experimental recording at 193 nm and 266 nm photon are shown in panel a with little smoothening. The theoretical results obtained by the wavepacket propagation method in the MCTDH framework [48] and the matrix diagonalization method are shown in panels b and c, respectively. It can be seen from Fig. 6.7 that the

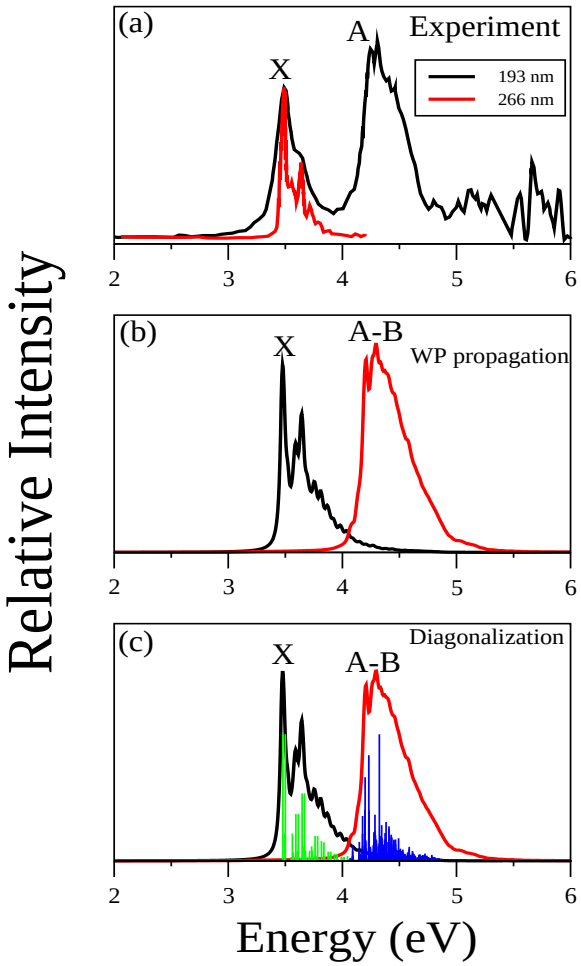

Figure 6.7: Spectrum generated due to the $\widetilde{X}$-$\widetilde{A}$-$\widetilde{B}$ coupled surface dynamics by time-dependent and time-independent quantum chemistry methods are shown in panel b and c, respectively. The experimental photoelectron spectrum of $H_2B_7^-$ is regenerated from Ref. [20] is shown in panel a. The relative intensity (in arbitary units) is plotted as a function of the energy (relative to the ground state of $H_2B_7^-$) of the final vibronic states.

results obtained by two different theoretical methods are consistent with each other and are in well accord with the envelopes recorded in the experiment. The numerical details of the matrix diagonalization and wavepacket propagation calculations are given in Table 6.9. The time autocorrelation function calculated during the wavepacket propagation is damped with an exponential function [$e^{(-t/\tau_r)}$, with τ_r = 33 fs] to generate the spectral envelope shown in panel b. The envelope in panel c is generated by convoluting the stick line spectrum of panel c with a Lorenzian function of ∼40 meV full width at the half maximum (FWHM). To facilitate the comparison with experiment, the origin 0_0^0 peak of the spectrum is placed at the adiabatic ionization energy of ∼3.49 eV estimated in the experiment of Wang et al. [20].

The low-energy part of the stick line spectrum of Fig. 6.7c corresponding to the vibronic structure of the $\widetilde{X}$ state is given in Table 6.10. Among the numerous stick lines, the assignments of some of intense lines are made in Table 6.10. The values of vibronic energy lines in Table 6.10 indicates that a little shift of energy locations of previously assigned peaks occured compared to uncoupled and reduce dimensional calculations (two-states-multi-modes) due to the incorporation of multi-states-multi-modes interaction. Several new energy lines are formed and some of the old energy lines are also diminished due this effect. As we discussed previously that the intensity of the fundamental of ν_8 is quenched by the coupling vibrational modes ν_{10} and ν_{11}. The near degenerate frequency values at the $\widetilde{X}$ state of H_2B_7 of ν_8 ($\sim$386 cm^{-1}), ν_{10} ($\sim$419 cm^{-1}) and ν_{11} ($\sim$304 cm^{-1}) and the inter-mode interaction between them may be the cause behind the quenching of fundamental intensity of ν_8 vibrational mode. On the other hand, when the frequency difference between the overtones of ν_8 and ν_{11} vibrational mode is increased, an intense peak of the first overtone of ν_8 is found at $\sim$770 cm^{-1}. Not only that, ν_8 forms the combination peaks with ν_{11} and ν_{10} at 1044 cm^{-1} and 1147 cm^{-1} from the 0_0^0 line. It can be seen from Table 6.10 that a little change of locations of the fundamental vibronic energy lines of totally symmetric modes (ν_1-ν_7) occurs compared to the uncoupled and two-states spectra (cf. panels a, b, c and d og Fig. 6.3) due to the multi-states-multi-modes effect. The most probable reason behind this is that the totally symmetric modes do not partcipate in the inter-state coupling between $\widetilde{X}$-$\widetilde{A}$ and $\widetilde{X}$-$\widetilde{B}$ states. Whereas, a noticeable change of vibronic energy locations of the fundamentals of ν_{10} and ν_{11} vibrational modes compared to two-states spectra shown in panels b, c and d of Fig. 6.3 are observed in Fig. 6.7c and those lines are given in Table 6.10. The participation of these vibrational modes in inter-state, $\widetilde{X}$-$\widetilde{A}$ and $\widetilde{X}$-$\widetilde{B}$, coupling is the reason behind the complex vibrational progression of these vibrational modes. It can be seen from Table 6.10 that the coupling vibrational modes ν_{10} and ν_{11} form combination peaks among themselves at $\sim$677 cm^{-1}, as well as with the fundamental and first over tone of totally symmetric modes at $\sim$865 cm^{-1}, $\sim$980 cm^{-1}, ... The totally symmetric vibrational modes also form combination peaks among themselves. All the probable assignments of fundamental, overtone and combination peaks in the energy range 0-2750 cm^{-1} of the coupled $\widetilde{X}$-$\widetilde{A}$-$\widetilde{B}$ states spectrum are given in Table 6.10. The spectral assignment discussed above is confirmed by performing block-improved relaxation calculations [36–38] both in reduced dimensions and exploring the full-dimensions.

6.3.5 Adiabatic state population analysis on $\widetilde{X}$-$\widetilde{A}$-$\widetilde{B}$ coupled state dynamics

The decay and growth of adiabatic state populations on $\widetilde{X}$-$\widetilde{A}$-$\widetilde{B}$ coupled state dynamics are shown in Fig. 6.8. In panel a of Fig. 6.8, the electronic populations of $\widetilde{X}$, $\widetilde{A}$ and $\widetilde{B}$ states of H_2B_7 is shown, when the wavepacket is initially prepared on the $\widetilde{A}$ state. Whereas in panel b, the initial wavepacket is prepared on the $\widetilde{B}$ state. Since, the initial excitation occurs in diabatic states, that causes the starting diabatic population of the

Table 6.10: Energetically low-lying vibronic energy levels (in cm^{-1}) for the $\widetilde{X}^2A_2$ electronic state of H_2B_7.

No.	Vibronic energy level	Assignment	No.	Vibronic energy level	Assignment
1	0.0	0	24	1361	ν_2
2	276	ν_{11}	25	1408	$\nu_5+\nu_{10}$
3	401	ν_{10}	26	1450	$2\nu_6$
4	553	$2\nu_{11}$	27	1517	$\nu_4+\nu_7$
5	594	ν_7	28	1588	$2\nu_7+\nu_{10}$
6	677	$\nu_{10}+\nu_{11}$	29	1600	$\nu_5+\nu_7$
7	727	ν_6	30	1650	$\nu_4+\nu_6$
8	770	$2\nu_8$	31	1683	$\nu_6+\nu_9$
9	804	$2\nu_{10}$	32	1727	$\nu_5+\nu_6$; $2\nu_6+\nu_{11}$
10	865	$\nu_7+\nu_{11}$	33	1825	$2\nu_4$
11	923	ν_4	34	1841	$\nu_3+\nu_7$
12	955	ν_9	35	1930	$\nu_4+\nu_5$
13	980	$\nu_7+\nu_{10}$	36	1955	$\nu_2+\nu_7$
14	1008	ν_5	37	1975	$\nu_3+\nu_6$
15	1044	$2\nu_8+\nu_{11}$	38	2014	$2\nu_5$
16	1106	$\nu_6+\nu_{10}$	39	2088	$\nu_2+\nu_6$
17	1147	$2\nu_8+\nu_{10}$	40	2253	$\nu_3+\nu_5$
18	1189	$2\nu_7$	41	2370	$\nu_2+\nu_5$
19	1232	$\nu_9+\nu_{11}$	42	2485	$2\nu_3$
20	1247	ν_3	43	2608	$\nu_2+\nu_3$
21	1285	$\nu_5+\nu_{11}$	44	2722	$2\nu_2$
22	1322	$\nu_4+\nu_{10}$; $\nu_6+\nu_7$	45	3210	ν_1
23	1355	$\nu_9+\nu_{10}$			

prepared state is 1.0. While, an adiabatic state is the admixture of diabatic states, that is why the initial adiabatic population of the prepared state is less than 1.0. An initial increase of population of the $\widetilde{A}$ state when the initial wavepacket is prepared in the $\widetilde{A}$ state can be seen from panel a. The data given in Table 6.8 reveal that the minimum of the $\widetilde{A}$-$\widetilde{B}$ CI is lower than the minmum of the $\widetilde{X}$-$\widetilde{A}$ CI and the $\widetilde{A}$-$\widetilde{B}$ CI and minimum of $\widetilde{B}$ state is energetically quasi-degenerate. This drives the transfer of $\widetilde{B}$ state population to the $\widetilde{A}$ state before initiating the transfer of $\widetilde{A}$ state population to $\widetilde{X}$ state via $\widetilde{X}$-$\widetilde{A}$ CI. After a certain induction period ($\sim$15 fs), the wavepacket prepared on $\widetilde{A}$ state accesses the $\widetilde{X}$-$\widetilde{A}$ CIs, which leads to an increase of electronic population of the $\widetilde{X}$ state. The non accessibility of the $\widetilde{X}$ state via $\widetilde{X}$-$\widetilde{A}$ CI, when the wavepacket is prepared in $\widetilde{A}$ state yields a structured envelope of the $\widetilde{X}$ state spectrum. Similarly, when the initial wavepacket is prepared on the $\widetilde{B}$ state, an instantaneous decrease of electronic population from $\widetilde{B}$ state to $\widetilde{A}$ state is observed. The reason behind this is the existance

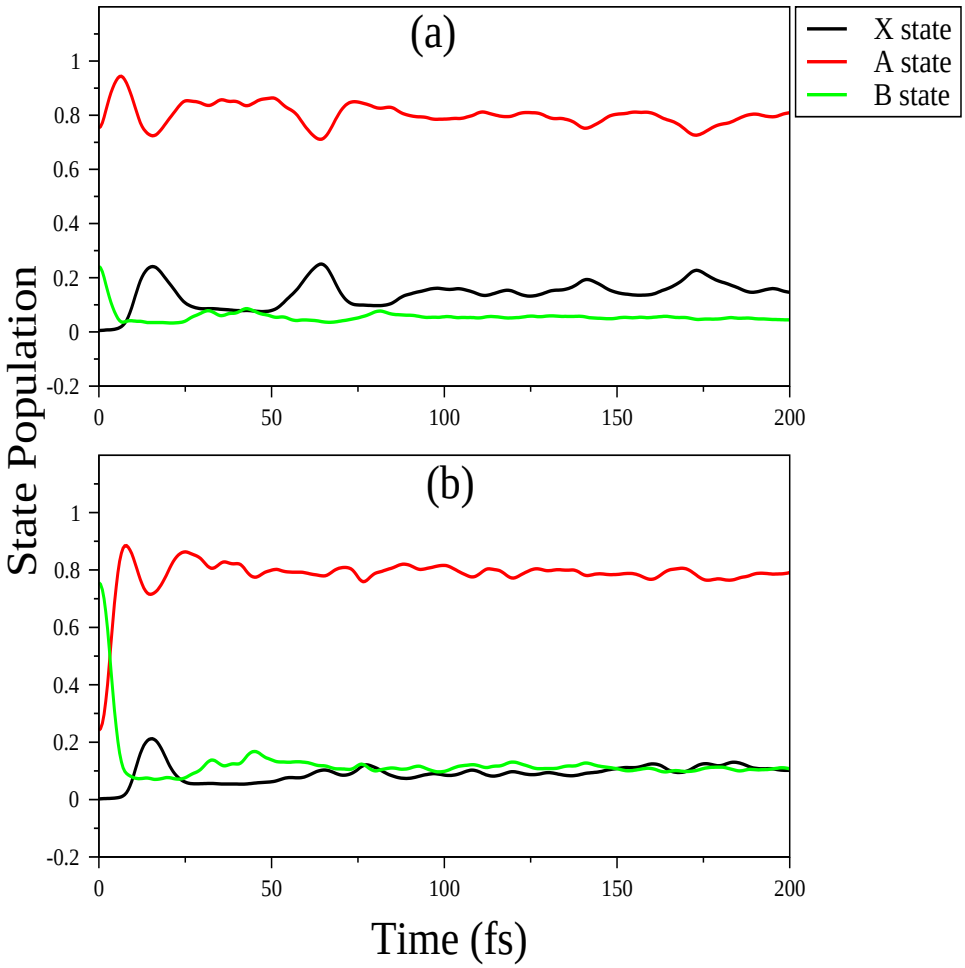

Figure 6.8: Adiabatic electronic population dynamics on the $\widetilde{X}$-$\widetilde{A}$-$\widetilde{B}$ coupled electronic states of H_2B_7. The adiabatic population of different states are shown by preparing the initial wave packet on the $\widetilde{A}$ and $\widetilde{B}$ states, in panel a and b, respectively.

of quasi-degeneracy between the $\widetilde{A}$-$\widetilde{B}$ CI (∼4.482 eV) and the energy minimum of the $\widetilde{B}$ state (∼4.480 eV). This quasi-degeneracy makes the radiationless transition from $\widetilde{B}$ to $\widetilde{A}$ state faster and the structure of the second band of H_2B_7 becomes broad.

6.3.6 The combined effect of $\widetilde{C}$ and $\widetilde{D}$ electronic states on the the $\widetilde{A}$-$\widetilde{B}$ coupled state spectrum

The above discussion mainly deals with the $\widetilde{X}$-$\widetilde{A}$-$\widetilde{B}$-coupled states dynamics and the theoretical results nicely reproduce the experimental spectra of Ref. [20]. The study becomes incomplete without the discussion of the effect of $\widetilde{C}$ and $\widetilde{D}$ states on the $\widetilde{X}$-$\widetilde{A}$-$\widetilde{B}$ coupled states dynamics of H_2B_7. A slight disagreement regarding the width and kincks (at ∼4.39 eV and ∼4.48 eV) of the second photoelectron band of $H_2B_7^-$ is found

in panels a and b of Fig. 6.7. This indicates that a certain impact of $\widetilde{A}$-$\widetilde{C}$, $\widetilde{A}$-$\widetilde{D}$, $\widetilde{B}$-$\widetilde{C}$ and $\widetilde{B}$-$\widetilde{D}$ interstate coupling might be present in the $\widetilde{X}$-$\widetilde{A}$-$\widetilde{B}$-coupled states dynamics of H_2B_7. The VDEs presented in Table 6.4 and the PESs presented in Fig. 6.2 indicate that the ground state ($\widetilde{X}$) is well separated from the $\widetilde{C}$ (vertically ∼2.19 eV) and $\widetilde{D}$ (vertically ∼2.36 eV) electronic states. As a result, the energetic location of the $\widetilde{X}$-$\widetilde{C}$ and $\widetilde{X}$-$\widetilde{D}$ CIs (cf. Table 6.8) is far above from the energy minimum of $\widetilde{C}$ and $\widetilde{D}$ state, respectively. Therefore, it is expected that the $\widetilde{X}$-$\widetilde{C}$ and $\widetilde{X}$-$\widetilde{D}$ interstate couplings have very less impact on the $\widetilde{X}$ state dynamics of H_2B_7. On the other hand, energetic proximity between the $\widetilde{A}$, $\widetilde{B}$, $\widetilde{C}$ and $\widetilde{D}$ electronic states is found (cf. Table 6.4 and Fig. 6.2) and the energetic location of the $\widetilde{A}$-$\widetilde{C}$, $\widetilde{B}$-$\widetilde{C}$ and $\widetilde{A}$-$\widetilde{D}$, $\widetilde{B}$-$\widetilde{D}$ CIs (cf. Table 6.8) is near to the energy minimum of $\widetilde{C}$ and $\widetilde{D}$ state, respectively. A vetting of Table 6.8 indicates the presence of quasi-degeneracy between the $\widetilde{B}$-$\widetilde{D}$ CI (∼5.335 eV) and the energy minimum of $\widetilde{D}$ state (∼5.316 eV), which induces a electronic population flow from $\widetilde{D}$ state to $\widetilde{B}$ state. Hence, an increment of natural band width of the seond photoelectron band of $H_2B_7^-$ is expected in this section compared to the $\widetilde{X}$-$\widetilde{A}$-$\widetilde{B}$-coupled states dynamics described in Section 6.3.4. The result of time-dependent nuclear dynamics calculations on the $\widetilde{X}$-$\widetilde{A}$-$\widetilde{B}$-$\widetilde{C}$-$\widetilde{D}$ coupled surfaces of H_2B_7 considering the above speculation is presented in Fig. 6.9. It is found that theoretical result (mainly second band) presented in Fig. 6.9 reproduces a better experimental [20] finding presented in panel a of Fig. 6.7 compared to the theoretical result presented in panel b of Fig. 6.7. The ground state spectrum presented in Fig. 6.9 indicates no structural change compared to the panel b of Fig. 6.7. This validate our speculation regarding the interstate effect between $\widetilde{X}$-$\widetilde{C}$ and $\widetilde{X}$-$\widetilde{D}$ states discussed in the earlier part of this section. Whereas, the second band structure of the Fig. 6.9 indicates clear knicks at ∼4.39 eV and ∼4.48 eV energy levels, which are improper in the second band of panel b of Fig. 6.7. A little increment of the width of the second band is also encountered by the inclusion of $\widetilde{A}$-$\widetilde{C}$, $\widetilde{A}$-$\widetilde{D}$, $\widetilde{B}$-$\widetilde{C}$ and $\widetilde{B}$-$\widetilde{D}$ interstate couplings in the $\widetilde{X}$-$\widetilde{A}$-$\widetilde{B}$-$\widetilde{C}$-$\widetilde{D}$ coupled state dynamics of H_2B_7. Overall, the $\widetilde{X}$-$\widetilde{A}$-$\widetilde{B}$-$\widetilde{C}$-$\widetilde{D}$ coupled state dynamics (cf. Fig. 6.9) provides better explanation of the experimental observations [20] than the $\widetilde{X}$-$\widetilde{A}$-$\widetilde{B}$ coupled state dynamics presented in the panel b of Fig. 6.7.

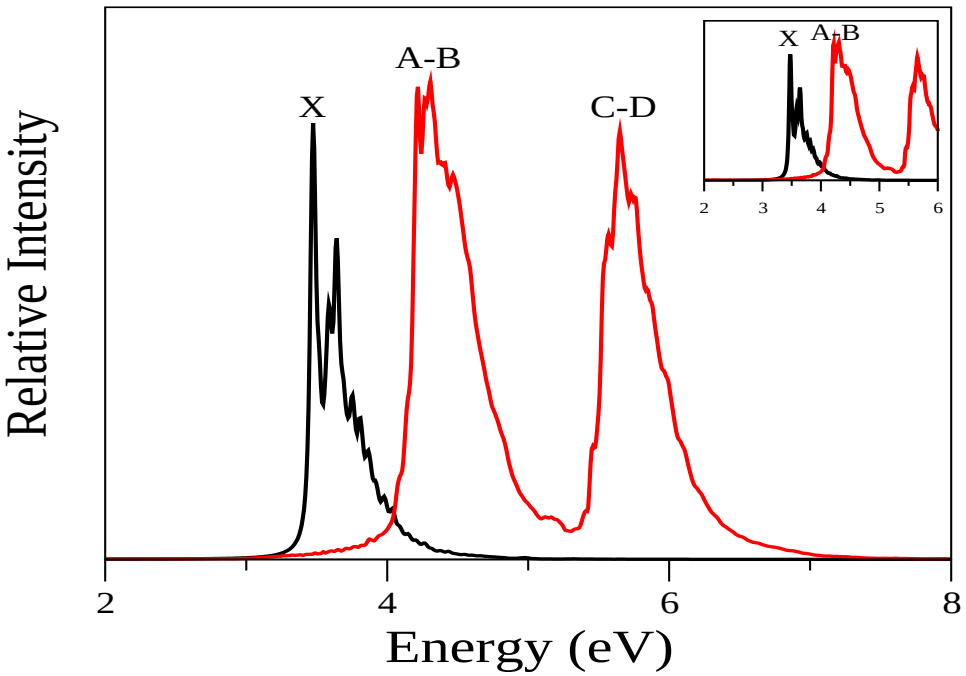

Figure 6.9: Spectrum generated due to the $\widetilde{X}$-$\widetilde{A}$-$\widetilde{B}$-$\widetilde{C}$-$\widetilde{D}$ coupled surface dynamics by time-dependent quantum chemistry method is shown. The relative intensity (in arbitary units) is plotted as a function of the energy (relative to the ground state of H_2B_7) of the final vibronic states. The combined effect of $\widetilde{C}$ and $\widetilde{D}$ electronic states on the $\widetilde{A}$-$\widetilde{B}$ coupled state spectrum is shown by the enlarge view of the spectrum in the inset of the figure.

6.4 Summary and Conclusions

A detailed theoretical study of photodetachment spectroscopy of $H_2B_7^-$ cluster is presented in this chapter. The study is motivated by the non availability of the detailed quantum dynamical study on this system. The topography of the PESs are analized by examining the various stationary points on them and quantum dynamics on the coupled electronic states are performed based on the estimated Hamiltonian parameters (cf. Tables 6.5, 6.6, 6.7). The block-improved relaxation method is employed to find out the role of vibrational modes onto the coupled-states dynamics. All these calculations are based on the extensive ab initio quantum chemistry calculations of the relevant electronic potential energy surfaces of the neutral H_2B_7 cluster in the normal coordinate range of -5.0≤**Q**≤5.0 and time-dependent and time-independent quantum dynamical calculations. A 5×5 diabatic Hamiltonian is constructed in normal coordinate representation and the Hamiltonian parameters are estimated by fitting the adiabatic form of this Hamiltonian to the *ab initio* calculated energy values. Analysis shows that the nuclear dynamics on the $\widetilde{X}$, $\widetilde{A}$ and $\widetilde{B}$ states of $H_2B_7^-$ are correlated with each other. The intensity of the totally symmetric vibrational modes are reduced by the incorporation of coupling vibrational modes via $\widetilde{X}$-$\widetilde{A}$ and $\widetilde{X}$-$\widetilde{B}$ inter-state coupling and spectrum of $\widetilde{X}$ becomes broader than the uncoupled spectrum of $\widetilde{X}$ due to this nonadiabatic effects. It is also found that coupling modes (ν_{10} and ν_{11}) form combination peaks with ν_2, ν_3, ν_4, ν_6 and ν_7 totally symmetric vibrational modes in the $\widetilde{X}$ state dynamics of H_2B_7. On the other hand, the activity of ν_8 vibrational mode is quenched in the $\widetilde{X}$ state dynamics of H_2B_7. The structure of the second band of photodetachment spectrum of $H_2B_7^-$ represents a composite vibronic structure of the $\widetilde{A}$ and $\widetilde{B}$ states. A near degenerate VDEs of $\widetilde{A}$ and $\widetilde{B}$ and a quasi-degeneracy between the $\widetilde{A}$-$\widetilde{B}$ CI and minimum of $\widetilde{B}$ state makes the second band of $H_2B_7^-$ more diffuse and broader compared to its first band. A detailed analysis indicates that the actvity of ν_6 and ν_8 totally symmetric vibrational modes is quenched in the dynamics of the $\widetilde{A}$ state via $\widetilde{X}$-$\widetilde{A}$ inter-state coupling through ν_{10} vibrational mode. A noticeable excitation of ν_8 vibrational mode is observed in the $\widetilde{B}$ state dynamics via $\widetilde{X}$-$\widetilde{B}$ inter-state coupling through same vibrational mode. In case of $\widetilde{A}$-$\widetilde{B}$ inter-state coupling, a constant pure electronic coupling arises, which is very rare in the literature. We have calculated this coupling (∼67 cm^{-1}) by using diabatization scheme and multiconfiguration quasidegenerate perturabation theory. The totally symmetric vibrational modes play a dual role of tunning and coupling vibrational modes on the $\widetilde{A}$-$\widetilde{B}$ coupled state dynamics. As a result, a frequency shift of the fundamentals, overtones and combination peaks of these modes is observed when compared with the uncoupled spectrum of $\widetilde{A}$ and $\widetilde{B}$ states. The overall theoretical spectra, generated in the $\widetilde{X}$-$\widetilde{A}$-$\widetilde{B}$ coupled state dynamics via time-dependent (cf. panel b of Fig. 6.7) and time-independent (cf. panel c of Fig. 6.7) quantum mechanical approaches, nicely reproduce the experimental photodetachment spectrum of $H_2B_7^-$ (shown in panel a of Fig. 6.7).

Bibliography

[1] H. Kato, K. Yamashita and K. Morokuma, Chem. Phys. Lett. **190**, 361 (1992).

[2] I. Boustani, Int. J. Quantum Chem. **52**, 1081 (1994).

[3] A. Ricca and C. W. Bauschlicher, Jr., Chem. Phys. **208**, 233 (1996).

[4] I. Boustani, Phys. Rev. B. **55**, 16426 (1997).

[5] H. -J. Zhai, L. S. Wang, A. N. Alexandrova, A. I. Boldyrev, and V. G. Zakrzewski, J. Phys. Chem. A **107**, 9319.(2003).

[6] H.-J. Zhai, L. S. Wang, A. N. Alexandrova, and A. I. Boldyrev, J. Chem. Phys. **117**, 7917 (2002).

[7] A. N. Alexandrova, A. I. Boldyrev, H.-J. Zhai, L. S. Wang, E. Steiner, and P. W. Fowler, J. Phys. Chem. A **107**, 1359 (2003).

[8] H.-J Zhai, L. S. Wang, A. N. Alexandrova, and A. I. Boldyrev, J. Phys. Chem. A **108**, 3509 (2004).

[9] H.-J. Zhai, A. N. Alexandrova, K. A. Birch, A. I. Boldyrev, and L. S. Wang, Angew. Chem., Int. Ed. Eng. **42**, 6004 (2003).

[10] H.-J. Zhai, B. Kiran, J. Li, and L. S. Wang, Nat. Mater. **2**, 827 (2003).

[11] A. P. Sergeeva, D. Yu. Zubarev, H.-J Zhai, A. I. Boldyrev, and L. S. Wang, J. Am. Chem. Soc. **130**, 7244 (2008).

[12] A. P. Sergeeva, B. B. Averkiev, H.-J. Zhai, A. I. Boldyrev, and L. S. Wang, J. Chem. Phys. **134**, 224304 (2011).

[13] W. Huang, A. P. Sergeeva, H.-J Zhai, B. B. Averkiev, L. S. Wang, and A. I. Boldyrev, Nat. Chem. **2**, 202 (2010).

[14] B. Kiran, S. Bulusu, H.J Zhai, S. Yoo, X. C. Zeng, and L.-S. Wang, Proc. Natl. Acad. Sci. U.S.A. **102**, 961 (2005).

[15] Z. A. Piazza, W.-L Li, C. Romanescu, A. P. Sergeeva, L. S. Wang, and A. I. Boldyrev, J. Chem. Phys. **136,** 104310 (2012).

[16] A. P. Sergeeva, Z. A. Piazza, C. Romanescu, W.-L. Li, A. I. Boldyrev, and L. S. Wang, J. Am. Chem. Soc. **134**, 18065 (2012).

[17] I. A. Popov, Z. A. Piazza, W.-L. Li, L. S. Wang, and A. I. Boldyrev, J. Chem. Phys. **139**, 144307 (2013).

[18] A. N. Alexandrova, A. I. Boldyrev, H.-J. Zhai, and L. S. Wang, Coord. Chem. Rev. **250**, 2811 (2006).

[19] A. N. Alexandrova, E. Koyle and A. I. Boldyrev. J. Mol. Model. **12**, 569 (2006).

[20] W. Li, C. Romanescu, T. Jian and L. S. Wang. J. Am. Chem. Soc. **134**, 13228-13231 (2012).

[21] H. J Zhai, L. S. Wang, D. Y. Zubarev and A. I. Boldyrev, J. Phys. Chem. A. **110**, 5 (2006).

[22] L. Hanley, J. L. Whitten and S. L. Anderson. J. Phys. Chem. **92**, 5803 (1988).

[23] L. Hanley and S. L. Anderson. J. Phys. Chem. **91**, 5161 (1987).

[24] L. Hanley and S. L. Anderson J. Chem. Phys. **89**, 2848 (1988).

[25] P. A. Hintz, S. A. Ruatta and S. L. Anderson. J. Chem. Phys. **92**, 292 (1990).

[26] S. A. Ruatta, P. A. Hintz and S. L. Anderson. J. Chem. Phys. **94**, 2833 (1991).

[27] P. A. Hintz, M. B. Sowa, S. A. Ruatta and S. L. Anderson. J. Chem. Phys. **94**, 6446 (1991).

[28] S. J. L. Placa, P. A. Roland and J. J. Wynne. Chem. Phys. Lett. **190**, 163 (1992).

[29] V. Bonacic-Koutecky, P. Fantucci and J. Koutecky. Chem. Rev. **91**, 1035 (1991).

[30] A. K. Ray, I. A. Howard and K. M. Kanal. Phys. Rev. B. **45**, 14247 (1992).

[31] Z. X. Wang and P. v. R. Schleyer. Science. **292**, 2465 (2001).

[32] J. Chandrasekhar, E. D. Jemmis, P. v. R. Schleyer, Tetra-hedron Lett. **39**, 3707 (1979).

[33] A. N. Alexandrova, A. I. Boldyrev, H.-J. Zhai, and L. S. Wang, J. Phys. Chem. A. **108**, 3509 (2004).

[34] S. Rajagopala Reddy and S. Mahapatra, J. Chem. Phys. **136**, 024323 (2012).

[35] S. Rajagopala Reddy and S. Mahapatra, J. Chem. Phys. **140**, 084311 (2014).

[36] H.-D. Meyer, F. Le Quere, C. Leonard, and F. Gatti, Chem.Phys. **329**, 179 (2006).

[37] L. J. Doriol, F. Gatti, C. Iung, and H.-D. Meyer, J.Chem.Phys. **129**, 224109 (2008).

[38] R. Sarkar and S. Mahapatra, J. Phys. Chem. A. **120**, 3504 (2016).

[39] H. Köppel, W. Domcke, and L.S. Cederbaum, in Advances in Chemical Physics, edited by I. Prigogine and S.A. Rice (John Wiley and Sons, Inc. Hoboken, NJ, 2007), Vol. 57. doi:10.1002/9780470142813.ch2.

[40] L. S. Cederbaum, W. Domcke and H. Köppel, Chem. Phys. Lett. **33**, 319(1978).

[41] C. Lanczos. J. Res. Nat. Bur. Stand. **45**, 255 (1950).

[42] J. Cullum and R. Willoughby, Lanczos Algorithms for Large Symmetric Eigenvalue Problems (Birkhäuser, Boston, 1985), Vols. I and II.

[43] W. Domcke and H. Köppel, Encyclopedia of Computational Chemistry, P. V. R. Schleyer, Ed.; Wiley: New York, 1998, P. 3166.

[44] L. S. Cederbaum, W. Domcke, H. Köppel, and W. von Niessen, Chem. Phys. **26**, 169 (1977).

[45] H. -D. Meyer, U. Manthe, L. S. Cederbaum, Chem. Phys. Lett. **165**, 73 (1990).

[46] U. Manthe, H. -D. Meyer and L. S. Cederbaum, J. Chem. Phys. **97**, 3199 (1992).

[47] M. H. Beck, A. Jäckle, G. A. Worth and H. -D. Meyer, Phys. Rep. **324**, 1-105 (2000).

[48] G. A. Worth, M. H. Beck, A. Jäckle, and H.-D. Meyer, The mctdh package, Version 8.4, (2007), University of Heidelberg, Heidelberg, Geramny. See: http://mctdh.uni-hd.de.

[49] T. H. Dunning Jr., J. Chem. Phys. **90**, 1007 (1989).

[50] Gaussian 09, Revision B.01, M. J. Frisch, G. W. Trucks, H. B. Schlegel, G. E. Scuseria, M. A. Robb, J. R. Cheeseman, G. Scalmani, V. Barone, B. Mennucci, G. A. Petersson, H. Nakatsuji, M. Caricato, X. Li, H. P. Hratchian, A. F. Izmaylov, J. Bloino, G. Zheng, J. L. Sonnenberg, M. Hada, M. Ehara, K. Toyota, R. Fukuda, J. Hasegawa, M. Ishida, T. Nakajima, Y. Honda, O. Kitao, H. Nakai, T. Vreven, J. A. Montgomery, Jr., J. E. Peralta, F. Ogliaro, M. Bearpark, J. J. Heyd, E. Brothers, K. N. Kudin, V. N. Staroverov, T. Keith, R. Kobayashi, J. Normand, K. Raghavachari, A. Rendell, J. C. Burant, S. S. Iyengar, J. Tomasi, M. Cossi, N. Rega, J. M. Millam, M. Klene, J. E. Knox, J. B. Cross, V. Bakken, C. Adamo, J. Jaramillo, R. Gomperts, R. E. Stratmann, O. Yazyev, A. J. Austin, R. Cammi, C. Pomelli, J. W. Ochterski, R. L. Martin, K. Morokuma, V. G. Zakrzewski, G. A. Voth, P. Salvador, J. J. Dannenberg, S. Dapprich, A. D. Daniels, O. Farkas, J. B. Foresman, J. V. Ortiz, J. Cioslowski, and D. J. Fox, Gaussian, Inc. Wallingford CT, 2010.

[51] H.-J. Werner, P. J. Knowles, G. Knizia, F. R. Manby, *et al.*, MOLPRO. version 2012.1, 2012.

[52] E. B. Wilson Jr., J. C. Decius, and P. C. Cross, Molecular vibrations (McGraw-Hill, New York, 1995).

[53] Mathematica 8.0; Wolfram Research, Inc., SystemModeler, Version 3.0, Champaign, IL (2012).

[54] H. Köppel, L.S. Cederbaum and W. Domcke, Chem. Phys. **69**, 175 (1982).

[55] Gamess Version= 5 Dec 2014 (R1); From Iowa State University; M. W. Schmidt, K. K. Baldridge, J. A. Boatz, S. T. Elbert et al. J. Comput. Chem. **14**, 1347 (1993).

7 Summary and future directions

A detailed theoretical investigation of the interaction between electronic and nuclear degrees of freedom and their impact on the quantum dynamics of the ground and excited electronic states of radical cations (CH_3F^+, $CH_2F_2^+$, $CD_2F_2^+$) and molecular cluster (H_2B_7) is mainly exemplified in this thesis. Thesis contents detailed account of vibronic coupling theory, mainly the nonadiabatic interactions in a C_{2v} point group symmetry. While the extention of vibronic coupling theory is studied to the higher symmetry molecules (in this thesis within C_{3v} point group symmetry) by considering the special case of Jahn-Teller effect in the ground degenerate state of CH_3F^+. The theoretical studies are based on construction of vibronic Hamiltonian in a diabatic electronic representation and the dimension of the Hamiltonian depends upon the number of considered electronic states for a particular system. A quasi-diabatic approach is used to derive the various Hamiltonian parameters. A special care has been taken to calculate the interstate couplings in the $\widetilde{A}$ and $\widetilde{B}$ states of H_2B_7 in Chapter 6. The same spatial symmetry of these states enforces us to use direct diabatization scheme in stead of quasi-diabatization approach. A 2-D potential energy fits of the calculated ab initio points are performed by following Levenberg-Marquardt algoritm for the simultaneous distortion of the two components of Jahn-Teller actvie modes in Chapter 3. This approach provides more accurate evaluation of the Jahn-Teller Hamiltonian parameters. The Hamiltonian constructed in each Chapter are applied for the nuclear dynamics study, both by time-independent and time-dependent quantum mechanical approach. Theoretically calculated vibronic structures of the photoelectron/photodetachment bands are reported and compared with the available experimental recordings. The theoretical results are found to be in good accord with the experiment. Latter, block-improved relaxation calculations are performed to assign the vibronic energy levels obtained from the time-independent quantum dynamical calculations. The important findings of this thesis are given below.

Chapter 3.

A nuclear dynamics study on the electronic states of relative higher symmetry radical cation, CH_3F^+ is studied in this chapter. Both the diagonal and off-diagonal terms of the constructed JT Hamiltonian are expanded by following higher-order Taylor series and ab initio quantum chemistry calculations are carried out in a large range of normal displacement coordinate. This expanded model of JT Hamiltonian provides more accurate description of the different stationary points of ground state PES of CH_3F^+ and latter, these stationary points are varified by unconstrained direct ab initio calculations. A first principles nuclear quantum dynamics calculations are carried out by time-independent and time-dependent methods and the results of these studies are closely correspond to

the measured ones in the recent experiments. Assignment of vibronic levels are carried out by carefully examining their locations obtained in various reduced dimensional calculations as well as by an explicit analysis of the corresponding vibronic wavefunctions. Such extensive analyses seem to confirm the assignment of fundamentals, various overtones and combination levels.

Chapter 4.

The electronic structure calculations of the $CH_2F_2^+$ and its deuterated isotopomer are perfomed in this chapter. The constructed Hamiltonian belongs to C_{2v} symmetry and it consists with four electronic states. The expansion of the Hamiltonian matrix are carried out upto second-order in diagonal elements and for off-diagonal elements first-order Taylor series approximation is considered. The ab initio energy points for $CH_2F_2^+$ are calculated by three different (CASSCF-MRCI, EOMIP and OVGF) quantum chemistry methods and a comparative account of the obtained data by three different levels of theory is made by following linear regression anlysis. The parameter set derived from the CASSCF-MRCI electronic energies is found to yield best results. Latter, the CASSCF-MRCI level of theory is utilized to perform the electronic structure calculations for $CD_2F_2^+$. A detailed topographical analysis of the four adiabatic electronic states of both $CH_2F_2^+$ and $CD_2F_2^+$ is carried out and multiple conical intersections among them are established. A different topography of the potential energy surfaces are found for $CH_2F_2^+$ and its deuterated analogue, due to the cosideration of mass-weighted normal coordinate representation. The vibronic coupling between the two closely lying excited states, $\widetilde{A}^2B_2$ and $\widetilde{B}^2A_1$, of $CH_2F_2^+$ is elaborately discussed in this chapter on the basis of two-states-single-mode model formalism. The result shows that the symmetry breaking and stabilization of lower coupled adiabatic surface is not possible through single mode interaction, rather it is possible via cummulative interaction of both coupling modes, ν_8 and ν_9.

Chapter 5.

The nuclear dynamics calculations of $CH_2F_2^+$ and its isotopomer ($CD_2F_2^+$) are carried out quantum mechanically both by time-independent and time-dependent methods in this chapter. The vibronic energy level spectrum of the electronic ground state of both $CH_2F_2^+$ and $CD_2F_2^+$ is examined at length. The energy levels appeared in the low energy part are compared with the available experimental results. These energy levels are assigned and discussed in relation to the various assignments reported in the literature. The wavepacket density plots at different eigen values are shwon by using block-improved relaxation method to ensure the fundamentals, overtones and combination peaks of different vibrational modes. The broad band photo-ionization spectrum of both the isotopomers compare well with the low-resolution experimental results. Our analysis on the vibronic levels of the $\widetilde{X}$ state of $CH_2F_2^+$ shows a close resemblance with the PFI-

ZEKE data. The progression on the $\widetilde{X}$ state spectrum of $CH_2F_2^+$ is mainly formed by the ν_2, ν_4, ν_7 and ν_8 vibrational modes and the excitation of the ν_3 vibrational mode is quenched by the ν_7 and ν_8 modes. In the $\widetilde{X}$ state of $CD_2F_2^+$, the vibrational modes ν_3, ν_4, ν_7 and ν_9 make most of the progressions. The excitation of the ν_2 vibrational mode is quenched by the non-totally symmetric vibrational modes in this case. Vibrations of both C-H/D and C-F characters participate in the spectral progression in the $\widetilde{X}$ state of both radical cations. Substantial reduction of vibrational frequencies (except ν_4) upon deuteration, increases the density of vibronic levels in the spectrum of $CD_2F_2^+$. This causes the spectral broadening in case of $CD_2F_2^+$. In contrast to the dynamics of the $\widetilde{X}$ state, the nonadiabatic coupling has much stronger effect on the dynamics of the $\widetilde{A}$, $\widetilde{B}$ and $\widetilde{C}$ states of both $CH_2F_2^+$ and $CD_2F_2^+$. The WP explores multiple intersection seams and quickly relaxes when dynamics is started in any of the three states. Such a fast nonradiative decay of the excited states causes a huge broadening of their vibronic structure as observed in the experiments.

Chapter 6.

The vibronic Hamiltonian constructed in this chapter, has the same form of the constructed Hamiltonian in Chapter 4. As five electronic states of H_2B_7 are considered in this study, the dimesion of the Hamiltonian is differnt from the Hamitonian constructed in Chapter 4. The present Hamiltonian differs from the Hamiltonian in Chapter 4, in the term corresponds to the $\widetilde{A}$-$\widetilde{B}$ interstate coupling, because of the availability of the same spatial symmtery between these states. An additional constant term is added to account the direct electronic coupling between these states. A detailed topography of 1-D PESs along totally symmetric vibrational modes and energetic location of different stationary points on the potential hypersurface of H_2B_7 are examined in this chapter. Analysis shows that the photodetachment bands are obtained due to the nuclear dynamics on the $\widetilde{X}$, $\widetilde{A}$ and $\widetilde{B}$ states. The intensity of the totally symmetric vibrational modes are reduced by the inclusion of coupling vibrational modes via $\widetilde{X}$-$\widetilde{A}$ and $\widetilde{X}$-$\widetilde{B}$ inter-state coupling and spectrum of $\widetilde{X}$ becomes broader than the uncoupled spectrum of $\widetilde{X}$ due to this nonadiabatic effects. It is also found that coupling modes (ν_{10} and ν_{11}) prefer to form combination peaks with ν_2, ν_3, ν_4, ν_6 and ν_7 totally symmetric vibrational modes in the $\widetilde{X}$ state dynamics of H_2B_7. The second band of the experimental recording of $H_2B_7^-$ is not solely correspond to the $\widetilde{A}$ state dynamics. A profound impact of $\widetilde{B}$ state dynamics is also found in this band. A near degenerate VDEs of $\widetilde{A}$ and $\widetilde{B}$ and a quasi-degeneracy between the $\widetilde{A}$-$\widetilde{B}$ CI and minimum of $\widetilde{B}$ state makes the second photodetachment band of $H_2B_7^-$ more diffuse and broader comparative to the first band. A constant pure electronic coupling is found during the consideration of $\widetilde{A}$-$\widetilde{B}$ interstate coupling. The calculated value of this constant ia $\sim$67 cm^{-1}.

The main advantage of this thesis is the availability of modifications of vibronic Hamiltonian, which can be used for same type of system. The higher-order Jahn-Teller Hamil-

tonian constructed in Chapter 3 can be used for same type of molecule or molecular ion with C_3 principal axis of symmetry for more accurate describtion of Jahn-Teller activity. The study of two-modes tunneling splitting of the vibronic energy level, which is very rare in the literature, needs further attention. A detailed topographical features of the electronic states in presence of nonadiabaticity is elaborately examined in Chapter 4 and phenomenon of "symmetry breaking" is also discussed. This phenomenon has immense impact on the nonadiabatic decay dynamics of the optically bright electronic state in presence of a close lying optically dark state. So this aspect can ne further exemplied in this regard. The series of vibronic dynamics study of partially hydrogenated boron clusters, which is initiated in Chapter 6 has immense impact on the boron chemistry and its electronic structure. Among these partially hydrogenated boron clusters, some of them have an open shell electronic configuration (e.g. $H_2B_8^-$). The removal of one electron from α and β molecular orbital produces a singlet and a triplet electronic states, respectively. The application of vibronic coupling theory in the singlet-triplet coupling may find new insight in the inter system crossing mechanism.

Curriculam Vitae:

Rudraditya Sarkar
Prof. S. Mahapatra Lab
School of Chemistry
University of Hyderabad
Hyderabad-500046
India
Email: *rudra.smgr@gmail.com*

List of Publications

1. D. Venkata Sai, K. P. Zuhail, **Rudraditya Sarkar** and Surajit Dhara., "Structure property correlation of bicyclohexane nematic liquid crystal", Liquid Crystals 42, 328-333, 2015.

2. **Rudraditya Sarkar** and S. Mahapatra., "Vibronic coupling in the first four electronic states of $CH_2F_2^+$", Molecular Physics 113, 3073-3084, 2015.

3. Indravath Krishna Naik, **Rudraditya Sarkar** and Samar K. Das., "Nickel(III)-bis(quinoxaline-dithiolato) Complexes, [Bu4N][NiIII(6,7-qdt)$_2$] and [PPh4][NiIII(ph2-6,7-qdt)$_2$]*$CHCl_3$: Synthesis, Spectroscopy, Electrochemistry and DFT Calculations", Eur. J. Inorg. Chem. 5523-5533, 2015.

4. **Rudraditya Sarkar** and S. Mahapatra., "Vibronic Dynamics of Electronic Ground State of $CH_2F_2^+$ and Its Deuterated Isotopomer", J. Phys. Chem. A. 120, 3504-3517, 2016.

5. **Rudraditya Sarkar**., "Non-adiabatic effects in the A^2B_2 and B^2A_1 states of $CH_2F_2^+$ through coupling vibrational modes", J. Phys. Conference series 759, 012058, 2016.

6. **Rudraditya Sarkar**, S. Rajagopala Reddy, S. Mahapatra and Horst. Köppel., "On the Jahn-Teller effect in the X^2E electronic ground state of CH_3F^+", Chem. Phys. 482, 39-51, 2017.

7. Indravath Krishna Naik, **Rudraditya Sarkar**, Vedichi Madhu, Ramababu Bolligarla and samar K. Das., "An organic receptor that generally shows cis-trans isomerism isolated in an intermediate conformation: synthesis, crystal structure, computation, Hirshfeld surfaces and 2D fingerprint plots", (accepted in J. Phys. Chem. A.) .

8. **Rudraditya Sarkar**, Daradi Bashyia and Raja. Kr. Rit."Molecular Design of Novel Nitrogen rich Tetrazine-based Energetic Material", (manuscript under preparation).

9. **Rudraditya Sarkar** and S. Mahapatra., "On the Vibronic Dynamics of the Electronic States of Hydrogenated Boron Cluster I. H_2B_7", (manuscript under preparation)

10. **Rudraditya Sarkar** and S. Mahapatra., "On the Vibronic Dynamics of the Electronic States of Hydrogenated Boron Cluster II. H_2B_8", (manuscript under preparation).

11. Arun Kumar kanakati, **Rudraditya Sarkar** and S. Mahapatra., "Vibronic Dynamics in the first six electronic states of penatafluorobenzene radical cation", (manuscript under preparation).

12. Arun Kumar Kanakati, **Rudraditya Sarkar** and S. Mahapatra.,"Role of optically dark $\pi\sigma^*$ state on the electronic population of optically active $\pi\pi^*$ state of pentafluorobenzene", (manuscript under preparation).

Presentations and participations in Conferences

1. 2015, Oral Presentation at XXVII IUPAP Conference on Computational Physics, December 2-5 2015, IIT Guwahati, India.

2. 2016, Oral Presentation at Chem-fest (2016), in-house symposium held at School of Chemistry, University of Hyderabad, February, 2016, Hyderabad, India.

3. 2016, Oral Presentation at Dr. K. V. Rao Research Awards, 2015-16, 11^{th} June, 2016, Hyderabad, India.

4. 2012, Theoretical Chemistry Symposium 2012, December 19-22, 2012, held at IIT Guwahati, India.

5. 2013, Current Trends in Theoretical Chemistry symposium, September 26-28, 2013 at Bhabha Atomic Research Centre, Mumbai, India

6. 2014, Recent Trends in Chemical Sciences symposium, November 17-18, 2014 at School of Chemistry, University of Hyderabad, Hyderabad, India.

7. 2015, Frontiers in Electronic Structure Theory symposium, May 26-28, 2015 at Goa, India.

8. 2016, A Tributary Symposium on 1000 years of Chemical Bonding by Gilbert N.Lewis, August 4-5, 2016 at CSIR-Indian Institute of Chemical Technology, Hyderabad, India.

9. 2012, 2013, 2014, 2015, 2016 Chem-fest, in-house symposium held at School of Chemistry, University of Hyderabad, February, Hyderabad, India.

10. 2008, Atomic Theory and Scientific Method, Science camp held on July 20, 2008 at PLT-I, Presidency College, Kolkata, India.

11. 2008, National Service Scheme, a seminar on Value: Gandhi and Tagore during July 27-28, 2008 at Indira Gandhi Centre for National Integration, Visva-Bharati, India.

12. 2011, International Year of Chemistry: Impact of Chemistry on our Lives, March 25, 2011 at Depart of Chemistry, Visva-Bharati, India.

MULTIMODE

ORIGINALITY REPORT

%19	%10	%15	%3
SIMILARITY INDEX	INTERNET SOURCES	PUBLICATIONS	STUDENT PAPERS

PRIMARY SOURCES

1	Sarkar, Rudraditya, and Susanta Mahapatra. "Vibronic coupling in the first four electronic states of CH2F+2", Molecular Physics, 2015. Publication	%10
2	universe.bits-pilani.ac.in Internet Source	%1
3	V. Sivaranjana Reddy. "Vibronic interactions in the photodetachment spectroscopy of phenide anion", The Journal of Chemical Physics, 2007 Publication	%1
4	casey.brown.edu Internet Source	%1
5	Kumar, R.R.. "Multistate and multimode vibronic dynamics: The Jahn-Teller and pseudo-Jahn-Teller effects in the ethane radical cation", Chemical Physics, 20061026 Publication	<%1
6	Mahapatra, S.. "Multimode Jahn-Teller and pseudo-Jahn-Teller coupling effects in the photoelectron spectrum of CH"3F", Chemical Physics, 20040913	<%1

	Publication	
7	aim.tkgristmill.com Internet Source	<%1
8	www.chimie.ens.fr Internet Source	<%1
9	www.pci.uni-heidelberg.de Internet Source	<%1
10	nist.gov Internet Source	<%1
11	T. S. Venkatesan. "Exploring the Jahn-Teller and pseudo-Jahn-Teller conical intersections in the ethane radical cation", The Journal of Chemical Physics, 2005 Publication	<%1
12	users.tricity.wsu.edu Internet Source	<%1
13	dosyayukleme.ahievran.edu.tr Internet Source	<%1
14	spectroscopy.chemistry.ohio-state.edu Internet Source	<%1
15	Kunitski, Maksim. "Structure and dynamics of molecules and molecular aggregates in gas phase studied by femtosecond spectroscopy", Publikationsserver der Goethe-Universität Frankfurt am Main, 2010. Publication	<%1

16	www.personalitytheory.org Internet Source	<%1
17	Submitted to Nottingham Trent University Student Paper	<%1
18	www.ccp6.ac.uk Internet Source	<%1
19	etheses.bham.ac.uk Internet Source	<%1
20	www.isu.ru Internet Source	<%1
21	molspect.mps.ohio-state.edu Internet Source	<%1
22	Submitted to Texas Christian University Student Paper	<%1
23	www.ksrnl.com Internet Source	<%1
24	conservancy.umn.edu Internet Source	<%1
25	opus.bibliothek.uni-wuerzburg.de Internet Source	<%1
26	Submitted to University of Surrey Student Paper	<%1
27	G. A. Worth. "Using the MCTDH wavepacket propagation method to describe multimode non-adiabatic dynamics.", International	<%1

	Reviews in Physical Chemistry/0144235X, 20080701 Publication	
28	fermi.uchicago.edu Internet Source	<%1
29	www.qucosa.de Internet Source	<%1
30	pamojsm2012.fr Internet Source	<%1
31	edoc.ub.uni-muenchen.de Internet Source	<%1
32	www.epj-conferences.org Internet Source	<%1
33	r-project.kr Internet Source	<%1
34	dspace.wul.waseda.ac.jp Internet Source	<%1
35	www-pbp.physik.hu-berlin.de Internet Source	<%1
36	b33r.steadynet.org Internet Source	<%1
37	ir.canterbury.ac.nz Internet Source	<%1
38	www.science-softcon.de Internet Source	<%1

39	Siebert, Torsten Uwe. "Four-Wave Mixing Techniques Applied to the Investigation of Non-Adiabatic Dynamics in Polyatomic Molecules", Universität Würzburg, 2002. Publication	<%1
40	kojn.mkzelda.net Internet Source	<%1
41	Submitted to Indian Institute of Science, Bangalore Student Paper	<%1
42	Harding, Michael. "Large-scale coupled-cluster calculations ", 09: Chemie, Pharmazie und Geowissenschaft. 09: Chemie, Pharmazie und Geowissenschaft, 2008. Publication	<%1
43	www.positron.edu.au Internet Source	<%1
44	ta.twi.tudelft.nl Internet Source	<%1
45	euspri-madrid2013.org Internet Source	<%1
46	www.coursehero.com Internet Source	<%1
47	www.publish.csiro.au Internet Source	<%1
48	aleph.physik.uni-kl.de Internet Source	<%1

49	Submitted to Indian Institute of Technology, Madras Student Paper	<%1
50	www.theo.chemie.tu-muenchen.de Internet Source	<%1
51	e.bangor.ac.uk Internet Source	<%1
52	Submitted to University of Birmingham Student Paper	<%1
53	nparc.cisti-icist.nrc-cnrc.gc.ca Internet Source	<%1
54	www.psyc.jmu.edu Internet Source	<%1
55	www.physics.uq.edu.au Internet Source	<%1
56	nhn.ou.edu Internet Source	<%1
57	lphys.chem.utoronto.ca Internet Source	<%1
58	Zgierski, Marek Z. Patchkovskii, Serguei. "Biradical radiationless decay channel in adenine and its derivatives (1).", Canadian Journal of Chemistry, Feb 2007 Issue Publication	<%1
59	www.eabcn.org Internet Source	<%1

60	inst.augie.edu Internet Source	<%1
61	ir.soken.ac.jp Internet Source	<%1
62	www.psi-k.org Internet Source	<%1
63	www.chem.au.dk Internet Source	<%1
64	Weichert, Andreas Riehn, Christoph Bruts. "High-resolution rotational coherence spectroscopy of the phenol dimer.", Journal of Physical Chemistry A, June 14 2001 Issue Publication	<%1
65	www.standardsforhighways.co.uk Internet Source	<%1
66	Submitted to University of Leeds Student Paper	<%1
67	www.mathkb.com Internet Source	<%1
68	Foroutan-Nejad, Cina Shafiee, Gholam Hos. "Ab initio charge density analysis of [([B.sub.6]C).sup.2-] and [B.sub.4][C.sub.3] species--how to de", Canadian Journal of Chemistry, May 2006 Issue Publication	<%1
69	traken.chem.yale.edu Internet Source	<%1

70	www.cwu.edu Internet Source	<%1
71	molspect.chemistry.ohio-state.edu Internet Source	<%1
72	www.chem.utah.edu Internet Source	<%1
73	arxiv.org Internet Source	<%1
74	Submitted to Chulalongkorn University Student Paper	<%1
75	icmol.es Internet Source	<%1
76	"Report Summarizes Molecular Spectroscopy Study Findings from Emory University. (Report)", Science Letter, Sept 14 2012 Issue Publication	<%1
77	pibbs.unm.edu Internet Source	<%1
78	holtmcdougal.hmhco.com Internet Source	<%1
79	tesisenxarxa.net Internet Source	<%1
80	Submitted to King's College Student Paper	<%1
81	Wolf, Martin Gerhard, Ertl. "Electron	

	Dynamics at Surfaces.", Science, May 26 2000 Issue Publication	<%1
82	cc.kangwon.ac.kr Internet Source	<%1
83	www.scribd.com Internet Source	<%1
84	www.qcri.or.jp Internet Source	<%1
85	booktype-demo.sourcefabric.org Internet Source	<%1
86	www.mpi-muelheim.mpg.de Internet Source	<%1
87	www.mpi-stuttgart.mpg.de Internet Source	<%1
88	onlinelibrary.wiley.com Internet Source	<%1
89	www.informatik.uni-kiel.de Internet Source	<%1
90	www.docstoc.com Internet Source	<%1
91	kennychowdhary.me Internet Source	<%1
92	pdsimage.wr.usgs.gov Internet Source	<%1

93	www.synchrotron-soleil.fr Internet Source	<%1
94	ion.chem.usu.edu Internet Source	<%1
95	www.zib.de Internet Source	<%1
96	vm.miigaik.ru Internet Source	<%1
97	www.brookmanstamps.com Internet Source	<%1
98	www.science.gov Internet Source	<%1
99	www.mpipks-dresden.mpg.de Internet Source	<%1
100	scholar.lib.vt.edu Internet Source	<%1
101	www-chem.unifr.ch Internet Source	<%1
102	cdn.intechopen.com Internet Source	<%1
103	Submitted to Mount St. Mary's University Student Paper	<%1
104	etheses.whiterose.ac.uk Internet Source	<%1
	turroserver.chem.columbia.edu	

105	Internet Source	<%1
106	www.atmos-chem-phys-discuss.net Internet Source	<%1
107	air.unimi.it Internet Source	<%1
108	www.eief.it Internet Source	<%1
109	root.genmapp.org Internet Source	<%1
110	edoc.hu-berlin.de Internet Source	<%1
111	www.chem.ubc.ca Internet Source	<%1
112	theochem.chem.rug.nl Internet Source	<%1
113	users.physik.fu-berlin.de Internet Source	<%1
114	viking.otago.ac.nz Internet Source	<%1
115	www.math.nps.navy.mil Internet Source	<%1
116	www.santilariocremona.it Internet Source	<%1
117	clasp-research.engin.umich.edu	

	Internet Source	<%1
118	chemistry.ncssm.edu Internet Source	<%1
119	www.cond-mat.de Internet Source	<%1
120	doc.isiri.org.ir Internet Source	<%1
121	frs.chemistry.ohio-state.edu Internet Source	<%1
122	www.chem.t.u-tokyo.ac.jp Internet Source	<%1
123	comp.chem.umn.edu Internet Source	<%1

EXCLUDE QUOTES	ON	EXCLUDE MATCHES	< 5 WORDS
EXCLUDE BIBLIOGRAPHY	ON		